

Lucas Fidon

Trustworthy Deep Learning for Medical Image Segmentation

King's College London
School of Biomedical Engineering & Imaging Sciences

A dissertation submitted in partial fulfilment
of the requirements for the degree of
Doctor of Philosophy

May 30, 2023

Technical Supervisor
Pr. Tom Vercauteren

Technical Co-Supervisor
Pr. Sébastien Ourselin

Clinical Supervisor
Pr. Jan Deprest

©2023
Lucas Fidon
All Rights Reserved

I, Lucas Fidon, confirm that the work presented in this thesis is my own. Where information has been derived from other sources, I confirm that this has been indicated in the thesis.

Abstract

Despite the recent success of deep learning methods at achieving new state-of-the-art accuracy for medical image segmentation, some major limitations are still restricting their deployment into clinics. One major limitation of deep learning-based segmentation methods is their lack of robustness to variability in the image acquisition protocol and in the imaged anatomy that were not represented or were underrepresented in the training dataset. This suggests adding new manually segmented images to the training dataset to better cover the image variability. However, in most cases, the manual segmentation of medical images requires highly skilled raters and is time-consuming, making this solution prohibitively expensive. Even when manually segmented images from different sources are available, they are rarely annotated for exactly the same regions of interest. This poses an additional challenge for current state-of-the-art deep learning segmentation methods that rely on supervised learning and therefore require all the regions of interest to be segmented for all the images to be used for training.

This thesis introduces new mathematical and optimization methods to mitigate those limitations. Our contributions are threefold.

We introduce the mathematical framework of *label-set loss functions*. This is an infinitely large family of loss functions that can be used to train a deep neural network using partially annotated images, that is images for which some but not necessarily all the regions of interest were segmented or images for which the segmentation of some of the regions of interest were grouped. We propose a method for converting any existing loss function into a label-set loss function and in addition we propose a new label-set loss function that we found to lead to improve segmentation accuracy.

We introduce an optimization algorithm for training deep neural networks using distributionally robust optimization (DRO). We propose to use DRO to improve the generalization of deep neural networks after training on underrepresented populations in the training dataset. We formally prove the convergence of the algorithm when applied to deep neural networks. We also give mathematical insights into the connection between DRO and the maximization of the worst-case performance.

We propose an approach for trustworthy deep learning for medical image segmentation based on Dempster-Shaffer theory. Trustworthy AI is a concept that has been increasingly discussed in sociology and in guidelines for the safe deployment

of emerging technologies such as the deep learning methods used for medical image segmentation. We present the first concrete mathematical framework and implementation of trustworthy AI for medical image segmentation. Our method aims at making a backbone deep learning segmentation algorithm trustworthy with respect to criteria, called *contracts of trust*, that are derived from expert knowledge and correspond to expectations of radiologists expert in the segmentation task at hand.

We illustrate and evaluate the proposed methods on several segmentation tasks with a focus on fetal brain 3D T2w MRI segmentation. The segmentation of fetal brain MRI is essential for the study of normal and abnormal fetal brain development. Reliable analysis and evaluation of fetal brain structures could also support diagnosis of central nervous system pathology, patient selection for fetal surgery, evaluation and prediction of outcome, hence also parental counselling. Fetal brain 3D T2w MRI segmentation presents multiple challenges that align with the limitations of current deep learning algorithms that this thesis aims to mitigate. The manually segmented fetal brain 3D T2w MRIs available are scarce and their level of annotations varies. There are variations in T2w MRI protocols used across clinical centers. Last but not least, there is a spectacular variation of the fetal brain anatomy across gestational ages and across normal and abnormal fetal brain anatomy.

Acknowledgments

First of all, I would like to thank my supervisors Tom Vercauteren, Sébastien Ourselin, and Jan Deprest for their unconditioned and consistent support since the first day we met. I wish to thank Tom Vercauteren for our weekly discussions about science that were particularly fruitful, and Michael Aertsen for teaching me so much about neuroanatomy and the development of the fetal brain.

I would like to thank all my colleagues and friends from London, Leuven, Vienna, Munich, and all the TRABIT family. I also would like to acknowledge the European Union for providing the funding for my PhD project under the Marie Skłodowska-Curie grant agreement TRABIT No 765148.

I am thankful to my parents, Alain and Marianne, and to my siblings, Alexia, Camille, Julia, and Pierre, for letting me follow my passion for science. I used to organize scientific conferences about dinosaurs for them when I was 5 years old. Little did we know that 23 years later I would defend a PhD about artificial intelligence applied to medical image segmentation.

List of Publications

First-author Articles in International Peer-reviewed Journals

1. Lucas Fidon, Elizabeth Viola, Nada Mufti, Anna David, Andrew Melbourne, Philippe Demaerel, Sébastien Ourselin, Tom Vercauteren, Jan Deprest and Michael Aertsen. *A spatio-temporal atlas of the developing fetal brain with spina bifida aperta*. Open Research Europe, volume 1, number 123, 2021.
2. Lucas Fidon, Michael Aertsen, Nada Mufti, Thomas Deprest, Doaa Emam, Frédéric Guffens, Ernst Schwartz, Michael Ebner, Daniela Prayer, Gregor Kasprian *et al.* *Distributionally robust deep learning using hardness weighted sampling*. Machine Learning for Biomedical Imaging, volume 1, 2022.
3. Lucas Fidon, Michael Aertsen, Florian Kofler, Andrea Bink, Anna L David, Thomas Deprest, Doaa Emam, Fr Guffens, András Jakab, Gregor Kasprian *et al.* *A Dempster-Shafer approach to trustworthy AI with application to fetal brain MRI segmentation*. arXiv preprint arXiv:2204.02779, 2022.

First-author Articles in International Peer-reviewed Conferences with Published Proceedings

1. Lucas Fidon, Michael Aertsen, Doaa Emam, Nada Mufti, Frédéric Guffens, Thomas Deprest, Philippe Demaerel, Anna L David, Andrew Melbourne, Sébastien Ourselin *et al.* *Label-set loss functions for partial supervision: application to fetal brain 3D MRI parcellation*. In International Conference on Medical Image Computing and Computer-Assisted Intervention, pages 647–657. Springer, 2021.
2. Lucas Fidon, Michael Ebner, Luis C Garcia-Peraza-Herrera, Marc Modat, Sébastien Ourselin and Tom Vercauteren. *Incompressible image registration using divergence-conforming B-splines*. In International Conference on Medical Image Computing and Computer-Assisted Intervention, pages 438–446. Springer, 2019.

First-author Articles in International Peer-reviewed Workshops with Published Proceedings

1. Lucas Fidon, Sébastien Ourselin and Tom Vercauteren. *Generalized Wasserstein Dice score, distributionally robust deep learning, and ranger for brain tumor segmentation: Brats 2020 challenge*. In International MICCAI Brainlesion Workshop, pages 200–214. Springer, 2020. **4th Place of the BraTS 2020 challenge**.
2. Lucas Fidon, Suprosanna Shit, Ivan Ezhov, Johannes C Paetzold, Sébastien Ourselin and Tom Vercauteren. *Generalized Wasserstein Dice loss, test-time augmentation, and transformers for the BraTS 2021 challenge*. In International MICCAI Brainlesion Workshop. Springer, 2021.
3. Lucas Fidon, Michael Aertsen, Nada Mufti, Thomas Deprest, Doaa Emam, Frédéric Guffens, Ernst Schwartz, Michael Ebner, Daniela Prayer, Gregor Kasprian *et al.* *Distributionally robust segmentation of abnormal fetal brain 3D MRI*. In Uncertainty for Safe Utilization of Machine Learning in Medical Imaging, and Perinatal Imaging, Placental and Preterm Image Analysis, pages 263–273. Springer, 2021.
4. Lucas Fidon, Michael Aertsen, Suprosanna Shit, Philippe Demaerel, Sébastien Ourselin, Jan Deprest and Tom Vercauteren. *Partial supervision for the FeTA challenge 2021*. In Uncertainty for Safe Utilization of Machine Learning in Medical Imaging, and Perinatal Imaging, Placental and Preterm Image Analysis. Springer, 2021.

Co-author Articles in International Peer-reviewed Journals

1. T Deprest, L Fidon, F De Keyzer, M Ebner, J Deprest, P Demaerel, L De Catte, T Vercauteren, S Ourselin, S Dymarkowski *et al.* *Application of automatic segmentation on super-resolution reconstruction MR images of the abnormal fetal brain*. American Journal of Neuroradiology, volume 44, number 4, pages 486–491, 2023.
2. D Emam, M Aertsen, L Van der Veeken, L Fidon, P Patkee, V Kyriakopoulou, L De Catte, F Russo, P Demaerel, T Vercauteren *et al.* *Longitudinal MRI evaluation of brain development in fetuses with congenital diaphragmatic hernia*

- around the time of fetal endotracheal occlusion*. American Journal of Neuro-radiology, 2023.
3. Nada Mufti, Michael Aertsen, Michael Ebner, Lucas Fidon, Premal Patel, Muhamad Bin Abdul Rahman, Yannick Brackenier, Gregor Ekart, Virginia Fernandez, Tom Vercauteren *et al.* *Cortical spectral matching and shape and volume analysis of the fetal brain pre-and post-fetal surgery for spina bifida: a retrospective study*. Neuroradiology, volume 63, number 10, pages 1721–1734, 2021.
 4. N. Mufti, J. Chappell, M. Aertsen, M. Ebner, L. Fidon, J. Deprest, A. L. David, A. Melbourne and the GIFT-Surg Imaging Working Group. *Assessment of longitudinal brain development using super-resolution magnetic resonance imaging following fetal open spina bifida surgery*. Ultrasound in Obstetrics & Gynecology, 2023.
 5. Luis C Garcia-Peraza-Herrera, Lucas Fidon, Claudia D’Ettorre, Danail Stoyanov, Tom Vercauteren and Sébastien Ourselin. *Image compositing for segmentation of surgical tools without manual annotations*. IEEE transactions on medical imaging, volume 40, number 5, pages 1450–1460, 2021.
 6. Florian Kofler, Ivan Ezhov, Lucas Fidon, Carolin M Pirkl, Johannes C Paetzold, Egon Burian, Sarthak Pati, Malek El Husseini, Fernando Navarro, Suprosanna Shit *et al.* *Robust, primitive, and unsupervised quality estimation for segmentation ensembles*. Frontiers in Neuroscience, volume 15, 2021.
 7. Kelly Payette, Hongwei Li, Priscille de Dumast, Roxane Licandro, Hui Ji, Md Mahfuzur Rahman Siddiquee, Daguang Xu, Andriy Myronenko, Hao Liu, Yuchen Pei *et al.* *Fetal brain tissue annotation and segmentation challenge results*. Medical Image Analysis, page 102833, 2023.
 8. Matthias Eisenmann, Annika Reinke, Vivienn Weru, Minu Dietlinde Tizabi, Fabian Isensee, Tim J Adler, Patrick Godau, Veronika Cheplygina, Michal Kozubek, Sharib Ali *et al.* *Biomedical image analysis competitions: The state of current participation practice*. arXiv preprint arXiv:2212.08568, 2022.

Co-author Articles in International Peer-reviewed Conferences with Published Proceedings

1. Muhammad Asad, Lucas Fidon and Tom Vercauteren. *ECONet: Efficient*

- convolutional online likelihood network for scribble-based interactive segmentation.* In Medical Imaging with Deep Learning. PMLR, 2022.
2. Florian Kofler, Suprosanna Shit, Ivan Ezhov, Lucas Fidon, Izabela Horvath, Rami Al-Maskari, Hongwei Li, Harsharan Bhatia, Timo Loehr, Marie Pi-raudet *al.* *blob loss: instance imbalance aware loss functions for semantic segmentation.* arXiv preprint arXiv:2205.08209, 2022.

Co-author Articles in International

Peer-reviewed Workshops with Published Proceedings

1. Hassna Irzan, Lucas Fidon, Tom Vercauteren, Sebastien Ourselin, Neil Marlow and Andrew Melbourne. *Min-cut max-flow for network abnormality detection: Application to preterm birth.* In Uncertainty for Safe Utilization of Machine Learning in Medical Imaging, and Graphs in Biomedical Image Analysis, pages 164–173. Springer, 2020.
2. Florian Kofler, Ivan Ezhov, Lucas Fidon, Izabela Horvath, Ezequiel de la Rosa, John LaMaster, Hongwei Li, Tom Finck, Suprosanna Shit, Johannes Paetzoldet *al.* *Deep quality estimation: Creating surrogate models for human quality ratings.* arXiv preprint arXiv:2205.10355, 2022.

Table of Contents

Abstract	5
Acknowledgments	7
List of Publications	9
1 Introduction	29
1.1 Background on Deep Learning for Medical Image Segmentation . . .	29
1.2 Trustworthy Deep Learning	33
1.3 Thesis Organization and Contributions	34
2 Related Work	37
2.1 Trustworthy AI	37
2.1.1 Background on Human-AI trust	37
2.1.2 Domain generalization	38
2.1.3 Information fusion for trustworthy medical image segmentation	39
2.2 Fetal Brain MRI Segmentation	40
2.2.1 Atlas-based fetal brain MRI segmentation methods.	41
2.2.2 Deep learning-based fetal brain MRI segmentation methods. .	43
2.2.3 Comparison of atlas-based and deep learning-based methods	45
2.2.4 Combining atlas-based and deep learning-based methods. . .	46
3 Fetal Brain 3D MRI Segmentation Dataset	47
3.1 Introduction	48
3.1.1 Spina Bifida Aperta	50
3.1.2 Super-Resolution and Reconstruction: From 2D to 3D	51
3.2 Fetal Brain MRI Dataset	52
3.2.1 Underlying MRI data	52
3.2.2 Fetal MRI Acquisition Details	55
3.2.3 Automatic Brain Extraction	55
3.2.4 Super-Resolution and Reconstruction	56
3.2.5 Semi-automatic Fetal Brain 3D MRI Segmentations	56
3.2.6 Data availability	61
3.3 Conclusion	63

4	Label-set Loss Functions for Partial Supervision	65
4.1	Introduction to partially supervised learning	65
4.2	Theory of Label-set Loss Functions	66
4.2.1	Label-set Loss Functions	67
4.2.2	Leaf-Dice: A Label-set Generalization of the Dice Loss	68
4.2.3	Converting Classical Loss Functions to Label-set Loss Functions	69
4.3	MRI Datasets	70
4.3.1	Fetal Brain MRI Data with Partial Segmentations	70
4.3.2	Brain Tumor multi-parametric MRI Dataset	71
4.4	Experiments	72
4.5	Conclusion	77
5	Distributionally Robust Deep Learning	81
5.1	Introduction on Distributionally Robust Deep Learning	82
5.2	Related Works	85
5.3	Methods	87
5.3.1	Supervised Deep Learning with Distributionally Robust Optimization	87
5.3.2	Hardness Weighted Sampling for Distributionally Robust Deep Learning	89
5.3.3	Overview of Theoretical Results	93
5.4	Experiments	95
5.4.1	Toy Example: MNIST Classification with a Class Imbalance	96
5.4.2	Medical Image Segmentation	97
5.5	Discussion and Conclusion	108
6	Spina Bifida Fetal Brain MRI Atlas	111
6.1	Introduction	112
6.2	Materials	114
6.3	Atlas Computation Method	115
6.3.1	Data Preprocessing	115
6.3.2	Atlas Construction	119
6.3.3	Semi-automatic Segmentation of the Atlas	123
6.4	Annotation Protocol of Anatomical Landmarks for Fetuses with Spina Bifida Aperta	124
6.4.1	Anterior horn of the right lateral ventricle	124
6.4.2	Anterior horn of the left lateral ventricle	125
6.4.3	Posterior tectum plate	125

6.4.4	Left cerebellar-brainstem junction	126
6.4.5	Right cerebellar-brainstem junction	126
6.4.6	Left deep grey border at foramen of Monro	126
6.4.7	Right deep grey border at foramen of Monro	127
6.4.8	Left deep grey border at anterior cavum septi pellucidi line .	127
6.4.9	Right deep grey border at the anterior cavum septi pellucidi line	128
6.4.10	Left deep grey border at posterior cavum septi pellucidi line .	128
6.4.11	Right deep grey border at the posterior cavum septi pellucidi line	129
6.5	Results	130
6.5.1	Intra-rater Variability for the Annotation of the Anatomical Landmarks	130
6.5.2	Automatic Segmentation of Fetal Brain 3D MRIs	132
6.6	Discussion	133
6.7	Limitations	135
6.8	Data Availability	136
6.9	Software Availability	136
6.10	Conclusion	136
7	A Dempster-Shafer approach to Trustworthy AI	139
7.1	Introduction on Trustworthy AI using a Fallback	140
7.2	Materials and Methods	144
7.2.1	Fetal brain MRI dataset	144
7.2.2	Background on Dempster-Shafer theory	144
7.2.3	A Dempster-Shafer approach to Trustworthy AI for medical image segmentation	147
7.2.4	Human expert scoring method for evaluating the trustworthi- ness of fetal brain 3D MRI segmentation	161
7.3	Code Availability	162
7.4	Results	163
7.5	Discussion	169
8	Conclusion	175
8.1	Conclusion	175
8.2	Discussion and Future Work	177
8.2.1	Semi-automatic segmentation for trustworthy AI	177
8.2.2	Future work on fetal brain segmentation	178

8.2.3	Impact of the fetal brain MRI segmentation algorithm developed in this thesis	179
Bibliography		181
Appendix		218
A.1	Appendix of chapter 3	220
A.1.1	Lexic of Fetal Neuroanatomy for Engineers	220
A.2	Proofs of chapter 4	222
A.2.1	Summary of mathematical notations	222
A.2.2	Proof of equation (4.3)	222
A.2.3	Proof that the leaf-Dice is a label-set loss function	223
A.2.4	Proof of equation (4.7)	223
A.2.5	Relation to the marginal Dice loss	224
A.3	Additional Experiments on BraTS 2021	225
A.4	Proofs of chapter 5	226
A.4.1	Summary of the Notations used in the Proofs	226
A.4.2	Evaluation of the Influence of β on the Segmentation Performance for BraTS	227
A.4.3	Importance Sampling Approximation in Algorithm 1	228
A.4.4	Proof of Example 5.3.1: Formula of the Sampling Probabilities for the KL Divergence	228
A.4.5	Proof of Lemma 5.3.1: Regularity Properties of R	230
A.4.6	Proof of Lemma 5.3.2: Formula of the Distributionally Robust Loss Gradient	232
A.4.7	Proof of Theorem 5.3.4: Distributionally Robust Optimization as Principled Hard Example Mining	233
A.4.8	Proof of Equivalence between (5.17) and (5.18): Link between DRO and Percentile Loss	236
A.4.9	Proof of Theorem 5.3.3: convergence of SGD with Hardness Weighted Sampling for Over-parameterized Deep Neural Networks with ReLU	237
A.5	Additional Results for chapter 7	258
A.5.1	Class-wise Quantitative Evaluation.	258
A.5.2	Tuning of the Registration Parameters	263
A.6	Proofs of chapter 7	264
A.6.1	Proof of the Formula (7.15) for the Anatomical BPA.	264
A.6.2	Proof of Equality (7.17).	269

List of Tables

4.1	Number of 3D MRI and number of manual segmentations available per tissue types. WM : white matter, Vent : ventricular system, Cer : cerebellum, ECSF : extra-ventricular CSF, CGM : cortical gray matter, DGM : deep gray matter, BS : brainstem, CC : corpus callosum.	70
4.2	Evaluation on the multi-centric testing fetal brain dataset (100 3D MRIs).	74
5.1	Training and Testing Fetal Drain 3D MRI Dataset Details. Other Abn: brain structural abnormalities other than spina bifida. There is no overlap of subjects between training and testing.	98
5.2	Evaluation of Distribution Robustness with Respect to the Pathology (260 3D MRIs). nnU-Net-ERM is the unmodified nnU-Net pipeline [Isensee 21] in which Empirical Risk Minimization (ERM) is used. nnU-Net-DRO is the nnU-Net pipeline modified to use the proposed <i>hardness weighted sampler</i> and in which Distributionally Robust Optimization (DRO) is therefore used. WM : White matter, In-CSF : Intra-axial CSF, Cer : Cerebellum. IQR: interquartile range, p_X : X^{th} percentile of the Dice score distribution in percentage. Best values are in bold.	102
5.3	Dice Score Evaluation on the BraTS 2019 Online Validation Set (125 cases). Metrics were computed using the BraTS online evaluation platform (https://ipp.cbica.upenn.edu/). ERM: Empirical Risk Minimization, DRO: Distributionally Robust Optimization, SGD: plain SGD (no momentum used), Nesterov: SGD with Nesterov momentum, IQR: Interquartile range. The best values are in bold.	103

- 6.1 **Evaluation of the reliability of the landmarks.** We report the estimated percentiles of distances in millimeters between first and second marking for each proposed landmarks. P_{75} : 75th percentile of distances in millimeters. P_{80} : 80th percentile of distances in millimeters. P_{95} : 95th percentile of distances in millimeters. Our reliability score is defined in section 6.5.1. **LALV**: Anterior Horn of the Left Lateral Ventricle, **RALV**: Anterior Horn of the Right Lateral Ventricle, **PTP**: Posterior Tectum Plate, **LCB**: Left Cerebellar Brainstem Junction, **RCB**: Right Cerebellar Brainstem Junction, **LFOM**: Left Deep Grey Border at Foramen of Monroe, **RFOM**: Right Deep Grey Border at Foramen of Monroe, **LACSP**: Left Deep Grey Border at Anterior Cavum Septi Pellucidi line, **RACSP**: Right Deep Grey Border at Anterior Cavum Septi Pellucidi line, **LPCSP**: Left Deep Grey Border at Posterior Cavum Septi Pellucidi line, **RPCSP**: Right Deep Grey Border at the Posterior Cavum Septi Pellucidi line. 132
- 6.2 **Evaluation of automatic fetal brain segmentation.** We report mean (standard deviation) for the Dice score (DSC) in percentages and the Hausdorff distance at 95% (HD95) in millimeters for the seven tissue types. The spina bifida atlas is the atlas contributed in this chapter. The normal atlas is a spatio-temporal atlas computed from 3D MRIs of fetuses with a normal brain [Gholipour 17]. **WM**: white matter, **Vent**: ventricular system, **Cer**: cerebellum, **CSF**: cerebrospinal fluid, **ECSF**: extra-axial CSF, **CGM**: cortical gray matter, **DGM**: deep gray matter, **BS**: brainstem. 134
- A.1 **Detailed evaluation on the BraTS 2019 online validation set (125 cases).** All the models in this table were trained using the default **SGD with Nesterov momentum** of nnU-Net [Isensee 21]. Dice scores were computed using the BraTS online platform for evaluation <https://ipp.cbica.upenn.edu/>. **ERM**: Empirical Risk Minimization, **DRO**: Distributionally Robust Optimization, **IS**: Importance Sampling is used, **IQR**: Interquartile range. The best values are in bold. 227

A.2 Tuning of the registration parameters. We report the population average of the mean-class Dice score (DSC) in percentages. We also report the average number of volumes that need to be registered for each configuration. This number is approximately proportional to the computational time for the segmentation computation. The 3D MRIs used were the fold 0 of the training dataset. The row highlighted in **blue** (resp. **orange**) correspond to the value of ΔGA selected for the neurotypical cases (resp. the spina bifida cases). A higher value of ΔGA leads to using more volumes in the fallback, registration-based segmentation method. Hence, this difference of ΔGA reflects the use of two neurotypical atlases [Gholipour 17, Wu 21] while only one spina bifida atlas [Fidon 21e] is available. . . 263

List of Figures

1.1	Diagram of a deep learning optimization pipeline. Deep learning optimization methods are made of four main components: 1) the design of the deep neural network architecture, 2) the per-sample loss function (e.g. the Dice loss) that determines the stochastic gradient, 3) the optimization problem (e.g. the empirical risk) that determines how to merge the stochastic gradients into one aggregated gradient, 4) the optimizer (e.g. SGD, Adam) that determines how the aggregated gradient is used to update the parameters of the deep neural network at each training iteration. In this work, we explore variants for the per-sample loss function, the population loss function and the optimizer for application to automatic brain tumor segmentation.	31
3.1	Illustration of the anatomical variability in fetal brain across gestational ages and diagnostics. 1: Control (22 weeks); 2: Control (26 weeks); 3: Control (29 weeks); 4: Spina bifida (19 weeks); 5: Spina bifida (26 weeks); 6: Spina bifida (32 weeks); 7: Dandy-walker malformation with corpus callosum abnormality (23 weeks); 8: Dandy-walker malformation with ventriculomegaly and periventricular nodular heterotopia (27 weeks); 9: Aqueductal stenosis (34 weeks).	49
3.2	Histogram of the gestational ages for each group of centers and for neurotypical, spina bifida, and other pathologies for the full dataset.	53
3.3	Proposed brain classes hierarchy for the developing fetal brain. . . .	57
3.4	Manual Segmentation Inter-rater Variability. The evaluation is performed using two manual segmentations for 78 3D MRIs from the FeTA dataset [Payette 21]. (left) the Dice score (in percentage) and (right) Hausdorff distance at 95% percentiles (HD95; in mm). WM: white matter, in-CSF: intra-axial cerebrospinal fluid, CER: cerebellum, ext-CSF: extra-axial cerebrospinal fluid, CGM: cortical gray matter, DGM: deep gray matter, BST: brainstem.	60

-
- 4.1 Illustration of partial annotations on a control fetal brain MRI [Gholipour 17].
 b) all the leaf-labels are annotated. c) partial annotations where cortical gray matter (CGM), deep gray matter (DGM), and brainstem (B) are not annotated. In this cases, unannotated voxels have the label-set annotation {CGM, DGM, B}. 67
- 4.2 Illustration of the partial annotations used for experiments on brain tumor segmentation. In blue is the tumor core, a label-set containing the enhancing tumor (yellow) and non-enhancing tumor (red). In purple is another label-set that contains the peritumoral edema (green) and the background. 71
- 4.3 Qualitative comparison on an open spina bifida case. Only the proposed Leaf-Dice loss provides satisfactory segmentations for all tissue types. 72
- 4.4 **Dice score evaluation for the ablation study on the ratio of partially segmented and fully segmented cases using the BraTS 2021 training dataset.** The **percentages** in the legend correspond to the percentage of fully-segmented cases used during training. The rest of the segmentation of the training dataset are converted into partial segmentations as described in Fig. 4.2. **Fully-supervised learning** (no hatches) corresponds to training with standard Dice loss plus cross entropy using only the fully segmented data. In this case the partially segmented cases are not used. **Partially-supervised learning** (hatches) corresponds to training with both fully-segmented and partially-segmented cases using the marginalized Dice loss plus the marginalized cross entropy. Each box plot results from 5-fold cross validation on the 1251 cases. Box limits are the first quartiles and third quartiles. The central ticks are the median values. The whiskers extend the boxes to show the rest of the distribution, except for points that are determined to be outliers. Outliers are data points outside the range median $\pm 1.5 \times$ interquartile range. 79

- 4.5 **Hausdorff distance at percentile 95% evaluation for the ablation study on the ratio of partially segmented and fully segmented cases using the BraTS 2021 training dataset.** The **percentages** in the legend correspond to the percentage of fully-segmented cases used during training. The rest of the segmentation of the training dataset are converted into partial segmentations as described in Fig. 4.2. **Fully-supervised learning** (no hatches) corresponds to training with standard Dice loss plus cross entropy using only the fully segmented data. In this case the partially segmented cases are not used. **Partially-supervised learning** (hatches) corresponds to training with both fully-segmented and partially-segmented cases using the marginalized Dice loss plus the marginalized cross entropy. Each box plot results from 5-fold cross validation on the 1251 cases. Box limits are the first quartiles and third quartiles. The central ticks are the median values. The whiskers extend the boxes to show the rest of the distribution, except for points that are determined to be outliers. Outliers are data points outside the range $\text{median} \pm 1.5 \times \text{interquartile range}$. Outliers higher than 50 mm are not displayed. 80
- 5.1 Illustration of the anatomical variability in fetal brain across gestational ages and diagnostics. 1: Control (22 weeks); 2: Control (26 weeks); 3: Control (29 weeks); 4: Spina bifida (19 weeks); 5: Spina bifida (26 weeks); 6: Spina bifida (32 weeks); 7: Dandy-walker malformation with corpus callosum abnormality (23 weeks); 8: Dandy-walker malformation with ventriculomegaly and periventricular nodular heterotopia (27 weeks); 9: Aqueductal stenosis (34 weeks). 85
- 5.2 **Experiments on MNIST.** We compare the learning curves at testing (top panels) and at training (bottom panels) for ERM with SGD (blue) and DRO with our SGD with hardness weighted sampling for different values of β ($\beta = 0.1$, $\beta = 1$, $\beta = 10$, $\beta = 100$). The models are trained on an imbalanced MNIST dataset (only 1% of the digits 3 kept for training) and evaluated on the original MNIST testing dataset. 97

- 5.3 Qualitative Results for Fetal Brain 3D MRI Segmentation using DRO.** a) Fetus with aqueductal stenosis (34 weeks). b) Fetus with spina bifida aperta (27 weeks). c) Fetus with Blake’s pouch cyst (29 weeks). d) Fetus with tuberous sclerosis complex (34 weeks). e) Fetus with spina bifida aperta (22 weeks). f) Fetus with spina bifida aperta (31 weeks). g) Fetus with spina bifida aperta (28 weeks). For cases a) and b), nnU-Net-ERM [Isensee 21] misses completely the cerebellum and achieves poor segmentation for the white matter and the ventricles. For case c), a large part of the Blake’s pouch cyst is wrongly included in the ventricular system segmentation by nnU-Net-ERM. This is not the case for the proposed nnU-Net-DRO. For case d), nnU-Net-ERM fails to segment the cerebellum correctly and a large part of the cerebellum is segmented as part of the white matter. In contrast, our nnU-Net-DRO correctly segment cerebellum and white matter for this case. For cases e) f) and g), we have added yellow arrows pointing to large parts of the brainstem that nnU-Net-ERM wrongly included in the cerebellum segmentation. nnU-Net-DRO does not make this mistake. We emphasise that the segmentation of the cerebellum for spina bifida aperta is essential for studying and evaluating the effect of surgery in-utero. 104
- 5.4 Dice scores distribution on the BraTS 2019 validation dataset for cases from a center of TCIA (76 cases) and cases from other centers (49 cases).** This shows that the lower interquartile range of DRO for the enhancing tumor comes specifically from a lower number of poor segmentations on cases coming from The Cancer Imaging Archive (TCIA). This suggests that DRO can deal with some of the confounding biases present in the training dataset, and lead to a model that is more fair. 105
- 6.1 Distribution of gestational ages for operated (fetal surgery) and non-operated fetal brains.** The dataset used to compute the atlas contains 39 magnetic resonance imaging (MRI) examinations of non-operated fetuses and 51 MRI examinations of operated fetuses. 114
- 6.2 Overview of the spatio-temporal atlas construction pipeline. MRI: magnetic resonance imaging.** 115

6.3	Overview of the proposed anatomical landmarks. Those landmarks were annotated for all the 3D reconstructed magnetic resonance imaging (MRI). They aim at improving the accuracy and the robustness of the image registration steps.	117
6.4	Anterior horn of the right lateral ventricle (green) and anterior horn of the left lateral ventricle (blue).	124
6.5	Posterior tectum plate (pink).	125
6.6	Right cerebellar-brainstem junction (turquoise) and left cerebellar-brainstem junction (pink).	125
6.7	Left deep grey matter border at foramen of Monro (dark olive) and right deep grey matter border at foramen of Monro (lime green). . .	126
6.8	Deep grey matter border with respect to the cavum septi pellucidi (CSP).	128
6.9	Our spatio-temporal atlas for spina bifida aperta - Part I (not operated). Publicly available here.	130
6.10	Spatio-temporal atlas for spina bifida aperta - Part II (operated). Publicly available here.	131
6.11	Cavum septi pellucidi (CSP) variation fetuses with 25 weeks of gestation. Yellow arrows indicate the anterior and posterior borders of the CSP as defined by the landmark localisation protocol. This visualisation illustrates the disparity between volumes in terms of shape and size of the CSP.	133

- 7.1 **Schematics of our principled method for trustworthy AI applied to medical image segmentation.** **a.** Deep neural networks for medical image segmentation (AI algorithm) are typically trained on images from a limited number acquisition centers. This is usually not sufficient to cover all the anatomical variability. **b.** When the trained AI algorithm is deployed, it will typically give satisfactory accuracy for images acquired with the same protocol as training images and with a health condition represented in the training dataset (left). However, the AI algorithm might fail with errors that are not anatomically plausible, for images acquired with a slightly different protocol as training images and/or representing anatomy underrepresented in the training dataset (right). **c.** Schematic of the proposed trustworthy AI algorithm. The backbone AI segmentation algorithm is coupled with a *fallback* segmentation algorithm. Experts knowledge about the anatomy is modelled using Dempster-Shafer theory. When part of the AI segmentation is found to contradict expert knowledge for a voxel, our trustworthy AI algorithm automatically switches to the fallback segmentation for this voxel. 143
- 7.2 **Composition of the training and testing datasets (total: 540 3D MRIs)** *In-scanner distribution* designates the 3D MRIs acquired at the same center as the training data. *Out-of-scanner distribution* designates the 3D MRIs acquired at different centers than the training data. This is the largest fetal brain MRI dataset reported to date. 145
- 7.3 **Implementation of the anatomical BPA for the white matter of a fetus with spina bifida.** The white matter basic probability assignment (BPA) is computed by dilating the white matter mask of the fallback algorithm $M^{\text{white matter}}$ using the margin $\eta_{\text{white matter}}$. The margin aims at eliminating the false negative for the mask $M^{\text{white matter}}$ and are estimated using the training dataset. The white matter BPA imposes that no white matter can be predicted outside the dilated mask. No constraint is imposed inside the dilated mask. The same approach is applied to all the regions of interest to be segmented. 153

- 7.4 **Illustration of the margin distance.** The margin distance is the minimal dilation radius to apply to the predicted binary mask so that it covers entirely the ground-truth binary mask. We have proposed to use the margin distance to define our margins used in our definition of the anatomical BPAs. 156
- 7.5 Illustration of the improved robustness of the proposed trustworthy AI method (TW-AI) as compared to a state-of-the-art AI method. (Top) 3D MRI of a neurotypical fetus at 28 weeks of gestation acquired at the same center as the training data for the AI. (Bottom) 3D MRI of a fetus with a high-flow dural sinus malformation at 28 weeks of gestation acquired at a different center as the training data for the AI. Severe violations of the anatomy by the AI, but not the TW-AI, are highlighted in white. 163
- 7.6 **Comparison of the backbone AI, fallback, and trustworthy AI segmentation algorithms.** In (a) (resp. (b)), we report for each algorithm the distributions of Dice scores (resp. Hausdorff distances at 95% percentile (HD95)) for in-scanner distribution ($n = 182$) and out-of-scanner distribution ($n = 167$) images and for neurotypical ($n = 141$), spina bifida ($n = 157$), and other pathologies ($n = 51$). In (c) (resp. (d)), we report mean and 95% confidence intervals for the Dice scores (resp. HD95) across gestational ages, for neurotypical and spina bifida cases. In (e), we report 4 scoring by a panel of 8 experts of the trustworthiness of the automatic segmentations for a subset of the out-of-scanner distribution testing 3D MRIs ($n = 50$). Each expert was asked to score from 0 (totally unacceptable) to 5 (perfect fit) the trustworthiness of each ROI. The scores displayed here are averaged across ROIs. Results per ROI can be found in the appendix (Fig. A.2, A.3, A.4, A.5, A.6). Box limits are the first quartiles and third quartiles. The central ticks are the median values. The whiskers extend the boxes to show the rest of the distribution, except for points that are determined to be outliers. Outliers are data points outside the range median $\pm 1.5 \times$ interquartile range. 168

- A.1 **Evaluating the capacity of the 3D U-Net architecture on the BraTS 2021 training dataset (1251 cases).** Wide 3D U-Net has the same architecture as 3D U-Net with twice as many features in every internal layers, i.e. it has approximately 4 times more trainable parameters. There is no difference of segmentation performance between the two models which suggests that the 3D U-Net is already large enough for training on this dataset. Each box plot results from 5-fold cross validation on the 1251 cases. Box limits are the first quartiles and third quartiles. The central ticks are the median values. The whiskers extend the boxes to show the rest of the distribution, except for points that are determined to be outliers. Outliers are data points outside the range median $\pm 1.5 \times$ interquartile range. 225
- A.2 **Dice score (in %) comparison of our AI, fallback, and trustworthy AI segmentation algorithms for fetal brain 3D MRI segmentation.** Dice scores are reported for all 3D MRI for 7 tissue types: white matter (**WM**), intra-axial cerebrospinal fluid (**in-CSF**), cerebellum (**Cer**), extra-axial cerebrospinal fluid (**Ext-CSF**), cortical gray matter (**CGM**), deep gray matter (**DGM**), brainstem (**BST**), and corpus callosum (**CC**). Box limits are the first quartiles and third quartiles. The central ticks are the median values. The whiskers extend the boxes to show the rest of the distribution, except for points that are determined to be outliers. Outliers are data points outside the range median $\pm 1.5 \times$ interquartile range. Fig. 7.6c was obtained from the same data after averaging the scores across regions of interest for each 3D MRI. 258
- A.3 **Hausdorff distance (in mm) comparison of our AI, fallback, and trustworthy AI segmentation algorithms for fetal brain 3D MRI segmentation.** The organization and legend of this figure is the same as in Fig. 7.6a, except that here the Hausdorff distance at 95% percentile is reported in place of the Dice score. To improve the visualization we have clipped the distances to a maximum value. The clipped outliers are still visible on the top of each boxplot. Fig. 7.6b was obtained from the same data after averaging the scores across regions of interest for each 3D MRI. Box limits are the first quartiles and third quartiles. The central ticks are the median values. The whiskers extend the boxes to show the rest of the distribution, except for points that are determined to be outliers. Outliers are data points outside the range median $\pm 1.5 \times$ interquartile range. 259

- A.4 Mean Dice score (in %) and 95% confidence interval as a function of the gestational age.** Here, we have used all the neurotypical and the spina bifida cases of the testing dataset. The trustworthy AI (in green) algorithm achieves similar or higher Dice scores than the best of the backbone AI (in blue) and the fallback (in orange) for all tissue type and all gestational age. Fig. 7.6c was obtained from the same data after averaging the scores across regions of interest for each 3D MRI. Box limits are the first quartiles and third quartiles. The central ticks are the median values. The whiskers extend the boxes to show the rest of the distribution, except for points that are determined to be outliers. Outliers are data points outside the range $\text{median} \pm 1.5 \times \text{interquartile range}$ 260
- A.5 Mean Hausdorff distance (in mm) and 95% confidence interval as a function of the gestational age.** Here, we have used all the neurotypical and the spina bifida cases of the testing dataset. The trustworthy IA (in green) algorithm achieves similar or lower Hausdorff distance than the best of the backbone AI (in blue) and the fallback (in orange) for all tissue type and all gestational age. Fig. 7.6d was obtained from the same data after averaging the scores across regions of interest for each 3D MRI. 261
- A.6 Experts scores for out-of-distribution 3D MRIs.** A panel of 8 experts performed 4 independent scoring for each ROI. The scores of different experts for a given region of interest and for a given 3D MRI were aggregated using averaging. Here, we have used 50 out-of-scanner distribution 3D MRIs from the FeTA dataset (20 neurotypical, 20 spina bifida, and 10 other pathologies). Box limits are the first quartiles and third quartiles. The central ticks are the median values. The whiskers extend the boxes to show the rest of the distribution, except for points that are determined to be outliers. Outliers are data points outside the range $\text{median} \pm 1.5 \times \text{interquartile range}$. Fig. 7.6e was obtained from the same data after averaging the scores across regions of interest for each 3D MRI. 262

Introduction

Table of Contents

1.1	Background on Deep Learning for Medical Image Segmentation	29
1.2	Trustworthy Deep Learning	33
1.3	Thesis Organization and Contributions	34

Foreword In this introductory chapter, the background on deep learning for medical image segmentation has used elements from [Fidon 20]. The review of related work in medical image segmentation using deep learning has been extended and additional references have been added. The background on trustworthy deep learning has used elements from [Fidon 21b, Fidon 22a, Fidon 22b].

1.1 Background on Deep Learning for Medical Image Segmentation

Medical image segmentation is the extraction of regions of interest (ROIs) from images, e.g. Magnetic Resonance Imaging (MRI). Segmentation is required for the computation of volume and surface-based biomarkers and therefore aims at the quantification of the anatomy. It has many applications in clinical research and clinical practice. Examples of applications of segmentation in fetal brain MRI can be found in Chapter 3. Manual medical image segmentation is time-consuming, requires highly skilled raters, and is subject to inter-rater and intra-rater variability. Automatic methods for medical image segmentation methods are therefore required.

Formally, automatic medical image segmentation consists in finding a function h , computable by a computer

$$\begin{aligned}
 h : \mathbb{R}^{N \times M} &\rightarrow \mathbf{L}^N \\
 \mathbf{x} &\mapsto \mathbf{y}
 \end{aligned}
 \tag{1.1}$$

where the variable \mathbf{x} corresponds to an image or volume, with M imaging modalities, to be segmented, N is the number of voxels in each image, the variable \mathbf{y} is the

automatic segmentation computed by h , and \mathbf{L} is a finite set of labels associated with the regions of interest to be segmented.

Deep learning for medical image segmentation is the field of research that studies automatic medical image segmentation in the case h is a deep neural network. This approach is the current state of the art in automatic medical image segmentation [Isensee 21]. A deep neural network h is parameterized by a set of parameters $\boldsymbol{\theta}$ that typically consists of millions of parameters. So as to produce relevant and accurate automatic segmentations, the parameters $\boldsymbol{\theta}$ of the deep neural network needs to be tuned automatically. This is performed during the *training* process of the deep neural network.

The ideal optimization problem that the training process aims to solve is

$$\boldsymbol{\theta}^* = \arg \min_{\boldsymbol{\theta} \in \Theta} \mathbb{E}_{(\mathbf{x}, \mathbf{y}) \sim \mathcal{X} \times \mathcal{Y}} [\mathcal{L}(h(\mathbf{x}; \boldsymbol{\theta}), \mathbf{y})] \quad (1.2)$$

where Θ is the space of parameters of the deep neural network h , $\mathcal{X} \times \mathcal{Y}$ is the joint probability distribution of all possible pairs (\mathbf{x}, \mathbf{y}) of input image or volume \mathbf{x} and its associated segmentation \mathbf{y} , and \mathcal{L} is a smooth per-volume loss function, i.e. a function that evaluates how good is the fit between any $h(\mathbf{x}; \boldsymbol{\theta})$ and \mathbf{y} for $(\mathbf{x}, \mathbf{y}) \sim \mathcal{X} \times \mathcal{Y}$ with lower value of the per-volume loss function indicating a better fit.

However, in practice it is impossible compute the expectation in (1.2), or to draw samples exactly from the joint distribution $\mathcal{X} \times \mathcal{Y}$, or even to have access to all the possible pairs (\mathbf{x}, \mathbf{y}) with a non-zeros probability under the joint probability $\mathcal{X} \times \mathcal{Y}$. Instead the pairs (\mathbf{x}, \mathbf{y}) available for training are limited to a predefined finite set of pairs $\{(\mathbf{x}_i, \mathbf{y}_i)\}_{i=1}^n$ where the \mathbf{x}_i are images or volumes that were acquired at one or a few acquisition centers and the segmentations \mathbf{y}_i have been manually segmented by experts to approximate the true segmentations. The set $\{(\mathbf{x}_i, \mathbf{y}_i)\}_{i=1}^n$ is called the *training dataset*. In current state-of-the-art deep learning pipelines for medical image segmentation, the ideal training optimization problem (1.2) is therefore approximated by the empirical risk minimization (ERM) problem to which regularization terms can be added

$$\boldsymbol{\theta}_{ERM}^* = \arg \min_{\boldsymbol{\theta} \in \Theta} \frac{1}{n} \sum_{i=1}^n \mathcal{L}(h(\mathbf{x}_i; \boldsymbol{\theta}), \mathbf{y}_i) \quad (1.3)$$

The main ingredients of the optimization problem (1.3) are: 1) the deep neural network architecture for h , 2) the per-sample loss function \mathcal{L} , 3) the optimization problem, here *empirical risk minimization* (ERM) corresponding to the minimization of the mean of the per-sample loss functions, and 4) the optimizer which is the

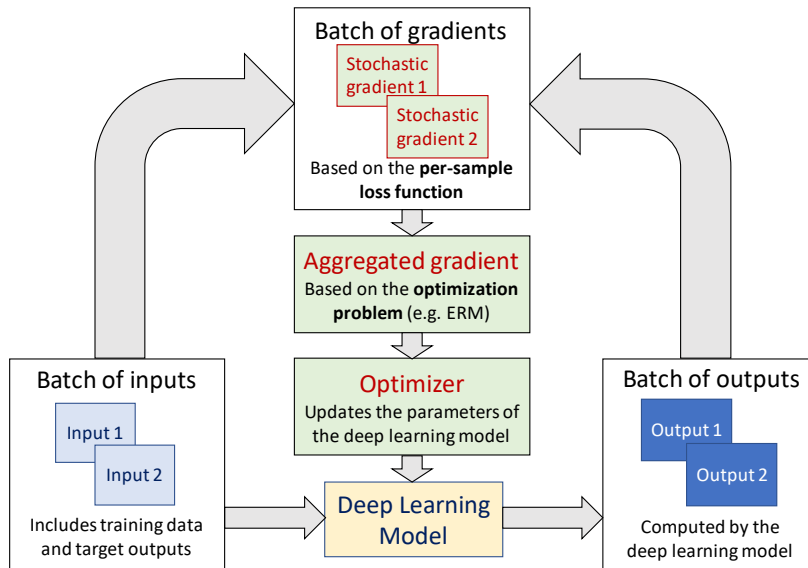


Figure 1.1: **Diagram of a deep learning optimization pipeline.** Deep learning optimization methods are made of four main components: 1) the design of the deep neural network architecture, 2) the **per-sample loss function** (e.g. the Dice loss) that determines the stochastic gradient, 3) the **optimization problem** (e.g. the empirical risk) that determines how to merge the stochastic gradients into one aggregated gradient, 4) the **optimizer** (e.g. SGD, Adam) that determines how the aggregated gradient is used to update the parameters of the deep neural network at each training iteration. In this work, we explore variants for the per-sample loss function, the population loss function and the optimizer for application to automatic brain tumor segmentation.

algorithm that allows finding an approximation of θ_{ERM}^* . A graphical representation is given in Fig. 1.1.

The optimization problem can include data augmentation, as formalized in vicinal risk minimization [Chapelle 00]. In a work that I have coauthored, we have formally shown how the optimization problem can also be extended to include synthetic data [Garcia-Peraza-Herrera 21]. The optimizer includes important hyper-parameters such as the batch size, the learning rate schedule, and the sampling strategy.

In recent years, important research efforts have been put into the development and optimization of deep neural network architectures for medical image segmentation. Research in deep neural network architectures in the context of medical image segmentation has been reviewed in [Lei 20, Liu 21b, Lundervold 19, Siddique 21]. In the following I give a very brief overview of the literature of deep neural network architecture for medical image segmentation and highlight my contribution to this

field.

Innovations on convolutional neural network (CNN) architectures, have led to significant improvement in segmentation accuracy [Bakas 18, Çiçek 16, Kamnitsas 16, Ronneberger 15, Wang 17], including papers I have authored [Fidon 17b, Fidon 17a] and papers I have coauthored [Li 17, Gibson 18, Chandra 18, Garcia-Peraza-Herrera 17, Wang 22a]. The development of nnU-Net ('no-new-Net') [Isensee 21] has shown that a well-tuned 2D U-Net [Ronneberger 15] or 3D U-Net [Çiçek 16] can achieve state-of-the-art results for a large set of medical image segmentation problems and datasets. The most recent developments, there has been several attempts to include transformer layers [Vaswani 17] to deep neural network architectures for medical image segmentation [Chen 21, Hatamizadeh 22, Wang 21, Xie 21]. The nnFormer ('not-another transFormer') [Zhou 21] has been found to outperform previous transformer-based architectures on three segmentation tasks. It is also the first transformer-based architecture to compete with nnU-Net in terms of segmentation accuracy. However, nnFormer does not significantly outperform nnU-Net [Zhou 21]. In my participation to the BraTS challenge 2021 [Fidon 21d], we have experimented with a transformer-based architecture, TransUNet [Chen 21], and found that it leads to lower Dice scores and higher Hausdorff distances than the 3D U-Net [Çiçek 16] used in nnU-Net [Isensee 21] on the BraTS challenge 2021 dataset. This is consistent with the observation that transformer-based architectures have not yet achieved a new state-of-the-art in medical image segmentation. In computer vision, recent results also suggest that pure convolutional neural networks can also outperform the most recent transformer-based architectures in this field [Liu 22b]. The 2D U-Net and 3D U-Net used in the current state-of-the-art pipeline nnU-Net were among the first convolutional neural network architectures proposed for medical image segmentation. This suggests that the improvement that the design of the deep neural network can still bring to medical image segmentation is more limited than what was previously thought.

In contrast to the deep neural networks architecture, relatively little attention has been paid to the other aspects of the deep learning optimization problems for medical image segmentation (1.3), namely the per-sample loss function, the population loss function, and the optimizer. The recent advances in per-sample loss functions have been reviewed in [Ma 21]. In my research work prior to my PhD, I have contributed the generalized Wasserstein Dice loss [Fidon 17a] which is a per-sample loss function that allows taking advantage of the hierarchical structure of the regions of interest during training.

Another relevant research topic in medical image segmentation is the study of the gap between the ideal training problem (1.2) and the surrogate empirical risk

minimization problem (1.3). We introduce this topic in the next section.

1.2 Deep Learning for Medical Image Segmentation is not Trustworthy Yet

Deep learning for medical image segmentation can reach super-human accuracy on average [Isensee 21] and yet most radiologists do not trust them [Allen 21, Cabitza 19]. This is partly because, for some cases, deep learning algorithms fail spectacularly with errors that violate expert knowledge about the segmentation task when the deep learning was applied across imaging protocol and anatomical pathologies [Allen 21, Fidon 21b, Gonzalez 21]. This sense of distrust is exacerbated by the current lack of clear fit-for-purpose regulatory requirements for deep learning-based medical image software [van Leeuwen 21]. The legal framework for the deployment in clinics of deep learning tools for medical segmentation is likely to soon become more stringent once the European Union has proposed its Artificial Intelligence Act to regulate AI and in particular deep learning [EU Commission 21]. A key requirement for AI algorithms for medical image segmentation prior to their deployment on the EU market will be to trustworthy [EU Commission 19, EU Commission 21].

One of the possible causes of the lack of robustness of the current state-of-the-art deep learning methods for medical image segmentation is the gap between the ideal training problem (1.2) and the surrogate empirical risk minimization (ERM) problem (1.3) used for training deep learning models in practice. Datasets used to train deep neural networks typically contain some underrepresented subsets of cases. These cases are not specifically dealt with by the training algorithms currently used for deep neural networks. This problem has been referred to as hidden stratification [Oakden-Rayner 20]. Hidden stratification has been shown to lead to deep learning models with good average performance but poor performance on underrepresented but clinically relevant subsets of the population [Larrazabal 20, Oakden-Rayner 20, Puyol-Antón 21]. In standard deep learning pipelines, this hidden stratification is ignored and the model is trained to minimize the mean per-example loss, which corresponds to the standard ERM problem as in (1.3). As a result, models trained with ERM are more likely to underperform on those examples from the underrepresented subdomains, seen as hard examples. This may lead to *unfair* AI systems [Larrazabal 20, Puyol-Antón 21]. For example, state-of-the-art deep learning models for brain tumor segmentation (currently trained using ERM) underperform for cases with confounding effects, such as low grade gliomas, despite achieving good average and median performance [Bakas 18].

For safety-critical systems, such as those used in healthcare, this greatly limits their usage as ethics guidelines of regulators such as [EU Commission 19] require AI systems to be technically robust and fair prior to their deployment in hospitals.

1.3 Thesis Organization and Contributions

This thesis is organized in eight chapters.

The **current chapter** (Introduction) provides a brief introduction on deep learning for medical image segmentation and trustworthiness of AI in this context. I started from the optimization problem that the training of deep neural networks attempts to solve. I identified four main components of this optimization: the deep neural network architecture, the per-sample loss function, the optimization problem, and the optimizer. The first component is the one that has been the most extensively studied in the literature. I gave a brief overview of the methods that have been proposed to tailor deep neural architectures for medical image segmentation. Last but not least, an introduction to the problem of trustworthy AI in deep learning and its importance for medical image segmentation was proposed.

In **Chapter 2** (Related Work), we give the definition of trustworthy AI used in this thesis and discuss previous work on trustworthy AI and on fetal brain MRI segmentation.

In **Chapter 3** (Fetal Brain 3D MRI Segmentation Dataset), we introduce the largest fetal brain 3D MRI segmentation dataset to date. The dataset contains 540 fetal brain 3D MRIs from 13 hospitals and manually segmented into seven tissue types. I discuss why trustworthiness is particularly important and challenging for this segmentation task. Fetal brain 3D MRI segmentation is the main application studied in this thesis. I also review the literature of automatic methods for fetal brain MRI segmentation. Furthermore, I give a detailed description of our fetal brain MRI segmentation dataset and how we have created it. The inter-rater variability for manual fetal brain 3D T2 weighted MRI is also evaluated.

As discussed in the current chapter, in contrast to the deep neural network architecture, the other three main components defining the training process in deep learning has been less studied in medical image segmentation. I hypothesize that innovation regarding those three aspects can help improving the robustness and segmentation accuracy of current state-of-the-art deep neural network architectures. In this thesis, a state-of-the-art 3D U-Net [Çiçek 16], as implemented in nnU-Net [Isensee 21], is the backbone deep neural network architecture used in all the deep learning-based pipelines for medical image segmentation. In Chapter 4 and Chapter 5 we propose new methods regarding the per-sample loss, the optimization

problem and the optimizer that can be used in (1.3).

In equation (1.3) it is assumed that a full manual segmentation \mathbf{y}_i is available for each training sample \mathbf{x}_i . This assumption characterizes **fully-supervised learning**. In **Chapter 4** (Label-set Loss Functions for Partial Supervision), we will relax this assumption and allow the training segmentations \mathbf{y}_i to be partial, i.e. some but not all the regions of interest may be manually segmented in \mathbf{y}_i . This setting corresponds to **partially supervised learning**. Partial manual segmentations are often present in medical image segmentation where larger training datasets are obtained by pooling data from different sources where images will have been manually segmented for different regions of interest. We found partially supervised learning to be a very useful tool while building our segmentation dataset for fetal brain 3D MRI. In Chapter 4, we show that training with partially segmented images is possible by changing the family of possible per-sample loss functions used in (1.3). We call this new family of per-sample loss functions the *label-set loss functions*.

In **Chapter 5** (Distributionally Robust Deep Learning), we propose an optimizer for training any deep neural network using **distributionally robust optimization** (DRO), a generalization of **empirical risk minimization** (ERM) used in (1.3). ERM weights every training sample equally. When subpopulations are underrepresented in the training dataset, as is typically the case in medical image segmentation, deep neural networks trained using ERM might underperform for new cases from those subpopulations. DRO aims to mitigate this problem by replacing the minimization problem (1.3) by a min-max optimization problem. Our method consists of a new sampling strategy that we call *hardness weighted sampling* and that can be used to convert an existing optimizer for ERM, e.g. Adam or SGD, into an optimizer for DRO. We show that the hardness weighted sampling is both computationally efficient and theoretically sound. We compared DRO to ERM on the segmentation tasks of fetal brain MRI segmentation and brain tumor segmentation using MRI. We found that DRO leads to improvement of some of the worst-case segmentation results.

As discussed in the previous section, the lack of trustworthiness of deep neural networks trained with the optimization problem (1.3) may be related to the gap between this optimization problem and the optimization problem (1.2). The methods proposed in Chapter 4 and Chapter 5 aim at improving the use of all available annotated data during the training of deep neural networks. However, it is currently unknown what amount of data would be required to train trustworthy deep neural networks and if collecting this amount of data would be feasible. It is therefore interesting to look for other kind of approaches than increasing the amount of an-

notated medical images to improve the trustworthiness of deep neural networks. In particular, expert knowledge about properties of the anatomy and properties of the image formation appears as a promising complement to annotated data.

In **Chapter 6** (Spina Bifida Fetal Brain MRI Atlas), we present our method to compute the first spatio-temporal brain T2 weighted MRI segmentation atlas for the developing fetal brain with spina bifida aperta. Previous fetal brain atlases were limited to population of fetuses with a normal development. Brain MRI atlases are the state-of-the-art representation for anatomical prior in a population of normal or pathological human brains. Spina bifida aperta (SBA), as described in Chapter 3, is the most common fetal brain disorder and the population of fetuses with abnormal brain development that we study the most in depth in this thesis. We propose a protocol for the annotation of anatomical landmarks in brain 3D MRI of fetuses with SBA with the aim of making spatial alignment of abnormal fetal brain MRIs more robust. In addition, we propose a weighted generalized Procrustes method based on the anatomical landmarks for the initialization of the atlas. The proposed weighted generalized Procrustes can handle temporal regularization and missing annotations. After initialization, the atlas is refined iteratively using non-linear image registration based on the image intensity and the anatomical landmarks. A semi-automatic method is used to obtain the segmentations of our fetal brain atlas. Our evaluation shows that using the proposed fetal brain atlas for SBA for an atlas-based segmentation method leads to improve segmentation accuracy on brain MRIs of fetuses with SBA as compared to using a normal fetal brain atlas.

In **Chapter 7** (A Dempster-Shafer approach to Trustworthy AI), we propose the first general method to make deep learning algorithms for medical image segmentation trustworthy. We propose a principled method for trustworthy AI that lies at the intersection of the mathematical theory of Dempster-Shafer and the psychological theory of human-AI trust. Our method, in which we propose the first principled and actionable implementation of a fallback and a fail-safe mechanism for deep learning algorithms, is a direct response for medical image segmentation to the EU guidelines for trustworthy AI published in 2019 and that upheld the AI act. Fetal brain atlases, such as the one developed in Chapter 6, play a central role in the proposed implementation of our trustworthy AI framework for fetal brain MRI segmentation. We report significant improvement on the fetal brain MRI segmentation using the largest fetal brain MRI segmentation dataset to date described in Chapter 3.

Finally, **Chapter 8** (Conclusion) concludes this thesis and provides avenues for future work.

Related Work on Fetal Brain Segmentation & Trustworthy AI

Table of Contents

2.1 Trustworthy AI	37
2.1.1 Background on Human-AI trust	37
2.1.2 Domain generalization	38
2.1.3 Information fusion for trustworthy medical image segmentation	39
2.2 Fetal Brain MRI Segmentation	40
2.2.1 Atlas-based fetal brain MRI segmentation methods.	41
2.2.2 Deep learning-based fetal brain MRI segmentation methods.	43
2.2.3 Comparison of atlas-based and deep learning-based methods	45
2.2.4 Combining atlas-based and deep learning-based methods.	46

Foreword This chapter presents previous work on trustworthy AI and fetal brain segmentation.

2.1 Trustworthy AI

In this section, we start by giving the definition of trustworthy AI used in this thesis. We then discuss the most related work.

2.1.1 Background on Human-AI trust

In this section, we describe the definition of human-AI trust and trustworthiness that we use in this thesis.

Artificial intelligence is defined as any automation perceived by the individual using it as having an intent [Jacovi 21].

Human-AI trust is multi-dimensional. For example, the user can trust an AI medical image segmentation algorithm for a given tissue type, for images coming from a given type of scanner, or for a given population and not another. This

observation that trust has several facets and is context-dependent [Hoffman 17] has motivated the introduction of *contractual trust* [Jacovi 21]. A **contract of trust** is an attribute of the AI algorithm which, if not fulfilled, causes a risk in using the AI algorithm. A contract of trust is not necessarily related to the accuracy of the AI algorithm for the task at hand.

For the automatic segmentation of the heart on chest CT images, one contract of trust could be: "The heart labels are always on the left side of the body." This contract is not directly related to the accuracy of the AI segmentation algorithm. The AI algorithm can fulfil this contract and yet compute an inaccurate segmentation of the heart. This contract can also be restricted to CT images of sufficient quality. This allows to model that contract may hold in the context of CT images of sufficiently high quality but not otherwise. Context can be added to the contract and several contracts can be derived from the contract above for different contexts. In addition, this contract does not apply to individuals with dextrocardia (their heart is located on the right).

An AI algorithm is defined as **trustworthy** with respect to a contract of trust if it provides guarantees that it will abide by the obligations of said contract [Jacovi 21].

The requirements proposed in the EU guidelines for trustworthy AI [EU Commission 19] are examples of contract or set of contracts of trust. One important requirement of trustworthy AI is the technical robustness and safety [EU Commission 19] which is the focus of our work. The EU guidelines propose to achieve trustworthiness in practice using a *fallback plan*. However, no technical means of implementing such plan have been provided or published. Problems with the backbone AI algorithm should be detected using a *fail-safe* algorithm and a *fallback* algorithm should be available.

In Chapter 7, we will present a theoretical framework for the implementation of a trustworthy AI system leveraging Dempster-Shafer theory to implement a failsafe fallback plan. And we will show how our framework can be used to maintain several concrete contracts of trust for fetal brain MRI segmentation.

2.1.2 Domain generalization

Domain generalization aims at improving out-of-distribution robustness without access to a labelled or unlabeled test distribution at training time [Bahmani 22, Wang 22b].

Trustworthy AI, as defined above, can fit into this definition and is therefore closely related to domain generalization. However, trustworthy AI aims at improv-

ing robustness not only for out-of-distribution data but also for in-distribution data. It depends on the contracts of trust that are considered.

Recent domain generalization methods for image segmentation are based on data augmentation during training [Zhang 20], test-time augmentation [Bahmani 22, Choi 21], adaptation of the batch normalization layers [Bahmani 22], denoising auto-encoder [Karani 21], specific loss functions [Choi 21], and shape prior [Liu 22a]. For a recent review on domain generalization we refer the reader to [Wang 22b].

The method the most related to our trustworthy AI method, described in Chapter 7, is the method based on shape prior of [Liu 22a]. In the test-time adaptation from shape dictionary method [Liu 22a], they first train a dictionary of explicit shape priors from the source domain. second, a regression branch is added to the segmentation network during training. The output of the regression branch are the coefficients that parameterize the shape prior. The shape prior is then concatenated with the deep features of the segmentation network before the last convolutional block. Finally, they use consistency and data augmentation to adapt the model parameters at test time. Only the batch normalization layers are updated via one step of gradient descent. However, The method is only evaluated for 2D binary segmentation with region of interests consisting of only one connected component per image and simple shapes. It is unclear how such method would generalize to multiple classes and to fetal brain segmentation without replacing the shape dictionary with a fetal brain atlas as proposed in Chapter 6 and Chapter 7.

2.1.3 Information fusion for trustworthy medical image segmentation

Information fusion methods based on probability theory have been proposed to combine different segmentations [Warfield 04, Welinder 10]. The Simultaneous Truth And Performance Level Estimation (STAPLE) algorithm weight each segmentation by estimating the sensitivity and specificity of each segmentations [Warfield 04]. In particular, these methods define only image-wise weights to combine the segmentations. Fusion methods with weights varying spatially have been proposed for the special case of atlas-based algorithms [Cardoso 15], but not in general as in our method. In the context of deep learning-based segmentation methods, simple averaging is used in state-of-the-art pipelines [Isensee 21]. Perhaps more importantly, fusion methods based on probability theory only cannot model imprecise or partial prior expert-knowledge [Warfield 04]. In contrast, the use of Dempster-Shafer theory in our method, described in Chapter 7, allows us a larger diversity of prior knowledge that is typically robust but imprecise. We show that our approach

based on Dempster-Shafer can model prior given by either atlases or voxel intensity prior distributions in the case of fetal brain segmentation and more priors could be modelled as well in other segmentation tasks.

2.2 Fetal Brain MRI Segmentation

To tackle the inaccuracy and limited reproducibility of manual measurements in fetal brain MRI [Aertsen 19], automatic methods for the segmentation of the fetal brain into a set of tissue types are necessary.

Fetal MRI data are specifically challenging to segment automatically due to several factors:

- the evolution of the shape and appearance of the fetal brain across gestational ages. The shape of the fetal brain surface changes during the gyrification process. The size and intensity contrast change across gestational ages and individuals during the myelination process [Dubois 14].
- the strong neuro-morphology variability in fetuses with spina bifida compared to controls (Chiari II malformation, ventriculomegaly, etc...)
- MRI sequences used for fetuses vary a lot from one hospital to the other, and even in the same hospital it changes continuously over time
- the presence of motion artifacts, especially before 3D super-resolution and reconstruction (SRR)
- the lack of standard SRR method, and all SRR used hyper-parameters that sometimes need to be adjusted manually to get an optimal outcome. In addition there is no consensus on the metric to use to evaluate SRR methods, which means that SRR hyper-parameters cannot be optimized automatically.

As a result, methods previously validated for adult brain MRIs or even neonatal brain MRIs can fail when applied to fetal brain MRIs.

Methods for automatic fetal brain segmentation using MRI have been reviewed in [Benkarim 17, Makropoulos 18, Rousseau 16, Torrents-Barrena 19]. We provide here an overview of the methods that have been proposed for the segmentation of the fetal brain into several clinically relevant tissue types. Unlike some of those reviews, we focus on fetuses and do not include segmentation methods developed and evaluated for neonates or preterms. There are two main groups of methods that have been proposed for fetal brain MRI segmentation: atlas-based and deep learning-based methods.

2.2.1 Atlas-based fetal brain MRI segmentation methods.

An atlas is a pair of two volumes: an image (e.g. a T2-weighted MRI) representing an average anatomy for a population and a label map (or probability map for a probabilistic atlas) associated with this image that indicates the delineation of structures in the image. In the context of MRI segmentation, atlases can be used as reference to transfer atlases' label maps to new MRI.

In [Habas 10b] the feasibility of atlas-based segmentation for fetal brain 3D MRI segmentation using a 3D atlas has been demonstrated for fetuses with a normal brain and aged between 20.5 weeks and 22.5 weeks of gestation at the time of MRI. They propose to use an atlas-based segmentation method based on Expectation-Maximization (EM) based on methods previously developed for adult brain MRI segmentation [Van Leemput 99, Wells 96]. Their method segment the cortical gray matter, the white matter, the germinal matrix and the lateral ventricles using 3D reconstructed MRI of the fetal brain. Their evaluation on a set of 14 normal fetal brain MRI suggests that using the segmentation atlas leads to more anatomically plausible and accurate segmentations as compared to using only the intensity and voxel neighborhood prior.

However, due to the change of the fetal brain anatomy across gestational ages, using a normative 3D atlas is not satisfactory for segmenting all the fetal brain MRI that are typically acquired from 20 weeks to 40 weeks of gestation. Instead, [Habas 10a] proposed to use a spatio-temporal atlas for fetal brain segmentation. In this case, the atlas is 4D instead of 3D and corresponds to the average growth of the fetal brain with one age-specific averaged volume per week of gestation. Spatio-temporal atlases allow to improve the propagation of the segmentation to fetal brain MRIs by registering it to the closest age-specific volume of the 4D atlas. They compute a spatio-temporal fetal brain MRI atlas for gestational ages 21 weeks to 24.5 weeks using 20 MRI examinations of fetuses with a normal brain. Using the same atlas-based registration algorithm as in their previous work, Habas et al found that using a spatio-temporal atlas rather than a 3D atlas as in [Habas 10b] leads to improve segmentation accuracy [Habas 10b]. Spatio-temporal atlases are used by all the atlas-based fetal brain segmentation methods that followed [Habas 10a].

In [Serag 12b], a spatio-temporal atlas for the normal fetal brain T2 weighted MRI from 23 weeks to 37 weeks is proposed. Brain hemispheres, ventricles, cortex and cerebrospinal fluid (CSF) are segmented in the atlas. Their method to compute a fetal brain spatio-temporal atlas is based on non-rigid registration parameterized using cubic B-splines [Rueckert 99] and temporal kernel regression [Davis 10] with an adaptive width [Serag 12a]. The dataset used to compute the atlas contains 80

T2 MRI studies of fetuses with a normal brain development at gestational ages from 21.7 weeks to 38.7 weeks. They reported qualitative and quantitative differences between age-matched spatio-temporal atlases computed using fetal and neonatal 3D T2 MRI. However, they do not evaluate the segmentation accuracy of atlas-based fetal brain segmentation using their fetal brain atlas. Their atlas is publicly available at <https://brain-development.org/brain-atlases/fetal-brain-atlases/>.

The work of [Gholipour 12] is the first to study the segmentation of abnormal fetal brain using MRI. Specifically, they study the automatic segmentation of the lateral ventricles in fetal brain MRI of fetuses either with a normal brain or with dilated ventricles, a condition called ventriculomegaly. They propose a new multi-atlas multi-shape method with soft constraints to avoid intersection among structures. In this case, the atlas consists of a dataset of fetal brain MRIs with manual segmentation. Segmentations from multiple atlas volumes are registered, propagated, and finally fused using the simultaneous truth and performance level estimation (STAPLE) algorithm [Warfield 04]. In their experiments they use a set of 25 fetal brain MRIs of fetuses with normal brain or ventriculomegaly and gestational age between 19 weeks and 38 weeks. They find that their multi-atlas method leads to more robust segmentation of the ventricles as compared to a single atlas method.

The problem of computing a spatio-temporal atlas using a few segmented 3D MRI and a majority of non-annotated 3D MRI is studied in [Dittrich 14]. They propose a method for the semi-supervised learning of a spatio-temporal latent atlas of fetal brain development with segmentation for the ventricles and the cortex. Their dataset consists of 44 MRI, including 32 fetuses with a normal brain and 13 fetuses with lissencephaly, a malformation of the cortical development. They applied their method to the computation of a spatio-temporal fetal brain atlas for gestational age from 20 weeks to 30 weeks.

In later work, new spatio-temporal fetal brain T2w MRI atlases have been proposed with improved sharpness, more tissue types segmented, and more specific fetal populations [Gholipour 17, Wu 21, Fidon 21e]. In [Gholipour 17], a spatio-temporal MRI atlas of the normal fetal brain from 21 weeks to 37 weeks of gestation is proposed. The hippocampi, amygdala, fornix, cerebellum, brainstem, caudate nuclei, thalami, subthalamic nuclei, lentiform nuclei, corpus callosum, lateral ventricles, developing white matter, cortical plate, and cerebrospinal fluid (CSF) are segmented in the proposed atlas. The same segmentation protocol as in the ALBERT neonatal brain atlas [Gousias 12, Gousias 13] has been used as a baseline and adapted when necessary for the lowest gestational ages using [Bayer 05]. The main components of their pipeline are symmetric diffeomorphic free-form deformation and kernel-based

temporal regression like in [Serag 12b]. Their spatio-temporal atlas has been computed using 81 MRIs of fetuses with a normal brain and gestational age between 19 weeks and 39 weeks. They show qualitatively that their atlas is sharper and better preserves anatomical details as compared to a previous fetal brain atlas. The proposed atlas is publicly available at http://crl.med.harvard.edu/research/fetal_brain_atlas/. Recently, a spatio-temporal fetal brain MRI atlas for the normal brain in the Chinese population for gestational ages from 22 weeks to 35 weeks has been proposed [Wu 21]. They used 115 fetal brain 3D MRIs of Chinese fetuses with a normal brain development with gestational ages from 22 weeks to 35 weeks to compute the atlas. Their method to compute the atlas is similar to the one used in [Gholipour 17]. They report quantitative anatomical differences between the proposed fetal brain atlas for the Chinese population and the fetal brain atlas [Gholipour 17]. In parallel, we have proposed the first spatio-temporal fetal brain MRI atlas for spina bifida aperta for gestational ages from 21 weeks to 34 weeks [Fidon 21e]. The atlas has been computed using 90 fetal brain 3D MRIs of operated and non-operated fetuses with spina bifida aperta and gestational ages from 21 weeks to 35 weeks. This is the first fetal brain atlas for a population with abnormal brains. Our experiments show that using the proposed atlas rather than the normal brain atlas [Gholipour 17] in an atlas-based segmentation method results in a higher segmentation accuracy for fetal brain MRI of fetuses with spina bifida aperta. The description of our method and experiments can be found in Chapter 6.

2.2.2 Deep learning-based fetal brain MRI segmentation methods.

We now give a brief review of the methods for fetal brain MRI segmentation based on deep learning. An introduction to deep learning for medical image segmentation can be found in Chapter 1.

Recently, the first methods using Convolutional Neural Networks (CNNs) for fetal brain MRI segmentation have been proposed [Khalili 19, Payette 19]. In [Khalili 19], the fetal brain is segmented into seven tissue types: the cerebellum, the basal ganglia, the basal thalami, the ventricular system, the white matter, the brainstem, the cortical gray matter, and the extracerebellar cerebrospinal fluid. The motivation of [Khalili 19] for using a CNN for fetal brain MRI segmentation is that compared to atlas-based methods requiring intensity inhomogeneity correction and complex preprocessing, CNNs can learn to be invariant to these inhomogeneities. Their CNN-based method segments the fetal brain directly in the low resolution 2D MRI slices and does not require to use a super-resolution and reconstruction

algorithm prior to the automatic segmentation. The main technical contribution of this work is a data augmentation method based on simulated intensity inhomogeneity artifacts for training the CNNs. Similarly to [Wang 17], they use a cascade of two 2D Convolutional Neural Networks (CNNs). The first CNN segments the intra-cranial volume in the original 2D slices. The second CNN takes as input a smaller image cropped around the intra-cranial volume segmented by the first CNN and segment the brain into seven tissue types. The two CNNs are based on the 2D U-net architecture [Ronneberger 15]. They train and evaluate their method using fetal brain MRI of 12 fetuses, all acquired in the same center. In addition, they used slices from 9 neonatal 3D MRIs to increase the size of their dataset. In [Payette 19], a 2D U-net [Ronneberger 15] is also used to segment the ventricular system in fetal brain MRIs. In addition, the model is trained and evaluated on fetuses with both normal brain and with spina bifida aperta, referred to as open spina bifida in [Payette 19]. They train their CNN using 46 fetal brain 3D MRIs, all acquired at the same center. However, the accuracy of the segmentation is evaluated on only 3 3D MRIs. In contrast to [Khalili 19], the segmentation is performed after super-resolution and reconstruction to obtain high-resolution fetal brain 3D MRIs. The use of 3D MRIs allows the longitudinal analysis of the ventricular system using the automatic segmentations. All the work following [Payette 19] performed automatic fetal brain MRI segmentation using 3D reconstructed MRI. In [Payette 20], the problem of the robustness of deep learning methods for fetal brain MRI to the choice of the 3D super-resolution and reconstruction (SRR) algorithm is studied. The use different SRR algorithms for transfer learning is proposed to make the deep neural network more robust to the SRR method used. In [Hong 20], a 2.5D deep learning approach with multi-view aggregation is proposed for the segmentation of the cortical gray matter. In contrast to previous work, they also propose to use a hybrid loss function that is the sum of the logarithmic Dice loss [Wong 18] and a novel boundary logarithmic Dice loss instead of the Dice loss [Milletari 16]. In [Fidon 22b], we have studied the problem of robustness of deep learning to abnormal anatomy underrepresented in the training dataset. We proposed to mitigate this problem by replacing the training optimization problem commonly used in deep learning, namely empirical risk minimization, by distributionally robust optimization. Our method and experiments are detailed in Chapter 5.

Recently, the first publicly available fetal brain 3D MRI dataset with manual segmentations has been released [Payette 21]. The dataset, called Fetal Tissue Annotation and Segmentation Dataset (FeTA), contains 50 fetal brain 3D MRIs in the first data release and 40 3D MRIs in the second data release. All 3D MRIs were acquired at the University Children’s Hospital Zurich. More details about the FeTA

dataset can be found in the next section. The FeTA dataset has allowed the organization of the first international challenge for automatic fetal brain MRI segmentation (<https://www.synapse.org/#!Synapse:syn25649159/wiki/610007>). All the top-performing methods in the FeTA challenge 2021 were based on deep learning and the 3D U-Net architecture [Çiçek 16].

Several work studied the problem of efficient annotation of fetal brain 3D MRIs for training a deep learning-based segmentation algorithm [Fetit 20, Fidon 21a, Fidon 21c]. In [Fetit 20], a human-in-the-loop approach is proposed. They alternate between automatic segmentation and manual refinement, and training a deep neural network based on the deep medic architecture [Kamnitsas 16]. An atlas-based method for neonatal fetal brain MRI [Makropoulos 14] has been used to initialize the first automatic segmentations. They used a total of 249 fetal brain 3D MRIs for training but their final deep learning-based segmentation model is not evaluated quantitatively. In [Fidon 21a], we proposed a family of loss functions, *the label-set loss functions*, is proposed to allow to train any deep neural network using partially segmented fetal brain 3D MRI. Partially segmented MRIs are MRIs in which some but not all the tissue types have been segmented manually. When present, the manual segmentation of a tissue type is supposed to be complete. A total of 146 partially segmented fetal brain 3D MRIs were used to train a 3D U-Net [Çiçek 16] using different loss functions and an independent testing set with 100 fetal brain 3D MRI, including MRI acquired from multiple centers, have been used to compare the different loss functions quantitatively. Details can be found in Chapter 4 of this thesis.

2.2.3 Comparison of atlas-based and deep learning-based methods

The experiments of [Khalili 19] suggest that their deep learning pipeline achieves similar segmentation accuracy to the atlas-based methods [Habas 10a, Serag 12b]. However, the different methods were not evaluated on the same data which limits this comparison. In [Zhao 22], a 3D U-Net [Çiçek 16] is used to segment the cerebrospinal fluid, the cortical gray matter, the white matter, the deep gray matter, the cerebellum, and the brainstem in fetal brain 3D MRIs. The 3D U-Net is shown to outperform an atlas-based segmentation method [Makropoulos 14] for MRIs of fetuses with a normal brain and acquired at the same center as the MRIs used to train the 3D U-Net. However, the selection of an atlas-based method [Makropoulos 14] was originally developed for neonatal MRI biases this comparison. Despite the findings of [Zhao 22], when an atlas-based method tailored to fetal brain MRI segmentation is used, empirical results in other work suggest that atlas-based method

can outperform state-of-the-art deep learning methods when evaluated on MRIs with a low quality [Payette 20] and on MRIs acquired at a different center than during training [Fidon 22a].

2.2.4 Combining atlas-based and deep learning-based methods.

In the early work of [Sanroma 18], two ensembling strategies to combine a multi-atlas segmentation method and a machine learning approach, like deep learning, have been studied. In [Li 21], three deep neural network are trained jointly. The first network learns to perform fetal brain 3D MRI segmentation, The second compute a spatio-temporal fetal brain MRI atlas, and the third network learns to register the atlas to the input and result in a second automatic segmentation of the output. In addition, a convolutional layer that combines the two automatic segmentation is trained end-to-end with the three previous networks. In [Fidon 22a] and Chapter 7, a method based on Dempster-Shafer theory is proposed to combine atlas-based and deep learning-based methods for fetal brain 3D MRI segmentation.

Fetal Brain 3D MRI Segmentation Dataset

Table of Contents

3.1	Introduction	48
3.1.1	Spina Bifida Aperta	50
3.1.2	Super-Resolution and Reconstruction: From 2D to 3D	51
3.2	Fetal Brain MRI Dataset	52
3.2.1	Underlying MRI data	52
3.2.2	Fetal MRI Acquisition Details	55
3.2.3	Automatic Brain Extraction	55
3.2.4	Super-Resolution and Reconstruction	56
3.2.5	Semi-automatic Fetal Brain 3D MRI Segmentations	56
3.2.6	Data availability	61
3.3	Conclusion	63

CHAPTER 3. FETAL BRAIN 3D MRI SEGMENTATION DATASET

Foreword This chapter presents the fetal brain MRI segmentation dataset that was created and used in this thesis.

Contributions:

- We have created the largest fetal brain 3D T2w MRI segmentation dataset to date.
- The construction of the fetal brain T2w MRI dataset has been lead by Michael Aertsen and myself under the supervision of Tom Vercauteren and Jan Deprest.
- I estimated the inter-rater variability in fetal brain MRI segmentation for: the white matter, the intra-axial cerebrospinal fluid (CSF), the cerebellum, the extra-axial CSF, the cortical gray matter, the deep gray matter, and the brainstem.
- The 3D reconstructed MRIs, except for the data from FeTA [Payette 21], were computed using NiftyMIC [Ebner 20] by: Michael Aertsen, Frédéric Guffens, and myself.
- The class hierarchy for fetal brain segmentation has been contributed by: Michael Aertsen, Ernst Schwartz, and myself.
- The manual segmentations of the fetal brain 3D MRIs have been contributed by: Michael Aertsen, Philippe Demaerel, Thomas Deprest, Doaa Emam, Frédéric Guffens, Nada Mufti, Esther van Elslander, the consortium of the FeTA dataset, and myself.
- Several persons have contributed fetal brain MRIs: Jan Deprest and Michael Aertsen for data from University Hospital Leuven, Anna David, Andrew Melbourne, and Nada Mufti for the data from University College London Hospital and various centers in the United Kingdom, Mary Rutherford for the data from King’s College London, Gregor Kasprian and Daniela Prayer for the data from Medical University of Vienna, and Kelly Payette and Andras Jakab for the data from University Children’s Hospital Zurich that they made publicly available in the FeTA dataset [Payette 21].

3.1 Introduction

The two main imaging modalities used in paediatric radiology are Ultrasound (US) and Magnetic Resonance Imaging (MRI). US is the standard imaging modality because it is widely available in clinic, real-time, low-cost, non-invasive and high-resolution. However, it has a small field-of-view, limited soft tissue contrast and poor image quality. As a result, MRI is used to complement ultrasound imaging and detect any additional potential abnormality that may be harder to visualize by the former. It has been shown that MRI allows to improve the management of

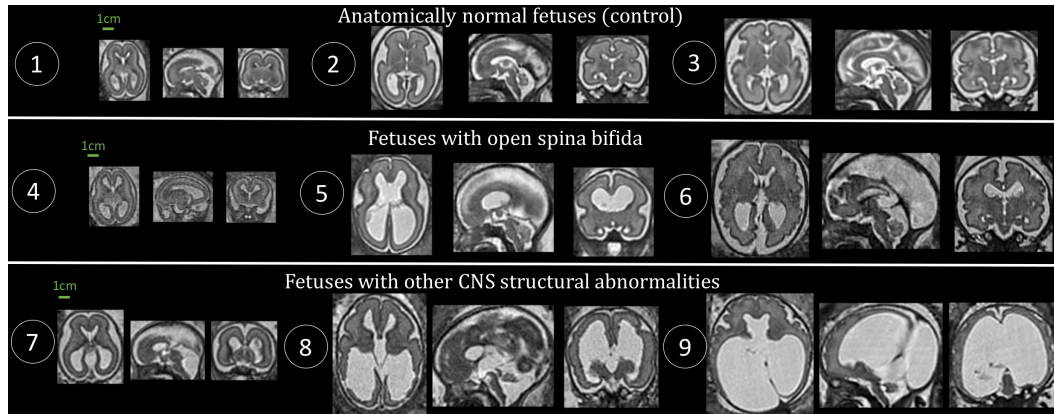


Figure 3.1: Illustration of the anatomical variability in fetal brain across gestational ages and diagnostics. 1: Control (22 weeks); 2: Control (26 weeks); 3: Control (29 weeks); 4: Spina bifida (19 weeks); 5: Spina bifida (26 weeks); 6: Spina bifida (32 weeks); 7: Dandy-walker malformation with corpus callosum abnormality (23 weeks); 8: Dandy-walker malformation with ventriculomegaly and periventricular nodular heterotopia (27 weeks); 9: Aqueductal stenosis (34 weeks).

fetuses with visible abnormalities in US [Simon 00, Kubik-Huch 00, Levine 03]. In the study of [Levine 03], for 31.7% of the fetuses with abnormal US findings, MRI findings lead to change of prognosis.

MRI is the current clinical standard to aid decision making, such as for prenatal surgery for spina bifida fetuses [Aertsen 19]. However, the motion of the fetus is a challenge for MRI as usual acquisition processes are slow in comparison to the movement of the fetus¹. Motion artefacts are addressed by using specific MRI acquisition protocols such as Single-Shot Fast Spin Echo (SSFSE) [Yamashita 97]. SSFSE is a fast imaging method to acquire thick, low resolution stacks of 2D MRI slices to reduce motion artifacts. Each stack of 2D MRI consists of a volume with high resolution and low amount of motion along two dimensions, and low resolution and high level of motion along the third dimension. Several stacks are acquired along orthogonal directions with the aim that every part of the fetal brain is visible in high resolution in at least one stack. One second or less per slice is required. Super-resolution and reconstruction (SRR) algorithms can be used to compute a high-resolution and motion-free reconstructed 3D MRI from the stacks of 2D MRI slices [Ebner 20]. More details about SRR algorithms is given in section 3.1.2. Manual measurements can then be obtained using the 2D MRI slices or a reconstructed 3D MRI selected by an expert [Aertsen 19, Khawam 21]. Many anatomical biomarkers of spina bifida have been proposed based on the knowledge of the clin-

¹See this [video](#) for an illustration of the motion of a fetus.

icians, but the choice of standard anatomical biomarkers for the diagnosis is still unclear [Aertsen 19]. Manual anatomical biomarkers measurements also suffer from large inter-rater and intra-rater variability, and is time-consuming.

In particular, studying shape and volume of different brain tissues is essential for the study of fetal brain development [Benkarim 17]. Reliable analysis and evaluation of fetal brain structures could also support diagnosis of central nervous system pathology, patient selection for fetal surgery, evaluation and prediction of outcome, hence also parental counselling [Aertsen 19, Danzer 20, Moise Jr 16, Sacco 19, Zarutskie 19]. Therefore, automatic methods for fetal brain segmentation in 3D is needed.

In this chapter, we give an introduction to 3D super-resolution and reconstruction algorithms that are required to obtain coherent and high-resolution isotropic MRI of the fetal brain for shape and volume analysis. We also review the literature of automatic fetal brain MRI segmentation. Our dataset for fetal brain 3D MRI segmentation is described. In particular, we evaluate the inter-rater variability in manual fetal brain MRI segmentation for the first time.

3.1.1 Spina Bifida Aperta

In this section, we give a short introduction of spina bifida aperta which is the brain defect studied the most in depth in this thesis.

Spina bifida aperta (SBA), also referred to as open spina bifida, open spinal dysraphism, or simply spina bifida in a context where there is no ambiguity with other sorts of spina bifida, is the most prevalent fetal brain defect. The prevalence of spina bifida is approximately 4.9 per 10,000 live births in Europe, and 3.17 in USA [Aertsen 19, Khoshnood 15]. Spina bifida aperta occurs when the neural tube fails to close in the first four weeks after conception [Adzick 11, Aertsen 19]. SBA is divided into two types: myelomeningocele and myeloschisis. Myelomeningocele (MMC) is the most frequent form of spina bifida aperta, where the spinal defect causes an extrusion of the spinal cord into a fluid filled sac. In both cases, SBA leads to an abnormal development of the central nervous system caused by leak of amniotic fluid. Most cases of SBA are accompanied by severe anatomical brain abnormalities [Pollenus 20] with enlargement of the ventricles and a type II Chiari malformation being most prevalent. The Chiari malformation type II is characterized by a small posterior fossa and hindbrain herniation in which the medulla, cerebellum, and fourth ventricle are displaced caudally into the direction of the spinal canal [Naidich 80]. This downwards displacement causes accumulation of fluid in the brain termed *hydrocephalus*. This is due to the obstruction of the nor-

mal flow of cerebrospinal fluid (CSF) around the body. This hydrocephalus often requires treatment after birth via means of a ventriculoperitoneal shunt in 80% of infants [Kahn 14]. However, shunts can get infected, and can fail requiring multiple surgical revisions which can lead to developmental delay [Geerdink 12, Sutton 99]. Motivated by the Management of Myelomeningocele Study (MOMS) randomized control trial published in 2011 [Adzick 11], patients are now evaluated and treated by surgery before birth. The corpus callosum of fetuses with SBA is also abnormal [Kunpalin 21, Pollenus 20] and has been found to be significantly smaller for fetuses with SBA than for normal fetuses [Crawley 14, Dennis 16, Kunpalin 21]. SBA fetuses have also smaller hippocampus [Treble-Barna 15], abnormal cortical thickness and gyrification [Mufti 21, Treble 13], and smaller deep gray matter volume and total brain volume [Hasan 08, Mandell 15]. The main neuroanatomy vocabulary specific to SBA can be found in Appendix A.1.1. For all those reasons the anatomy of the brain of fetuses with SBA differs from the normal fetal brain anatomy. In addition, the mechanisms underlying those anatomical brain abnormalities remain incompletely understood [Danzer 20].

The benefits of in-utero surgery have to be balanced with the higher risk of preterm birth and possible long term consequences for the mother [Moldenhauer 17]. However, an optimum patient selection criteria for predicting which patients would benefit more from the surgery are still being optimized [Moldenhauer 17]. The segmentation of fetal brain MRI is essential for the quantitative study of fetal brain development [Benkarim 17]. Reliable analysis and evaluation of fetal brain structures using segmentation and registration algorithms could also support diagnosis of central nervous system pathology, patient selection for fetal surgery, evaluation and prediction of outcome, hence also parental counselling [Aertsen 19, Danzer 20, Moise Jr 16, Sacco 19, Zarutskie 19]. Literature on computer-assisted fetal brain MRI processing is briefly reviewed in the next section of this chapter.

3.1.2 Super-Resolution and Reconstruction: From 2D to 3D

One of the main challenges for qualitative and quantitative analysis using fetal brain MRI is the motion of the fetus. This motivated the creation of specific MRI sequences for fetal MRI that are designed to produce multiple stacks of 2D slices rather than a 3D image. However, those 2D MRI slices typically have lower through-plane resolution, suffers from motion between neighboring slices, motion artefact, and suboptimal cross-section. The inaccuracy of manual measurements in 2D MRI slices is also due to the manual selection of a few slices [Aertsen 19].

To tackle this issue, 3D super resolution and reconstruction (SRR) algorithms

have been proposed to improve the resolution, and remove motion between neighboring slices and motion artefacts present in the original 2D MRI slices [Ebner 20, Tourbier 17, Gholipour 10, Rousseau 06, Kainz 15, Kim 09, Kuklisova-Murgasova 12, Alansary 17, Hou 18]. The output of the 3D super resolution and reconstruction algorithm is a reconstructed 3D MRI of the fetal brain with an isotropic image resolution. A detailed review of the literature of SRR algorithms for fetal brain MRI can be found in [Ebner 19, see Chapter 2].

Briefly, SRR algorithms aim at combining a set of low-resolution stacks of 2D MRI slices that are acquired for a patient into a unique high-resolution 3D MRI volumes. Current state-of-the-art SRR algorithms all have the same structure:

1. localization and segmentation of the fetal brain in the 2D MRI slices
2. iteratively alternate between motion correction and volumetric reconstruction

The localization and segmentation step is sometimes manual in some methods.

In this thesis, I have used the fully-automatic SRR pipeline proposed in [Ebner 20] which is one of the current state of the art SRR methods.

It is hypothesized that the reconstructed 3D MRIs facilitates the qualitative and quantitative anatomical analysis of fetal brain MRI as compared to the original stacks of 2D MRI slices. It has been shown that it leads to better visualization and could become an essential tool in the spina bifida clinical pipeline [Zarutskie 19]. A comparison of manual biometric measurements performed on both the original 2D MRIs and the reconstructed 3D MRIs for the same studies has shown a good agreement [Khawam 21]. This suggests that manual measurements can be safely performed on reconstructed 3D MRIs. Reconstructed 3D MRIs are also likely to facilitate the manual delineation of the fetal brain structures compared to the original stacks of 2D MRI slices.

3.2 A Large and Multi-centric Fetal Brain 3D MRI Segmentation Dataset

In this section, I describe the fetal brain MRI dataset that we have built during my PhD and that supports the work that is described in the following chapters.

3.2.1 Underlying MRI data

We have collected a dataset with a total of 540 fetal brain 3D MRIs with neurotypical or abnormal brain development and from 13 sources of data across 6 countries. A graphical summary of the dataset can be found in Fig. 3.2.

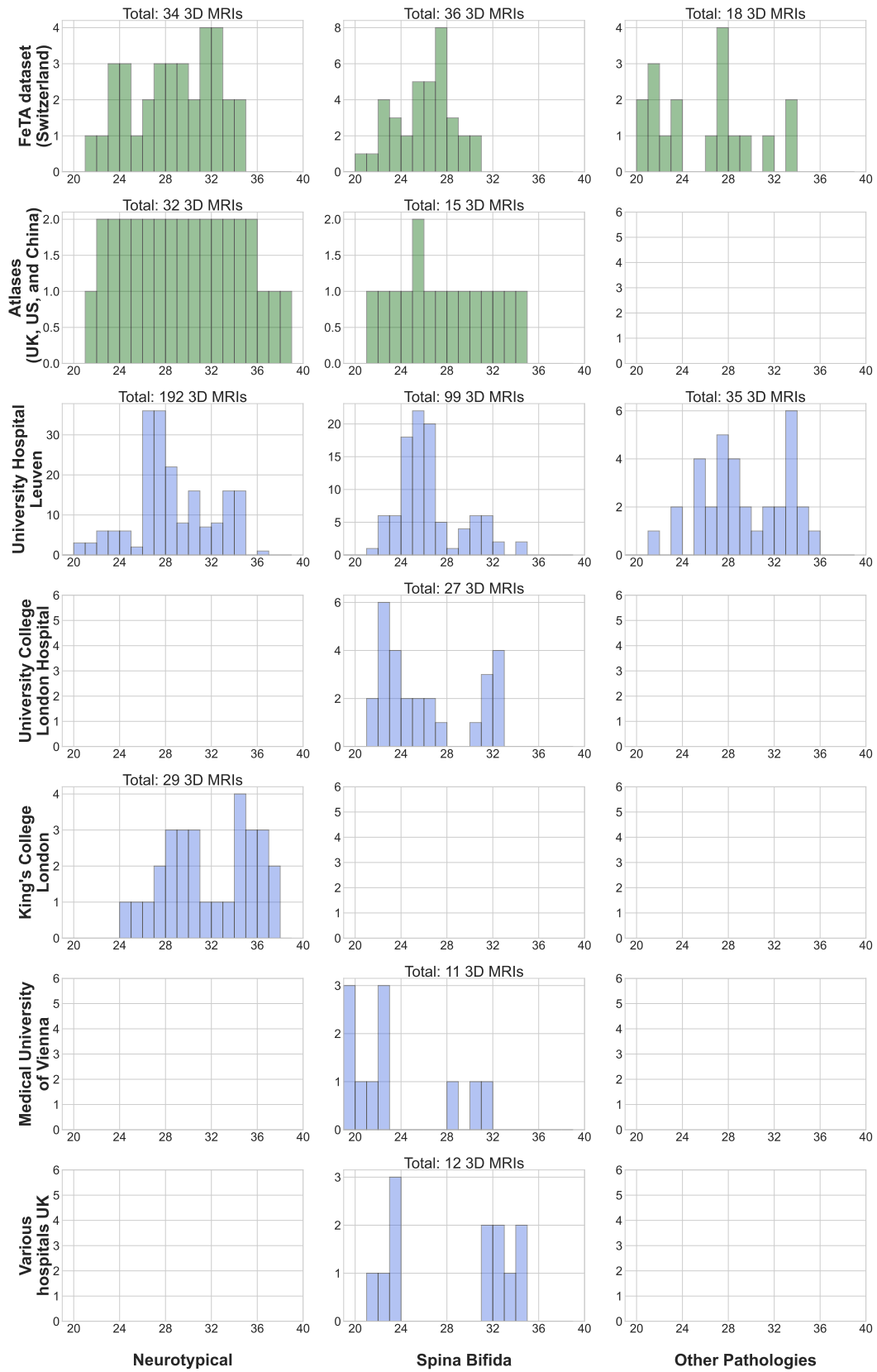


Figure 3.2: Histogram of the gestational ages for each group of centers and for neurotypical, spina bifida, and other pathologies for the full dataset.

CHAPTER 3. FETAL BRAIN 3D MRI SEGMENTATION DATASET

The dataset consists of 326 3D MRIs acquired at University Hospital Leuven (UHL), 88 3D MRIs from the FeTA dataset [Payette 21] (data release 1 and 2), 11 3D MRIs acquired at Medical University of Vienna (MUV), 29 3D MRIs acquired at King’s College London (KCL), 27 3D MRIs acquired at University College London Hospital (UCLH), 4 3D MRIs acquired at Manchester (MCT), 4 3D MRIs acquired at Belfast (BFT), 2 3D MRIs acquired at Cork (CRK), 1 3D MRIs acquired at Newcastle (NCS), 1 3D MRIs acquired at Liverpool (LVP), and 47 3D MRIs from three fetal brain brain atlases. The three open-access fetal brain spatio-temporal atlases consist of 18 population-averaged 3D MRIs computed from fetal neurotypical brain MRIs acquired at Boston Children’s Hospital, USA [Gholipour 17], 14 population-averaged 3D MRIs computed from fetal neurotypical brain MRIs acquired in China [Wu 21], and 15 population-averaged 3D MRIs computed from fetal spina bifida brain MRIs acquired at UHL and UCLH [Fidon 21e].

Data from UHL includes 192 3D MRIs of neurotypical fetuses, 99 3D MRIs of fetuses with spina bifida aperta, and 35 3D MRIs of fetuses with an abnormal brain anatomy due to a condition other than spina bifida. The majority of the neurotypical fetuses was scanned for a suspected abnormality somewhere else than in the brain, while a minority was scanned for screening of brain abnormality but was proven neurotypical after MRI. The 35 3D MRIs of fetuses with other abnormalities consisted of: 3 examinations of a case with an enlarged subarachnoid space, 3 cases of intraventricular hemorrhage, 1 cases of intracranial hemorrhage, 1 case with a partial rhombencefalosynapsis, 1 case with a closed lip Schizencephaly, 4 cases with dandy-walk malformation, 1 case with an unilateral ventriculomegaly due to a hemorrhage, 1 case with choroid plexus papilloma, 1 case with high flow Dura isinus malformation, 7 cases with corpus callosum agnesis, 1 case with corpus callosum agenesis with interhemispheric cyst, temporal cysts and delayed gyration, 2 cases with tuberous sclerosis, 1 case with a Blake’s pouch cyst, 2 cases with aqueductal stenosis, 1 case with an idiopathic dilatation of the lateral ventricles, 2 cases with cytomegalovirus encephalitis, and 1 case with parenchyma loss due to a vasculo-ischemic insult.

Data from the open-access FeTA dataset [Payette 21] includes 34 3D MRIs of fetuses with a normal brain development, 36 3D MRIs of fetuses with spina bifida aperta, and 18 3D MRIs of fetuses with an abnormal brain anatomy due to conditions other than spina bifida. Those 18 3D MRIs of fetuses with other abnormalities consisted of: 3 cases with heterotopia, 8 cases with ventriculomegaly without spina bifida, 2 cases with aqueductal stenosis, 2 cases with interhemispheric cyst, 1 case with cerebellar hemorrhage, 1 case with a Dural sinus malformation, and 1 case with Bilateral subependymal cysts and temporal cysts.

Data from KCL consists exclusively of brain 3D MRIs of fetuses with a normal brain development. Data from MUV, UCLH, MCT, BFT, CRK, NCS, and LVP consist only of 3D MRIs of fetuses diagnosed with spina bifida aperta.

3.2.2 Fetal MRI Acquisition Details

All the MRI examinations at UHL, UCLH, MCT, CRK, NCS, BFT, LVP, KCL, and MUV were performed as part of clinical routine following abnormal findings during ultrasound examination. For each study, at least three orthogonal T2-weighted HASTE series of the fetal brain were collected on a 1.5T scanner, except for the MRI acquired at MUV for which T2-weighted TSE series were used. The MRIs from UHL and UCLH were acquired with an echo time of 133ms, a repetition time of 1000ms, with no slice overlap nor gap, pixel size 0.39mm to 1.48mm, and slice thickness 2.50mm to 4.40mm. The MRIs from MCT, CRK, NCS, BFT, and LVP were acquired with an echo time of 145ms, a repetition time of 9953ms, with no slice overlap nor gap, pixel size 0.56mm to 1.25mm, and slice thickness 3mm to 4mm. The MRI from KCL were acquired with an echo time of 160ms, a repetition time of 15,000ms, a slice overlap of 1.5mm, and a slice thickness of 2.5mm. For patients imaged at MUV, a 1.5T scanner was used, applying an echo time of 140ms, a repetition time of 53,189ms, slice gap of 0.4mm, pixel size 0.9mm to 1.37mm, and slice thickness 3mm to 4mm. In all acquisition centers, a radiologist attended all the acquisitions for quality control. The dataset contains longitudinal MRI examinations with up to 5 examinations per fetus. Fetuses with spina bifida were diagnosed with spina bifida aperta at fetal ultrasound examinations. In addition, MRI examinations for spina bifida fetuses were performed either for unoperated fetuses or after open fetal surgery performed before 26 weeks of gestation to close the spina bifida aperta defect. In particular, the MRI studies from MUV all correspond to unoperated spina bifida fetuses and longitudinal data.

3.2.3 Automatic Brain Extraction

Automatic segmentation of the fetal brain in the raw 2D MRIs are obtained using a deep learning-based method [Ranzini 21]. Those brain masks are an input required by the 3D super resolution and reconstruction algorithm described below. A public implementation of the deep learning pipeline `MONAI-fbs` [Ranzini 21] is used in this study to obtain the brain masks. The main git branch, commit `bcab52a`, was used.

3.2.4 Super-Resolution and Reconstruction

The reconstructed fetal brain 3D MRIs were obtained using `NiftyMIC` [Ebner 20] a state-of-the-art super resolution and reconstruction algorithm. The volumes were all reconstructed to a resolution of 0.8 mm isotropic. `NiftyMIC` version 0.8 with Python 3.8 has been used. The 2D MRIs were also corrected for image intensity bias field as implemented in `SimpleITK` version 1.2.4. Our pre-processing improves the resolution, and removes motion between neighboring slices and motion artefacts present in the original 2D slices [Ebner 20].

The 3D super resolution and reconstruction algorithm [Ebner 20] also combines the 2D brain masks. This results in a 3D brain mask for the 3D reconstructed MRI that is computed fully-automatically.

All the reconstructed 3D MRIs and 3D brain masks were rigidly aligned to a spatio-temporal fetal brain atlas [Gholipour 17] as implemented in `NiftyMIC` [Ebner 20] version 0.8. All the reconstructed 3D MRIs are therefore aligned to a standard clinical view in which the axes are aligned with the axial, sagittal, and coronal planes of the fetal brain. This facilitates the manual delineation and annotation of the fetal brain structures. The target time-point in the neurotypical 4D atlas is chosen based on the brain volume computed using the automatic 3D brain mask.

3.2.5 Semi-automatic Fetal Brain 3D MRI Segmentations

In this section, we describe the method that we have used to perform the manual segmentation of the fetal brain 3D MRIs. In this work, we call **manual segmentation** every segmentation that has been checked by an expert for every slice and corrected wherever necessary. In particular, initialization of the segmentations was obtained using an automatic segmentation methods and/or from another, potentially less experienced, raters.

Manual Segmentation

The 3D reconstructed fetal brain MRIs were segmented for eight tissue types:

1. the white matter (excluding the corpus callosum; see below),
2. the intra-axial cerebrospinal fluid (ventricular system with the cavum septi pellucidi and cavum verga),
3. the cerebellum,
4. the extra-axial cerebrospinal fluid,

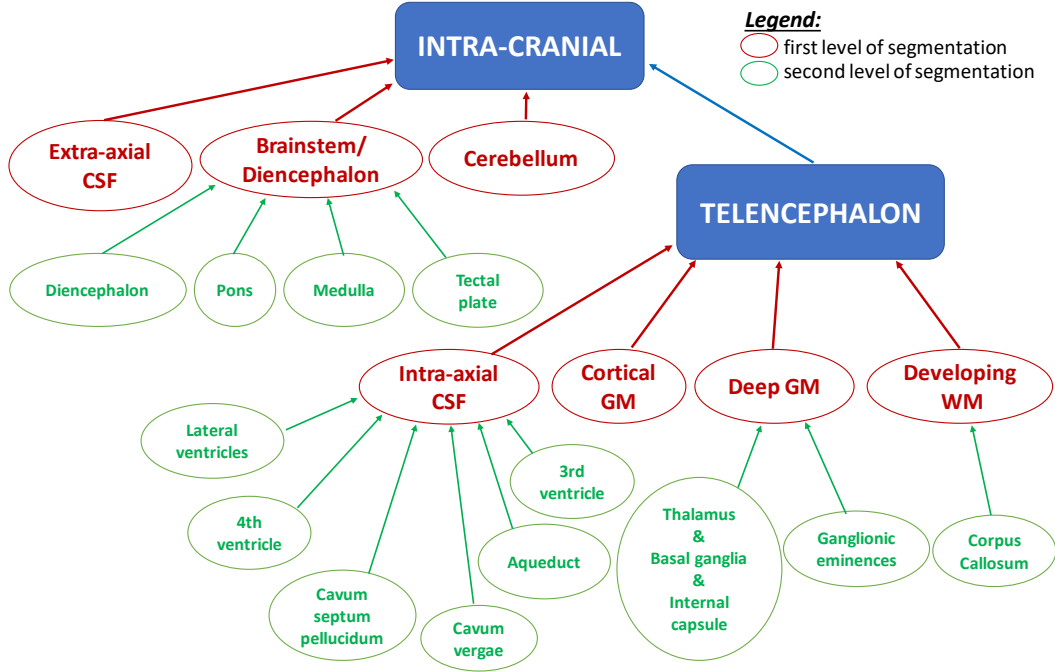


Figure 3.3: Proposed brain classes hierarchy for the developing fetal brain.

5. the cortical gray matter,
6. the deep gray matter,
7. the brainstem,
8. the corpus callosum

Those tissue types follow the hierarchy that we propose in Fig. 3.3.

The labelling protocol used for white matter, intra-axial CSF, cerebellum, extra-axial CSF, cortical gray matter, deep gray matter, and brainstem is based on the segmentation guidelines that were used for the FeTA dataset [Payette 21]. We have made the following amendments to the FeTA segmentation guidelines. The corpus callosum, that is not present in FeTA, was segmented. As a result, the corpus callosum was excluded from the white matter manual segmentations. We use the term *intra-axial CSF* rather than *ventricular system* as in FeTA because, in addition to the lateral ventricles, third ventricle, and fourth ventricle, this region also contains the cavum septum pellucidum and the cavum vergae that are not part of the ventricular system [Tubbs 11]. We also add that the cortical gray matter separates the white matter from the extra-axial CSF. In particular, the white matter should never be directly in contact with the extra-axial CSF. The two tissue types

are always separated by a fine layer of cortical gray matter.

The eight tissue types were segmented for our dataset by Michael Aertsen, a paediatric radiologist at University Hospital Leuven specialized in fetal brain anatomy, and by Thomas Deprest, Doeem Emam, Esther Van Elslander, Frédéricis Guffens, Lucas Fidon, and Nada Mufti under the supervision of Michael Aertsen who trained them, and quality controlled and corrected their manual segmentations.

Manual segmentations were all performed using the software ITK-SNAP [Yushkevich 16]. The segmentation was performed iteratively in the three views (axial, sagittal, and coronal). The rigid registration of the 3D MRI to a normalized atlas space during the super-resolution and reconstruction step (see section 3.2.4) made this process easier for the raters. The manual segmentation of the different tissue types was performed jointly with the different tissue types represented as different layers in the segmentation nifti file. We found in preliminary work, that this sped up the manual segmentation process and avoided inconsistencies between layers as compared to working with separate binary segmentation files with one file per tissue type. It was observed that raters tended to under-segment the tissue types when they performed manual segmentations using separated files for the different tissue types. We attribute this to a form of imposter syndrome. In case experts are not entirely sure about the assignment of a voxel to a given tissue types, experts will prefer to not segment the voxel. However, this implicitly attributes those missed voxels to the background segmentation layer and lead to under-segmentation. In contrast, when performing the segmentation for all the tissue types jointly, the experts are forced to chose the label the most likely for every voxel inside the brain.

AI-assisted Manual Segmentation

To reduce the time required for the manual segmentation, the segmentation were all initialized using automatic segmentation methods. As the number of manual segmentations was increasing, the automatic segmentation methods was progressively refined. The more manual segmentations were available, the better were the automatic initial segmentations, and the faster it was to correct the automatic segmentations to obtain more manual segmentations.

The first automatic initial segmentations have been computed using an atlas-based segmentation method originally developed for the brain MRI segmentation of infants born preterm [Orasanu 16]. Once a dozen of manual segmentations were available we trained a deep learning-based segmentation algorithm based on 3D U-Net [Çiçek 16] for fetal brain 3D MRI segmentation. The deep learning method has been progressively re-trained and improved, and has progressively replaced the

atlas-based method.

The registration-based approach sometimes lead to unsatisfactory initial segmentations. This was in particular the case for the youngest fetuses at the time of MRI acquisition and for the fetuses with an abnormal brain anatomy. We hypothesize that the use of a neonatal brain atlas [Kuklisova-Murgasova 11] in the atlas-based method [Orasanu 16] may account for this. This was one of the motivations for developing our fetal brain spatio-temporal atlas for the developing fetal brain with spina bifida aperta [Fidon 21e] (see chapter 6).

It is worth noting that the deep learning pipeline has also been found to compute segmentations that were suboptimal, yet superior to the atlas-based method on average, for the youngest fetuses and the fetuses with an abnormal brain anatomy. We hypothesized that it was partly due to the underrepresentation of abnormal brain anatomy in the training dataset. To mitigate this problem, we have added 3D MRIs of fetal brains with various and severe brain abnormal anatomy early in the construction of the dataset. In addition, we have developed a new training method for deep neural network based on distributionally robust optimization [Fidon 22b, Fidon 21b] (see chapter 5).

The manual segmentation was also stratified in terms of the tissue types that were segmented. The first 200 fetal brain 3D MRIs were, initially, segmented only for the white matter, the intra-axial CSF, and the cerebellum. Later, some of those fetal brain MRI have been also segmented for the extra-axial CSF. Eventually, the remaining tissue types were added and new fetal brain MRIs were systematically segmented for all the tissue types, including control and correction by an expert.

The manual segmentations publicly available as part of the FeTA [Payette 21] dataset were also corrected [Fidon 21c, Fidon 21b] to reduce the variability against the published segmentation guidelines that was released with the FeTA dataset. The corpus callosum was added to the manual segmentations of the FeTA dataset 3D MRIs.

Inter-rater Variability

We have estimated the inter-rater variability using all the 3D MRIs from the public fetal brain dataset FeTA [Payette 21] by comparing our refined manual segmentations against the original manual segmentations available with the FeTA dataset.

In [Payette 21], the inter-rater variability has been previously estimated for only 9 fetal brain 3D MRIs.

The inter-rater variability is evaluated for all the tissue types except for the corpus callosum that was not present in the original FeTA manual segmentations

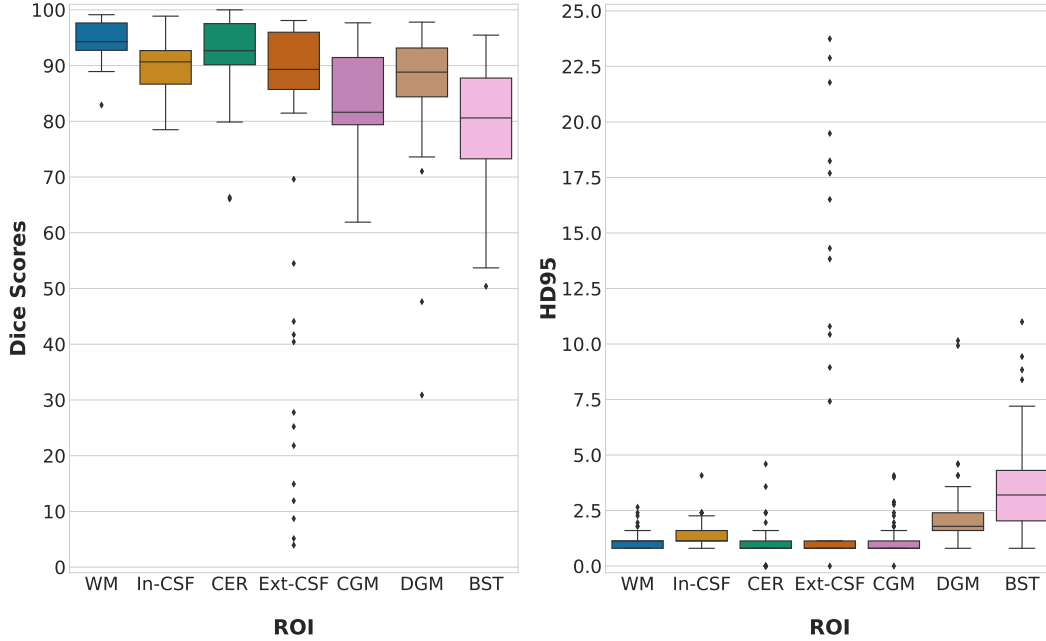


Figure 3.4: **Manual Segmentation Inter-rater Variability.** The evaluation is performed using two manual segmentations for 78 3D MRIs from the FeTA dataset [Payette 21]. (left) the Dice score (in percentage) and (right) Hausdorff distance at 95% percentiles (HD95; in mm). WM: white matter, in-CSF: intra-axial cerebrospinal fluid, CER: cerebellum, ext-CSF: extra-axial cerebrospinal fluid, CGM: cortical gray matter, DGM: deep gray matter, BST: brainstem.

using the Dice scores and the Hausdorff distance at 95% percentiles. The results of the inter-rater variability can be found in Fig. 3.4.

We obtained a mean \pm standard deviation of Dice scores (in %) of 94.7 ± 3.1 for the white matter, 89.9 ± 4.5 for the intra-axial CSF, 92.5 ± 6.2 for the cerebellum, 81.0 ± 25.4 for the extra-axial CSF, 83.7 ± 7.9 for the cortical gray matter, 87.2 ± 10.0 for the deep gray matter, and 79.6 ± 10.7 for the brainstem.

We also obtained a mean \pm standard deviation of Hausdorff distance at 95% percentiles (in mm) of 1.1 ± 0.4 for the white matter, 1.3 ± 0.5 for the intra-axial CSF, 1.0 ± 0.7 for the cerebellum, 3.3 ± 6.0 for the extra-axial CSF, 1.1 ± 0.7 for the cortical gray matter, 2.2 ± 1.6 for the deep gray matter, and 3.6 ± 2.1 for the brainstem.

Those average metric performances are similar to the one achieved by a state-of-the-art deep learning pipeline (nnU-Net [Isensee 21]) when trained and evaluated on MRI data acquired in the same center (see chapter 7 and Fig. A.2 A.3). This suggests that current state-of-the-art deep learning methods achieve human-level performance when evaluated on MRI data acquired at the same center as the data

used for training. It is worth noting that here we compare segmentation performances measured on different 3D MRIs.

The inter-rater variability for the extra-axial CSF, cortical gray matter, deep gray matter, and brainstem appears higher than for the white matter, intra-axial CSF, and cerebellum. In particular, outliers with high variations are observed for the extra-axial CSF, deep gray matter, and brainstem. Those results are consistent with the large inter-rater variability previously measured for the extra-axial CSF in [Payette 21].

For the original FeTA manual segmentations, the raters annotated some of the tissue types in an indirect manner. For example, the extra-axial CSF was not segmented directly but instead was obtained by subtracting all the other tissue types to the manually segmented intracranial space. For neurotypical fetal brains and most abnormal fetal brains the extra-axial CSF delimits the intra-cranial space, which justifies this strategy. However, for the 3D MRIs of spina bifida with gestational ages of 27 weeks or less we observed that this is often not the case. This may account for the outliers observed for the extra-axial CSF in Fig. 3.4.

It is worth noting that our refined manual segmentations are based on the original manual segmentations. This might bias the refined manual segmentation towards the original manual segmentations. In addition, different annotation tools were used for the original FeTA segmentations [Payette 21] and our refined segmentations. The original FeTA segmentations were performed using the draw tool in 3D slicer, in only one plane for each tissue type, and the annotations were performed manually only on every second or third slice. In addition, no spatial alignment to a standard clinical view using an atlas was performed prior to manual segmentation. In contrast, our refined manual segmentations have been performed after rigid registration to a fetal brain atlas [Gholipour 17] and annotation were performed densely using the three planes and the paint tool in ITK-SNAP. Therefore, the variability measured in Fig.3.4 is not only due to the different raters. We also hypothesize that the refined manual segmentations are more accurate than the original FeTA manual segmentations.

3.2.6 Data availability

Access to the data from UHL will require approval by the ethics committee at UHL. Access to the data acquired at UCLH, MCT, BFT, CRK, NCS, and LVP will require approval by the Caldicott guardian at UCLH. Access to the data from MUV can be requested using the contact details available at <https://www.cir.meduniwien.ac.at/research/fetal/>. Access to the data from KCL will require

CHAPTER 3. FETAL BRAIN 3D MRI SEGMENTATION DATASET

approval by the ethics committee at KCL.

The FeTA dataset [Payette 21] is publicly available on Synapse: <https://doi.org/10.7303/syn23747212>. Access requires registration to Synapse and agreement to the terms of use. The manual segmentations for the fetal brain MRI of FeTA dataset, that we have contributed in this work and our previous work [Fidon 21b, Fidon 21c], are publicly available on Zenodo: <https://doi.org/10.5281/zenodo.5148612> under the term of the Creative Commons Attribution-NonCommercial-NoDerivs 3.0 Unported license (CC BY-NC-ND 3.0). Access to the data is restricted. Readers and reviewers can apply for access to the data by filling in a form. The only requirement is to acknowledge that the applicant will not use those data for commercial purposes.

The first spatio-temporal atlas of the normal developing fetal brain [Gholipour 17] that we have used is publicly available at http://crl.med.harvard.edu/research/fetal_brain_atlas/. Access requires readers to fill in an access form. Alternatively, one can download the fetal brain atlas directly from the NiftyMIC [Ebner 20] GitHub repository. The second spatio-temporal atlas of the normal developing fetal brain [Wu 21], that was based on a Chinese population, is publicly available at <https://github.com/DeepBMI/FBA-Chinese>. The spina bifida spatio-temporal atlas [Fidon 21e] is publicly available on Synapse under the terms of the Creative Commons Zero "No rights reserved" data waiver (CC0 1.0 Public domain dedication): <https://www.synapse.org/#!Synapse:syn25887675/wiki/611424>. Access requires registration to Synapse and agreement to the terms of use.

The fetal brain 3D T2w MRI segmentation protocol that was used for the manual segmentations can be found at <http://neuroimaging.ch/feta>.

3.3 Conclusion

In this chapter, we have reviewed the literature on fetal brain MRI segmentation. We identified two main groups of methods: the atlas-based methods and the deep learning-based methods. We have outlined how the work presented in this thesis has contributed to atlas-based methods (Chapter 6), to deep learning-based methods (Chapter 4 and Chapter 5), and to the comparison and combination of atlas-based and deep learning-based methods (Chapter 7).

Our fetal brain 3D MRI dataset and the pre-processing applied to all the the 3D MRIs have also been described. We will therefore whenever possible refer to this chapter in the rest of this thesis for the fetal brain data used in our experiments. With 540 fetal brain 3D MRIs from a total of 13 hospitals, our dataset is the largest fetal brain MRI segmentation dataset to date. Only subsets of the dataset are used in some chapters because we had not completed the dataset at the time of publication or submission.

Future work. The dataset described in this chapter is for a large part private. Releasing publicly all or part of the private fetal brain MRI data is part of future work. For now, we were able to make public our refined manual segmentations for the FeTA 2021 dataset.

The high inter-rater variability measured in this chapter for some tissue types also suggest that a precise labeling protocol for fetal brain MRI is still needed.

Label-set Loss Functions for Partial Supervision

Table of Contents

4.1	Introduction to partially supervised learning	65
4.2	Theory of Label-set Loss Functions	66
4.2.1	Label-set Loss Functions	67
4.2.2	Leaf-Dice: A Label-set Generalization of the Dice Loss . .	68
4.2.3	Converting Classical Loss Functions to Label-set Loss Functions	69
4.3	MRI Datasets	70
4.3.1	Fetal Brain MRI Data with Partial Segmentations	70
4.3.2	Brain Tumor multi-parametric MRI Dataset	71
4.4	Experiments	72
4.5	Conclusion	77

Foreword This chapter is to a large extent an *in extenso* reproduction of [Fidon 21a]. However, the experiments on BraTS in this chapter are new and have not been previously published.

4.1 Introduction to partially supervised learning

As detailed in Chapter 3, the parcellation of fetal brain MRI is essential for the study of fetal brain development [Benkarim 17]. Reliable analysis and evaluation of fetal brain structures could also support diagnosis of central nervous system pathology, patient selection for fetal surgery, evaluation and prediction of outcome, hence also parental counselling [Aertsen 19, Danzer 20, Moise Jr 16, Sacco 19, Zarutskie 19]. Deep learning sets the state of the art for the automatic parcellation of fetal brain MRI [Fetit 20, Khalili 19, Payette 20, Payette 19]. Training a deep learning model requires a large amount of accurately annotated data. However, manual parcellation of fetal brain 3D MRI requires highly skilled raters and is time-consuming.

Training a deep neural network for segmentation with partially segmented images is known as partially supervised learning [Zhou 19]. Recent studies have proposed to use partially supervised learning for body segmentation in CT [Dmitriev 19, Fang 20, Shi 21, Zhou 19] and for the joined segmentation of brain tissues and lesions in MRI [Dorent 21, Roulet 19]. One of the main challenges in partially supervised learning is to define loss functions that can handle partially segmented images. Several previous studies have proposed to adapt existing loss functions for fully supervised learning using a somewhat ad hoc marginalization method [Fang 20, Roulet 19, Shi 21]. Theoretical motivations for such marginalisation were missing. It also remains unclear whether it is the only way to build loss functions for partially supervised learning.

In this chapter, we give the first theoretical framework for loss functions in partially supervised learning. We call those losses *label-set loss functions*. While in a fully supervised scenario, each voxel is assigned a single label, which we refer to as a *leaf-label* hereafter to avoid ambiguity; with partial supervision, each voxel is assigned a combined label, which we refer to as a *label-set*. As illustrated in Fig. 4.1, a typical example of partial supervision arises when there are missing leaf-label annotations. In which case the regions that were not segmented manually are grouped under one label-set (*unannotated*). Our theoretical contributions are threefold: 1) We introduce an axiom that label-set loss functions must satisfy to guarantee compatibility across label-sets and leaf-labels; 2) we propose a generalization of the Dice loss, leaf-Dice, that satisfies our axiom for the common case of missing leaf-labels; and 3) we demonstrate that there is one and only one way to convert a classical segmentation loss for fully supervised learning into a loss function for partially supervised learning that complies with our axiom. This theoretically justifies the marginalization method used in previous work [Fang 20, Roulet 19, Shi 21].

In our experiments, we propose the first application of partial supervision to fetal brain 3D MRI segmentation. We use 244 fetal brain volumes from 3 clinical centers, to evaluate the automatic segmentation of 8 tissue types for both normal fetuses and fetuses with open spina bifida. We compare the proposed leaf-Dice to another label-set loss [Shi 21] and to two other baselines. Our results support the superiority of label-set losses that comply with the proposed axiom and show that the leaf-Dice loss significantly outperforms the three other methods.

4.2 Theory of Label-set Loss Functions

In fully-supervised learning, we learn from ground-truth segmentations $\mathbf{g} \in \mathbf{L}^N$ where N is the number of voxels and \mathbf{L} is the set of final labels (e.g. white matter,

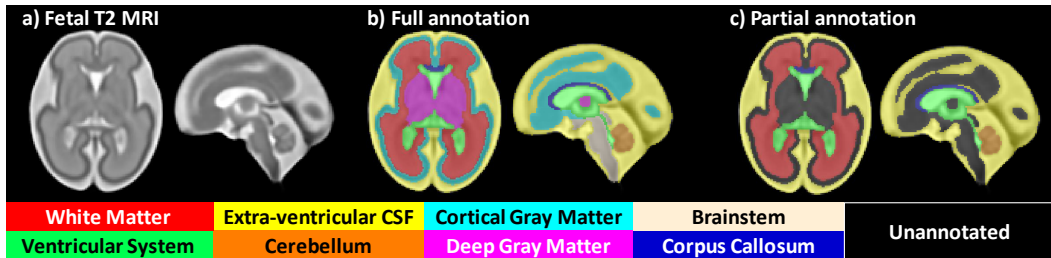


Figure 4.1: Illustration of partial annotations on a control fetal brain MRI [Gholipour 17]. b) all the leaf-labels are annotated. c) partial annotations where cortical gray matter (CGM), deep gray matter (DGM), and brainstem (B) are not annotated. In this cases, unannotated voxels have the label-set annotation $\{\text{CGM}, \text{DGM}, \text{B}\}$.

ventricular system). We denote elements of \mathbf{L} as *leaf-labels*. In contrast, with partial supervision, $\mathbf{g} \in (2^{\mathbf{L}})^N$, where $2^{\mathbf{L}}$ is the set of subsets of \mathbf{L} . In other words, each voxel annotation is a *set* of leaf-labels (a *label-set*). The label-set of an annotated white matter voxel would be simply $\{\text{white matter}\}$, and the label-set of a voxel that could be either white matter or deep gray matter would be $\{\text{white matter}, \text{deep gray matter}\}$. In both fully-supervised and partially-supervised learning, the network is trained to perform full segmentation predictions: $\mathbf{p} \in P(\mathbf{L})^N$, where $P(\mathbf{L})$ is the space of probability vectors for leaf-labels.

4.2.1 Label-set Loss Functions

A loss function $\mathcal{L}_{\text{partial}}(\cdot, \cdot)$ for partially supervised learning can be any differentiable function that compares a proposed probabilistic network output for leaf-labels, $\mathbf{p} \in P(\mathbf{L})^N$, and a partial label-set ground-truth annotation, $\mathbf{g} \in (2^{\mathbf{L}})^N$,

$$\mathcal{L}_{\text{partial}} : P(\mathbf{L})^N \times (2^{\mathbf{L}})^N \rightarrow \mathbb{R} \quad (4.1)$$

However, such $\mathcal{L}_{\text{partial}}$, in general, may consider all possible label-sets as independent and ignore the relationship between a label-set and its constituent leaf-labels. We claim that segmentation loss functions for partially supervised learning must be compatible with label-set inclusion. The terms *set* and *inclusion* refer to the definitions of *set* and *inclusion* in set theory [Bourbaki 04]. For example, in the case of three leaf-labels $\mathbf{L} = \{l_1, l_2, l_3\}$, let voxel i be labeled with the label-set $g_i = \{l_1, l_2\}$. We know that the true leaf-label is either l_1 or l_2 . Therefore the exemplar leaf-label probability vectors $\mathbf{p}_i = (0.4, 0.4, 0.2)$, $\mathbf{q}_i = (0.8, 0, 0.2)$, and $\mathbf{h}_i = (0, 0.8, 0.2)$ need to be equivalent conditionally to the ground-truth partial annotation g_i . That is, the value of the loss function should be the same whether the predicted leaf-label

probability vector for voxel i is \mathbf{p}_i , \mathbf{q}_i , or \mathbf{h}_i .

Formally, let us define the marginalization function Φ as

$$\Phi : P(\mathbf{L})^N \times (2^{\mathbf{L}})^N \rightarrow P(\mathbf{L})^N \quad \text{s.t.} \quad \forall i, c, \begin{cases} \tilde{p}_{i,c} = \frac{1}{|g_i|} \sum_{c' \in g_i} p_{i,c'} & \text{if } c \in g_i \\ \tilde{p}_{i,c} = p_{i,c} & \text{if } c \notin g_i \end{cases}$$

$$(\mathbf{p}, \mathbf{g}) \mapsto (\tilde{p}_{i,c})_{i=1 \dots N, c \in \mathbf{L}}$$

where $|\cdot|$ is the number of elements in a set. In the previous example, $\Phi(\mathbf{p}; \mathbf{g})_i = \Phi(\mathbf{q}; \mathbf{g})_i = \Phi(\mathbf{h}; \mathbf{g})_i = (0.4, 0.4, 0.2)$.

We define **label-set loss functions** as the functions $\mathcal{L}_{\text{partial}}$ that satisfy the axiom

$$\forall \mathbf{g}, \forall \mathbf{p}, \mathbf{q}, \quad \Phi(\mathbf{p}; \mathbf{g}) = \Phi(\mathbf{q}; \mathbf{g}) \implies \mathcal{L}_{\text{partial}}(\mathbf{p}, \mathbf{g}) = \mathcal{L}_{\text{partial}}(\mathbf{q}, \mathbf{g}) \quad (4.2)$$

We demonstrate that a loss \mathcal{L} is a label-set loss function if and only if

$$\forall (\mathbf{p}, \mathbf{g}), \quad \mathcal{L}(\mathbf{p}, \mathbf{g}) = \mathcal{L}(\Phi(\mathbf{p}; \mathbf{g}), \mathbf{g}) \quad (4.3)$$

See the supplementary material for a proof of this equivalence.

4.2.2 Leaf-Dice: A Label-set Generalization of the Dice Loss

In this section, as per previous work [Dmitriev 19, Dorent 21, Fang 20, Roulet 19, Shi 21, Zhou 19], we consider the particular case in which, per training example, there is only one label-set that is not a singleton and contains all the leaf-labels that were not manually segmented in this example. An illustration for fetal brain segmentation can be found in Fig.4.1.

We propose a generalization of the mean class Dice Loss [Fidon 17a, Milletari 16] for this particular case and prove that it satisfies our axiom (4.2).

Let $\mathbf{g} \in (2^{\mathbf{L}})^N$ be a partial label-set segmentation such that there exists a label-set $\mathbf{L}'_{\mathbf{g}} \subsetneq \mathbf{L}$ that contains all the leaf-labels that were not manually segmented for this subject. Therefore, \mathbf{g} takes its values in $\{\mathbf{L}'_{\mathbf{g}}\} \cup \{\{c\} \mid c \in \mathbf{L} \setminus \mathbf{L}'_{\mathbf{g}}\}$. We demonstrate that the leaf-Dice loss defined below is a label-set loss function

$$\forall \mathbf{p}, \quad \mathcal{L}_{\text{Leaf-Dice}}(\mathbf{p}, \mathbf{g}) = 1 - \frac{1}{|\mathbf{L}|} \sum_{c \in \mathbf{L}} \frac{2 \sum_i \mathbb{1}(g_i = \{c\}) p_{i,c}}{\sum_i \mathbb{1}(g_i = \{c\})^\alpha + \sum_i p_{i,c}^\alpha + \epsilon} \quad (4.4)$$

where $\alpha \in \{1, 2\}$ (in line with the variants of soft Dice encountered in practice), and $\epsilon > 0$ is a small constant. A proof that $\mathcal{L}_{\text{Leaf-Dice}}$ satisfies (4.3) can be found in the supplementary material. It is worth noting that using $\mathcal{L}_{\text{Leaf-Dice}}$ is not equivalent to just masking out the unannotated voxels, i.e. the voxels i such that

$g_i = \mathbf{L}'_{\mathbf{g}}$. Indeed, for all the $c \in \mathbf{L} \setminus \mathbf{L}'_{\mathbf{g}}$, the term $\sum_i p_{i,c}^\alpha$ in the denominator pushes $p_{i,c}$ towards 0 for all the voxels indices i including the indices i for which $g_i = \mathbf{L}'_{\mathbf{g}}$. As a result, when $g_i = \mathbf{L}'_{\mathbf{g}}$, only the $p_{i,c}^\alpha$ for $c \notin \mathbf{L}'_{\mathbf{g}}$ are pushed toward 0, which in return pushes the $p_{i,c}^\alpha$ for $c \in \mathbf{L}'_{\mathbf{g}}$ towards 1 since $\sum_{c \in \mathbf{L}} p_{i,c} = 1$.

4.2.3 Converting Classical Loss Functions to Label-set Loss Functions

In this section, we demonstrate that there is one and only one canonical method to convert a segmentation loss function for fully supervised learning into a label-set loss function for partially supervised learning satisfying (4.3).

Formally, a label-set segmentation \mathbf{g} can be seen as a soft segmentation using an injective function $\Psi : (2^{\mathbf{L}})^N \hookrightarrow P(\mathbf{L})^N$ that satisfies the relation

$$\forall \mathbf{g} \in (2^{\mathbf{L}})^N, \forall i, c, \quad [\Psi(\mathbf{g})]_{i,c} > 0 \implies c \in g_i \quad (4.5)$$

Note however, that the function Ψ is not unique. Following the maximum entropy principle leads to choose

$$\Psi_0 : (g_i) \mapsto (\tilde{p}_{i,c}) \quad \text{s.t.} \quad \forall i, c \begin{cases} \tilde{p}_{i,c} = \frac{1}{|g_i|} & \text{if } c \in g_i \\ \tilde{p}_{i,c} = 0 & \text{otherwise} \end{cases} \quad (4.6)$$

We are interested in converting a loss function for fully-supervised learning $\mathcal{L}_{fully} : P(\mathbf{L})^N \times P(\mathbf{L})^N \rightarrow \mathbb{R}$ into a label-set loss function for partial supervision defined as $\mathcal{L}_{partial}(\mathbf{p}, \mathbf{g}) = \mathcal{L}_{fully}(\mathbf{p}, \Psi(\mathbf{g}))$.

Assuming that \mathcal{L}_{fully} is minimal if and only if the predicted segmentation and the soft ground-truth segmentation are equal, we demonstrate in the supplementary material that $\mathcal{L}_{partial}$ is a label-set loss function if and only if

$$\forall (\mathbf{p}, \mathbf{g}) \in P(\mathbf{L})^N \times (2^{\mathbf{L}})^N, \quad \begin{cases} \mathcal{L}_{partial}(\mathbf{p}, \mathbf{g}) = \mathcal{L}_{fully}(\Phi(\mathbf{p}; \mathbf{g}), \Psi(\mathbf{g})) \\ \Psi(\mathbf{g}) = \Psi_0(\mathbf{g}) \end{cases} \quad (4.7)$$

Therefore, the only way to convert a fully-supervised loss to a loss for partially-supervised learning that complies with our axiom (4.2) is to use the marginalization function Φ on the predicted segmentation and Ψ_0 on the ground-truth partial segmentation. For clarity, we emphasise that the Leaf-Dice is a generalisation rather than a conversion of the Dice loss.

Table 4.1: Number of 3D MRI and number of manual segmentations available per tissue types. **WM**: white matter, **Vent**: ventricular system, **Cer**: cerebellum, **ECSF**: extra-ventricular CSF, **CGM**: cortical gray matter, **DGM**: deep gray matter, **BS**: brainstem, **CC**: corpus callosum.

Split	Condition	MRI	WM	Vent	Cer	ECSF	CGM	DGM	BS	CC
Training	Atlas	18	18	18	18	18	18	18	18	18
Training	Control	116	116	116	116	54	0	0	0	18
Training	Spina Bifida	30	30	30	30	0	0	0	0	0
Testing	Control	34	34	34	34	34	15	15	15	0
Testing	Spina Bifida	66	66	66	66	66	25	25	25	41

Related Work.

When \mathcal{L}_{fully} is the mean class Dice loss [Fidon 17a, Milletari 16] and the values of \mathbf{g} are a partition of \mathbf{L} , like in section 4.2.2, one can prove that $\mathcal{L}_{partial}$ is the marginal Dice loss [Shi 21] (proof in supplementary material). Similarly, when \mathcal{L}_{fully} is the cross entropy loss, $\mathcal{L}_{partial}$ is the marginal cross entropy loss [Fang 20, Roulet 19, Shi 21]. Note that in [Fang 20, Roulet 19, Shi 21], the marginalization approach is proposed as a possible method to convert the loss function. We prove that this is the only method.

4.3 MRI Datasets

4.3.1 Fetal Brain MRI Data with Partial Segmentations

In this section, we describe the fetal brain 3D MRI datasets that were used. This is a subset of the dataset described in Chapter 3. Details about the MRI data acquisition and pre-processing are described in Chapter 3.

Training Data for Fully Supervised Learning. 18 fully-annotated control fetal brain MRI from a spatio-temporal fetal brain MRI atlas [Gholipour 17].

Training Data for Partially Supervised Learning. 18 fully-annotated volumes from the fully-supervised dataset, combined with 146 partially annotated fetal brain MRI from a private dataset. The segmentations available for those 3D MRI are detailed in Table 4.1.

Multi-centric Testing Data. The testing dataset contains a total of 100 fetal brain 3D MRI. This includes 60 volumes from University Hospital Leuven and 40

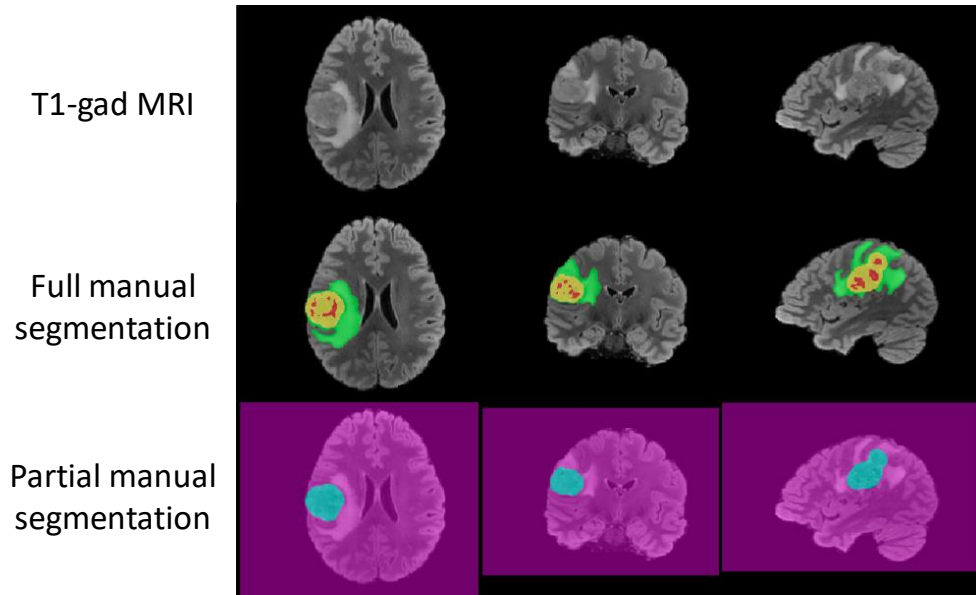


Figure 4.2: Illustration of the partial annotations used for experiments on brain tumor segmentation. In blue is the tumor core, a label-set containing the enhancing tumor (yellow) and non-enhancing tumor (red). In purple is another label-set that contains the peritumoral edema (green) and the background.

volumes from the publicly available FeTA dataset [Payette 21]. The segmentations available for those 3D MRI are detailed in Table 4.1. The 3D MRI of the FeTA dataset come from a different center than the training data. Automatic brain masks for the FeTA data were obtained using atlas affine registration with a normal fetal brain and a spina bifida spatio-temporal atlas [Fidon 21e, Gholipour 17].

4.3.2 Brain Tumor multi-parametric MRI Dataset

We have used the BraTS 2021 training dataset¹ [Baid 21] in our experiments. The dataset contains 1251 cases, and the same four MRI sequences (T1, ceT1, T2, and FLAIR) for all cases, corresponding to patients with either a high-grade Gliomas [Bakas 17b] or a low-grade Gliomas [Bakas 17c]. All the cases were manually segmented for peritumoral edema, enhancing tumor, and non-enhancing tumor core using the same labeling protocol [Menze 14, Bakas 18, Bakas 17a, Baid 21]. For each case, the four MRI sequences are available after co-registration to the same anatomical template, interpolation to 1mm isotropic resolution, and skull stripping [Menze 14].

¹<https://www.synapse.org/#!Synapse:syn25829067/wiki/610865>

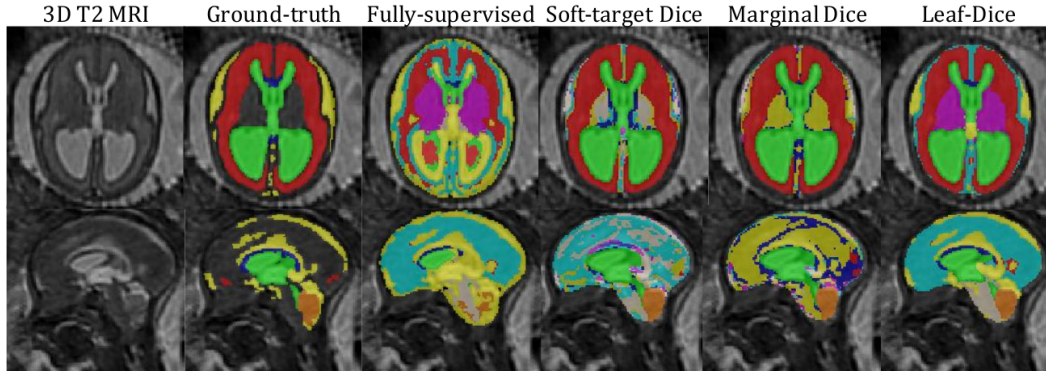


Figure 4.3: Qualitative comparison on an open spina bifida case. Only the proposed Leaf-Dice loss provides satisfactory segmentations for all tissue types.

Partial Labels for Brain Tumor Segmentation. The 1215 studies of BraTS 2021 training dataset are all fully-segmented. To perform an ablation study on the ratio of partially and fully segmented samples, we have created partial segmentation for all of them using two label-set: the tumor core containing the enhancing tumor and the non-enhancing tumor, and a label-set containing the background and the peritumoral edema. An illustration is given in Fig. 4.2. Such partial segmentations correspond to the manual segmentations that would be typically available in clinical data used for resection surgery or radiotherapy.

4.4 Experiments

In this section, we compare three partially supervised methods and one fully supervised method using the fetal brain 3D MRI dataset described in section 4.3. We also perform an ablation study on the ratio of partially segmented and fully segmented cases using the BraTS 2021 dataset as described in section 4.3.

Deep Learning Pipeline for Fetal Brain Segmentation. We use a 3D U-Net [Çiçek 16] architecture with 5 levels, leaky ReLU and instance normalization [Ulyanov 16]. For training and inference, the entire volumes were used as input of the 3D U-Net after padding to $144 \times 160 \times 144$ voxels. For each method of Table 4.2, an ensemble of 10 3D U-Net is used. Using an ensemble of models makes the comparison of segmentation results across methods less sensitive to the random initialization of each network. Each 3D U-Net is trained using a random split of the training dataset into 90% for training and 10% for early stopping. During training, we used a batch size of 3, a learning rate of 0.001, and Adam [Kingma 14] optimizer with default hyperparameter values. The learning rate was tuned for the fully super-

vised learning baseline. Random right/left flip, random scaling, gamma intensity augmentation, contrast augmentation, and additive Gaussian noise were used as data augmentation during training. Our code for the label-set loss functions and the deep learning pipeline are publicly available^{2,3}.

Deep Learning Pipeline for Brain Tumor Segmentation. We have also used pipeline based on 3D U-Net for the experiments on brain tumor segmentation. The details of the deep learning pipeline can be found in our previous work [Fidon 21d].

For the ablation study on BraTS, we perform an ablation study on the ratio of partially segmented and fully segmented cases. We compare training with fully-supervised learning using only the fully-segmented cases and training with partially-supervised learning using both fully-segmented and partially-segmented cases. For fully-supervised learning we use the sum of the Dice loss and the cross entropy loss. For partially-supervised learning we use the sum of the marginalized Dice loss and the marginalized cross entropy. It is worth noting that the leaf-Dice loss cannot be used in this case because all voxels are annotated using label-set for partially-segmented cases. This is because with the proposed definition of the leaf-Dice loss function, the loss is uniformly equal to 1 and its gradient to 0 when all voxels are annotated using label-sets containing more than one element.

The BraTS 2021 dataset was split into 5 folds and the same folds were used for all the experiments on brain tumor segmentation. Each configuration is evaluated using 5-fold cross validation on the 1251 cases of the BraTS 2021 dataset.

Hardware. For training we used NVIDIA Tesla V100 GPUs. Training each model took from one to two days. For inference, we used a NVIDIA GTX 1070 GPU. The inference for a 3D MRI takes between one and two minutes. It is worth noting that the proposed loss functions are not the computational bottleneck during training and have no influence on the inference time.

Specificities for each Loss Function for Fetal Brain Segmentation. Baseline 1 is trained using fully supervised learning, the mean class Dice loss [Fidon 17a, Milletari 16], referred as \mathcal{L}_{Dice} , and the training dataset for fully supervised learning of Section 4.3 (18 training volumes only). The three other methods are trained using partially supervised learning and the training dataset for partially supervised learning of Section 4.3. Baseline 2 is trained using the soft-target Dice loss function defined as $\mathcal{L}_{Dice}(\mathbf{p}, \Psi_0(\mathbf{g}))$, where Ψ_0 is defined in (4.6). Note that Baseline 2 does

²<https://github.com/LucasFidon/label-set-loss-functions>

³<https://github.com/LucasFidon/fetal-brain-segmentation-partial-supervision-miccai21>

Table 4.2: Evaluation on the multi-centric testing fetal brain dataset (100 3D MRIs).

We report mean (standard deviation) for the Dice score (DSC) in percentages and the Hausdorff distance at 95% (HD95) in millimeters for the eight tissue types. Methods underlined are trained using partially supervised learning and can therefore take advantage of the training volumes that are partially annotated (146 volumes) while the baseline trained with fully-supervised learning can only use the fully-annotated volumes (18 volumes). The same testing images and annotations are used for all methods for evaluation. **Loss functions in bold** satisfy the axiom of label-set loss functions. Best mean values are in bold. Mean values significantly better with $p < 0.01$ (resp. worse) than the ones achieved by the fully-supervised learning baseline are marked with a * (resp. a †).

Model	Metric	WM	Vent	Cer	ECSF	CGM	DGM	BS	CC
Baseline 1	DSC	76.4 (12.5)	72.1 (18.8)	67.3 (28.6)	63.9 (31.3)	47.3 (10.9)	72.7 (8.7)	56.0 (27.7)	51.6 (10.5)
	HD95	3.3 (1.2)	4.8 (3.7)	4.9 (5.2)	7.3 (7.8)	5.3 (0.9)	5.8 (2.1)	9.1 (8.2)	5.1 (3.1)
<u>Baseline 2</u>	DSC	89.5* (6.5)	87.5* (9.6)	87.2* (10.3)	37.7† (34.2)	31.4† (14.8)	18.2† (20.5)	20.2† (13.1)	12.0† (10.8)
	Soft-target Dice	HD95	1.7* (1.3)	1.6* (2.2)	2.2* (4.5)	7.1 (6.8)	6.2† (2.0)	24.2† (9.0)	33.9† (5.9)
<u>Baseline 3</u>	DSC	89.6* (6.7)	87.7* (10.4)	87.6* (9.5)	66.6* (27.7)	43.9 (15.1)	37.8† (11.3)	39.4† (16.8)	11.1† (12.3)
	Marginal Dice	HD95	1.7* (1.3)	1.6* (2.2)	2.4* (5.4)	6.2* (7.6)	4.4* (1.4)	26.7† (6.7)	33.4† (6.1)
<u>Ours</u>	DSC	91.5* (6.7)	90.7* (8.9)	89.6* (10.1)	75.3* (24.9)	56.6* (14.3)	71.4 (8.6)	61.5* (21.7)	62.0* (10.9)
	Leaf-Dice	HD95	1.5* (1.1)	1.4* (2.0)	1.7* (1.8)	5.4* (8.3)	3.9* (1.3)	7.3† (2.3)	7.9 (4.0)

not satisfy the label-set axiom (4.2). Baseline 3 is trained using the marginal Dice loss [Shi 21]. Our method is trained using the proposed Leaf-Dice loss defined in (4.4). The loss functions of Baseline 3 and our method satisfy the axiom of label-set loss functions (4.2).

Statistical Analysis. We used the two-sided Wilcoxon signed-rank test. Differences in mean values are considered significant when $p < 0.01$.

Comparison of Fully Supervised and Partially Supervised Learning. The quantitative evaluation for fetal brain MRI segmentation can be found in Table 4.2. The partially supervised learning methods of Table 4.2 all perform significantly bet-

ter than the fully supervised learning baseline in terms of Dice score and Hausdorff distance on the tissue types for which annotations are available for all the training data of Table 4.1, i.e. white matter, ventricles, and cerebellum. Some tissue types segmentations are scarce in the partially supervised training dataset as can be seen in Table 4.1, i.e. cortical gray matter, deep gray matter, brainstem, and corpus callosum. This makes it challenging for partially supervised methods to learn to segment those tissue types. Only Leaf-Dice achieves similar or better segmentation results than the fully supervised baseline for the scarce tissue types, except in terms of Hausdorff distance for the deep gray matter. The extra-ventricular CSF is an intermediate case with almost half the data annotated. The Leaf-Dice and the Marginalized Dice significantly outperforms the fully supervised baseline for all metrics for the extra-ventricular CSF, and the soft-target Dice performs significantly worse than this baseline.

The quantitative evaluation for brain tumor segmentation in MRI can be found in Fig. 4.4 for the Dice score and Fig. 4.5 for the Hausdorff distance. Here we compare partially-supervised learning and fully-supervised learning for different percentages of fully segmented cases in the training dataset: 1%, 5%, 10%, 25%, 50%, and 100% (fully segmented dataset).

The tumor core is one of the label-set and is therefore always segmented for every cases independently to the percentage. However, in theory, only the partially-supervised method using a label-set loss, exploits all of them all the time. We observe that the segmentation performance of the partially-supervised method is consistently optimal in terms of Dice scores and Hausdorff distances for all percentages. This suggests that the labels-set loss function allows the 3D U-Nets to learn to segment the tumor core to the same level of accuracy using partial and full segmentations. For 1%, 5% and 10% the partially-supervised method outperforms the fully-supervised method for the tumor core with a large margin for the two metrics. For higher percentages, the partially-supervised method achieves similar or slightly better metric values than the fully-supervised method for the tumor core.

For 1% and 5%, the partially-supervised method also outperforms the fully-supervised method for all the other regions in terms of Hausdorff distance, in particular at the queue of the Hausdorff distance distribution with the highest values. For the Dice score it is less clear. For 1% the tail of the Dice score distribution shows higher values for the partially-supervised method for whole tumor, edema, and non-enhancing tumor but not for enhancing tumor. Overall, this suggests that when many more partially segmented cases than fully-segmented cases are available for training, partially-supervised learning with a label-set loss function can help improving the robustness for the regions not annotated in the partially-segmented

data.

For percentages strictly higher than 5, the partially-supervised learning method achieve similar or lower segmentation performance for the regions not segmented in the partially-segmented data for the two metrics. This is in contrast to the higher segmentation performance for the tumor core reported above for the partially supervised method. We hypothesize this might be because the label-set loss implicitly put a higher weight on the tumor core as compared to the other regions and that the number of additional partially segmented cases is not enough to compensate this weighting effect in this case.

It also worth noting, that there are little differences of performance between percentages 100, 50, and 25 for the fully-supervised method for the two metrics. In other words, using only a quarter of the training dataset with fully-supervised learning already leads to segmentation performances similar to using the full training dataset. In the appendix A.3 we have performed experience with a larger 3D U-Net with 4 times more trainable parameters using the full training dataset with fully-supervised learning. We found no improvements after increasing the capacity of the 3D U-Net. This suggests we may have reached a stage for BraTS where more training data does not lead to much better segmentations even though many outliers remain present.

Comparison of Loss Functions for Partially Supervised Learning. The Leaf-Dice performs significantly better than the soft-target Dice for all tissue types and all metrics. The Marginal Dice performs significantly better than the soft-target Dice in terms of Dice score for extra-ventricular CSF, cortical gray matter, deep gray matter, and brainstem. Since the soft-target Dice loss is the only loss that does not satisfy the proposed axiom for label-set loss functions, this suggests label-set loss functions satisfying our axiom perform better in practice.

In addition, our Leaf-Dice performs significantly better than the Marginal Dice [Shi 21] for all metrics and all tissue types. The qualitative results of Fig. 4.3 also suggest that Leaf-Dice performs better than the other approaches. The Marginal Dice loss and the soft-target Dice loss are obtained by adapting the existing Dice loss function for fully-annotated volumes to partially-annotated volumes. This is not the case of the leaf-Dice that has been proposed specifically for partially-annotated volumes. This suggests that using a converted fully supervised loss function, as proposed in section 4.2.3 and in previous work [Fang 20, Roulet 19, Shi 21], may be outperformed by dedicated generalised label-set loss functions.

Outliers and worst-case performance in the brain tumor segmentation experiment. In this section, we study the consistency of the outliers across methods for brain tumor segmentation. The goal is to address the question: are the cases with poor segmentations always the same when using fully supervised learning or partially supervised learning and when using different ratio of the manual annotations in the BraTS 2021 dataset?

For simplicity, let us define as outliers the brain tumor segmentations for which the Dice score for at least one of the ROIs is equal to 0.

We have computed the intersection over union of the set of outliers for every method compared to training on the full dataset with all the annotations (the "100%" model in Figure 4.4). This metric measures the overlap of the set of outliers across models.

We find that all the intersection over unions of the sets of outliers are between 50% and 71%. If the threshold of the Dice score used to define outliers is chosen to be "Dice score $\leq 25\%$ ", all the intersection over unions of the sets of outliers are between 55% and 82%. And for "Dice score $\leq 50\%$ ", all the intersection over unions of the sets of outliers are between 68% and 87%.

The outliers are therefore highly consistent across methods. In particular, it implies that the majority of the outliers cannot be attributed to the stochasticity of the training method.

There are several possible causes for those recurrent outliers. This could be a limitation the nnU-Net deep learning pipeline [Isensee 21] that we use for all models. Only the annotations and the loss vary across the models that we have compared. The recurrent outliers could also be due to suboptimal manual annotations. A third possible cause, would be that the recurrent outliers correspond to isolated samples out of the training domain distribution. Assessing the later for BraTS 2021 is not possible because other than the volumes and the manual segmentations, no center or patient information are publicly available. The problem of robustness to underrepresented and out-of-distribution samples is studied in Chapter 5 and Chapter 7 of this thesis.

4.5 Conclusion

In this chapter, we present the first axiomatic definition of label-set loss functions for training a deep learning model with partially segmented images. We propose a generalization of the Dice loss, Leaf-Dice, that complies with our axiom for the common case of missing labels that were not manually segmented. We prove that loss functions that were proposed in the literature for partially supervised learning

satisfy the proposed axiom. In addition, we prove that there is one and only one way to convert a loss function for fully segmented images into a label-set loss function for partially segmented images.

We propose the first application of partially supervised learning to fetal brain 3D MRI segmentation and brain tumor segmentation in MRI. Our experiments illustrate the advantage of using partially segmented images in addition to fully segmented images for the two segmentation tasks. The comparison of our Leaf-Dice to three baselines suggests that label-set loss functions that satisfy our axiom perform significantly better for fetal brain 3D MRI segmentation.

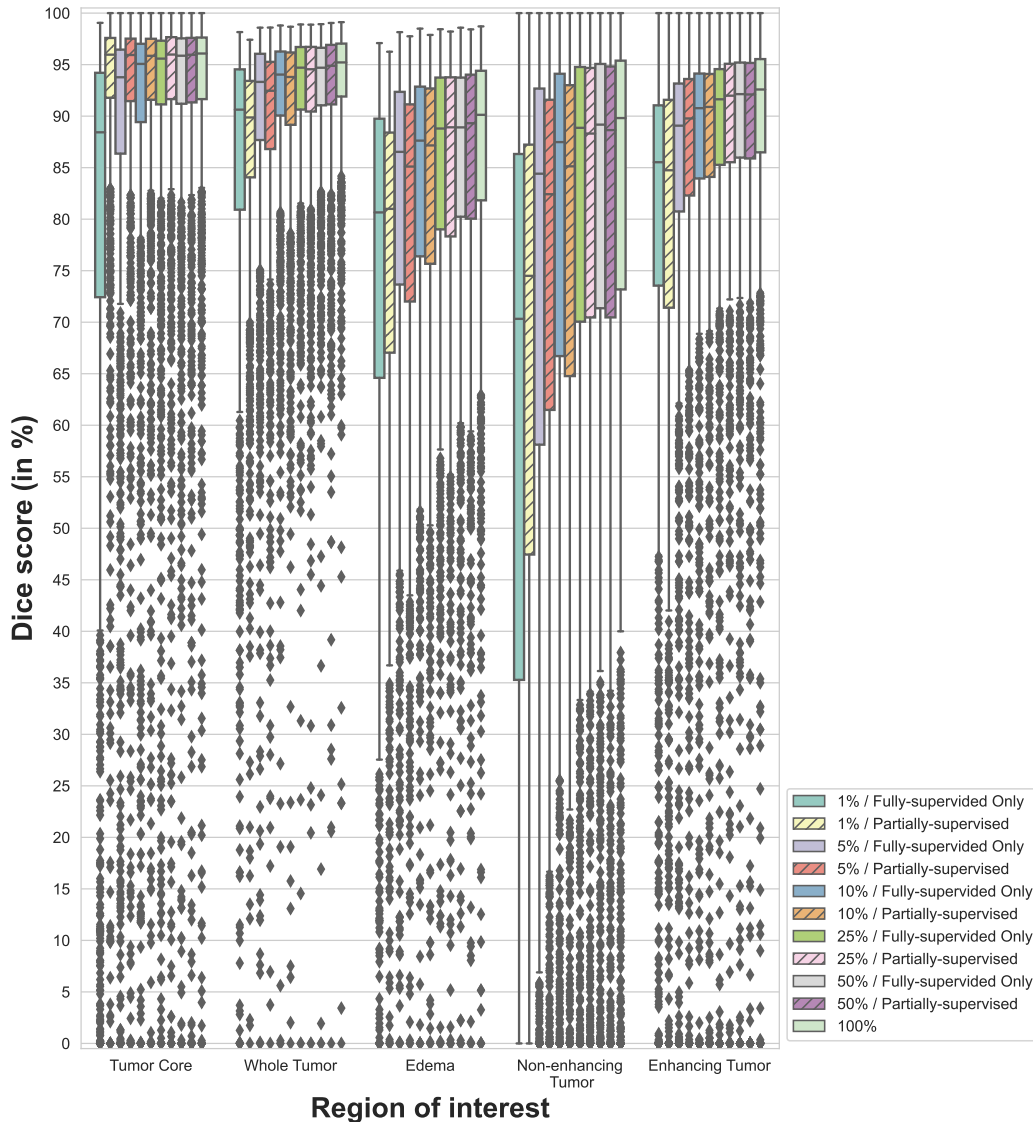


Figure 4.4: **Dice score evaluation for the ablation study on the ratio of partially segmented and fully segmented cases using the BraTS 2021 training dataset.** The percentages in the legend correspond to the percentage of fully-segmented cases used during training. The rest of the segmentation of the training dataset are converted into partial segmentations as described in Fig. 4.2. **Fully-supervised learning** (no hatches) corresponds to training with standard Dice loss plus cross entropy using only the fully segmented data. In this case the partially segmented cases are not used. **Partially-supervised learning** (hatches) corresponds to training with both fully-segmented and partially-segmented cases using the marginalized Dice loss plus the marginalized cross entropy. Each box plot results from 5-fold cross validation on the 1251 cases. Box limits are the first quartiles and third quartiles. The central ticks are the median values. The whiskers extend the boxes to show the rest of the distribution, except for points that are determined to be outliers. Outliers are data points outside the range $\text{median} \pm 1.5 \times \text{interquartile range}$.

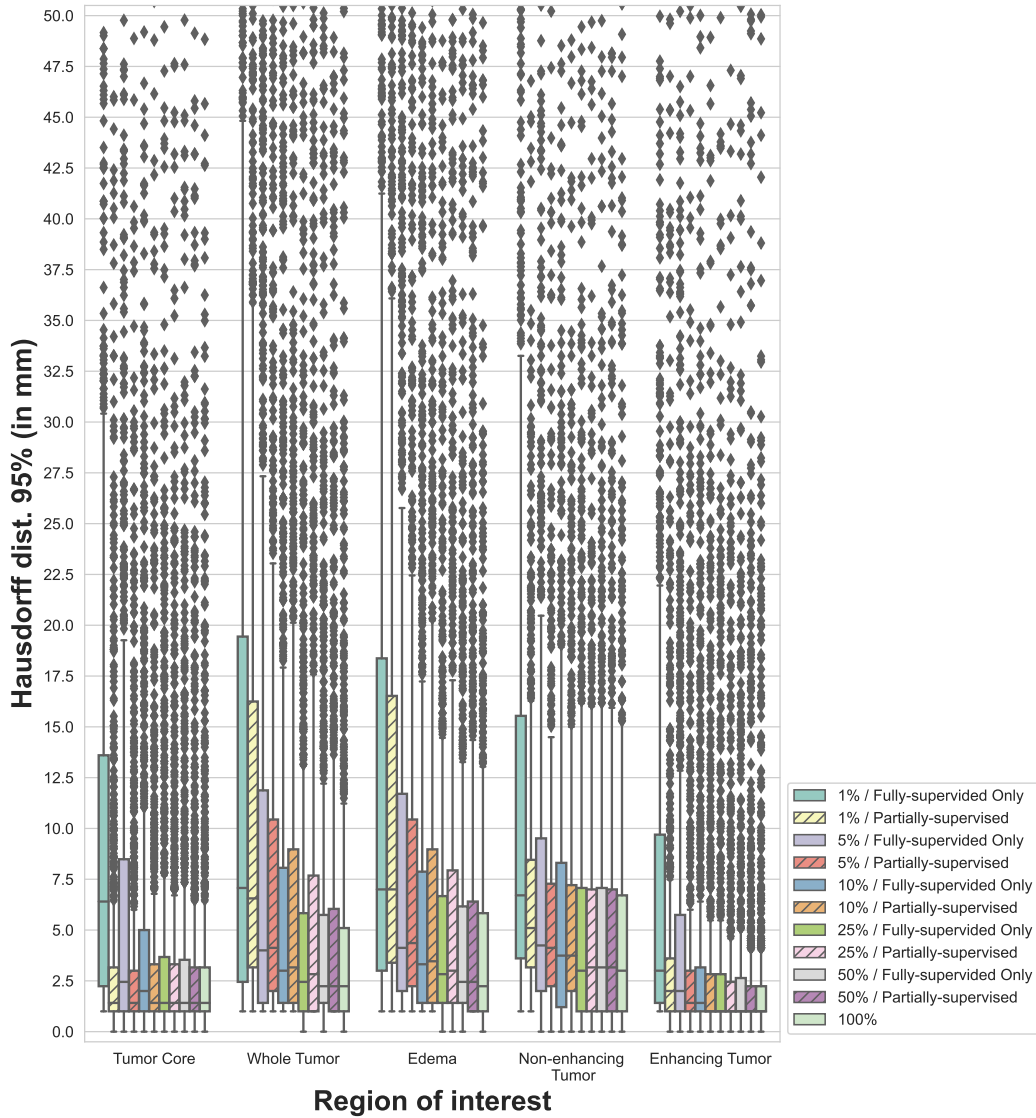


Figure 4.5: Hausdorff distance at percentile 95% evaluation for the ablation study on the ratio of partially segmented and fully segmented cases using the BraTS 2021 training dataset. The percentages in the legend correspond to the percentage of fully-segmented cases used during training. The rest of the segmentation of the training dataset are converted into partial segmentations as described in Fig. 4.2. **Fully-supervised learning** (no hatches) corresponds to training with standard Dice loss plus cross entropy using only the fully segmented data. In this case the partially segmented cases are not used. **Partially-supervised learning** (hatches) corresponds to training with both fully-segmented and partially-segmented cases using the marginalized Dice loss plus the marginalized cross entropy. Each box plot results from 5-fold cross validation on the 1251 cases. Box limits are the first quartiles and third quartiles. The central ticks are the median values. The whiskers extend the boxes to show the rest of the distribution, except for points that are determined to be outliers. Outliers are data points outside the range $\text{median} \pm 1.5 \times \text{interquartile range}$. Outliers higher than 50 mm are not displayed.

Distributionally Robust Deep Learning using Hardness Weighted Sampling

Table of Contents

5.1	Introduction on Distributionally Robust Deep Learning	82
5.2	Related Works	85
5.3	Methods	87
5.3.1	Supervised Deep Learning with Distributionally Robust Optimization	87
5.3.2	Hardness Weighted Sampling for Distributionally Robust Deep Learning	89
5.3.3	Overview of Theoretical Results	93
5.4	Experiments	95
5.4.1	Toy Example: MNIST Classification with a Class Imbalance	96
5.4.2	Medical Image Segmentation	97
5.5	Discussion and Conclusion	108

Foreword This chapter is to a large extent an *in extenso* reproduction of [Fidon 22b] and [Fidon 21b]. Limiting failures of machine learning systems is of paramount importance for safety-critical applications. In order to improve the robustness of machine learning systems, Distributionally Robust Optimization (DRO) has been proposed as a generalization of Empirical Risk Minimization (ERM). However, its use in deep learning has been severely restricted due to the relative inefficiency of the optimizers available for DRO in comparison to the widespread variants of Stochastic Gradient Descent (SGD) optimizers for ERM. We propose SGD with hardness weighted sampling, a principled and efficient optimization method for DRO in machine learning that is particularly suited in the context of deep learning. Similar to a hard example mining strategy in practice, the proposed algorithm is straightforward to implement and computationally as efficient as SGD-based optimizers used for deep learning, requiring minimal overhead computation. In contrast to typical ad hoc hard mining approaches, we prove the convergence of our DRO algorithm for over-parameterized deep learning networks with ReLU activation and finite number of layers and parameters. Our experiments on fetal brain 3D MRI segmentation and brain tumor segmentation in MRI demonstrate the feasibility and the usefulness of our approach. Using our hardness weighted sampling for training a state-of-the-art deep learning pipeline leads to improved robustness to anatomical variabilities in automatic fetal brain 3D MRI segmentation using deep learning and to improved robustness to the image protocol variations in brain tumor segmentation. Our code is available at <https://github.com/LucasFidon/HardnessWeightedSampler>.

5.1 Introduction on Distributionally Robust Deep Learning

As discussed in Chapter 1, datasets used to train deep neural networks typically contain some underrepresented subsets of cases. These cases are not specifically dealt with by the training algorithms currently used for deep neural networks. This problem has been referred to as hidden stratification [Oakden-Rayner 20]. Hidden stratification has been shown to lead to deep learning models with good average performance but poor performance on underrepresented but clinically relevant subsets of the population [Larrazabal 20, Oakden-Rayner 20, Puyol-Antón 21]. In Figure 5.1 we give an example of hidden stratification in fetal brain MRI. The presence of abnormalities associated with diseases with low prevalence [Aertsen 19] exacerbates the anatomical variability of the fetal brain between 18 weeks and 38 weeks of gestation.

While uncovering the issue, the study of [Oakden-Rayner 20] does not study the cause or propose a method to mitigate this problem. In addition, the work

of [Oakden-Rayner 20] is limited to classification. In standard deep learning pipelines, this hidden stratification is ignored and the model is trained to minimize the mean per-example loss, which corresponds to the standard Empirical Risk Minimization (ERM) problem. As a result, models trained with ERM are more likely to underperform on those examples from the underrepresented subdomains, seen as *hard examples*. This may lead to *unfair* AI systems [Larrazabal 20, Puyol-Antón 21]. For example, state-of-the-art deep learning models for brain tumor segmentation (currently trained using ERM) underperform for cases with confounding effects, such as low grade gliomas, despite achieving good average and median performance [Bakas 18]. For safety-critical systems, such as those used in healthcare, this greatly limits their usage as ethics guidelines of regulators such as [EU Commission 19] require AI systems to be technically robust and fair prior to their deployment in hospitals.

Distributionally Robust Optimization (DRO) is a robust generalization of ERM that has been introduced in convex machine learning to model the uncertainty in the training data distribution [Chouzenoux 19, Duchi 16, Namkoong 16, Rafique 18]. Instead of minimizing the mean per-example loss on the training dataset, DRO seeks to optimize for the hardest *weighted* empirical training data distribution around the (uniform) empirical training data distribution. This suggests a link between DRO and Hard Example Mining. However, DRO as a generalization of ERM for machine learning still lacks optimization methods that are principled and computationally as efficient as SGD in the non-convex setting of deep learning. Previously proposed principled optimization methods for DRO consist in alternating between approximate maximization and minimization steps [Jin 19, Lin 19, Rafique 18]. However, they differ from SGD methods for ERM by the introduction of additional hyperparameters for the optimizer such as a second learning rate and a ratio between the number of minimization and maximization steps. This makes DRO difficult to use as a drop-in replacement for ERM in practice.

In contrast, efficient weighted sampling methods, including Hard Example Mining [Chang 17, Loshchilov 16, Shrivastava 16] and weighted sampling [Berger 18, Puyol-Antón 21], have been empirically shown to mitigate class imbalance issues and to improve deep embedding learning [Harwood 17, Suh 19, Wu 17]. However, even though these works typically start from an ERM formulation, it is not clear how those heuristics formally relate to ERM in theory. This suggests that bridging the gap between DRO and weighted sampling methods could lead to a principled Hard Example Mining approach, or conversely to more efficient optimization methods for DRO in deep learning.

Given an efficient solver for the inner maximization problem in DRO, DRO

could be addressed by maintaining a solution of the inner maximization problem and using a minimization scheme akin to the standard ERM but over an adaptively weighted empirical distribution. However, even in the case where a closed-form solution is available for the inner maximization problem, it would require performing a forward pass over the entire training dataset at each iteration. This cannot be done efficiently for large datasets. This suggests identifying an approximate, but practically usable, solution for the inner maximization problem based on a closed-form solution.

From a theoretical perspective, analysis of previous optimization methods for non-convex DRO [Jin 19, Lin 19, Rafique 18] made the assumption that the model is either smooth or weakly-convex, but none of those properties are true for deep neural networks with ReLU activation functions that are typically used.

In this chapter, we propose SGD with *hardness weighted sampling*, a novel, principled optimization method for training deep neural networks with DRO and inspired by Hard Example Mining, that is computationally as efficient as SGD for ERM. Compared to SGD, our method only requires introducing an additional softmax layer and maintaining a stale per-example loss vector to compute sampling probabilities over the training data. In the context of the hardness weighted sampler, *stale* means that the loss values in the loss vector are not always up-to-date with the current values of the weights of the network. In other words, we update the loss value of a training image in the loss vector only when this image is in the training batch rather than updating it during every training iteration. This is critical to making the hardness sampling method computationally efficient. Indeed, updating the loss values for the entire training set at every iteration requires an additional computational complexity of $O(n)$, while updating only for the images in the batch requires no additional computation since the loss values for the batch are already computed for the update of the model’s weights.

This work is an extension of our previous preliminary work [Fidon 21b] in which we applied the proposed *hardnes weighted sampler* to distributionally robust fetal brain 3D MRI segmentation and studied the link between DRO and the minimization of percentiles of the per-example loss. In this extension, we formally introduce our *hardness weighted sampler* and we generalize recent results in the convergence theory of SGD with ERM and over-parameterized deep learning networks with ReLU activation functions [Allen-Zhu 19b, Allen-Zhu 19a, Cao 20, Zou 19] to our SGD with hardness weighted sampling for DRO. This is, to the best of our knowledge, the first convergence result for deep learning networks with ReLU trained with DRO. We also formally link DRO in our method with Hard Example Mining. As a result, our method can be seen as a principled Hard Example Mining

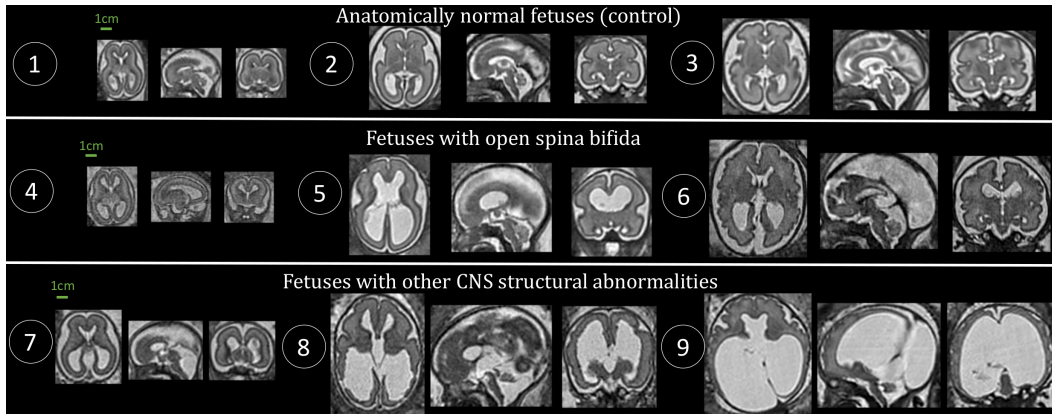


Figure 5.1: Illustration of the anatomical variability in fetal brain across gestational ages and diagnostics. 1: Control (22 weeks); 2: Control (26 weeks); 3: Control (29 weeks); 4: Spina bifida (19 weeks); 5: Spina bifida (26 weeks); 6: Spina bifida (32 weeks); 7: Dandy-walker malformation with corpus callosum abnormality (23 weeks); 8: Dandy-walker malformation with ventriculomegaly and periventricular nodular heterotopia (27 weeks); 9: Aqueductal stenosis (34 weeks).

approach. In terms of experiments, we have extended the evaluation on fetal brain 3D MRI with 69 additional fetal brain 3D MRIs. We have also added experiments on brain tumor segmentations and experiments on image classification with MNIST as a toy example. We show that our method outperforms plain SGD in the case of class imbalance, and improves the robustness of a state-of-the-art deep learning pipeline for fetal brain segmentation and brain tumor segmentation. We evaluate the proposed methodology for the automatic segmentation of white matter, ventricles, and cerebellum based on fetal brain 3D T2w MRI. We used a total of 437 fetal brain 3D MRIs including anatomically normal fetuses, fetuses with spina bifida aperta, and fetuses with other central nervous system pathologies for gestational ages ranging from 19 weeks to 40 weeks. Our empirical results suggest that the proposed training method based on distributionally robust optimization leads to better percentiles values for abnormal fetuses. In addition, qualitative results shows that distributionally robust optimization allows to reduce the number of clinically relevant failures of nnU-Net. For brain tumor segmentation our DRO-based method allows reducing the interquartile range of the Dice scores of 2% for the segmentation of the enhancing tumor and the tumor core regions.

5.2 Related Works

An optimization method for group-DRO was proposed in [Sagawa 20]. In contrast to the formulation of DRO that we study in this paper, their method requires

additional labels allowing to identify the underrepresented group in the training dataset. However, those labels may not be available or may even be impossible to obtain in most applications. [Sagawa 20] show that, when associated with strong regularization of the weights of the network, their group DRO method can tackle spurious correlations that are known a priori in some classification problems. It is worth noting that, in contrast, no regularization was necessary in our experiments with MNIST.

Biases of convolutional neural networks applied to medical image classification and segmentation has been studied in the literature. State-of-the-art deep neural networks for brain tumor segmentation underperform for cases with confounding effects, such as low grade gliomas [Bakas 18]. It has been shown that scans coming from 15 different studies can be re-assigned with 73.3% accuracy to their source using a random forest classifier [Wachinger 19]. A state-of-the-art deep neural networks for the diagnosis of 14 thoracic diseases using X-ray trained on a dataset with a gender bias underperform on X-ray of female patients [Larrazabal 20]. And a state-of-the-art deep learning pipeline for cardiac MRI segmentation was found to underperform when evaluated on racial groups that were underrepresented in the training dataset [Puyol-Antón 21]. To mitigate this problem, [Puyol-Antón 21] proposed to use a stratified batch sampling approach during training that shares similarities with the group-DRO approach mentioned above [Sagawa 20]. In contrast to our hardness weighted sampler, their stratified batch sampling approach requires additional labels, such as the racial group, that may not be available for training data. In addition, they do not study the formal relationship between the use of their stratified batch sampling approach and the training optimization problem.

In this chapter, we focus on DRO with a ϕ -divergence [Csiszár 04]. In this case, the data distributions that are considered in the DRO problem (5.3) are restricted to sharing the support of the empirical training distribution. In other words, the weights assigned to the training data can change, but the training data itself remains unchanged. Another popular formulation is DRO with a Wasserstein distance [Chouzenoux 19, Duchi 16, Sinha 18, Staib 17]. In contrast to ϕ -divergences, using a Wasserstein distance in DRO seeks to apply small data augmentation to the training data to make the deep learning model robust to small deformation of the data, but the sampling weights of the training data distribution typically remains unchanged. In this sense, DRO with a ϕ -divergence and DRO with a Wasserstein distance can be considered as orthogonal endeavours. While we show that DRO with ϕ -divergence can be seen as a principled Hard Exemple Mining method, it has been shown that DRO with a Wasserstein distance can be seen as a principled

adversarial training method [Sinha 18, Staib 17].

Among the other methods recently proposed for DRO, just train twice [Liu 21a] proposes a method for classification that requires only to label the images of the validation dataset as hard examples. The method consists in first training for the classification task at hand an identification deep neural network using standard ERM, second identifying the training samples misclassified by the identification network as hard samples, and finally train a new model for the classification task with a higher and fixed sampling weight for the hard samples. The group labels of the validation dataset are used to tune the four DRO-specific hyperparameters of the identification network. Those hyperparameters consist of one weight for the hard samples, and the number of epochs, the learning rate and the weight decay for the identification model. In contrast, our method uses dynamic weights that are updated at each training iteration, does not require additional group labelling on the validation dataset, and requires to tune only one hyperparameter specific to DRO. In addition, just train twice is specific to classification problems.

Multiplicative weighting and weighted sampling affect the optimization dynamic in different ways. Multiplicative weighting corresponds to adapting the learning rate, i.e. the size of the gradient descent step, but the number of gradient evaluation remains uniform across the training dataset. In contrast, with weighted sampling the learning rate is not affected and instead gradient evaluation is performed more frequently for the training samples with a higher weight. When importance sampling is used, both multiplicative weighting and multiplicative sampling are used. The effect of *multiplicative weighting* during training, rather than *weighted sampling* used in our algorithm, has been studied empirically by [Byrd 19] for image classification. They find that the effect of multiplicative weighting vanishes over training for classification tasks in which we can achieve zero loss on the training dataset. However, *multiplicative weighting* and *weighted sampling* affect the optimization dynamic in different ways. This may explain why we did not observe this vanishing effect in our experiments on classification and segmentation. Previous work have also studied empirical and convergence results of DRO for linear models [Hu 18].

5.3 Methods

5.3.1 Supervised Deep Learning with Distributionally Robust Optimization

Standard training procedures in machine learning are based on Empirical Risk Minimization (ERM) [Bottou 18]. For a neural network h with parameters θ , a

per-example loss \mathcal{L} , and a training dataset $\{(x_i, y_i)\}_{i=1}^n$, where x_i are the inputs and y_i are the labels, the ERM problem corresponds to

$$\min_{\theta} \left\{ \mathbb{E}_{(x,y) \sim \mathbf{p}_{\text{train}}} [\mathcal{L}(h(x; \theta), y)] = \frac{1}{n} \sum_{i=1}^n \mathcal{L}(h(x_i; \theta), y_i) \right\} \quad (5.1)$$

where $\mathbf{p}_{\text{train}}$ is the empirical uniform distribution on the training dataset. This may include the use of a finite or infinite number of data augmentations. For our theoretical results, we suppose that $\mathbf{p}_{\text{train}}$ contains a finite number of examples. In general, $\mathbf{p}_{\text{train}}$ can contain an infinite number of data due to data augmentation [Chapelle 00]. This case is discussed in section 5.3.2. Optionally, \mathcal{L} can contain a parameter regularization term that is only a function of θ .

The ERM training formulation assumes that $\mathbf{p}_{\text{train}}$ is an unbiased approximation of the true data distribution. However, this is generally impossible in domains such as medical image computing. This makes models trained with ERM at risk of underperforming on images from parts of the data distribution that are underrepresented in the training dataset.

In contrast, Distributionally Robust Optimization (DRO) is a family of generalization of ERM in which the uncertainty in the training data distribution is modelled by minimizing the worst-case expected loss over an *uncertainty set* of training data distributions [Rahimian 19].

In this paper, we consider training deep neural networks with DRO based on a ϕ -divergence. We denote $\Delta_n := \{(p_i)_{i=1}^n \in [0, 1]^n \mid \sum_{i=1}^n p_i = 1\}$ the set of empirical training data probabilities vectors under consideration (i.e. the uncertainty set). The different probabilities vectors in Δ_n correspond to all the possible weighting of the training dataset. Every \mathbf{p} in Δ_n gives a weight to each training examples but keep the examples the same. We use the following definition of ϕ -divergence in the remainder of the paper.

Definition 5.3.1 (ϕ -divergence). *Let $\phi : \mathbb{R}_+ \rightarrow \mathbb{R}$ be two times continuously differentiable on $[0, n]$, ρ -strongly convex on $[0, n]$, i.e. $\exists \rho > 0, \forall z, z' \in [0, n], \phi(z') \geq \phi(z) + \phi'(z)(z' - z) + \frac{\rho}{2}(z - z')^2$, and satisfying $\forall z \in \mathbb{R}, \phi(z) \geq \phi(1) = 0, \phi'(1) = 0$. The ϕ -divergence D_ϕ is defined as, for all $p = (p_i)_{i=1}^n, q = (q_i)_{i=1}^n \in \Delta_n$,*

$$D_\phi(q||p) = \sum_{i=1}^n p_i \phi\left(\frac{q_i}{p_i}\right) \quad (5.2)$$

We refer to our example 5.3.1 on page 91 to highlight that the KL divergence is indeed a ϕ -divergence.

The DRO problem for which we propose an optimizer for training deep neural

networks can be formally defined as

$$\min_{\boldsymbol{\theta}} \left\{ R(\mathbf{L}(h(\boldsymbol{\theta}))) := \max_{q \in \Delta_n} \left(\mathbb{E}_{(x,y) \sim q} [\mathcal{L}(h(x; \boldsymbol{\theta}), y)] - \frac{1}{\beta} D_{\phi}(q \| \mathbf{p}_{\text{train}}) \right) \right\} \quad (5.3)$$

where $\mathbf{p}_{\text{train}}$ is the uniform empirical distribution, and $\beta > 0$ an hyperparameter. The choice of β and ϕ controls how the unknown training data distribution q is allowed to differ from $\mathbf{p}_{\text{train}}$. Here and thereafter, we use the notation $\mathbf{L}(h(\boldsymbol{\theta})) := (\mathcal{L}(h(x_i; \boldsymbol{\theta}), y_i))_{i=1}^n$ to refer to the vector of loss values of the n training samples for the value $\boldsymbol{\theta}$ of the parameters of the neural network h .

In the remainder of the paper, we will refer to R as the *distributionally robust loss*.

5.3.2 Hardness Weighted Sampling for Distributionally Robust Deep Learning

In the case where h is a non-convex predictor (such as a deep neural network), existing optimization methods for the DRO problem (5.3) alternate between approximate minimization and maximization steps [Jin 19, Lin 19, Rafique 18], requiring the introduction of additional hyperparameters compared to SGD. However, these are difficult to tune in practice and convergence has not been proven for non-smooth deep neural networks such as those with ReLU activation functions.

In this section, we present an SGD-like optimization method for training a deep learning model h with the DRO problem (5.3). We first highlight, in Section 5.3.2, mathematical properties that allow us to link DRO with stochastic gradient descent (SGD) combined with an adaptive sampling that we refer to as *hardness weighted sampling*. In Section 5.3.2, we present our Algorithm 1 for distributionally robust deep learning. Then, in Section 5.3.3, we present theoretical convergence results for our hardness weighted sampling.

A sampling approach to Distributionally Robust Optimization

The goal of this subsection is to show that a stochastic approximation of the gradient of the *distributionally robust loss* can be obtained by using a weighted sampler. This result is a first step towards our Algorithm 1 for efficient training with the *distributionally robust loss* presented in the next subsection.

Our analysis of the properties of the *distributionally robust loss* R relies on the Fenchel duality [Moreau 65] and the notion of Fenchel conjugate [Fenchel 49].

Definition 5.3.2 (Fenchel Conjugate Function). *Let $f : \mathbb{R}^m \rightarrow \mathbb{R} \cup \{+\infty\}$ be a proper function. The Fenchel conjugate of f is defined as $\forall \mathbf{v} \in \mathbb{R}^m, f^*(\mathbf{v}) =$*

$$\max_{\mathbf{x} \in \mathbb{R}^m} \langle \mathbf{v}, \mathbf{x} \rangle - f(\mathbf{x}).$$

To reformulate R as an unconstrained optimization problem over \mathbb{R}^n (rather than constraining it to Δ_n), we define

$$\forall \mathbf{p} \in \mathbb{R}^n, \quad G(\mathbf{p}) = \frac{1}{\beta} D_\phi(\mathbf{p} \| \mathbf{p}_{\text{train}}) + \delta_{\Delta_n}(\mathbf{p}) \quad (5.4)$$

where δ_{Δ_n} is the characteristic function of the closed convex set Δ_n , i.e.

$$\forall \mathbf{p} \in \mathbb{R}^n, \quad \delta_{\Delta_n}(\mathbf{p}) = \begin{cases} 0 & \text{if } \mathbf{p} \in \Delta_n \\ +\infty & \text{otherwise} \end{cases} \quad (5.5)$$

The distributionally robust loss R in (5.3) can now be rewritten using the Fenchel conjugate function G^* of G . This allows us to obtain regularity properties for R .

Lemma 5.3.1 (Regularity of R). *If ϕ satisfies Definition 5.3.1 (i.e. can be used for a ϕ -divergence), then G and R satisfy the following:*

$$G \text{ is } \left(\frac{n\rho}{\beta}\right)\text{-strongly convex} \quad (5.6)$$

$$\forall \boldsymbol{\theta}, \quad R(\mathbf{L}(h(\boldsymbol{\theta}))) = \max_{\mathbf{q} \in \mathbb{R}^n} (\langle \mathbf{L}(h(\boldsymbol{\theta})), \mathbf{q} \rangle - G(\mathbf{q})) = G^*(\mathbf{L}(h(\boldsymbol{\theta}))) \quad (5.7)$$

$$R \text{ is } \left(\frac{\beta}{n\rho}\right)\text{-gradient Lipschitz continuous.} \quad (5.8)$$

Equation (5.7) follows from Definition 5.3.2. Proofs of (5.6) and (5.8) can be found in Appendix A.4.5. According to (5.6), the optimization problem (5.7) is strictly convex and admits a unique solution in Δ_n , which we denote as

$$\bar{\mathbf{p}}(\mathbf{L}(h(\boldsymbol{\theta}))) = \arg \max_{\mathbf{q} \in \mathbb{R}^n} (\langle \mathbf{L}(h(\boldsymbol{\theta})), \mathbf{q} \rangle - G(\mathbf{q})) \quad (5.9)$$

Thanks to those properties, we can now show the following lemma that is essential for the theoretical foundation of our Algorithm 1. Equation (5.10) states that the gradient of the distributionally robust loss R is a weighted sum of the the gradients of the per-example losses (i.e. the gradients computed by the backpropagation algorithm in deep learning) with the weights given by the empirical distribution $\bar{\mathbf{p}}(\mathbf{L}(h(\boldsymbol{\theta})))$. We further show that straightforward analytical formulas exist for $\bar{\mathbf{p}}$, and give an example of such probability distribution for the Kullback-Leibler (KL) divergence.

Lemma 5.3.2 (Stochastic Gradient of the Distributionally Robust Loss). *For all*

θ , we have

$$\nabla_{\theta}(R \circ \mathbf{L} \circ h)(\theta) = \mathbb{E}_{(x,y) \sim \bar{\mathbf{p}}(\mathbf{L}(h(\theta)))} [\nabla_{\theta} \mathcal{L}(h(x; \theta), y)] \quad (5.10)$$

The proof is found in Appendix A.4.6. We now provide a closed-form formula for $\bar{\mathbf{p}}$ given $\mathcal{L}(h(\theta))$ for the KL divergence as the choice of ϕ -divergence.

Example 5.3.1. For $\phi : z \mapsto z \log(z) - z + 1$, D_{ϕ} is the Kullback-Leibler (KL) divergence:

$$D_{\phi}(\mathbf{q} \parallel \mathbf{p}) = D_{\text{KL}}(\mathbf{q} \parallel \mathbf{p}) = \sum_{i=1}^n q_i \log \left(\frac{q_i}{p_i} \right) \quad (5.11)$$

In this case, we have (see Appendix A.4.4 for a proof)

$$\bar{\mathbf{p}}(\mathbf{L}(h(\theta))) = \text{softmax}(\beta \mathbf{L}(h(\theta))) \quad (5.12)$$

Proposed Efficient Algorithm for Distributionally Robust Deep Learning

We now describe our algorithm for training deep neural networks with DRO using our hardness weighted sampling.

Algorithm 1 Training procedure for DRO with Hardness Weighted Sampling.

Require: $\{(x_i, y_i)\}_{i=1}^n$: training dataset with $n > 0$ the number of training samples.

Require: $b \in \{1, \dots, n\}$: batch size.

Require: \mathcal{L} : (any) smooth per-example loss function.

Require: $\beta > 0$: robustness parameter defining the distributionally robust optimization problem.

Require: θ_0 : initial parameter vector for the model h to train.

Require: \mathbf{L}_{init} : initial stale per-example loss values vector.

- 1: $t \leftarrow 0$ (initialize the time step)
 - 2: $\mathbf{L} \leftarrow \mathbf{L}_{init}$ (initialize the vector stale loss values)
 - 3: **while** θ_t has not converged **do**
 - 4: $\mathbf{p}_t \leftarrow \text{softmax}(\beta \mathbf{L})$ ▷ online estimation of the *hardness weights*
 - 5: $I \sim \mathbf{p}_t$ ▷ hardness weighted sampling
 - 6: **if** importance sampling is not used **then**
 - 7: $\forall i \in I, w_i = 1$
 - 8: **else**
 - 9: $\forall i \in I, w_i \leftarrow \exp(\beta(\mathcal{L}(h(x_i; \theta), y_i) - L_i))$ ▷ importance sampling weights
 - 10: $\forall i \in I, w_i \leftarrow \text{clip}(w_i, [w_{min}, w_{max}])$ ▷ clip the weights for stability
 - 11: $\forall i \in I, L_i \leftarrow \mathcal{L}(h(x_i; \theta), y_i)$ ▷ update the vector of stale loss values
 - 12: $\mathbf{g}_t \leftarrow \frac{1}{b} \sum_{i \in I} w_i \nabla_{\theta} \mathcal{L}(h(x_i; \theta), y_i)$
 - 13: $\theta_{t+1} \leftarrow \theta_t - \eta \mathbf{g}_t$ ▷ gradient descent step
 - 14: **Output:** θ_t
-

Equation (5.10) implies that $\nabla_{\boldsymbol{\theta}} \mathcal{L}(h(\mathbf{x}_i; \boldsymbol{\theta}), y_i)$ is an unbiased estimator of the gradient of the distributionally robust loss gradient when i is sampled with respect to $\bar{\mathbf{p}}(\mathbf{L}(h(\boldsymbol{\theta})))$. This suggests that the distributionally robust loss can be minimized efficiently by SGD by sampling mini-batches with respect to $\bar{\mathbf{p}}(\mathbf{L}(h(\boldsymbol{\theta})))$ at each iteration. However, even though closed-form formulas were provided in Example 5.3.1 for $\bar{\mathbf{p}}$, evaluating exactly $\mathbf{L}(h(\boldsymbol{\theta}))$, i.e. doing one forward pass on the whole training dataset at each iteration, is computationally prohibitive for large training datasets.

In practice, we propose to use a stale version of the vector of per-example loss values by maintaining an online history of the loss values of the examples seen during training $\left(\mathcal{L}(h(\mathbf{x}_i; \boldsymbol{\theta}^{(t_i)}), y_i)\right)_{i=1}^n$, where for all i , t_i is the last iteration at which the per-example loss of example i has been computed. Using the Kullback-Leibler divergence as ϕ -divergence, this leads to the SGD with hardness weighted sampling algorithm proposed in Algorithm 1.

When data augmentation is used, an infinite number of training examples is virtually available. In this case, we keep one stale loss value per example irrespective of any augmentation as an approximation of the loss for this example under any augmentation.

Importance sampling is often used when sampling with respect to a desired distribution cannot be done exactly [Kahn 53]. In Algorithm 1, an up-to-date estimation of the per-example losses (or equivalently the hardness weights) in a batch is only available *after* sampling and evaluation through the network. Importance sampling can be used to compensate for the difference between the initial and the updated stale losses within this batch. We propose to use importance sampling in steps 9-10 of Algorithm 1 and highlight that this is especially useful to deal with data augmentation. Indeed, in this case, the stale losses for the examples in the batch are expected to be less accurate as they were estimated under a different augmentation. For efficiency, we use the following approximation $w_i = \frac{p_i^{new}}{p_i^{old}} \approx \exp(\beta(\mathcal{L}(h(\mathbf{x}_i; \boldsymbol{\theta}), y_i) - L_i))$ where we have neglected the typically small change in the denominator of the softmax. More details are given in Appendix A.4.3. To tackle the typical instabilities that can arise when using importance sampling [Owen 00], the importance weights are clipped.

Compared to standard SGD-based training optimizers for the mean loss, our algorithm requires only an additional softmax operation per iteration and to store an additional vector of scalars of size n (number of training examples), thereby making it well suited for deep learning applications.

5.3.3 Overview of Theoretical Results

In this section, we present convergence guarantees for Algorithm 1 in the framework of over-parameterized deep learning. We further demonstrate properties of our hardness weighted sampling that allow to clarify its link with Hard Example Mining and with the minimization of percentiles of the per-sample loss on the training data distribution.

Convergence of SGD with Hardness Weighted Sampling for Over-parameterized Deep Neural Networks with ReLU

Convergence results for over-parameterized deep learning have recently been proposed in [Allen-Zhu 19a]. Their work gives convergence guarantees for deep neural networks h with any activation functions (including ReLU), and with any (finite) number of layers L and parameters m , under the assumption that m is large enough. In our work, we extend the convergence theory developed by [Allen-Zhu 19a] for ERM and SGD to DRO using the proposed SGD with hardness weighted sampling and stale per-example loss vector (as stated in Algorithm 1). The proof in Appendix A.4.9 deals with the challenges raised by the non-linearity of R with respect to the per-sample stale loss and the non-uniform dynamic sampling used in Algorithm 1.

Theorem 5.3.3 (Convergence of Algorithm 1 for neural networks with ReLU). *Let \mathcal{L} be a smooth per-example loss function, $b \in \{1, \dots, n\}$ be the batch size, and $\epsilon > 0$. If the number of parameters m is large enough, and the learning rate is small enough, then, with high probability over the randomness of the initialization and the mini-batches, Algorithm 1 (without importance sampling) guarantees $\|\nabla_{\theta}(R \circ \mathbf{L} \circ h)(\theta)\| \leq \epsilon$ after a finite number of iterations.*

A detailed description of the assumption for this theorem is described in Appendix A.4.5 and its proof can be found in Appendix A.4.9. Our proof does not cover the case where importance sampling is used. However, our empirical results suggest that convergence guarantees still hold with importance sampling.

Link between Hardness Weighted Sampling and Hard Example Mining

In this section, we discuss the relationship between the proposed hardness weighted sampling for DRO and Hard Example Mining. The following result shows that using the proposed *hardness weighted sampler* the hard training examples, those training examples with relatively high values of the loss, are sampled with higher probability.

Theorem 5.3.4. *Let a ϕ -divergence that satisfies Definition 5.3.1, and $\mathbf{L} = (L_i)_{i=1}^n \in \mathbb{R}^n$ a vector of loss values for the examples $\{\mathbf{x}_1, \dots, \mathbf{x}_n\}$. The proposed hardness weighted sampling probabilities vector $\bar{\mathbf{p}}(\mathbf{L}) = (\bar{p}_i(\mathbf{L}))_{i=1}^n$ defined as in (5.9) verifies:*

1. *For all $i \in \{1, \dots, n\}$, \bar{p}_i is an increasing function of L_i .*
2. *For all $i \in \{1, \dots, n\}$, \bar{p}_i is a non-increasing function of any L_j for $j \neq i$.*

See Appendix A.4.7 for the proof. The second part of Theorem 5.3.4 implies that as the loss of an example diminishes, the sampling probabilities of all the other examples increase. As a result, the proposed SGD with hardness weighted sampling balances exploitation (i.e. sampling the identified *hard examples*) and exploration (i.e. sampling any example to keep the record of *hard examples* up to date). Heuristics to enforce this trade-off are often used in Hard Example Mining methods [Berger 18, Harwood 17, Wu 17].

Link between DRO and the Minimization of a Loss Percentile

In this section, we show that the DRO problem (5.3) using the KL divergence is equivalent to a relaxation of the minimization of the per-example loss percentile shown thereafter in equation (5.13).

Instead of the average per-example loss (5.1), for robustness, one might be more interested in minimizing the percentile l_α at α (e.g. 5%) of the per-example loss function. Formally, this corresponds to the minimization problem

$$\min_{\boldsymbol{\theta}, l_\alpha} l_\alpha \quad \text{such that} \quad p_{\text{train}}(\mathcal{L}(h(\mathbf{x}; \boldsymbol{\theta}), y) \geq l_\alpha) \leq \alpha \quad (5.13)$$

where p_{train} is the empirical distribution defined by the training dataset. In other words, if $\alpha = 0.05$, the optimal $l_\alpha^*(\boldsymbol{\theta})$ of (5.13) for a given value set of parameters $\boldsymbol{\theta}$ is the value of the loss such that the per-example loss function is worse than $l_\alpha^*(\boldsymbol{\theta})$ 5% of the time. As a result, training the deep neural network using (5.13) corresponds to minimizing the percentile of the per-example loss function $l_\alpha^*(\boldsymbol{\theta})$.

Unfortunately, the minimization problem (5.13) cannot be solved directly using stochastic gradient descent to train a deep neural network. We now propose a tractable upper bound for $l_\alpha^*(\boldsymbol{\theta})$ and show that it can be solved in practice using distributionally robust optimization.

The Chernoff bound [Chernoff 52] applied to the per-example loss function and

the empirical training data distribution states that for all l_α and $\beta > 0$

$$p_{\text{train}}(\mathcal{L}(h(\mathbf{x}; \boldsymbol{\theta}), y) \geq l_\alpha) \leq \frac{\exp(-\beta l_\alpha)}{n} \sum_{i=1}^n \exp(\beta \mathcal{L}(h(\mathbf{x}_i; \boldsymbol{\theta}), \mathbf{y}_i)) \quad (5.14)$$

To link this inequality to the minimization problem (5.13), we set $\beta > 0$ and

$$\hat{l}_\alpha(\boldsymbol{\theta}) = \frac{1}{\beta} \log \left(\frac{1}{\alpha n} \sum_{i=1}^n \exp(\beta \mathcal{L}(h(\mathbf{x}_i; \boldsymbol{\theta}), \mathbf{y}_i)) \right) \quad (5.15)$$

In this case, we have

$$p_{\text{train}}(\mathcal{L}(h(\mathbf{x}; \boldsymbol{\theta}), y) \geq \hat{l}_\alpha(\boldsymbol{\theta})) \leq \alpha = \frac{\exp(-\beta \hat{l}_\alpha(\boldsymbol{\theta}))}{n} \sum_{i=1}^n \exp(\beta \mathcal{L}(h(\mathbf{x}_i; \boldsymbol{\theta}), \mathbf{y}_i)) \quad (5.16)$$

$\hat{l}_\alpha(\boldsymbol{\theta})$ is therefore an upper bound for the optimal $l_\alpha^*(\boldsymbol{\theta})$ in equation (5.13), independently to the value of $\boldsymbol{\theta}$. Equation (5.13) can therefore be relaxed by

$$\min_{\boldsymbol{\theta}} \frac{1}{\beta} \log \left(\sum_{i=1}^n \exp(\beta \mathcal{L}(h(\mathbf{x}_i; \boldsymbol{\theta}), \mathbf{y}_i)) \right) \quad (5.17)$$

where $\beta > 0$ is a hyperparameter, and where the term $\frac{1}{\beta} \log \left(\frac{1}{\alpha n} \right)$ was dropped as being independent of $\boldsymbol{\theta}$. While in (5.17), α does not appear in the optimization problem directly anymore, β essentially acts as a substitute for α . The higher the value of β , the higher weights the per-example losses with a high value will have in (5.17).

We give a proof in Appendix A.4.8 that (5.17) is equivalent to solving the following DRO problem

$$\min_{\boldsymbol{\theta}} \max_{\mathbf{q} \in \Delta_n} \left(\sum_{i=1}^n q_i \mathcal{L}(h(\mathbf{x}_i; \boldsymbol{\theta}), \mathbf{y}_i) - \frac{1}{\beta} D_{KL} \left(\mathbf{q} \parallel p_{\text{train}} \right) \right) \quad (5.18)$$

This is a special case of the DRO problem (5.3) where ϕ is chosen as the KL-divergence and it corresponds to the setting of Algorithm 1.

5.4 Experiments

In this section, we experiment with the proposed *hardness weighted sampler* for DRO as implemented in the proposed Algorithm 1. In the subsection 5.4.1, we give a toy example with the task of automatic classification of digits in the case where the digit 3 is underrepresented in the training dataset. And in subsection 5.4.2,

we report the results of our experiments on two medical image segmentation tasks: fetal brain segmentation using 3D MRI, and brain tumor segmentation using 3D MRI.

5.4.1 Toy Example: MNIST Classification with a Class Imbalance

The goal of this subsection is to illustrate key benefits of training a deep neural network using DRO in comparison to ERM when a part of the sample distribution is underrepresented in the training dataset. We take the MNIST dataset [LeCun 98] as a toy example, in which the task is to automatically classify images representing digits between 0 and 9. In addition, we verify the ability of our Algorithm 1 to train a deep neural network for DRO and illustrates the behaviour of SGD with hardness weighted sampling for different values of β .

Material: We create a bias between training and testing data distribution of MNIST [LeCun 98] by keeping only 1% of the digits 3 in the training dataset, while the testing dataset remains unchanged.

For our experiments on MNIST, we used a Wide Residual Network (WRN) [Zagoruyko 16]. The family of WRN models has proved to be very efficient and flexible, achieving state-of-the-art accuracy on several dataset. More specifically, we used WRN-16-1 [Zagoruyko 16, section 2.3]. For the optimization we used a learning rate of 0.01. No momentum or weight decay were used. No data augmentation was used. For DRO no importance sampling was used. We used a GPU NVIDIA GeForce GTX 1070 with 8GB of memory for the experiments on MNIST.

Results: Our experiment suggests that DRO and ERM lead to different optima. Indeed, DRO for $\beta = 10$ outperforms ERM by more than 15% of accuracy on the underrepresented class, as illustrated in Figure 5.2. This suggests that DRO is more robust than ERM to domain gaps between the training and the testing dataset. In addition, Figure 5.2 suggests that DRO with our SGD with hardness weighted sampling can converge faster than ERM with SGD.

Furthermore, the variations of learning curves with β shown in Figure 5.2 are consistent with our theoretical insight. As β decreases to 0, the learning curve of DRO with our Algorithm 1 converges to the learning curve of ERM with SGD.

For large values of β (here $\beta \geq 10$), instabilities appear before convergence in the **testing learning curves**, as illustrated in the top panels of Figure 5.2. However, the bottom left panel of Figure 5.2 shows that the **training loss curves** for $\beta \geq 10$ were stable there. We also observe that during iterations where instabilities appear on the **testing set**, the standard deviation of the per-example loss on the **training**

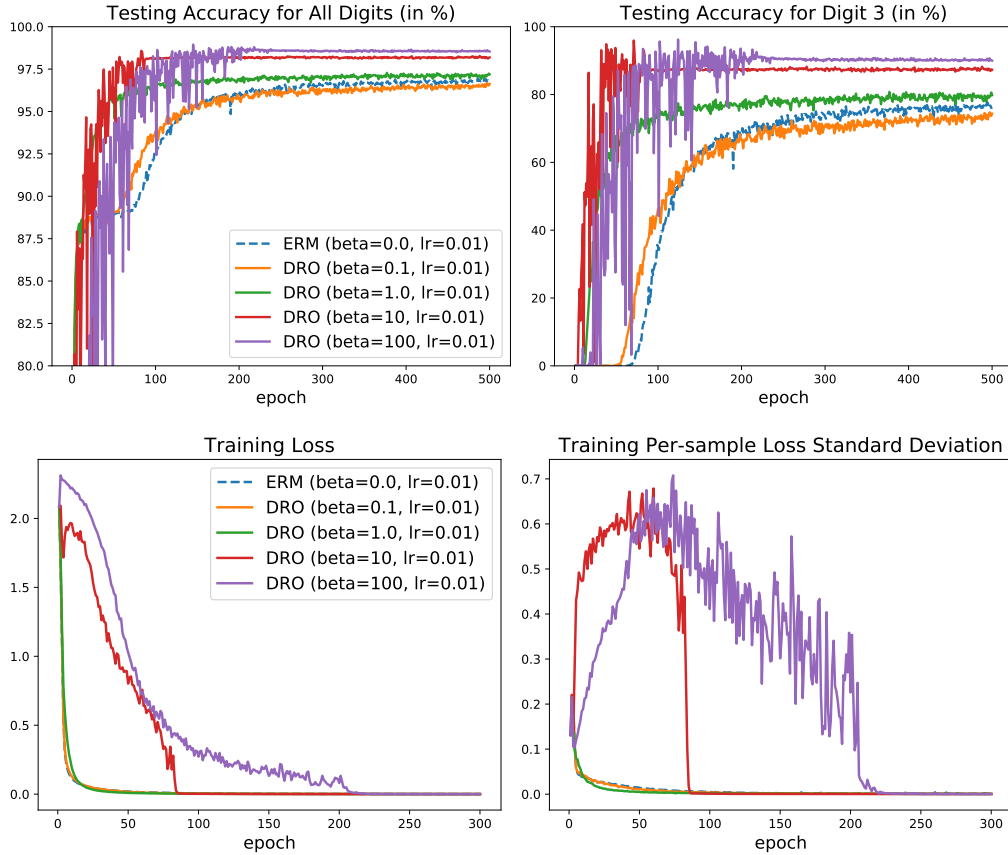


Figure 5.2: **Experiments on MNIST.** We compare the learning curves at testing (top panels) and at training (bottom panels) for ERM with SGD (blue) and DRO with our SGD with hardness weighted sampling for different values of β ($\beta = 0.1$, $\beta = 1$, $\beta = 10$, $\beta = 100$). The models are trained on an imbalanced MNIST dataset (only 1% of the digits 3 kept for training) and evaluated on the original MNIST testing dataset.

set is relatively high (i.e. the hardness weighted probability is further away from the uniform distribution). This suggests that the apparent instabilities on the **testing set** are related to differences between the distributionally robust loss and the mean loss.

5.4.2 Medical Image Segmentation

In this section, we illustrate the application of Algorithm 1 to improve the robustness of deep learning methods for medical image segmentation. We first discuss the specificities of applying the proposed *hardness weighted sampling* to medical image segmentation in relation to the use of patch-based sampling. We evaluated the proposed method on two applications: fetal brain 3D MRI segmentation using

a subset of the dataset described in Chapter 3, and brain tumor multi-sequence MRI segmentation using the BraTS 2019 dataset [Bakas 17b, Bakas 17c].

Hardness Weighted Sampler with Large Images

In medical image segmentation, the image used as input of the deep neural network are typically large 3D volumes. For this reason, state-of-the-art deep learning pipelines use patch-based sampling rather than full-volume sampling during training with ERM [Isensee 21] as described in subsection 5.4.2.

This raised the question of what is the training distribution p_{train} in the ERM (5.1) and DRO (5.3) optimization problems. Here, since the patches are large enough to cover most of the brains, we consider that patches are good approximation of the whole volumes and p_{train} is the distribution of the full volumes. Therefore, in the hardness weighted sampler of Algorithm 1, we have only one weight per full volume.

In the case the full volumes are too large to be well covered by the patches, one can divide each full volume into a finite number of subvolumes prior to training. For example, for chest CT, one can divide the volumes into left and right lungs [Tilborghs 20].

Material

Table 5.1: **Training and Testing Fetal Drain 3D MRI Dataset Details.** Other Abn: brain structural abnormalities other than spina bifida. There is no overlap of subjects between training and testing.

Train/Test	Origin	Condition	Volumes	Gestational age (in weeks)
Training	Atlas	Control	18	[21, 38]
Training	FeTA	Control	5	[22, 28]
Training	UHL	Control	116	[20, 35]
Training	UHL	Spina Bifida	28	[22, 34]
Training	UHL	Other Abn	10	[23, 35]
Testing	FeTA	Control	31	[20, 34]
Testing	FeTA	Spina Bifida	38	[21, 31]
Testing	FeTA	Other Abn	16	[20, 34]
Testing	UHL	Control	76	[22, 37]
Testing	UHL and MUV	Spina Bifida	74	[19, 35]
Testing	UHL	Other Abn	25	[21, 40]

Fetal Brain Dataset. The fetal brain MRI dataset used in this chapter is a subset of the dataset described in Chapter 3. In this paragraph, we only specify which fetal brain 3D MRI were used and refer to Chapter 3 for the description of the data acquisition and processing. A summary of the data used in this chapter is given in Table 5.1.

We used the 18 control fetal brain 3D MRIs of the spatio-temporal fetal brain atlas¹ [Gholipour 17] for gestational ages ranging from 21 weeks to 38 weeks. We also used 80 volumes from the publicly available FeTA MICCAI challenge dataset² [Payette 21] and the 10 3D MRIs from the testing set of the first release of the FeTA dataset for which manual segmentations are not publicly available. In addition, we used 329 3D MRIs from a private dataset. All images in the private dataset were part of routine clinical care and were acquired at University Hospital Leuven (UHL) and Medical University of Vienna (MUW) due to congenital malformations seen on ultrasound. In total, 102 cases with spina bifida aperta, 35 cases with other central nervous system pathologies, and 192 cases with other malformations, though with normal brain, and referred as controls, were included. The gestational age at MRI ranged from 19 weeks to 40 weeks. Some of those 3D MRIs and their manual segmentations were used in previous studies [Emam 23, Fidon 21e, Fidon 21a, Mufti 21].

Brain Tumor Dataset. We have used the BraTS 2019 dataset because it is the last edition of the BraTS challenge for which information about the image acquisition center is available at the time of writing. The dataset contains the same four MRI sequences (T1, ceT1, T2, and FLAIR) for 448 cases, corresponding to patients with either a high-grade Gliomas or a low-grade Gliomas. All the cases were manually segmented for peritumoral edema, enhancing tumor, and non-enhancing tumor core using the same labeling protocol [Menze 14, Bakas 18, Bakas 17a]. We split the 323 cases of the BraTS 2019 *training* dataset into 268 for training and 67 for validation. In addition, the BraTS 2019 *validation* dataset that contains 125 cases was used for testing.

Deep Learning Pipeline. The deep learning pipeline used was based on nnU-Net [Isensee 21], which is a generic deep learning pipeline for medical image segmentation, that has been shown to outperform other deep learning pipelines on 23 public datasets without the need to manually tune the loss function or the deep neural network architecture. Specifically, we used nnU-Net version 2 in 3D-full-resolution mode which is the recommended mode for isotropic 3D MRI data and

¹http://crl.med.harvard.edu/research/fetal_brain_atlas/

²DOI: 10.7303/syn25649159

the code is publicly available at <https://github.com/MIC-DKFZ/nnUNet>.

Like most deep learning pipelines in the literature, nnU-Net is based on ERM. For clarity, in the following we will sometimes refer to the unmodified nnU-Net as nnU-Net-ERM.

The meta-parameters used for the deep learning pipeline used were determined automatically using the heuristics developed in nnU-Net [Isensee 21]. The 3D CNN selected for the brain tumor data is based on 3D U-Net [Çiçek 16] with 5 (resp. 6) levels for fetal brain segmentation (resp. brain tumor segmentation) and 32 features after the first convolution that are multiplied by 2 at each level with a maximum set at 320. The 3D CNN uses leaky ReLU activation, instance normalization [Ulyanov 16], max-pooling downsampling operations and linear upsampling with learnable parameters. In addition, the network is trained using the addition of the mean Dice loss and the cross entropy, and deep supervision [Lee 15]. The default optimization step is SGD with a momentum of 0.99 and Nesterov update, a batch size of 4 (resp. 2) for fetal brain segmentation (resp. brain tumor segmentation), and a decreasing learning rate defined for each epoch t as

$$\eta_t = 0.01 \times \left(1 - \frac{t}{t_{max}}\right)^{0.9}$$

where t_{max} is the maximum number of epochs fixed as 1000. Note that in nnU-Net, one epoch is defined as equal to 250 batches, irrespective of the size of the training dataset. A patch size of $96 \times 112 \times 96$ (resp. $128 \times 192 \times 128$) was selected for fetal brain segmentation (resp. brain tumor segmentation), which is not sufficient to fit the whole brain of all the cases. As a result, a patch-based approach is used as often in medical image segmentation applications. A large number of data augmentation methods are used: random cropping of a patch, random zoom, gamma intensity augmentation, multiplicative brightness, random rotations, random mirroring along all axes, contrast augmentation, additive Gaussian noise, Gaussian blurring and simulation of low resolution. nnU-Net automatically splits the training data into 5 folds 80% training/20% validation. For the experiments on brain tumor segmentation, only the networks corresponding to the first fold were trained. For the experiments on fetal brain segmentation, 5 models were trained, one for each fold, and the predicted class probability maps of the 5 models are averaged at inference to improve robustness [Isensee 21]. GPUs NVIDIA Tesla V100-SXM2 with 16GB of memory were used for the experiments. Training each network took from 4 to 6 days.

Our only modifications of the nnU-Net pipeline is the addition of our hardness weighted sampling when "DRO" is indicated and for some experiments we modified

the optimization update rule as indicated in Table 5.2. Our implementation of the nnU-Net-DRO training procedure is publicly available at <https://github.com/LucasFidon/HardnessWeightedSampler>. If "ERM" is indicated and nothing is indicated about the optimization update rule, it means that nnU-Net [Isensee 21] is used without any modification.

Hyper-parameters of the Hardness Weighted Sampler. For brain tumor segmentation, we tried the values $\{10, 100, 1000\}$ of β with or without importance sampling. Using $\beta = 100$ with importance sampling lead to the best mean dice score on the validation split of the training dataset. For fetal brain segmentation, we tried only $\beta = 100$ with importance sampling. When importance sampling is used, the clipping values $w_{min} = 0.1$ and $w_{max} = 10$ are always used. No other values of w_{max} and w_{min} have been tested.

Metrics. We evaluate the quality of the automatic segmentations using the Dice score [Dice 45, Fidon 17a]. We are particularly interested in measuring the statistical risk of the results as a way to evaluate the robustness of the different methods.

In the BraTS challenge, this is usually measured using the interquartile range (IQR) which is the difference between the percentiles at 75% and 25% of the the metric values [Bakas 18]. We therefore reported the mean, the median and the IQR of the Dice score in Table 5.3. For fetal brain segmentation, in addition to the mean, median, and IQR, we also report the percentiles of the Dice score at 25%, 10%, and 5%. In Table 5.2, we report those quantities for the Dice scores of the three tissue types white matter, intra-axial CSF, and cerebellum.

For each method, nnU-Net is trained 5 times using different train/validation splits and different random initializations. The 5 same splits, computed randomly, are used for the two methods. The results for fetal brain 3D MRI segmentation in Table 5.2 are for the ensemble of the 5 3D U-Nets. Ensembling is known to increase the robustness of deep learning methods for segmentation [Isensee 21]. It also makes the evaluation less sensitive to the random initialization and to the stochastic optimization.

Results. The quantitative comparison of nnU-Net-ERM and nnU-Net-DRO on fetal brain 3D MRI segmentation for the three different central nervous system conditions control, spina bifida, and other abnormalities can be found in Table 5.2.

For spina bifida and other brain abnormalities, the proposed nnU-Net-DRO achieves same or higher mean Dice scores than nnU-Net-ERM [Isensee 21] with +0.5 percentage points (pp) for white matter and +1pp for the cerebellum of spina

Table 5.2: **Evaluation of Distribution Robustness with Respect to the Pathology (260 3D MRIs).** **nnU-Net-ERM** is the unmodified nnU-Net pipeline [Isensee 21] in which Empirical Risk Minimization (ERM) is used. **nnU-Net-DRO** is the nnU-Net pipeline modified to use the proposed *hardness weighted sampler* and in which Distributionally Robust Optimization (DRO) is therefore used. **WM**: White matter, **In-CSF**: Intra-axial CSF, **Cer**: Cerebellum. IQR: interquartile range, p_X : X^{th} percentile of the Dice score distribution in percentage. Best values are in bold.

Method	CNS	ROI	Dice Score (%)					
			Mean	Median	IQR	P_{25}	P_{10}	P_5
(baseline) nnU-Net-ERM	Controls (107 volumes)	WM	94.4	95.2	2.8	93.3	91.5	90.6
		In-CSF	90.3	92.4	6.4	87.8	80.7	79.0
		Cer	95.7	97.0	3.4	94.2	91.3	90.4
	Spina Bifida (112 volumes)	WM	89.6	92.1	4.1	89.5	80.6	73.8
		In-CSF	91.4	93.9	6.4	89.6	86.9	83.7
		Cer	76.8	87.8	11.1	80.4	15.8	0.0
	Other Abn. (41 volumes)	WM	90.3	92.6	4.6	90.1	88.0	71.6
		In-CSF	87.4	87.9	10.4	82.7	77.7	75.9
		Cer	90.4	92.8	5.4	90.7	87.5	81.4
(ours) nnU-Net-DRO	Controls (107 volumes)	WM	94.4	95.3	3.0	93.2	91.1	90.1
		In-CSF	90.4	92.7	6.2	87.9	81.7	79.1
		Cer	95.7	97.1	3.3	94.2	91.4	90.1
	Spina Bifida (112 volumes)	WM	90.1	92.2	4.0	89.9	81.6	74.8
		In-CSF	91.6	94.1	6.4	90.0	86.7	83.6
		Cer	77.8	87.9	9.7	82.0	43.3	0.0
	Other Abn. (41 volumes)	WM	90.4	92.6	4.7	90.2	88.2	73.5
		In-CSF	87.9	88.1	9.5	83.3	80.4	77.7
		Cer	91.3	93.0	5.5	90.7	87.5	82.7

bifida cases and +0.9pp for the cerebellum for other abnormalities. In addition, nnU-Net-DRO achieves comparable (at most 0.1pp of difference) or lower IQR than nnU-Net-ERM with -1.4pp for the cerebellum of spina bifida cases and -0.9pp for the intra-axial CSF of cases with other abnormalities. For controls, the mean, median, and IQR of the Dice scores of nnU-Net-DRO and nnU-Net-ERM differ by less than 0.2pp for the three tissue types. This suggests that nnU-Net-DRO is more robust to anatomical variabilities associated with abnormal brains, while retaining the same segmentation performance on neurotypical cases.

In terms of median Dice score, nnU-Net-DRO and nnU-Net-ERM differ by less than 0.3pp for all tissue types and conditions. Therefore the differences in terms

Table 5.3: **Dice Score Evaluation on the BraTS 2019 Online Validation Set (125 cases)**. Metrics were computed using the BraTS online evaluation platform (<https://ipp.cbica.upenn.edu/>). ERM: Empirical Risk Minimization, DRO: Distributionally Robust Optimization, SGD: plain SGD (no momentum used), Nesterov: SGD with Nesterov momentum, IQR: Interquartile range. The best values are in bold.

Optim. problem	Optim. update	Enhancing Tumor			Whole Tumor			Tumor Core		
		Mean	Median	IQR	Mean	Median	IQR	Mean	Median	IQR
ERM	SGD	71.3	86.0	20.9	90.4	92.3	6.1	80.5	88.8	17.5
DRO	SGD	72.3	87.2	19.1	90.5	92.6	6.0	82.1	89.7	15.2
ERM	Nesterov	73.0	87.1	15.6	90.7	92.6	5.4	83.9	90.5	14.3
DRO	Nesterov	74.5	87.3	13.8	90.6	92.6	5.9	84.1	90.0	12.5

of mean Dice scores mentioned above are not due to improved segmentation in the middle of the Dice score performance distribution.

The comparison of the percentiles at 25%, 10%, and 5% of the Dice score allows us to compare methods at the tail of the Dice scores distribution where segmentation methods reach their worst-case performance. For spina bifida, nnU-Net-DRO achieves higher values of percentiles than nnU-Net-ERM for the white matter (+1.0pp for \mathbf{p}_{10} and +1.0pp for \mathbf{p}_5), and for the cerebellum (+1.6pp for \mathbf{p}_{25} and +27.5pp for \mathbf{p}_{10}). And for other brain abnormalities, nnU-Net-DRO achieves higher values of percentiles than nnU-Net-ERM for the white matter (+1.9pp for \mathbf{p}_5), for the intra-axial CSF (+0.6pp for \mathbf{p}_{25} , +2.3pp for \mathbf{p}_{10} and +1.8pp for \mathbf{p}_5), and for the cerebellum (+1.3pp for \mathbf{p}_5). All the other percentile values differ by less than 0.5pp of Dice score between the two methods. This suggests that nnU-Net-DRO achieves better worst case performance than nnU-Net-ERM for abnormal cases. However, both methods have a percentile at 5% of the Dice score equal to 0 for the cerebellum of spina bifida cases. This indicates that both methods completely miss the cerebellum for spina bifida cases in 5% of the cases.

As can be seen in the qualitative results of Figure 5.3, there are cases for which nnU-Net-ERM predicts an empty cerebellum segmentation while nnU-Net-DRO achieves satisfactory cerebellum segmentation. There were no cases for which the converse was true. However, there were also spina bifida cases for which both methods failed to predict the cerebellum. Robust segmentation of the cerebellum for spina bifida is particularly relevant for the evaluation of fetal brain surgery for spina bifida aperta [Aertsen 19, Danzer 20, Sacco 19]. All the spina bifida 3D MRIs with missing cerebellum in the automatic segmentations were 3D MRIs from

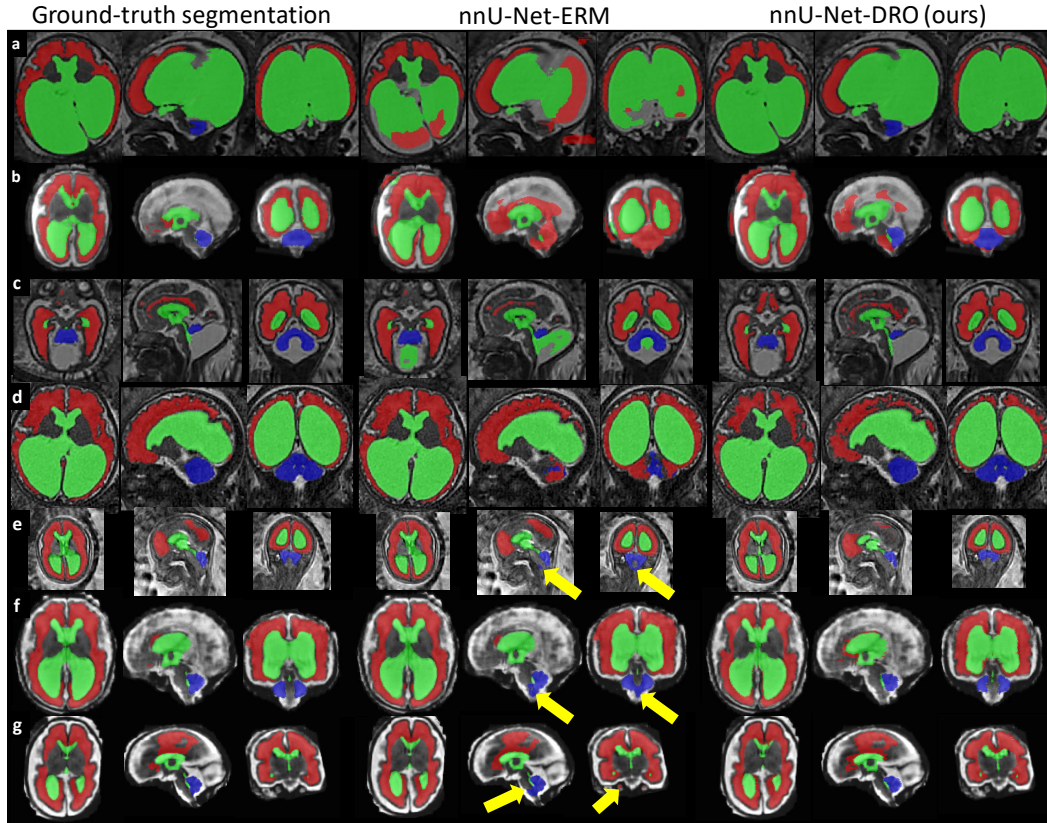


Figure 5.3: **Qualitative Results for Fetal Brain 3D MRI Segmentation using DRO.** a) Fetus with aqueductal stenosis (34 weeks). b) Fetus with spina bifida aperta (27 weeks). c) Fetus with Blake’s pouch cyst (29 weeks). d) Fetus with tuberous sclerosis complex (34 weeks). e) Fetus with spina bifida aperta (22 weeks). f) Fetus with spina bifida aperta (31 weeks). g) Fetus with spina bifida aperta (28 weeks). For cases a) and b), nnU-Net-ERM [Isensee 21] misses completely the cerebellum and achieves poor segmentation for the white matter and the ventricles. For case c), a large part of the Blake’s pouch cyst is wrongly included in the ventricular system segmentation by nnU-Net-ERM. This is not the case for the proposed nnU-Net-DRO. For case d), nnU-Net-ERM fails to segment the cerebellum correctly and a large part of the cerebellum is segmented as part of the white matter. In contrast, our nnU-Net-DRO correctly segment cerebellum and white matter for this case. For cases e) f) and g), we have added yellow arrows pointing to large parts of the brainstem that nnU-Net-ERM wrongly included in the cerebellum segmentation. nnU-Net-DRO does not make this mistake. We emphasise that the segmentation of the cerebellum for spina bifida aperta is essential for studying and evaluating the effect of surgery in-utero.

the FeTA dataset [Payette 21] and represented brains of fetuses with spina bifida before they were operated on. The cerebellum is more difficult to detect using MRI before surgery as compared to early or late after surgery [Aertsen 19, Danzer 07].

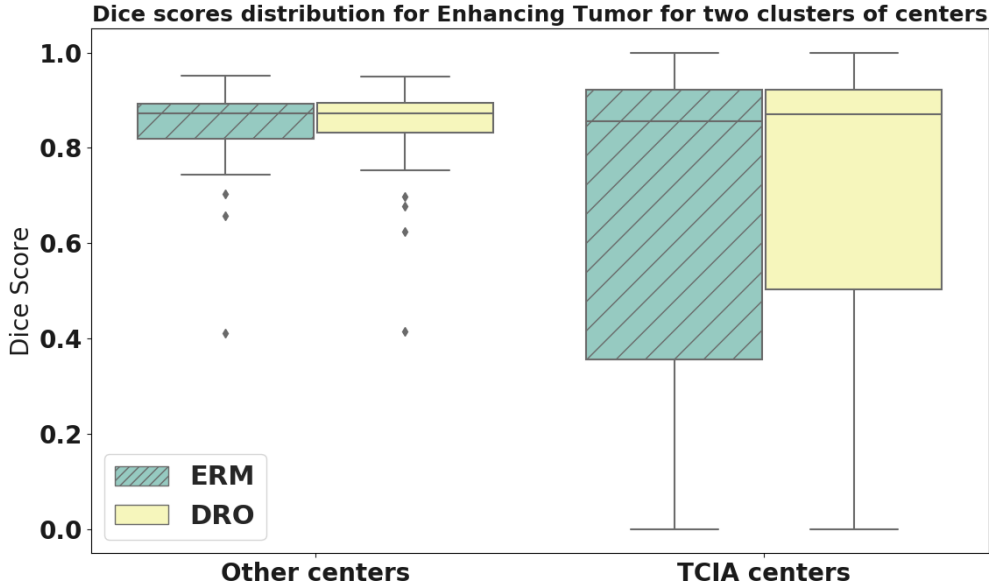


Figure 5.4: Dice scores distribution on the BraTS 2019 validation dataset for cases from a center of TCIA (76 cases) and cases from other centers (49 cases). This shows that the lower interquartile range of DRO for the enhancing tumor comes specifically from a lower number of poor segmentations on cases coming from The Cancer Imaging Archive (TCIA). This suggests that DRO can deal with some of the confounding biases present in the training dataset, and lead to a model that is more fair.

No 3D MRI with the combination of those two factors were present in the training dataset (Table. 5.1). This might explain why DRO did not help improving the segmentation quality for those cases. DRO aims at improving the performance on subgroups that were underrepresented in the training dataset, not subgroups that were not represented at all.

In Table 5.2, it is worth noting that overall the Dice score values decrease for the white matter and the cerebellum between controls and spina bifida and abnormal cases. It was expected due to the higher anatomical variability in pathological cases. However, the Dice score values for the ventricular system tend to be higher for spina bifida cases than for controls. This can be attributed to the large proportion of spina bifida cases with enlarged ventricles because the Dice score values tend to be higher for larger regions of interest.

For our experiments on brain tumor segmentation, Table 5.3 summarizes the performance of training nnU-Net using ERM or using DRO. Here, we experiment with two SGD-based optimizers. For both ERM and DRO, the optimization update rule used was either plain SGD without momentum (SGD), or SGD with a Nesterov

momentum equal to 0.99 (Nesterov). Especially, for the latter, this implies that step 12 of Algorithm 1 is modified to use SGD with Nesterov momentum. It was also the case for our experiments on fetal brain 3D MRI segmentation. For DRO, the results presented here are for $\beta = 100$ and using importance sampling (step 6 of Algorithm 1).

As illustrated in Table 5.3, for both ERM and DRO, the use of SGD with Nesterov momentum outperforms plain-SGD for all metrics and all regions of interest. This result was expected for ERM, for which it is common practice in the deep learning literature to use SGD with a momentum. Our results here suggest that the benefit of using a momentum with SGD is retained for DRO.

For both optimizers, DRO outperforms ERM in terms of IQR for the enhancing tumor and the tumor core by approximately 2pp of Dice score, and in terms of mean Dice score for the enhancing tumor by 1pp for the plain-SGD and 1.5pp for SGD with Nesterov momentum. For plain-SGD, DRO also outperforms ERM in terms of mean Dice score for the tumor core by 1.6pp. The IQR is the global statistic used in the BraTS challenge to measure the level of robustness of a method [Bakas 18]. In addition, Figure 5.4 shows that the lower IQR of DRO for the enhancing tumor comes specifically from a lower number of poor segmentations on cases coming from The Cancer Imaging Archive (TCIA). This suggests that DRO can deal with some of the confounding biases present in the training dataset, and lead to a model that is more fair with respect to the acquisition center of the MRI.

Since the same improvements are observed independently of the optimization update rule used. This suggests that in practice Algorithm 1 still converges when a momentum is used, even if Theorem 5.3.3 was only demonstrated to hold for plain-SGD.

The value $\beta = 100$ and the use of importance sampling was selected based on the mean Dice score on the validation split of the training dataset. Results for $\beta \in \{10, 100, 1000\}$ with Nesterov momentum and with or without importance sampling can be found in Appendix A.4.2 Table A.1. The tendency described previously still holds true for the enhancing tumor for β equal to 10 or 100 with and without importance sampling. The mean Dice score is improved by 0.4pp to 2.3pp and the IQR is reduced by 1.3pp to 2.3pp for the four DRO models as compared to the ERM model. For the tumor core with $\beta = 100$ mean and IQR are improved over ERM with and without importance sampling. However, for $\beta = 10$ with importance sampling there was a loss of performance as compared to ERM for the whole tumor. This problem was not observed with $\beta = 10$ without importance sampling. For the other models with β equal to 10 or 100 similar Dice score performance similar to the one ERM was observed for the whole tumor. This suggests that overall the use

of ERM or DRO does not affect the segmentation performance of the whole tumor. One possible explanation of this is that Dice scores for the whole tumor are already high for almost all cases when ERM is used with a low IQR. In addition, DRO and the *hardness weighted sampler* are sensitive to the loss function, here the mean-class Dice loss plus cross entropy loss. In the case of brain tumor segmentation, we hypothesise that the loss function is more sensitive to the segmentation performance for the tumor core and the enhancing tumor than for the whole tumor.

When β becomes too large ($\beta = 1000$) a decrease of the mean and median Dice score for all regions is observed as compared to ERM. In this case, DRO tends towards the maximization of the worst-case example only which appears to be unstable using our Algorithm 1. In contrast, when β is too small, DRO tends towards ERM. The value of β controls the number of training samples with a sampling probability that is high enough to allow those samples to be sampled regularly during training. This leads to the question: what is a good range of values for β ? We hypothesize that good values of β are of the order of the inverse of the standard deviation of the vector of per-volume (stale) losses during the training epochs that precede convergence. It corresponds, up to one order of magnitude, to the values we have found in practice. However, it is difficult to conclude on a rule for setting β from those observation. In theory, one can show that the sampling probabilities in our hardness weighted sampler are independent to the mean of the vector of per-volume (stale) losses. It is easy to see it for the softmax and one can prove it in the general case with any ϕ -divergence (according to our definition of ϕ -divergence). It is therefore intuitive to think about the inverse of the standard deviation of the vector of losses. It is possible to prove mathematically that the sampling probabilities is not invariant to this variance. However, it remains unclear how to characterize rigorously what is a good value for β . Maybe using a schedule for β during training could lead to improve results but this would introduce more hyperparameters and we have not investigated it.

For all values of β the use of importance sampling, as described in steps 6-8 of Algorithm 1, improves the IQR of the Dice scores for the enhancing tumor and the tumor core. We therefore recommend to use Algorithm 1 with importance sampling.

Efficiency of Algorithm 1: The main additional computational cost is Algorithm 1 is due to the hardness weighted sampling in steps 4 and 5 that is dependent on the number n of training examples. We have computed that steps 4 and 5 together take less than 1 second for up to $n = 10^8$ using a batch size of 1 and the function `random.choice` of Numpy version 1.21.1. For our brain tumor segmentation training set of $n=268$ volumes and a batch size of 2, the additional memory

usage of Algorithm 1 is only 2144 bytes of memory (one float array of size n) and the additional computational time is approximately 10^{-4} seconds per iteration using the Python library `numpy`, i.e. approximately 0.005% of the total duration of an iteration. The size of the training dataset for fetal brain 3D MRI segmentation being lower, the additional memory usage and the additional computational time are even lower than for brain tumor segmentation.

5.5 Discussion and Conclusion

In this chapter, we have shown that efficient training of deep neural networks with Distributionally Robust Optimization (DRO) with a ϕ -divergence is possible.

The proposed *hardness weighted sampler* for training a deep neural network with Stochastic Gradient Descent (SGD) for DRO is as straightforward to implement, and as computationally efficient as SGD for Empirical Risk Minimization (ERM). It can be used for deep neural networks with any activation function (including ReLU), and with any per-example loss function. We have shown that the proposed approach can formally be described as a principled Hard Example Mining strategy (Theorem 5.3.4) and is related to minimizing the percentile of the per-example loss distribution (5.13). In addition, we prove the convergence of our method for over-parameterized deep neural networks (Theorem 5.3.3). Thereby, extending the convergence theory of deep learning of [Allen-Zhu 19a]. This is, to the best of our knowledge, the first convergence result for training a deep neural network based on DRO.

In practice, we have shown that our hardness weighted sampling method can be easily integrated in a state-of-the-art deep learning framework for medical image segmentation. Interestingly, the proposed algorithm remains stable when SGD with momentum is used.

The high anatomical variability of the developing fetal brain across gestational ages and pathologies hampers the robustness of deep neural networks trained by maximizing the average per-volume performance. Specifically, it limits the generalization of deep neural networks to abnormal cases for which few cases are available during training. In this paper, we propose to mitigate this problem by training deep neural networks using Distributionally Robust Optimization (DRO) with the proposed hardness weighted sampling. We have validated the proposed training method on a multi-centric dataset of 437 fetal brain T2w 3D MRIs with various diagnostics. nnU-Net trained with DRO achieved improved segmentation results for pathological cases as compared to the unmodified nnU-Net, while achieving similar segmentation performance for the neurotypical cases. Those results suggest that

nnU-Net trained with DRO is more robust to anatomical variabilities than the original nnU-Net that is trained with ERM. In addition, we have performed experiments on the open-source multiclass brain tumor segmentation dataset BraTS [Bakas 18]. Our results on BraTS suggests that DRO can help improving the robustness of deep neural network for segmentation to variations in the acquisition protocol of the images.

However, we have also found in our experiments that all deep learning models, either trained with ERM or DRO, failed in some cases. For example, the models evaluated all missed the cerebellum in at least 5% of the spina bifida aperta cases. As a result, while our results do suggest that DRO with our method can improve the robustness of deep neural networks for segmentation, they also show that DRO alone with our method does not provide a guarantee of robustness. DRO with a ϕ -divergence reweights the examples in the training dataset but cannot account for subsets of the true distribution that are not represented at all in the training dataset.

We have shown that the additional computational cost of the proposed hardness weighted sampling is small enough to be negligible in practice and requires less than one second for up to $n = 10^8$ examples. The proposed Algorithm 1 is therefore as computationally efficient as state-of-the-art deep learning pipeline for medical image segmentation. However, when data augmentation is used, an infinite number of training examples is virtually available. We mitigate this problem using importance sampling and only one probability per non-augmented example. We found that importance sampling led to improved segmentation results.

We have also illustrated in our experiments that reporting the mean and standard deviation of the Dice score is not enough to evaluate the robustness of deep neural networks for medical image segmentation. A stratification of the evaluation is required to assess for which subgroups of the population and for which image protocols a deep learning model for segmentation can be safely used. In addition, not all improvements of the mean and standard deviation of the Dice score are equally relevant as they can result from improvements of either the best or the worst segmentation cases. Regarding the robustness of automatic segmentation methods across various conditions, one is interested in improvements of segmentation metrics in the tail of the distribution that corresponds to the worst segmentation cases. To this end, one can report the interquartile range (IQR) and measures of risk such as percentiles.

A Spatio-temporal Atlas of the Developing Fetal Brain with Spina Bifida Aperta

Table of Contents

6.1	Introduction	112
6.2	Materials	114
6.3	Atlas Computation Method	115
6.3.1	Data Preprocessing	115
6.3.2	Atlas Construction	119
6.3.3	Semi-automatic Segmentation of the Atlas	123
6.4	Annotation Protocol of Anatomical Landmarks for Fetuses with Spina Bifida Aperta	124
6.4.1	Anterior horn of the right lateral ventricle	124
6.4.2	Anterior horn of the left lateral ventricle	125
6.4.3	Posterior tectum plate	125
6.4.4	Left cerebellar-brainstem junction	126
6.4.5	Right cerebellar-brainstem junction	126
6.4.6	Left deep grey border at foramen of Monro	126
6.4.7	Right deep grey border at foramen of Monro	127
6.4.8	Left deep grey border at anterior cavum septi pellucidi line	127
6.4.9	Right deep grey border at the anterior cavum septi pellucidi line	128
6.4.10	Left deep grey border at posterior cavum septi pellucidi line	128
6.4.11	Right deep grey border at the posterior cavum septi pellucidi line	129
6.5	Results	130
6.5.1	Intra-rater Variability for the Annotation of the Anatomical Landmarks	130

6.5.2	Automatic Segmentation of Fetal Brain 3D MRIs	132
6.6	Discussion	133
6.7	Limitations	135
6.8	Data Availability	136
6.9	Software Availability	136
6.10	Conclusion	136

Foreword This chapter is to a large extent an *in extenso* reproduction of [Fidon 21e]. The fetal brain atlas computed in this chapter plays a central role in the proposed implementation of our trustworthy AI framework for fetal brain MRI segmentation described in Chapter 7.

- The annotation protocol was developed by Elizabeth Viola under the supervision of Michael Aertsen and myself.
- The manual annotation of the landmarks on the 3D MRI has been performed by Elizabeth Viola.
- The intra-rater variability study for the anatomical landmarks has been performed by Elizabeth Viola.
- The method for computing the atlas has been developed and implemented by myself.
- 3D super-resolution and reconstruction of the fetal brain MRIs has been performed by myself using the library `NiftyMIC`.

6.1 Introduction

As discussed in Chapter 3, the anatomy of the brain of fetuses with SBA differs from the normal fetal brain anatomy. In addition, the mechanisms underlying those anatomical brain abnormalities remain incompletely understood [Danzer 20].

Brain atlases are used to study common trends and variations in the brain anatomy of a population. They provide a model of a population of brain magnetic resonance images (MRIs) that represents the average brain anatomy of a population, allow the comparison of measurements in a cohort study, and can be used for the automatic segmentation of brain MRI [Dittrich 14, Habas 10a, Makropoulos 18, Serag 12b]. Atlases can also be used to measure variability in the brain anatomy of an individual as compared to the whole population [Dittrich 14]. Age and disease specific atlases allow a more accurate model of specific populations of human brains to be obtained [Evans 12].

Previous work on fetal brain atlases has focused on age-specific atlases by proposing various spatio-temporal fetal brain MRI atlases [Dittrich 14, Dittrich 11,

Gholipour 17, Habas 10a, Serag 12b, Zhan 13, Wu 21]. A spatio-temporal atlas does not consist in only one average volume, but instead consists in a collection of age-specific average volumes. This allows the development of the fetal brain anatomy to be modelled. However, existing studies have only used brain MRIs of fetuses with a normal brain development, except for one study that combined fetuses with a normal brain and fetuses with lissencephaly in the same atlas [Dittrich 14]. In particular, no fetal brain atlas for the developing fetal brain with SBA has been proposed in the literature.

In this chapter, we propose the first spatio-temporal fetal brain MRI atlas for SBA. Our atlas covers all the weeks of gestation between 21 weeks and 34 weeks. This range of gestational ages is of particular interest for SBA because it starts before the time at which in-utero surgery for SBA is currently performed [Danzer 20] and covers most of the time until birth. The atlas is computed using 90 fetal brain MRIs from 37 fetuses with SBA. We hypothesise that the high variability of the brain anatomy in SBA is one of the main challenges in adapting methods developed for normal fetal brain atlases for SBA. To tackle this issue, we propose a semi-automatic method for the computation of the proposed fetal brain MRI atlas for SBA. We propose a protocol for the annotation of 11 anatomical landmarks in fetal brain 3D MRI of fetuses. Those anatomical landmarks are used for two things in our pipeline. The anatomical landmarks are used firstly to initialize the computation of the atlas using a weighted generalized Procrustes method and secondly to regularize the non-linear image registration of fetal brain 3D MRIs to the atlas.

We performed an intra-rater variability evaluation for the proposed landmarks using a subset of 31 3D MRIs from our cohort. Based on this evaluation, 4 anatomical landmarks were excluded and 7 were selected to help for the computation of the spatio-temporal atlas. In addition, we evaluated the automatic fetal brain segmentations computed using the proposed atlas for SBA on 40 fetal brain 3D MRIs of the publicly available FeTA dataset [Payette 21]. It contains 15 MRIs of normal fetuses and 25 MRIs of fetuses with SBA. We compared the automatic segmentations computed using our SBA atlas to the segmentations computed using a state-of-the-art normal fetal brain MRI atlas [Gholipour 17]. We have found that the proposed SBA atlas outperforms the normal fetal brain atlas on cases with SBA. The proposed spatio-temporal fetal brain MRI atlas for SBA is made publicly available here.

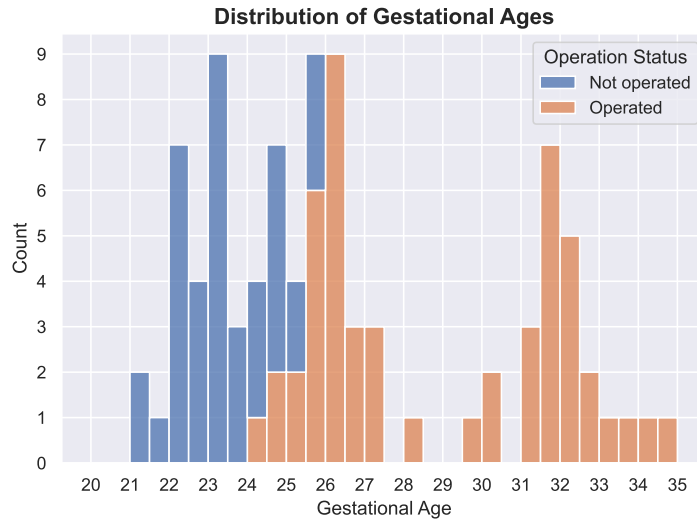


Figure 6.1: **Distribution of gestational ages for operated (fetal surgery) and non-operated fetal brains.** The dataset used to compute the atlas contains 39 magnetic resonance imaging (MRI) examinations of non-operated fetuses and 51 MRI examinations of operated fetuses.

6.2 Materials

In this section, we describe the fetal brain MRI data used to compute the atlas and for the evaluation of automatic segmentations obtained using the atlas. This is a subset of the dataset described in Chapter 3. We will therefore refer to Chapter 3 whenever possible regarding details about the data and processing that were used.

Spina bifida aperta cohort used to compute the spatio-temporal atlas A total of 90 fetal brain MRI examinations from 37 fetuses were used in this work. The dataset contains longitudinal MRI examinations with up to 5 examinations per fetus. In addition, 51 of the MRI examinations were performed after open fetal surgery performed before 26 weeks of gestation, to close the spina bifida aperta defect. The distribution of gestational ages for MRI examinations and whether they were done before or after surgery can be found in Figure 6.1.

Details about the MRI data acquisition can be found in Chapter 3.

Fetal brain 3D MRI used for the evaluation of automatic segmentation

For the evaluation of automatic fetal brain segmentation we have used the publicly available FeTA dataset [Payette 21] (first release). The FeTA dataset contains 40 reconstructed 3D MRI, including 15 MRIs of fetuses with a normal brain and 25 MRIs of fetuses with spina bifida aperta. For all the 3D MRI, segmentations are

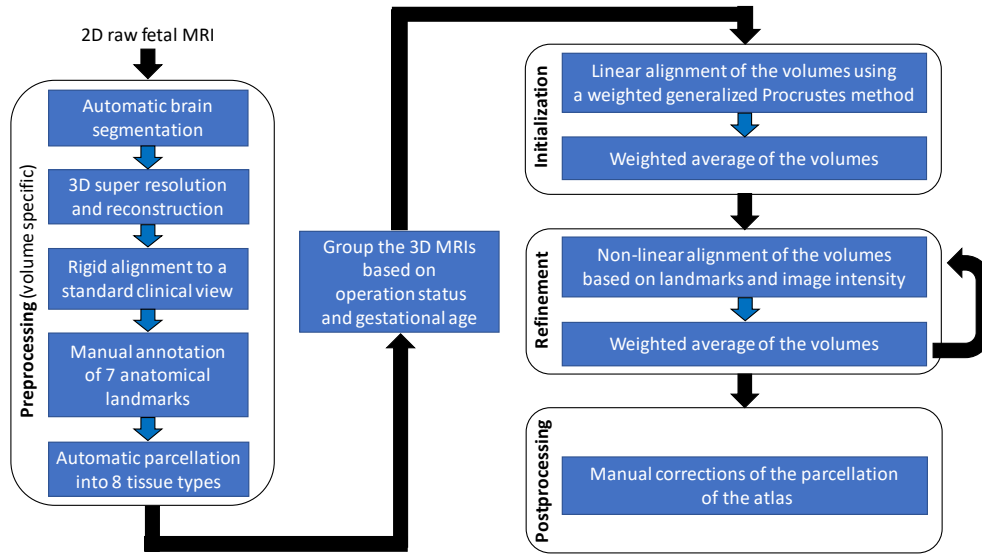


Figure 6.2: **Overview of the spatio-temporal atlas construction pipeline. MRI: magnetic resonance imaging.**

available for seven tissue types: white matter, ventricular system, cerebellum, extra-axial cerebrospinal fluid, cortical gray matter, deep gray matter, and brainstem. More details about those data can be found in Chapter 3.

Spatio-temporal atlas for the normal developing fetal brain For comparison to a spatio-temporal atlas of the normal developing fetal brain, we have used the publicly available spatio-temporal fetal brain atlas [Gholipour 17]. This atlas contains 18 3D MRI of average normal fetal brain for gestational ages ranging from 21 weeks to 38 weeks.

6.3 Atlas Computation Method

In this section, we describe our pipeline for computing the spina bifida aperta (SBA) spatio-temporal fetal brain atlas. An overview of the pipeline can be found in Figure 6.2.

6.3.1 Data Preprocessing

In this subsection, we give details about the preprocessing steps as can be found in Figure 6.2.

Automatic brain segmentation

One of the main challenges in fetal brain MRI is the motion of the fetus. To tackle this issue, MRI sequences used for fetal MRI are designed to produce multiple stacks of 2D slices rather than a 3D image. Original 2D slices typically have lower resolution, suffers from motion between neighboring slices, motion artefact, and suboptimal cross-section [Ebner 20].

Automatic segmentation of the fetal brain in the raw 2D MRI are obtained using a deep learning-based method [Ranzini 21]. Those brain masks are an input required by the 3D super resolution and reconstruction algorithm described below. A public implementation of the deep learning pipeline `MONAIfbs` [Ranzini 21], used in this study to obtain the brain masks, can be found at here (main git branch, commit `bcab52a`).

3D super resolution and reconstruction

We use a 3D super resolution and reconstruction algorithm to improve the resolution, and remove motion between neighboring slices and motion artefacts present in the original 2D slices [Ebner 20]. The output of the 3D super resolution and reconstruction algorithm [Ebner 20] is a reconstructed 3D MRI of the fetal brain with an isotropic image resolution of 0.8 mm. We hypothesize that the reconstructed 3D MRI facilitates the manual delineation and annotation of the fetal brain structures as compared to the original 2D slices.

We used a state-of-the-art 3D super resolution and reconstruction algorithm [Ebner 20] publicly available in the `NiftyMIC` pipeline version 0.8 with Python 3.8. The original 2D MRI slices were also corrected for bias field in the `NiftyMIC` pipeline version 0.8 using a N4 bias field correction step as implemented in `SimpleITK` version 1.2.4. The 3D super resolution and reconstruction algorithm [Ebner 20] also combines the brain masks obtained in section section 6.3.1. This results in a 3D brain mask for the 3D reconstructed MRI that is computed fully-automatically.

Rigid alignment to a standard clinical view

The 3D reconstructed MRI were rigidly aligned to a time-point volume of the control fetal brain 4D atlas [Gholipour 17] as implemented in `NiftyMIC` [Ebner 20] version 0.8. All the 3D reconstructed MRIs are therefore aligned to a standard clinical view in which the axes are aligned with the axial, sagittal, and coronal planes of the fetal brain. This facilitates the manual delineation and annotation of the fetal brain structures. The target time-point in the control 4D atlas is chosen based on the brain volume computed using the automatic 3D brain mask.

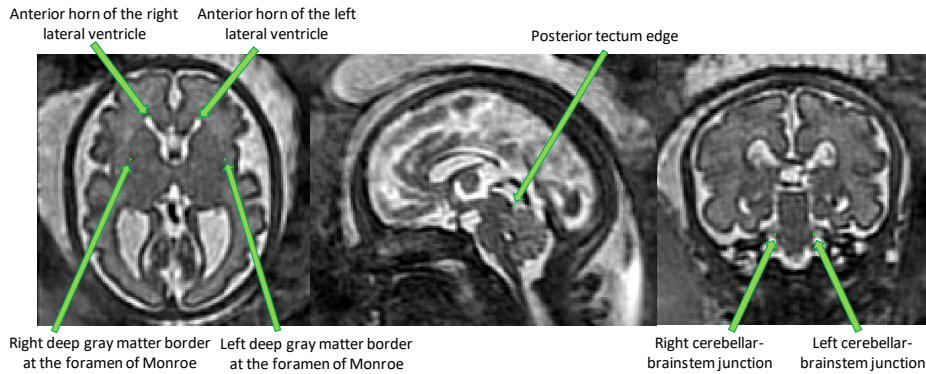


Figure 6.3: **Overview of the proposed anatomical landmarks.** Those landmarks were annotated for all the 3D reconstructed magnetic resonance imaging (MRI). They aim at improving the accuracy and the robustness of the image registration steps.

Anatomical landmarks

Seven anatomical landmarks were manually annotated to regularize and improve the accuracy of the image registration steps used in the computation of the spina bifida 4D atlas. Details can be found in section section 6.3.2.

The anatomical landmarks that were selected are: the right and left anterior horn of the lateral ventricles, the posterior tectum plate, the right and left junctions between the cerebellum and the brainstem, and the right and left deep gray matter border at the foramen of Monroe. An illustration of those anatomical landmarks can be found in Figure 6.3.

Those landmarks include anatomical structures that have been reported to be reliably identifiable in the fetal MRI clinical research literature [Aertsen 19, Garel 01, Geerdink 12]. Another selection criteria was to choose landmarks that are spread over the fetal brain anatomy to efficiently support image registration. Our proposed annotation protocol can be found in section 6.4.

The manual annotations of the 90 3D reconstructed MRIs were performed. Manual annotations of landmarks were performed using the software ITK-SNAP [Yushkevich 16] version 3.8.0. The annotation of one volume took 12 min on average. It is worth noting, that landmarks can be missing, especially for fetal MRIs before 26 weeks of gestation.

The intra-rater reliability for the anatomical landmarks has been evaluated, as described in Section section 6.5.1. The proposed anatomical landmarks protocol also included the right and left deep gray matter border at the anterior cavum septi pellucidi line and the right and left deep gray matter border at the posterior cavum septi pellucidi line. However, those landmarks were found to be unreliable and often

missing due to the high variation in shape of the cavum septi pellucidi. For this reason, those landmarks were not used for the computation of the atlas but they are present in the annotation protocol. Details can be found in Section section 6.5.1.

Age and operation status specific groups of 3D reconstructed MRIs

The 3D reconstructed MRIs were grouped with respect to their operation status and their gestational age. Each group of 3D reconstructed MRIs went through the atlas construction pipeline described in section section 6.3.2 and lead to the computation of a unique volume of our spatio-temporal atlas.

SBA surgery affects the evolution of the fetal brain anatomy [Aertsen 19, Danzer 20, Mufti 21]. Therefore, we have chosen to separate the 3D reconstructed MRIs of operated and non-operated fetuses. A group either contains only 3D reconstructed MRIs of fetuses that have been operated for SBA in-utero, or contains only 3D reconstructed MRIs of fetuses that have not been operated.

Each group is assigned with a gestational age ranging from 21 weeks to 34 weeks. Volumes are included in a group only if the gestational age at the time of the acquisition is within 9 days of the gestational age of the group. The description of the cohort used can be found in section section 6.2 and the distribution of gestation ages can be found in Figure 6.1. As can be seen in Figure 6.9 and Figure 6.10, groups for non-operated fetuses covers the gestational ages from 21 weeks to 25 weeks and groups for operated fetuses covers gestational ages from 25 weeks to 34 weeks.

A group is excluded if it contains less than three 3D reconstructed MRIs. In addition, we excluded a group if it did not include both 3D reconstructed MRIs with gestational ages higher and lower than the gestational age of the group. This avoids, for example, to have a group for non-operated fetuses at 26 weeks of gestation that would contain only MRIs at gestational ages 25 weeks or less.

Data augmentation: We used right-left flipping as a data augmentation to synthetically increase the amount of volumes in each group. This encourages the atlas to be symmetrical with respect to the central sagittal plane. Right-left flipping has been used in several previous studies on brain MRI atlases [Fonov 11, Grabner 06]. Imposing symmetry between right and left hemispheres of the atlas volumes aims at reducing potential biases in the cohort used to compute the atlas. In addition, it allows to use the atlas for the study of asymmetry between right and left hemispheres [Grabner 06]. Asymmetry between brain hemispheres for normal fetuses has been described as well as the role of hemispheric asymmetry in isolated corpus callosum agenesis. [Glatter 20, Kasprian 11]. To the best of our knowledge,

hemispheric asymmetry has not been studied yet in SBA.

6.3.2 Atlas Construction

In this section we describe the different steps for the computation of the spina bifida atlas as can be seen in the Initialization and Refinement boxes of the pipeline overview in Figure 6.2.

Weighted average of the volumes

In this section, we describe the method to average the intensity of 3D reconstructed MRIs after spatial alignment. As described in section section 6.3.1, data are grouped with respect to their operation status and gestational age. After aligning spatially all the 3D reconstructed MRIs of a group, we average their image intensity to obtain an average fetal brain MRI for the group.

Weighted average: To reflect the gestational age associated with each group, we used a time-weighted average. The weight for the volume i is defined using a Gaussian kernel as follow

$$w_i = \frac{1}{\sqrt{2\pi}\sigma} \exp\left\{\left(-\frac{1}{2}\left(\frac{GA_i - GA_{target}}{\sigma}\right)^2\right)\right\} \quad (6.1)$$

where GA_{target} is the gestational age of the group and GA_i is the gestational age of volume i . The standard deviation value is set to $\sigma = 3$ days.

In addition, we average each image and its symmetric by right-left flipping to impose to the average volume to be exactly symmetric with respect to the central sagittal plane. This is performed in addition to the data augmentation described in section section 6.3.1.

Formally, let $\{I_i\}_{i=1}^N$ be a set of N co-registered 3D reconstructed MRIs to average. The weighted average is computed as

$$I_{average} = \frac{1}{2N} \sum_{i=1}^N w_i (I_i + S(I_i)) \quad (6.2)$$

where S is the operator that computes the symmetric of a volume with respect to the central sagittal plane.

Preprocessing: Before averaging, we transform the intensity of each volume linearly to set the mean (resp. the standard deviation) of the image intensity inside the brain mask to 2000 (resp. 500). Those values were set to approximate the intensity profile of a spatio-temporal fetal brain atlas of normal fetuses [Gholipour 17].

Weighted generalized Procrustes

In this section, we describe the optimization method that we used for the joint initial linear alignment of the volumes in a group of 3D reconstructed MRIs. This method is based on a weighted generalized Procrustes method and uses only the anatomical landmarks. Especially, note that the image intensity is not used.

Generalized Procrustes methods [Gower 75] aims at matching simultaneously n configurations of landmarks using linear spatial transformations. Generalized Procrustes methods (without constraints) can be defined as optimization problems of the form [Gower 75, Gower 10]

$$\min_{\{M_i, t_i\}} \frac{1}{2} \sum_{i=1}^n \sum_{k=1}^K \left\| M_i x_{i,k} + t_i - \frac{1}{n} \sum_{j=1}^n (M_j x_{j,k} + t_j) \right\|^2 \quad (6.3)$$

where n is the number of samples, K is the number of landmarks, $x_{i,k}$ is the vector of coordinates for the landmark k of sample i , t_i is the translation for the sample i , and M_i is the linear transformation for the sample i . In this work we restrict the linear transformations M_i to be anisotropic scaling transformations.

However, for the computation of the spina bifida atlas we have to take into account that landmarks can be missing for some samples. We also would like to weight differently the samples based on their gestational age alike what is done for the weighted average of the 3D reconstructed MRIs in section section 6.3.2.

In this work, we introduce weights in the generalized Procrustes methods. A weight of zeros represents a missing landmark for a sample. The proposed weighted generalized Procrustes method corresponds to the optimization problem

$$\min_{\{M_i, t_i\}} \frac{1}{2} \sum_{i=1}^n \sum_{k=1}^K w_{i,k} \left\| M_i x_{i,k} + t_i - \frac{\sum_{j=1}^n w_{j,k} (M_j x_{j,k} + t_j)}{\sum_{j=1}^n w_{j,k}} \right\|^2 \quad (6.4)$$

where $w_{i,k} \geq 0$ is the weight for the landmark k of sample i . For landmark k , sample i of gestational age GA_i , and the target gestational age GA_{target} , we propose to define the weight $w_{i,k}$ as

$$w_{i,k} = \begin{cases} 0 & \text{if landmark } k \text{ is missing for sample } i \\ 0 & \text{if } |GA_i - GA_{target}| > 3\sigma \\ \frac{1}{\sqrt{2\pi}\sigma} \exp\left\{-\frac{1}{2} \left(\frac{GA_i - GA_{target}}{\sigma}\right)^2\right\} & \text{otherwise} \end{cases} \quad (6.5)$$

The standard deviation value is $\sigma = 3$ days.

We assume that every landmark was annotated at least once in each group. As

a result, $\forall k, \sum_{j=1}^n w_{j,k} > 0$ and the fractions used in (6.4) are well defined.

In general, the optimization problem (6.3) admits an infinity of solutions, including the trivial solution that send all the landmarks to the origin. To tackle this issue, constraints on the size of the system are added [Gower 75, Gower 10]. The optimization problem (6.4) suffers from the same under-specification problem. We therefore choose to constrain the center of mass of the barycenter of the system and the size of the system because it is the most intuitive approach. This leads to the optimization problem

$$\begin{aligned}
& \min_{\{M_i, t_i\}, \{g_k\}} \frac{1}{2} \sum_{i=1}^n \sum_{k=1}^K w_{i,k} \|M_i x_{i,k} + t_i - g_k\|^2 \\
& \text{s.t.} \quad \frac{1}{K} \sum_{k=1}^K g_k = \frac{1}{K} \sum_{k=1}^K \frac{\sum_{j=1}^n w_{j,k} x_{j,k}}{\sum_{j=1}^n w_{j,k}} \\
& \text{and} \quad \frac{1}{K} \sum_{k=1}^K \left\| g_k - \frac{1}{K} \sum_{l=1}^K g_l \right\|^2 = \frac{1}{K} \sum_{k=1}^K \left\| \frac{\sum_{j=1}^n w_{j,k} x_{j,k}}{\sum_{j=1}^n w_{j,k}} - \frac{1}{K} \sum_{l=1}^K \frac{\sum_{j=1}^n w_{j,l} x_{j,l}}{\sum_{j=1}^n w_{j,l}} \right\|^2
\end{aligned} \tag{6.6}$$

This optimization problem can be solved efficiently using an alternating least squares approach [Gower 10].

Non-linear image registration

In this section, we describe the non-linear image registration method that we used for the refinement step of the 4D atlas as can be seen in Figure 6.2. In the refinement step, intermediate atlas MRI volumes have already been computed for all time points. The goal of this step is to improve the image sharpness of the intermediate atlas MRI volumes by registering all the 3D reconstructed MRIs to the intermediate MRI volumes and computing new weighted average volumes using the method described in section section 6.3.2.

We used `NiftyReg` [Modat 10] to perform non-linear image registration using image intensity and the anatomical landmarks. The non-linear image registration optimization problem is the following

$$\min_{\Theta} \mathcal{L}(I_{subject}, I_{atlas}, \phi(\Theta)) + R(\Theta) \tag{6.7}$$

where $I_{subject}$ is the 3D reconstructed MRI to be aligned to the 3D atlas time point I_{atlas} and $\phi(\Theta)$ is a spatial transformation parameterized by cubic B-splines of parameters Θ .

The regularization term R is a linear combination of the bending energy [Ashburner 07]

(BE) and the linear energy [Ashburner 07] (LE) regularization functions applied to $\phi(\Theta)$

$$R(\Theta) = \alpha_{BE} BE(\phi(\Theta)) + \alpha_{LE} LE(\phi(\Theta)) \quad (6.8)$$

with $\alpha_{BE} = 0.1$ and $\alpha_{LE} = 0.3$. More details about the methodology used to tune image registration parameters can be found below.

The data term \mathcal{L} is a linear combination of the local normalized cross correlation (LNCC) [Cachier 03] and the squared euclidean distances between the landmarks positions

$$\begin{aligned} \mathcal{L}(I_{subject}, I_{atlas}, \phi(\Theta)) = & \alpha_{LNCC} LNCC(I_{subject}, I_{atlas} \circ \phi(\Theta)) \\ & + \alpha_{LMKS} \sum_{k \in \Omega_{LMKS}} \left\| \phi(\Theta)(x_k^{subject}) - x_k^{atlas} \right\|^2 \end{aligned} \quad (6.9)$$

where Ω_{LMKS} is the set of landmarks that are present for both $I_{subject}$ and I_{atlas} , $\alpha_{LMKS} = 0.001$ and $\alpha_{LNCC} = (1 - \alpha_{LMKS})(1 - \alpha_{BE} - \alpha_{LE})$ as implemented in `NiftyReg` [Modat 10]. The standard deviation of the Gaussian kernel of the LNCC was set to 6 mm. More details about the methodology used to tune image registration parameters can be found below.

Implementation details: Registrations that solve the optimization problem (6.7) were computed using the publicly available code for `NiftyReg` [Modat 10]. We used the latest version of the code on the master branch (git commit `99d584e`).

The transformation ϕ in (6.7) is parameterized by cubic B-Splines of order 3 with a grid spacing equal to 3 mm. `NiftyReg` [Modat 10] uses a pyramidal approach to solve (6.7). We used 3 levels of pyramid which is the default value in `NiftyReg`. The brain mask were used to mask the voxels outside the brain.

The transformation ϕ in (6.7) was initialized with an affine transformation. The affine transformation was computed using a symmetric block-matching approach [Modat 14] based on image intensities and the brain masks. The implementation of the affine image registration method is included in `NiftyReg`.

Parameters tuning: The parameters α_{BE} , α_{LE} , α_{LMKS} , and the standard deviation of the Gaussian kernel of the LNCC of equations (6.8) and (6.9) were tuned using a grid search. The other parameters of the image registration were not tuned. The values of α_{BE} were $\{0.001, 0.01, 0.03, 0.1, 0.3\}$, the values of α_{LE} were $\{0.01, 0.03, 0.1\}$, the values of α_{LMKS} were $\{0.0003, 0.001, 0.003\}$, and the values for the standard deviation of the LNCC were $\{1, 2, 4, 6, 8\}$. We also tried to use the normalized mutual information (NMI) in place of the LNCC. There are no additional hyper-parameters related to NMI.

We selected the best set of parameter values using a subset of 22 pairs of 3D reconstructed MRIs covering the range of gestational ages available. The selection criteria was the mean of the Dice scores for the white matter, the ventricular system, and the cerebellum between volumes after non-linear registration. Details about the segmentation protocol can be found in section section 6.3.3.

It is worth noting that the gradients of the different terms of the objective function in (6.7) have different scales. Therefore, comparing the contribution of the different terms based on their weights is misleading. Our parameter tuning protocol suggests that all the terms of the objective function are important to obtain optimal image registration results.

6.3.3 Semi-automatic Segmentation of the Atlas

In this section, we describe the semi-automatic method that was used to obtain the segmentation for the proposed spatio-temporal atlas for SBA.

The fetal brains were divided into a total of eight tissue types: white matter (excluding the corpus callosum), ventricular system with the cavum septi pellucidi and cavum vergae, cerebellum, extra-axial cerebrospinal fluid, cortical gray matter, deep gray matter, brainstem, and corpus callosum. A visualization of the segmentations of those tissue types can be found in Figure 6.9 and Figure 6.10. The annotation protocol follows the annotation guidelines of the FeTA dataset [Payette 21]. In addition, the corpus callosum was also delineated.

Automatic 3D tissue types probability maps were obtained using a deep learning pipeline trained using partially supervised learning [Fidon 21c]. An ensemble of ten deep neural networks trained using the Leaf-Dice loss [Fidon 21c] has been used. The code and the pre-trained networks used for the automatic segmentation are available here. An average 3D tissue types probability maps for the atlas was obtained using a weighted average method analogous to the one described in section section 6.3.2 for the 3D reconstructed MRIs. Formally, let $\{P_i\}_{i=1}^N$ be a set of N co-registered 3D tissue types probability maps to average. The weighted average is computed as

$$P_{average} = \frac{1}{2N} \sum_{i=1}^N w_i (P_i + S(P_i)) \quad (6.10)$$

where S is the operator that computes the symmetric of a volume with respect to the central sagittal and the weights w_i are defined as in section section 6.3.2. An initial segmentation of the atlas was obtained using the tissue types of maximum probability for each voxel.

The initial segmentations of the spatio-temporal atlas were quality controlled

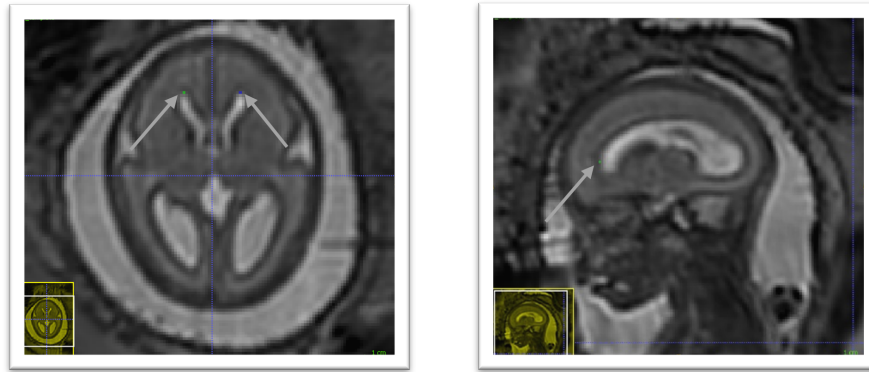


Figure 6.4: Anterior horn of the right lateral ventricle (green) and anterior horn of the left lateral ventricle (blue).

and corrected when necessary by authors LF and MA, a paediatric radiologist specialized in fetal brain anatomy with eight years of experience in segmenting fetal brain MRIs. Manual segmentations were performed using the software ITK-SNAP [Yushkevich 16] version 3.8.0.

6.4 Annotation Protocol of Anatomical Landmarks for Fetuses with Spina Bifida Aperta

In this section, protocols designed for the selection of imaging landmarks in MRI images of fetal brains with spina bifida aperta (SBA) are outlined. This is aimed to improve the accuracy of image registration. A total of 11 anatomical landmarks per study have been selected for initial assessment. Four in each cerebral hemisphere and three in the posterior fossa.

The first seven landmarks described below were found to be sufficiently reliable. The last four landmarks involving the cavum septi pellucidi were found to be insufficiently reliable.

6.4.1 Anterior horn of the right lateral ventricle

In the axial plane identify the right lateral ventricle. Use the view in the sagittal plane to select the most anterior slice reached by the ventricle. When this slice is not unique, which occurs when the anterior border of the ventricle is flattened, select the slice at the centre. With the smallest possible marker the most anterior border. The border is considered as the brighter intensity value of the two lines of intensity values showing the greatest difference.

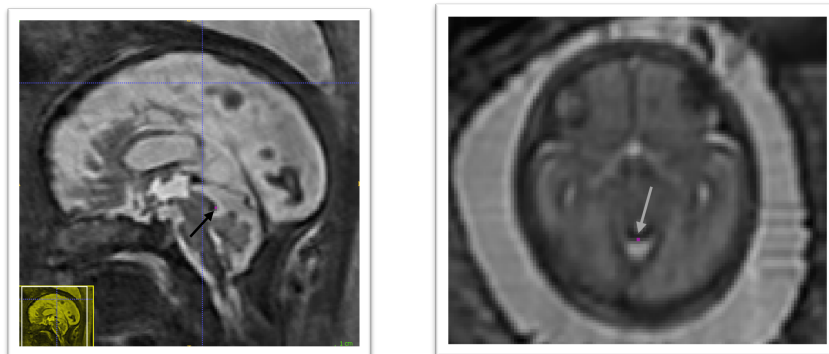


Figure 6.5: Posterior tectum plate (pink).

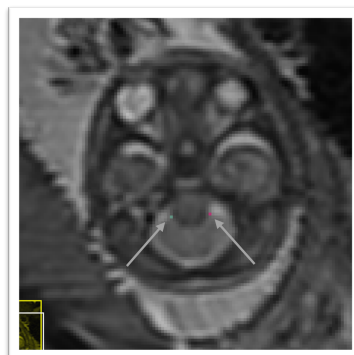


Figure 6.6: Right cerebellar-brainstem junction (turquoise) and left cerebellar-brainstem junction (pink).

6.4.2 Anterior horn of the left lateral ventricle

In the axial plane identify the Left Lateral Ventricle. Use the view in the sagittal plane to select the most anterior slice reached by the ventricle. When this slice is not unique, which occurs when the anterior border of the ventricle is flattened, select the slice at the centre. With the smallest possible marker the most anterior border. The border is considered as the brighter intensity value of the two lines of intensity values showing the greatest difference.

6.4.3 Posterior tectum plate

Using the sagittal and axial planes locate the tectum. In the axial plane select the midline sagittal slice. Confirm using the sagittal plane that the axial slice is viewing the most prominent part of the tectum. Using the smallest marker select the most posterior point of the tectum tissue. This considered to be the lower intensity value of the two intensity values at the posterior peak showing the greatest difference.

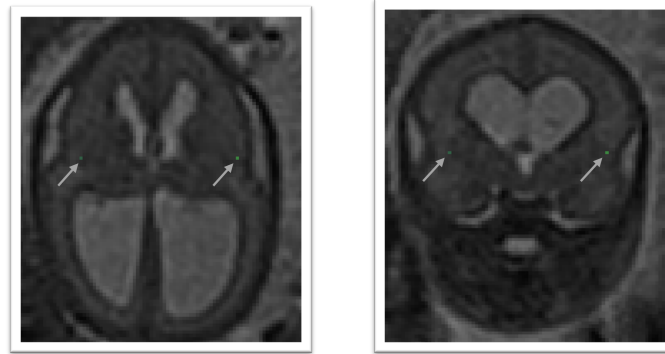


Figure 6.7: Left deep grey matter border at foramen of Monro (dark olive) and right deep grey matter border at foramen of Monro (lime green).

6.4.4 Left cerebellar-brainstem junction

In the axial view we locate the cerebellum and select the slice with the greatest cerebellar width, preferably where the posterior fossa also is seen at its greatest width. The brainstem is found just anterior to the cerebellum and directly meets with the cerebellum along its posterior borders. In this area, we select with the smallest possible marker the most anterior point where the cerebellum and brainstem meet on the left side. The marker should be within cerebellar tissue as oppose to the tissue of the brainstem.

6.4.5 Right cerebellar-brainstem junction

In the axial view we locate the cerebellum and select the slice with the greatest cerebellar width, preferably where the posterior fossa also is seen at its greatest width. The brainstem is found just anterior to the cerebellum and directly meets with the cerebellum along its posterior borders. In this area, we select with the smallest possible marker the most anterior point where the cerebellum and brainstem meet on the right side. The marker should be within cerebellar tissue as oppose to the tissue of the brainstem.

6.4.6 Left deep grey border at foramen of Monro

In the axial view locate the foramen of Monro or the interventricular foramen. The paired foramina connect the lateral ventricles to the third ventricle. The point where the foramina lead into the third ventricle, a horseshoe or trough shaped border is formed anteriorly. If not visible in this way, it can also be observed in the coronal view connecting the anterior horns of the lateral ventricle to the third ventricle. Select the mid-sagittal slice and trace a horizontal line left across from this border.

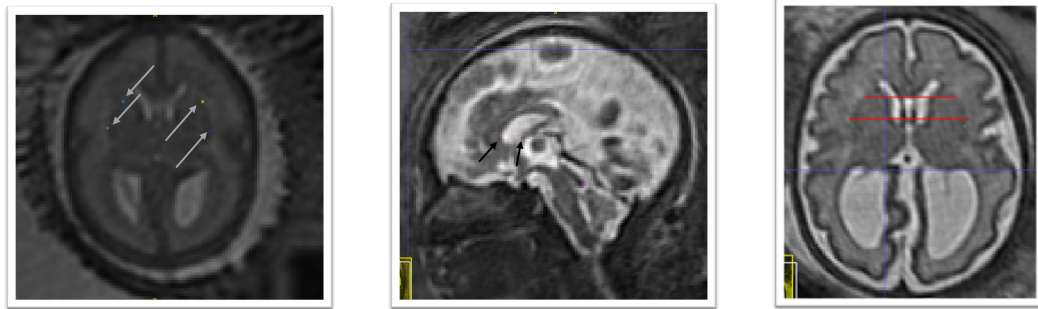
The correct position of the line is considered as the row of brighter intensity value of the two rows of intensity values showing the greatest contrast. The edge of the deep grey matter on the left side which should be visible forming a darker grey arch from the left anterior horn to the left posterior horn of the lateral ventricles. Using the smallest possible marker, mark the edge of the deep grey matter where it intersects with the line.

6.4.7 Right deep grey border at foramen of Monro

In the axial view locate the foramen of Monro or the interventricular foramen. The paired foramina connect the lateral ventricles to the third ventricle. The point where the foramina lead into the third ventricle, a horseshoe or trough shaped border is formed anteriorly. If not visible in this way, it can also be observed in the coronal view connecting the anterior horns of the lateral ventricle to the third ventricle. Select the mid-sagittal slice and trace a horizontal line right across from this border. The correct position of the line is considered as the row of brighter intensity value of the two rows of intensity values showing the greatest contrast. The edge of the deep grey matter on the right side which should be visible forming a darker grey arch from the right anterior horn to the right posterior horn of the lateral ventricles. Using the smallest possible marker, mark the edge of the deep grey matter where it intersects with the line.

6.4.8 Left deep grey border at anterior cavum septi pellucidi line

In the axial view locate the cavum septi pellucidi (CSP), a cavity in the fetal brain, the leaflets of the septum pellucidum are located between the anterior horns of the lateral ventricles. Select the slice in which the anterior wall of the cavity is found most anteriorly. If there is significant abnormality in this structure it may be helpful to use the sagittal plane to assist in defining this area. Trace a horizontal line left across from the anterior wall of the cavum septi pellucidi. The correct position of the line is considered as the row of brighter intensity value of the two rows of intensity values showing the greatest contrast. The edge of the deep grey matter on the left side forms a darker arch from the left anterior horn to the left posterior horn of the lateral ventricles. Using the smallest possible marker mark the edge of the deep grey matter where it intersects with that line.



(a) Left deep grey border at anterior CSP line (yellow), right deep grey border at the anterior CSP line (light blue), left deep grey border at posterior CSP line (dark blue), right deep grey border at the posterior CSP line (orange).

(b) Sagittal view of the position of the horizontal lines used to guide the marking of the deep grey borders at CSP (red).

(c) Axial view of the position of the horizontal lines used to guide the marking of the deep grey borders at CSP (red).

Figure 6.8: Deep grey matter border with respect to the cavum septi pellucidum (CSP).

6.4.9 Right deep grey border at the anterior cavum septi pellucidum line

In the axial view locate the cavum septi pellucidum (CSP), a cavity in the fetal brain, the leaflets of the septum pellucidum are located between the anterior horns of the lateral ventricles. Select the slice in which the anterior wall of the cavity is found most anteriorly. If there is significant abnormality in this structure it may be helpful to use the sagittal plane to assist in defining this area. Trace a horizontal line right across from the anterior wall of the cavum septi pellucidum. The correct position of the line is considered as the row of brighter intensity value of the two rows of intensity values showing the greatest contrast. The edge of the deep grey matter on the right side forms a darker arch from the right anterior horn to the right posterior horn of the lateral ventricles. Using the smallest possible marker mark the edge of the deep grey matter where it intersects with that line.

6.4.10 Left deep grey border at posterior cavum septi pellucidum line

In the axial view locate the cavum septi pellucidum, a cavity in the fetal brain, the leaflets of the septum pellucidum are located between the anterior horns of the lateral ventricles. Select the slice in which the anterior wall of the cavity is found

most anteriorly. If there is significant abnormality in this structure it may be helpful to use the sagittal plane to assist in defining this area. At this level trace a horizontal line left across from the posterior wall of the cavum septi pellucidi. The correct position of the line is considered as the row of brighter intensity value of the two rows of intensity values showing the greatest contrast. The edge of the deep grey matter on the left side forms a darker arch from the left anterior horn to the left posterior horn of the lateral ventricles. Using the smallest possible marker mark the edge of the deep grey matter where it intersects with that line.

6.4.11 Right deep grey border at the posterior cavum septi pellucidi line

In the axial view locate the cavum septi pellucidi, a cavity in the fetal brain, the leaflets of the septum pellucidum are located between the anterior horns of the lateral ventricles. Select the slice in which the anterior wall of the cavity is found most anteriorly. In this slice trace a horizontal line right across from the posterior wall of the cavum septi pellucidi. The correct position of the line is considered as the row of brighter intensity value of the two rows of intensity values showing the greatest contrast. The edge of the deep grey matter on the right side forms a darker arch from the right anterior horn to the right posterior horn of the lateral ventricles. Using the smallest possible marker mark the edge of the deep grey matter where it intersects with that line.

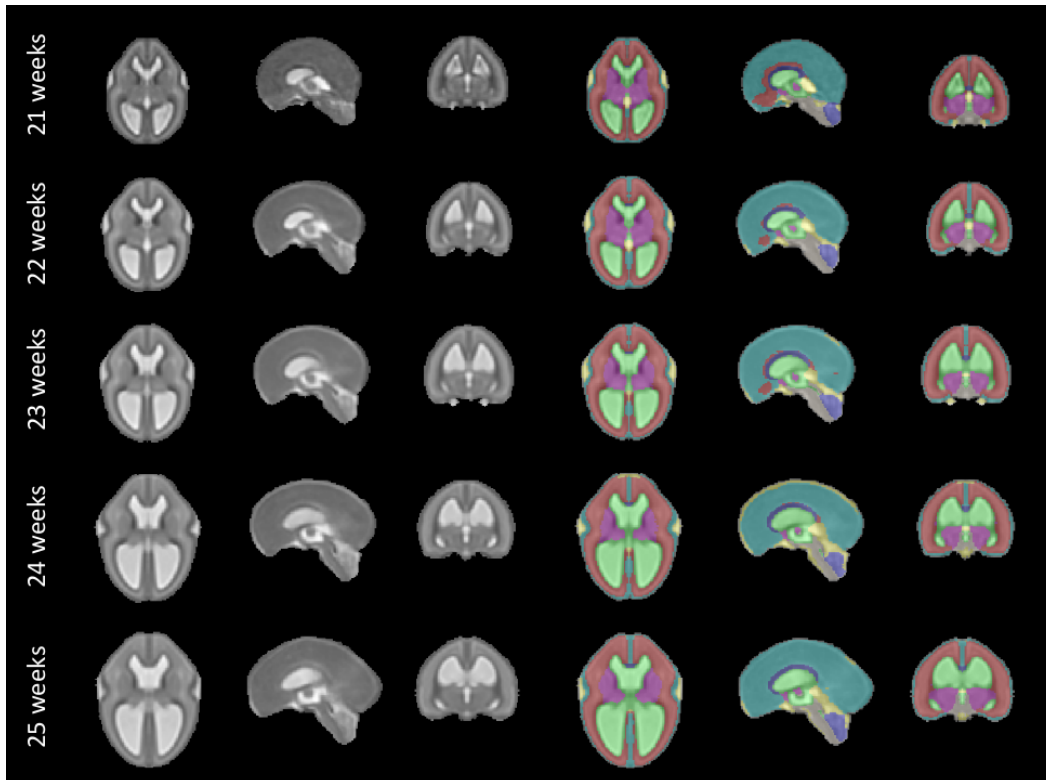


Figure 6.9: **Our spatio-temporal atlas for spina bifida aperta - Part I (not operated)**. Publicly available [here](#).

6.5 Results

6.5.1 Intra-rater Variability for the Annotation of the Anatomical Landmarks

To assess intra-rater variability, a subset of 31 3D reconstructed MRIs, selected at random, were marked two times by the same rater, EV. The mean gestational age was 26.2 weeks and the range of gestational ages in the reliability set was 22 – 34 weeks. Those statistics closely match the one of the full cohort as described in section 6.2 (the mean gestational age is 26.1 weeks and the range is 21 – 35 weeks for the full dataset). The two ratings were performed with an interval of at least three weeks to mitigate the bias caused by observer recollection. A landmark was marked absent when the anatomical position described by the protocol was not found within the volume.

The two landmark placements are said to be in agreement if the second landmark placement is inside a $3 \times 3 \times 3$ voxel cube where the original placement is the central voxel. When 95% of the second landmarks fall within this radius, the

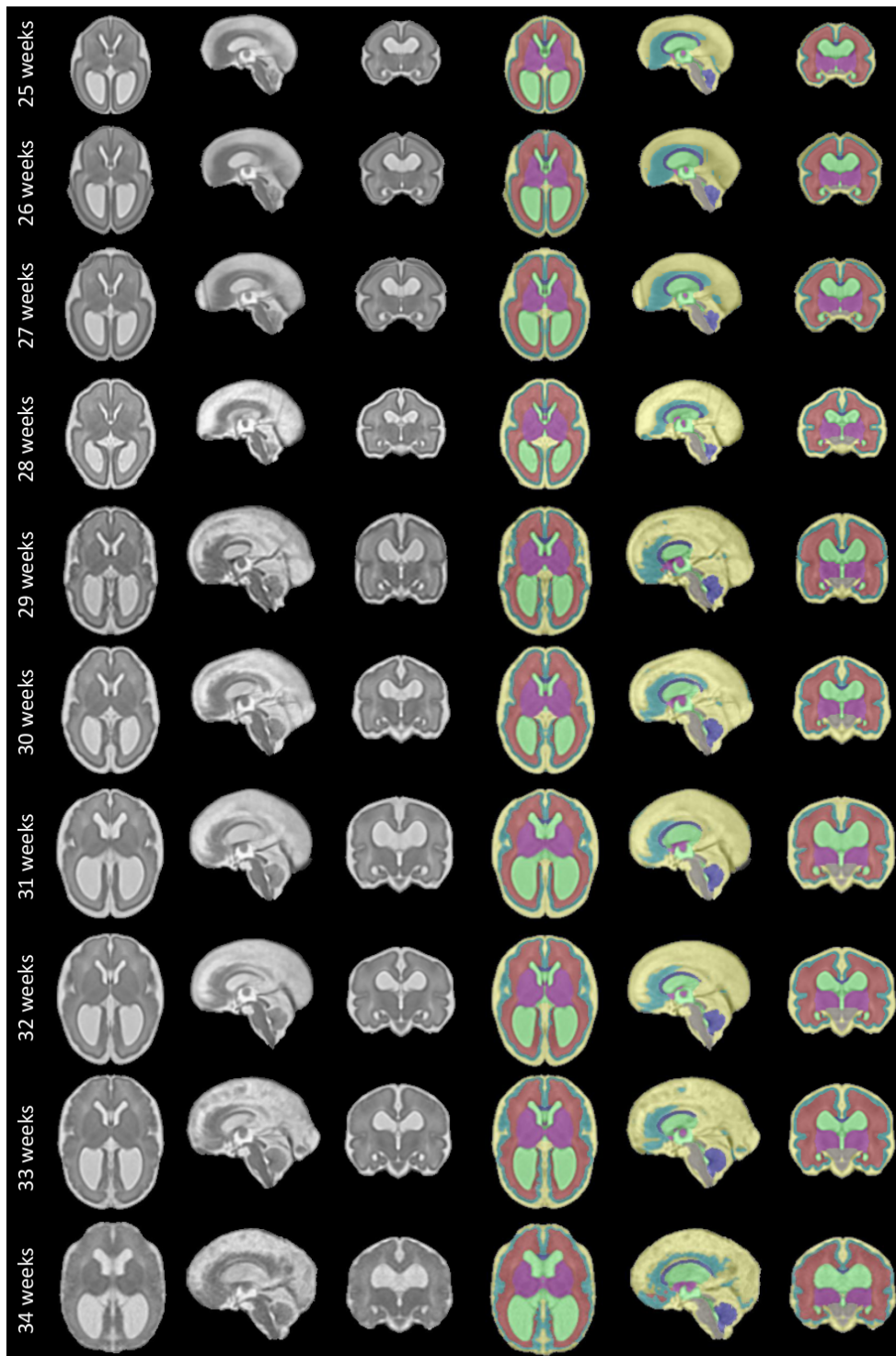


Figure 6.10: Spatio-temporal atlas for spina bifida aperta - Part II (operated). Publicly available here.

Table 6.1: **Evaluation of the reliability of the landmarks.** We report the estimated percentiles of distances in millimeters between first and second marking for each proposed landmarks. P_{75} : 75th percentile of distances in millimeters. P_{80} : 80th percentile of distances in millimeters. P_{95} : 95th percentile of distances in millimeters. Our reliability score is defined in section 6.5.1. **LALV**: Anterior Horn of the Left Lateral Ventricle, **RALV**: Anterior Horn of the Right Lateral Ventricle, **PTP**: Posterior Tectum Plate, **LCB**: Left Cerebellar Brainstem Junction, **RCB**: Right Cerebellar Brainstem Junction, **LFOM**: Left Deep Grey Border at Foramen of Monro, **RFOM**: Right Deep Grey Border at Foramen of Monro, **LACSP**: Left Deep Grey Border at Anterior Cavum Septi Pellucidi line, **RACSP**: Right Deep Grey Border at Anterior Cavum Septi Pellucidi line, **LPCSP**: Left Deep Grey Border at Posterior Cavum Septi Pellucidi line, **RPCSP**: Right Deep Grey Border at the Posterior Cavum Septi Pellucidi line.

Landmark	Ratio of Missing (%)	P_{75} (mm)	P_{80} (mm)	P_{95} (mm)	Reliability
LALV	0	1.73	1.95	3.02	Good
RALV	0	1.70	1.91	2.96	Good
PTP	3	1.15	1.29	2.00	Excellent
LCB	0	1.70	1.90	2.95	Good
RCB	0	1.78	2.00	3.10	Good
LFOM	3	2.83	3.17	4.91	Poor
RFOM	0	2.50	2.81	4.35	Satisfactory
LACSP	16	2.74	3.07	4.77	Poor
RACSP	29	2.59	2.91	4.51	Satisfactory
LPCSP	16	3.35	3.76	5.83	Poor
RPCSP	16	3.12	3.50	5.43	Poor

landmark is considered ‘Excellent’ in terms of intra-rater reliability, when 80% of are in agreement, intra-rater reliability is considered ‘Good’, where 75% fall within the radius of agreement intra-rater reliability is considered ‘Satisfactory’. For landmarks with a probability of agreement of less than 75%, the reliability is considered ‘Poor’. The probabilities that pairs of landmarks are in agreement is estimated based on the assumption that the distribution of distances between first and second marks is Gaussian.

6.5.2 Automatic Segmentation of Fetal Brain 3D MRIs

In this section, we compare the automatic segmentations obtained either using an atlas of normal fetal brains [Gholipour 17] or using the proposed atlas for spina bifida aperta (SBA). The quantitative evaluation can be found in Table 6.2.

We studied the automatic segmentation of fetal brain 3D MRIs into seven tissue types. Fetal brain 3D MRIs from the FeTA dataset [Payette 21] were used for the



Figure 6.11: Cavum septi pellucidum (CSP) variation fetuses with 25 weeks of gestation. Yellow arrows indicate the anterior and posterior borders of the CSP as defined by the landmark localisation protocol. This visualisation illustrates the disparity between volumes in terms of shape and size of the CSP.

evaluation. More details about the dataset used for the evaluation can be found in section section 6.2.

The automatic segmentations are obtained in two steps: first a volume of the atlas, chosen based on the gestational age, is registered to each fetal brain 3D MRI, and second, after registration, the segmentation of the atlas is propagated. Non-linear image registration is implemented as described in section section 6.3.2. In particular, we used the same hyper-parameter values. The automatic segmentations for the corpus callosum and the white matter were merged into white matter, since the corpus callosum is part of the white matter segmentation in the FeTA dataset.

Automatic segmentations for the SBA cases are computed using either a normal fetal brain atlas [Gholipour 17] or our SBA fetal brain atlas as can be seen in the last four rows of Table 6.2. In addition, we have also compute automatic segmentations for the normal brain cases using the normal fetal brain atlas [Gholipour 17] as can be seen in the first two rows of Table 6.2. The evaluation was performed for each tissue type using the Dice score [Dice 45, Fidon 17a] and the Hausdorff distance at percentile 95 [Hausdorff 91].

6.6 Discussion

The proposed spatio-temporal atlas for spina bifida aperta (SBA) is illustrated in Figure 6.9 and Figure 6.10 (see *Data availability* [Fidon 21f] and *Software availability* for full atlas). As described in section section 6.2, the cohort used to compute this atlas contains longitudinal data. This longitudinal dataset of 90 MRIs might be less representation of the whole SBA population than a dataset of 90 MRI that would contain only singletons. However, the use of longitudinal data adds some

Table 6.2: **Evaluation of automatic fetal brain segmentation.** We report mean (standard deviation) for the Dice score (DSC) in percentages and the Hausdorff distance at 95% (HD95) in millimeters for the seven tissue types. The spina bifida atlas is the atlas contributed in this chapter. The normal atlas is a spatio-temporal atlas computed from 3D MRIs of fetuses with a normal brain [Gholipour 17]. **WM**: white matter, **Vent**: ventricular system, **Cer**: cerebellum, **CSF**: cerebrospinal fluid, **ECSF**: extra-axial CSF, **CGM**: cortical gray matter, **DGM**: deep gray matter, **BS**: brainstem.

Atlas	Cohort	Metric	WM	Vent	Cer	ECSF	CGM	DGM	BS
Normal	Normal	DSC	87.1 (2.3)	83.8 (4.4)	86.9 (3.7)	86.7 (2.3)	67.9 (5.3)	82.7 (3.2)	81.7 (3.2)
		HD95	1.9 (0.6)	1.2 (0.2)	1.6 (0.4)	1.2 (0.4)	1.5 (0.6)	2.7 (0.7)	2.5 (0.5)
Normal	Spina Bifida	DSC	69.4 (16.4)	79.9 (8.0)	50.2 (31.3)	49.6 (35.7)	41.7 (21.6)	69.6 (14.5)	62.2 (21.2)
		HD95	4.3 (2.2)	3.5 (2.8)	5.8 (4.2)	10.3 (9.8)	4.1 (2.6)	4.3 (2.5)	3.9 (2.7)
Spina Bifida	Spina Bifida	DSC	80.6 (6.4)	84.0 (10.1)	69.8 (15.6)	54.9 (26.3)	48.8 (15.9)	77.2 (5.1)	71.2 (10.9)
		HD95	3.4 (1.6)	2.0 (1.4)	2.7 (0.8)	9.6 (9.1)	3.2 (1.7)	3.0 (0.7)	3.1 (1.2)

implicit temporal consistency in the atlas.

The landmarks in the ventricles, the posterior tectum plate, and at the junction of the cerebellar and the brainstem were all found to be reliable enough in terms of distance between successive marks by the same rater as can be seen in Table 6.1. In addition, those anatomical landmarks were always present, except for the posterior tectum plate that was missing for one reconstructed 3D MRI. However, the landmarks in the deep gray were almost all found to be poorly reliable in terms of distance between successive marks by the same rater. One can group the landmarks in the deep gray matter into two groups: the landmarks based on the foramen of Monro, and the landmarks based on the cavum septi pellucidi. The landmarks based on the foramen of Monro were almost always present. This is in contrast with the landmarks based on the cavum septi pellucidi that were missing up to 29% of the time. In Figure 6.11, we give an illustration of the anatomical variability of the cavum septi pellucidi in fetuses with SBA. This suggests that the position of landmarks based on the cavum septi pellucidi can vary widely from one subject to the other. As a result, we choose to use the two landmarks based on the foramen of Monro for the computation of the atlas, but to excluded the four

landmarks based on the cavum sseptum pellucidum.

The evaluation of automatic segmentation of fetal brain 3D MRIs in Table 6.2 suggests that using the proposed atlas for SBA leads to more accurate segmentation of SBA cases than a normal fetal brain atlas. The proposed atlas for SBA outperforms the normal fetal brain atlas in terms of mean Dice scores and mean Hausdorff distances for all tissue types. The proposed atlas also leads to lower standard deviations of Dice scores and Hausdorff distances for all tissue types except for the ventricular system. This suggests that automatic segmentation using image registration of an atlas is more robust for SBA when a SBA atlas is used.

In addition, when comparing automatic segmentations of normal fetuses and fetuses with SBA obtained using a normal fetal brain atlas we found a decrease of segmentation accuracy in terms of Dice scores and hausdorff distances for all tissue types. For the cerebellum, the mean Dice score decreased from 86.9% for normal fetuses to 50.2% for fetuses with SBA. This can be attributed to the Chiari malformation type II which is found in most SBA cases [Pollenus 20]. The decrease of mean Dice score and the increase of mean Hausdorff distance for the extra-axial cerebrospinal fluid (CSF) can be attributed to the quasi absence of extra-axial CSF in fetuses with SBA.

6.7 Limitations

In this chapter, we have used MRIs of operated and non-operated fetuses, ie that have or have not undergone fetal surgery to close the spina bifida aperta (SBA) defect in utero. *In-utero* fetal surgery is currently recommended to be performed prior to 26 weeks of gestation. The surgery has been found to influence the evolution of the fetal brain anatomy starting within one week after the operation [Aertsen 19]. Therefore, a normative atlas for SBA should be computed using only MRIs of non-operated fetuses. This limitation of our work is however due to the clinical data used. To make this limitation clear we have separated the atlas into two parts as illustrated in Figure 6.9 and Figure 6.10. This separations is also reflected in the data structure chosen to share the atlas, as detailed in the next section [Fidon 21f].

In Figure 6.1, it is worth noting that relatively little cases are available in the range of gestational ages 27 – 31 weeks. As a result, the proposed atlas might be less representative of the SBA population in this range of gestational ages. In particular, this might explain why the ventricle size does not appear to increase linearly for those gestational ages as can be seen in Figure 6.10.

6.8 Data Availability

Zenodo: A Spatio-temporal Atlas of the Developing Fetal Brain with Spina Bifida Aperta. <https://doi.org/10.5281/zenodo.5524312> [Fidon 21f].

The project contains 15 folders, each corresponding to a unique volume of our spatio-temporal fetal brain atlas, as illustrated in Figure 6.9 and Figure 6.10, and contains four nifti files:

- `srr.nii.gz` (average 3D reconstructed MRI).
- `mask.nii.gz` (3D brain mask).
- `parcellation.nii.gz` (3D segmentation of the fetal brain into 8 tissue types as described in section section 6.3.3).
- `lmks.nii.gz` (annotations for the 7 anatomical landmarks described in section section 6.3.1).

Data are available under the terms of the Creative Commons Zero "No rights reserved" data waiver (CC0 1.0 Public domain dedication). Codes and scripts are available under the terms of the BSD-3-Clause license.

Alternatively, it is possible to download A Spatio-temporal Atlas of the Developing Fetal Brain with Spina Bifida Aperta on Synapse: <https://doi.org/10.7303/syn25887675>. It is necessary to create a synapse account to be able to download the data.

6.9 Software Availability

Source code available from: <https://github.com/LucasFidon/spina-bifida-MRI-atlas>

Archived source code at the time of publication: <https://doi.org/10.5281/zenodo.5524312> [Fidon 21f]

License: BSD-3-Clause

6.10 Conclusion

In this chapter, we propose the first spatio-temporal fetal brain MRI atlas for spina bifida aperta (SBA).

We propose a semi-automatic pipeline for the computation of spatio-temporal fetal brain atlas. Our pipeline relies on four main components:

- `MONAIlbs` [Ranzini 21], an automatic method for fetal brain extraction in 2D fetal MRIs.

- NiftyMIC [Ebner 20], a 3D super resolution and reconstruction algorithm that allows to obtain isotropic and motion-free volumetric MRI of the fetal brain.
- A proposed protocol for the annotation of 7 anatomical landmarks in 3D reconstructed fetal brain MRIs.
- A proposed weighted generalize Procrustes method for an unbiased initialization of the atlas based on the anatomical landmarks.

We find that the proposed atlas outperforms a state-of-the-art fetal brain atlas for the automatic segmentation of brain 3D MRIs of fetuses with SBA. This suggests that the proposed atlas for SBA provides a better anatomical prior about the peri-surgical SBA brain. We hypothesise that this atlas could also help improving fetal brain MRI segmentation methods that lacks such prior, such as segmentation methods based on deep learning [Fidon 21c]. We investigate this research question in Chapter 7.

Recently, deep learning-based methods for computing brain atlases that can be conditioned on variables such as the gestational age have been proposed [Dalca 19, Dey 21]. In particular, some of those methods attempt to address the problem of robustness of registration and atlas construction algorithms to missing spatial correspondences [Bône 20]. Such missing correspondences are critical in the case for spina bifida aperta. Applying those methods to spina bifida atlases construction has not yet been explored and is an interesting research direction for future work.

A Dempster-Shafer approach to Trustworthy AI with application to Fetal Brain MRI Segmentation

Table of Contents

7.1	Introduction on Trustworthy AI using a Fallback	140
7.2	Materials and Methods	144
7.2.1	Fetal brain MRI dataset	144
7.2.2	Background on Dempster-Shafer theory	144
7.2.3	A Dempster-Shafer approach to Trustworthy AI for medical image segmentation	147
7.2.4	Human expert scoring method for evaluating the trustworthiness of fetal brain 3D MRI segmentation	161
7.3	Code Availability	162
7.4	Results	163
7.5	Discussion	169

Foreword This chapter is adapted from [Fidon 22a]. Deep learning models for medical image segmentation can fail unexpectedly and spectacularly for pathological cases and for images acquired at different centers than those used for training, with labeling errors that violate expert knowledge about the anatomy and the intensity distribution of the regions to be segmented. Such errors undermine the trustworthiness of deep learning models developed for medical image segmentation. Mechanisms with a fallback method for detecting and correcting such failures are essential for safely translating this technology into clinics and are likely to be a requirement of future regulations on artificial intelligence (AI). Here, we propose a principled trustworthy AI theoretical framework and a practical system that can augment any backbone AI system using a fallback method and a fail-safe mechanism based on Dempster-Shafer theory. Our approach relies on an actionable definition of trustworthy AI. Our method automatically discards the voxel-level labeling predicted by the backbone AI that are likely to violate expert knowledge and relies on a fallback atlas-based segmentation method for those voxels. We demonstrate the effectiveness of the proposed trustworthy AI approach on the largest reported annotated dataset of fetal T2w MRI consisting of 540 manually annotated fetal brain 3D MRIs with neurotypical or abnormal brain development and acquired from 13 sources of data across 6 countries. We show that our trustworthy AI method improves the robustness of a state-of-the-art backbone AI for fetal brain MRI segmentation on MRIs acquired across various centers and for fetuses with various brain abnormalities.

7.1 Introduction on Trustworthy AI using a Fallback

As discussed in Chapter 1, the legal framework for the deployment in clinics of AI tools for medical segmentation is likely to soon become more stringent once the European Union has proposed its Artificial Intelligence Act to regulate AI and AI trust is at the core of this proposal [EU Commission 19, EU Commission 21]. Trust is an attitude of the human user and, in particular, AI trust is context-dependent. In contrast, AI trustworthiness is an attribute of the AI system [Jacovi 21, Hoffman 17]. It is worth noting that a human user can trust an AI system that is not trustworthy and conversely. Guidelines for trustworthy AI claim that AI trustworthiness must precede trust in the deployment of AI systems to avoid miscalibration of the human trust with respect to the trustworthiness of an AI system [EU Commission 19]. In Psychology, trust of humans in AI can be defined as the belief of the human user that the AI system will satisfy the criteria of a set of contracts of trust. This contract-based definition of human-AI trust reflects the plurality and the context-dependency of human-AI trust. In particular, the user may trust an AI system for one population or one type of scanner but not trust it for others. An AI system

is trustworthy to a contract of trust if it can maintain this contract in all situations within the contract scope. The EU ethics guidelines for trustworthy AI, that upheld the AI Act, advocate that “AI systems should have safeguards that enable a *fallback* plan in case of problems” [EU Commission 19]. We argue that those safeguards should implement a *fail-safe* mechanism in relation with a collection of contracts of trust so as to improve the trustworthiness of the overall system.

In this chapter, we propose the first trustworthy AI framework with a fail-safe and a fallback for medical image segmentation (see A Dempster-Shafer approach to Trustworthy AI for medical image segmentation). The proposed framework consists of three main components: first, a backbone AI algorithm, that can be any AI algorithm for the task at hand, second, a fallback segmentation algorithm, that can be any safe segmentation algorithm but potentially less precise than the backbone AI algorithm, and third, a fail-safe method that automatically detects local conflicts between the backbone AI algorithm prediction and the contracts of trust and switches to the fallback algorithm in case of conflicts. This is illustrated for fetal brain 3D MRI segmentation in Fig. 7.1. The proposed principled fail-safe method is based on Dempster-Shafer (DS) theory. DS theory allows to model partial information about the task, which is typically the case for expert knowledge. For example, in human brain anatomy, one piece of expert knowledge is that the cerebellum is located in the lower back part of the brain. This gives us information only about the segmentation of the cerebellum while a segmentation algorithms will typically compute segmentation for many other tissue types in addition to the cerebellum. The Dempster’s rule of combination of DS theory is an efficient mathematical tool to combine independent sources of information that discards contradictions among the sources (see Background on Dempster-Shafer theory). In our framework, the AI-based segmentation and each expert knowledge are treated as independent sources of information and the Dempster’s rule of combination is employed to act as the fail-safe (see Fail-safe mechanism: switching between the AI algorithm and the fallback).

To demonstrate the applicability of the developed trustworthy AI framework, we propose one implementation for fetal brain segmentation in MRI. For the backbone AI model, we used the state-of-the-art deep learning-based segmentation pipeline nnU-Net [Isensee 21] (see nnU-Net as backbone AI segmentation algorithm). For the fallback model we used a registration-based segmentation method inspired by the state-of-the-art multi-atlas method GIF [Cardoso 15] (see Multi-atlas segmentation as fallback segmentation algorithm). We also show that our fail-safe formulation is flexible enough to model both spatial location-based (see Dempster-Shafer anatomical contract of trust for fetal brain segmentation) and intensity-based (see

Dempster-Shafer intensity-based contract of trust for fetal brain segmentation) contracts of trust about the regions of interest to be segmented (see General case with multiple contracts of trust:). Spatial location-based fail-safes are implemented using the masks of the regions of interest computed by the registration-based fallback algorithm. However, in the fail-safe, the masks are interpreted differently. In this case, the mask of a region R is used only to exclude labeling voxels outside of the mask as belonging to R . This is illustrated in Fig. 7.1c. Inspired by the margins used for safety in radiation therapy planning to account for spatial registration errors [Niyazi 16, Andres 20], we first add spatial margins to the fallback masks before excluding the labels seen as anatomically unlikely according to the dilated fallback masks. While allowing the masks to overlap, this helps preventing miscoverage of the regions of interest that is the only source of error in this formulation of the fail-safe.

We evaluated the proposed trustworthy AI method on fetal brain segmentation into eight tissue types using 3D T2w MRI. The segmentation of fetal brain MRI is essential to study normal and abnormal fetal brain development. In the future, reliable analysis and evaluation of fetal brain structures could also support diagnosis of central nervous system pathology, patient selection for fetal surgery, evaluation and prediction of outcome, hence also parental counselling. In particular, fetal brain 3D T2w MRI segmentation presents multiple challenges for trustworthy AI [Fidon 21b]. There are variations in T2w MRI protocols used across clinical centers and there is a spectacular variation of the fetal brain anatomy across gestational ages and across normal and abnormal fetal brain anatomy.

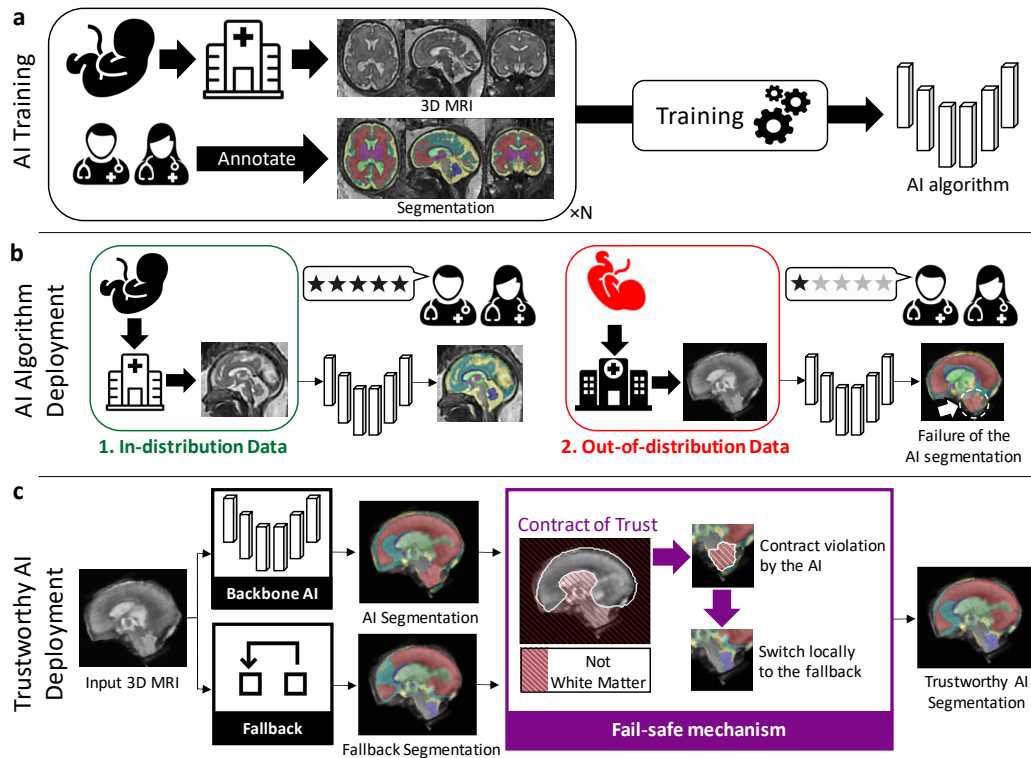


Figure 7.1: **Schematics of our principled method for trustworthy AI applied to medical image segmentation.** **a.** Deep neural networks for medical image segmentation (AI algorithm) are typically trained on images from a limited number acquisition centers. This is usually not sufficient to cover all the anatomical variability. **b.** When the trained AI algorithm is deployed, it will typically give satisfactory accuracy for images acquired with the same protocol as training images and with a health condition represented in the training dataset (left). However, the AI algorithm might fail with errors that are not anatomically plausible, for images acquired with a slightly different protocol as training images and/or representing anatomy underrepresented in the training dataset (right). **c.** Schematic of the proposed trustworthy AI algorithm. The backbone AI segmentation algorithm is coupled with a *fallback* segmentation algorithm. Experts knowledge about the anatomy is modelled using Dempster-Shafer theory. When part of the AI segmentation is found to contradict expert knowledge for a voxel, our trustworthy AI algorithm automatically switches to the fallback segmentation for this voxel.

7.2 Materials and Methods

7.2.1 Fetal brain MRI dataset

We have collected a dataset with a total of 540 fetal brain 3D MRIs with neurotypical or abnormal brain development and from 13 sources of data across 6 countries. The dataset and data processing used are described in Chapter 3.

The composition of the training and testing datasets is summarized in Fig.7.2. The training dataset consists of the 47 volumes from the three fetal brain atlases, 144 neurotypical cases from UHL and 28 spina bifida cases from UHL. The rest of the data is used for testing ($n = 349$). In the testing dataset, 3D MRIs that were acquired at UHL are designated as *in-scanner-distribution* while the data from other acquisition centers are designated as *out-of-scanner-distribution* data.

Mathematical notations

- \mathbf{C} : the set of all classes to be segmented
- $2^{\mathbf{C}}$: the set of all subsets of \mathbf{C}
- \mathbf{x} : a voxel or a pixel
- Ω : the set of all voxels or pixels (image domain)
- p : a probability vector
- m : a basic probability assignment (BPA) in Dempster-Shafer theory
- \oplus : Dempster's rule of combination

7.2.2 Background on Dempster-Shafer theory

In this section, we give a brief background on Dempster-Shafer theory where we introduce solely the mathematical concepts that will be used for our method: the basic probability assignment (BPA) and Dempster's rule of combination.

In Dempster-Shafer theory [Shafer 76], *basic probability assignments* are a generalization of probabilities that allow to model partial information and to combine different sources of information using Dempster's rule.

Let \mathbf{C} be the set of all classes and $2^{\mathbf{C}}$ the set of all subsets of \mathbf{C} . A **basic probability assignment (BPA)** on \mathbf{C} is a function $m : 2^{\mathbf{C}} \mapsto [0, 1]$ that satisfies

$$\begin{cases} m(\emptyset) = 0 \\ \sum_{A \subseteq \mathbf{C}} m(A) = 1 \end{cases} \quad (7.1)$$

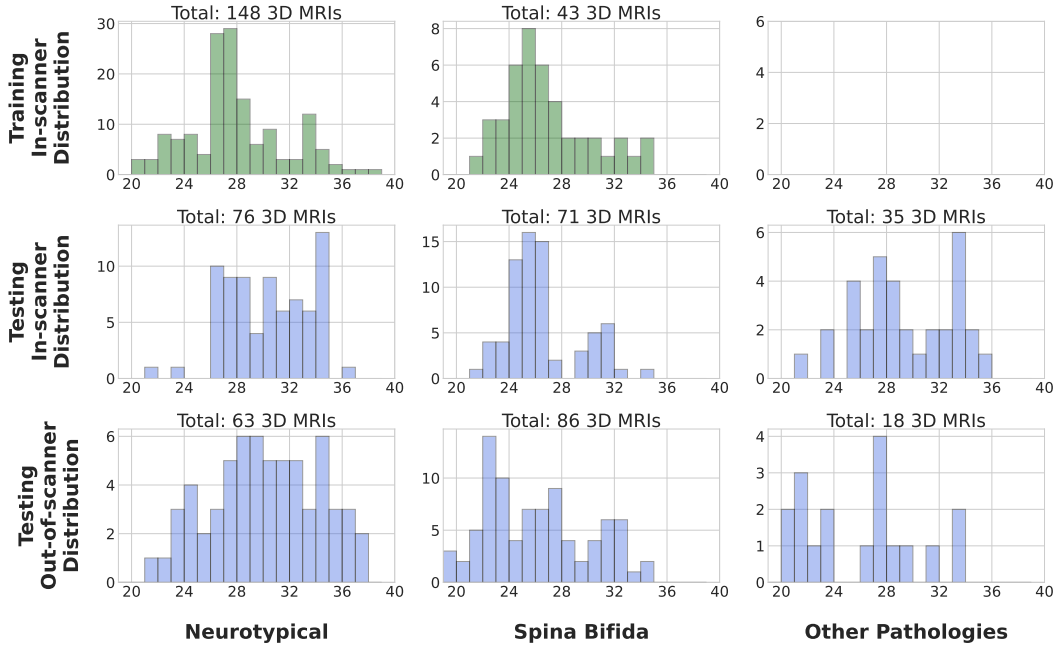


Figure 7.2: **Composition of the training and testing datasets (total: 540 3D MRIs)** *In-scanner distribution* designates the 3D MRIs acquired at the same center as the training data. *Out-of-scanner distribution* designates the 3D MRIs acquired at different centers than the training data. This is the largest fetal brain MRI dataset reported to date.

Probabilities on \mathbf{C} are functions $p : \mathbf{C} \mapsto [0, 1]$ that satisfy $\sum_{c \in \mathbf{C}} p(c) = 1$. Probabilities are equivalent to the BPAs that assign non-zeros weights only to the singletons, i.e. the sets $A = \{c\}$ for $c \in \mathbf{C}$. Indeed, given a probability p the BPA $m^{(p)}$ associated with p is defined as: $\forall c \in \mathbf{C}, m^{(p)}(\{c\}) = p(c)$ and $\forall A \subset \mathbf{C}$ with $|A| \neq 1$, $m^{(p)}(A) = 0$. Basic probability assignments on \mathbf{C} are therefore more general than probabilities on \mathbf{C} .

For $A \subset \mathbf{C}$, $m(A)$ is the probability that our knowledge about the true label is exactly and only: "the true class is one of the classes in A ". In particular, it does not imply that $m(B) > 0$ for any set B such that $B \subsetneq A$ or $A \subsetneq B$. This is in contrast to probabilities that can weight only the individual classes. BPAs allow to represent more precisely than probabilities what we know (and don't know) about the true class of a voxel. For example, the extreme case where we know nothing about the true class can be represented by the BPA m such that $m(\mathbf{C}) = 1$. The best one can do to try representing this case with probabilities is to define a probability p such that $\forall c \in \mathbf{C}, p(c) = \frac{1}{|\mathbf{C}|}$. However, this choice of p corresponds to the knowledge that the class distribution is uniformly random which is different from knowing nothing about the true class.

We now introduce the concept of *complete contradiction* between BPAs which we need for Dempster's rule of combination. Two BPAs on \mathbf{C} , m_1 and m_2 , are said to be **completely contradictory** if

$$\sum_{E, F \subset \mathbf{C} | E \cap F = \emptyset} m_1(E)m_2(F) = 1 \quad (7.2)$$

Following (7.1), m_1 and m_2 are completely contradictory if and only if one cannot form a pair of overlapping sets of classes (A, B) such that m_1 commits some belief to A , i.e. $m_1(A) > 0$, and m_2 commits some belief to B , i.e. $m_2(B) > 0$.

Dempster's rule of combination

Dempster's rule of combination allows to combine any pair (m_1, m_2) of BPAs on \mathbf{C} that are not completely contradictory using the formula

$$\forall A \subset \mathbf{C}, \quad (m_1 \oplus m_2)(A) = \begin{cases} \frac{\sum_{E, F \subset \mathbf{C} | E \cap F = A} m_1(E)m_2(F)}{1 - \sum_{E, F \subset \mathbf{C} | E \cap F = \emptyset} m_1(E)m_2(F)} & \text{if } A \neq \emptyset \\ 0 & \text{if } A = \emptyset \end{cases} \quad (7.3)$$

For any pairs (m_1, m_2) of BPAs on \mathbf{C} that are not completely contradictory, $m_1 \oplus m_2$ is also a BPA on \mathbf{C} . In addition, the relation \oplus is symmetrical and associative.

Special case of combining a probability with a BPA

One particular case that will be useful for our method is the combination of a probability p on \mathbf{C} , which we consider as a BPA, with a generic BPA m on \mathbf{C} using Dempster's rule of combination.

Since p is a probability, for $A \subset \mathbf{C}$, $p(A)$ can be non-zeros only if A is a singleton, i.e. if it exists a class $c \in \mathbf{C}$ such that $A = \{c\}$. For simplicity, we will therefore use the abusive notation when considering p as a BPA: $p(c) := p(A) = p(\{c\})$.

The relation of complete contradiction (7.2) between p and m can be simplified

$$\sum_{E, F \subset \mathbf{C} | E \cap F = \emptyset} p(E)m(F) = \sum_{c \in \mathbf{C}} \sum_{F \subset (\mathbf{C} \setminus \{c\})} p(c)m(F) = 1 \quad (7.4)$$

Similarly, if p and m are not completely contradictory, the Dempster's rule

between p and m can be simplified. Let $A \subset \mathbf{C}$, $A \neq \emptyset$, using (7.3) we have

$$\begin{aligned} (p \oplus m)(A) &= \frac{\sum_{E, F \subset \mathbf{C} | E \cap F = A} p(E)m(F)}{1 - \sum_{E, F \subset \mathbf{C} | E \cap F = \emptyset} p(E)m(F)} \\ &= \frac{\sum_{c \in \mathbf{C}, F \subset \mathbf{C} | \{c\} \cap F = A} p(c)m(F)}{1 - \sum_{c \in \mathbf{C}} \sum_{F \subset (\mathbf{C} \setminus \{c\})} p(c)m(F)} \end{aligned} \quad (7.5)$$

We remark that $p \oplus m$ is also a probability on \mathbf{C} . Indeed, let $c \in \mathbf{C}$, it can exist $F \subset \mathbf{C}$ such that $\{c\} \cap F = A$ only if A is the singleton $A = \{c\}$ (we have assumed $A \neq \emptyset$). Therefore if A is not a singleton, i.e. $|A| > 1$, the sum on the numerator is empty and equal to 0. As a result, we can write for any class $c \in \mathbf{C}$

$$\begin{aligned} (p \oplus m)(c) &= \frac{\sum_{c' \in \mathbf{C}, F \subset \mathbf{C} | \{c'\} \cap F = \{c\}} p(c')m(F)}{1 - \sum_{c' \in \mathbf{C}} \sum_{F \subset (\mathbf{C} \setminus \{c'\})} p(c')m(F)} \\ &= \frac{p(c) \sum_{F \subset \mathbf{C} | c \in F} m(F)}{1 - \sum_{c' \in \mathbf{C}} \sum_{F \subset (\mathbf{C} \setminus \{c'\})} p(c')m(F)} \end{aligned} \quad (7.6)$$

7.2.3 A Dempster-Shafer approach to Trustworthy AI for medical image segmentation

In this section, we present the formulation of our method for trustworthy AI-based medical image segmentation.

Our trustworthy AI segmentation method consists of three main components: 1) a backbone AI segmentation algorithm; 2) a fallback segmentation algorithm; and 3) and a fail-safe method that detects area of conflict between the AI algorithm segmentation and the contracts of trust and switches to the fallback algorithm for those regions. An illustration for the task of fetal brain MRI segmentation is given in Fig. 6.2.

The AI segmentation algorithm is a high-accuracy segmentor that can be, for example, a state-of-the-art convolutional neural network for medical image segmentation. The fallback segmentation algorithm is a segmentor that might achieve lower accuracy than the AI, but is superior to the AI for other desirable properties such as robustness. The AI and fallback segmentation algorithms take as input an image to be segmented and compute for each voxel of the image a probabilities vector with one probability for each class to be segmented.

The fail-safe mechanism aims at detecting erroneous predictions of the AI segmentation algorithm that contradict one of the contracts of trust. The contracts of trust embed domain knowledge such as "there can't be white matter in this part of the brain" or "hyperintense voxels on T2 fetal brain MRI are always cerebrospinal fluid". It is worth noting that, in general, those contracts are not sufficient to seg-

ment an entire image. Most contract will not enforce a specific segmentation but rather impose that the automatic segmentation meets certain constraints. The fail-safe mechanism is not a segmentation algorithm. In the context of image segmentation, contract of trusts can only reduce the set of possible classes and reweights the class probabilities of the segmentation of a pixel or voxel. To implement the fail-safe mechanism, we propose to use a basic probability assignment (BPA) that acts on the backbone AI and the fallback class probabilities using Dempster's rule of combination (7.6). In addition, we assume that the fallback class probabilities never completely contradicts the BPA representing the contracts of trust. As a result, Dempster's rule of combination can be used to switch automatically between the backbone AI algorithm and the fallback algorithm when the AI class probabilities completely contradict the BPA.

Formally, the trustworthy segmentation prediction is defined for an input image I and for all voxel position \mathbf{x} as

$$p_{I,\mathbf{x}}^{\text{TWAI}} = \left((1 - \epsilon)p_{I,\mathbf{x}}^{\text{AI}} + \epsilon p_{I,\mathbf{x}}^{\text{fallback}} \right) \oplus m_{I,\mathbf{x}}^{\text{fail-safe}} \quad (7.7)$$

where \oplus is the Dempster's combination rule (7.3), $p_{I,\mathbf{x}}^{\text{AI}}$ is the class probability prediction of the AI segmentation algorithm for voxel \mathbf{x} of image I , $p_{I,\mathbf{x}}^{\text{fallback}}$ is the class probability prediction of the fallback segmentation for voxel \mathbf{x} of image I , and $m_{I,\mathbf{x}}^{\text{fail-safe}}$ is the BPA of the fail-safe mechanism for voxel \mathbf{x} of image I . The parameter ϵ is a constant between 0 and 1.

Toy example: trustworthy traffic lights.

One contract of trust for a trustworthy traffic light system at a crossing is that green should not be shown in all directions of the crossing at the same time. To maintain this contract, traffic light controllers may use a fail-safe conflict monitor unit to detect conflicting signals and switch to a fallback light protocol. One possible fallback is to display flashing warning signal for all traffic lights.

Formally, for the example of two traffic lights at a single-lane passage, the set of classes is all the pairs of color the two traffic light can display at the same time $\mathbf{C} = \{(c_1, c_2) \mid c_1, c_2 \in \{\text{green, orange, red, flash}\}\}$.

Let p^{backbone} be the probability of the pair of traffic lights for the default light algorithm. The probability of the fallback algorithm p^{fallback} is then defined such as $p^{\text{fallback}}(\text{flash, flash}) = 1$. The contract of trust is m defined as $m^{\text{not-all-green}}(\mathbf{C} \setminus \{(\text{green, green})\}) = 1$.

Let $\epsilon \in]0, 1]$, the trustworthy light algorithm is given by

$$p^{\text{TWAI}} = \left((1 - \epsilon)p^{\text{backbone}} + \epsilon p^{\text{fallback}} \right) \oplus m^{\text{not-all-green}} \quad (7.8)$$

Using (7.6), we obtain

$$\begin{aligned} p^{\text{TWAI}}(\text{(green, green)}) &= 0 \\ p^{\text{TWAI}}(\text{(flash, flash)}) &= \frac{\epsilon p^{\text{fallback}}(\text{flash, flash})}{1 - (1 - \epsilon)p^{\text{backbone}}(\text{(green, green)})} \end{aligned} \quad (7.9)$$

where the amount of conflict (7.4) between p^{backbone} and $m^{\text{not-all-green}}$ is equal to $p^{\text{backbone}}(\text{(green, green)})$ and the amount of conflict between p^{fallback} and $m^{\text{not-all-green}}$ is equal to 0. In the case of complete contradiction between the default algorithm and the contract of trust, i.e. $p^{\text{backbone}}(\text{(green, green)}) = 1$, the trustworthy algorithm switch completely to the fallback algorithm with $p^{\text{TWAI}}(\text{(flash, flash)}) = p^{\text{fallback}}(\text{flash, flash}) = 1$.

Fail-safe mechanism: switching between the AI algorithm and the fallback

In this section, we describe how the the fail-safe mechanism $m^{\text{fail-safe}}$ allows to switch between the backbone AI segmentation algorithm and the fallback segmentation algorithm.

In our framework, we assume that the fallback segmentation algorithm always produces segmentation probabilities that do not contradict entirely the BPA of the contracts of trust. A trivial example of such fallback, is the uniform segmentation algorithm that assigns an equal probability to all the classes to be segmented and for all voxels. In contrast, we do not make such compatibility assumption for the AI segmentation algorithm. Not only does this make our approach applicable with any AI segmentation algorithm, but our method also relies on the incompatibility between the AI segmentation algorithm prediction and the contracts of trust to detect failure of the AI segmentation algorithm and to switch to the fallback segmentation algorithm. Formally, however small ϵ is, as long as it remains strictly positive ($\epsilon > 0$), when $p_{I,x}^{\text{AI}}$ is completely contradictory with $m_{I,x}^{\text{fail-safe}}$, we obtain that $p_{I,x}^{\text{TWAI}}$ depends only on $p_{I,x}^{\text{fallback}}$ and not on $p_{I,x}^{\text{AI}}$. On the contrary, when $p_{I,x}^{\text{AI}}$ is not contradictory with $m_{I,x}^{\text{fail-safe}}$, we obtain that $p_{I,x}^{\text{TWAI}}$ depends mainly on $p_{I,x}^{\text{AI}}$ and the contribution of $p_{I,x}^{\text{fallback}}$ is negligible for ϵ small enough.

This is due to a property of Dempster's rule of combination that can be illustrated by the following example of pairs of BPAs [Zadeh 79]. Let $\epsilon_1, \epsilon_2 \in]0, 1]$ and

let m_1 and m_2 two BPAs on $\{a, b, c\}$ defined by: $m_1(\{a\}) = 1 - \epsilon_1$, $m_1(\{b\}) = \epsilon_1$, $m_1(\{c\}) = 0$, $m_2(\{a\}) = 0$, $m_2(\{b\}) = \epsilon_2$, and $m_2(\{c\}) = 1 - \epsilon_2$. We obtain $(m_1 \oplus m_2)(\{b\}) = 1$, however small $\epsilon_1, \epsilon_2 > 0$ are.

This characteristic of Dempster’s rule of combination has sometimes been pointed out as counter-intuitive and as a motivation against the use of this operation [Zadeh 79]. In contrast, we believe this to be an interesting characteristic and we use this property at our advantage to implement the fail-safe mechanism to switch between the AI algorithm and the fallback algorithm. We recommend to choose a value of ϵ small compared to 1. As a result, the fallback class with the highest probability becomes the trustworthy AI prediction highest probability only when the AI highest probabilities prediction have been eliminated by the contracts of trust BPAs under the Dempster’s combination rule. In this sense, the fallback probabilities act as a discounting factor in Dempster Shafer theory [Shafer 76, Smets 93]. Rolf Haenni [Haenni 02] summarized the motivation for the use of such discounting coefficient by Sherlock Holmes’ statement [Doyle 10]: “When you have eliminated the impossible, whatever remains, however improbable, must be the truth”.

Here, we consider the case in which the AI algorithm predicted probability $p_{I,\mathbf{x}}^{\text{AI}}$ is completely contradictory with $m_{I,\mathbf{x}}^{\text{fail-safe}}$ for a voxel \mathbf{x} . Using (7.4), this implies

$$\begin{cases} \sum_{c' \in \mathbf{C}} \left(\sum_{\mathbf{C}' \subset (\mathbf{C} \setminus \{c'\})} p_{I,\mathbf{x}}^{\text{AI}}(c') m_{I,\mathbf{x}}^{\text{fail-safe}}(\mathbf{C}') \right) = 1 \\ \forall c' \in \mathbf{C}, \forall \mathbf{C}' \subset \mathbf{C} \mid c' \in \mathbf{C}', \quad p_{I,\mathbf{x}}^{\text{AI}}(c') m_{I,\mathbf{x}}^{\text{fail-safe}}(\mathbf{C}') = 0 \end{cases}$$

Since by construction of our Trustworthy AI approach, the fallback algorithm probability $p_{I,\mathbf{x}}^{\text{fallback}}$ is *not* completely contradictory with $m_{I,\mathbf{x}}^{\text{fail-safe}}$, we have that $\left((1 - \epsilon)p_{I,\mathbf{x}}^{\text{AI}} + \epsilon p_{I,\mathbf{x}}^{\text{fallback}} \right)$ is not completely contradictory with $m_{I,\mathbf{x}}^{\text{fail-safe}}$. Using Dempster’s rule of combination (7.6) we obtain, for every class $c \in \mathbf{C}$

$$p_{I,\mathbf{x}}^{\text{TWAI}}(c) = \frac{\sum_{\mathbf{C}' \subset \mathbf{C} \mid c \in \mathbf{C}'} \left((1 - \epsilon)p_{I,\mathbf{x}}^{\text{AI}}(c) + \epsilon p_{I,\mathbf{x}}^{\text{fallback}}(c) \right) m_{I,\mathbf{x}}^{\text{fail-safe}}(\mathbf{C}')}{1 - \sum_{c' \in \mathbf{C}} \sum_{\mathbf{C}' \subset (\mathbf{C} \setminus \{c'\})} \left((1 - \epsilon)p_{I,\mathbf{x}}^{\text{AI}}(c') + \epsilon p_{I,\mathbf{x}}^{\text{fallback}}(c') \right) m_{I,\mathbf{x}}^{\text{fail-safe}}(\mathbf{C}')}$$

Since, in this illustrative case, we assume that $p_{I,\mathbf{x}}^{\text{AI}}$ is completely contradictory with

$m_{I,\mathbf{x}}^{\text{fail-safe}}$ and $\epsilon > 0$, $p_{I,\mathbf{x}}^{\text{TWAI}}(c)$ becomes

$$\begin{aligned} p_{I,\mathbf{x}}^{\text{TWAI}}(c) &= \frac{\sum_{\mathbf{C}' \subset \mathbf{C} \mid c \in \mathbf{C}'} \epsilon p_{I,\mathbf{x}}^{\text{fallback}}(c) m_{I,\mathbf{x}}^{\text{fail-safe}}(\mathbf{C}')}{1 - (1 - \epsilon) - \sum_{c' \in \mathbf{C}} \sum_{\mathbf{C}' \subset (\mathbf{C} \setminus \{c'\})} \epsilon p_{I,\mathbf{x}}^{\text{fallback}}(c') m_{I,\mathbf{x}}^{\text{fail-safe}}(\mathbf{C}')} \\ &= \frac{\sum_{\mathbf{C}' \subset \mathbf{C} \mid c \in \mathbf{C}'} p_{I,\mathbf{x}}^{\text{fallback}}(c) m_{I,\mathbf{x}}^{\text{fail-safe}}(\mathbf{C}')}{1 - \sum_{c' \in \mathbf{C}} \sum_{\mathbf{C}' \subset (\mathbf{C} \setminus \{c'\})} p_{I,\mathbf{x}}^{\text{fallback}}(c') m_{I,\mathbf{x}}^{\text{fail-safe}}(\mathbf{C}')} \\ &= \left(p_{I,\mathbf{x}}^{\text{fallback}} \oplus m_{I,\mathbf{x}}^{\text{fail-safe}} \right) (c) \end{aligned}$$

In this last equality, one can observe that, however small $\epsilon > 0$ can be, the trustworthy AI prediction for voxel \mathbf{x} does not depend anymore on the AI algorithm probability but only on the fallback algorithm probability. In other words, we have switched totally from the backbone AI algorithm to the fallback algorithm.

General case with multiple contracts of trust:

In general, $m_{I,\mathbf{x}}^{\text{fail-safe}}$ is a sum of contracts of trust BPAs that are not completely contradictory and $m_{I,\mathbf{x}}^{\text{fail-safe}}$ can be written as

$$m_{I,\mathbf{x}}^{\text{fail-safe}} = \bigoplus_{k=1}^K m_{I,\mathbf{x}}^{(k)} \quad (7.10)$$

where each $m_{I,\mathbf{x}}^{(k)}$ is a basic probability assignment (BPA), K is the number of BPAs, and $\bigoplus_{k=1}^K$ is the Dempster's rule of combination (7.3) of K BPAs computed in any order. $\bigoplus_{k=1}^K$ is well defined because Dempster's rule of combination \oplus is associative and because the $m_{I,\mathbf{x}}^{(k)}$ are not completely contradictory. The $m_{I,\mathbf{x}}^{(k)}$ represent the contracts of trust in our framework.

Specifically, for medical image segmentation we propose the following trustworthy AI model:

$$p_{I,\mathbf{x}}^{\text{TWAI}} = \left((1 - \epsilon) p_{I,\mathbf{x}}^{\text{AI}} + \epsilon p_{I,\mathbf{x}}^{\text{fallback}} \right) \oplus m_{I,\mathbf{x}}^{\text{anatomy}} \oplus m_{I,\mathbf{x}}^{\text{intensity}} \quad (7.11)$$

where $m_{I,\mathbf{x}}^{\text{anatomy}}$ is the anatomical contract of trust BPA for voxel \mathbf{x} of image I , and $m_{I,\mathbf{x}}^{\text{intensity}}$ is the intensity contract of trust BPA for voxel \mathbf{x} of image I . The definitions and properties of $m_{I,\mathbf{x}}^{\text{anatomy}}$ and $m_{I,\mathbf{x}}^{\text{intensity}}$ will be derived in following two subsections of this section Dempster-Shafer anatomical contract of trust for fetal brain segmentation and Dempster-Shafer intensity-based contract of trust for fetal brain segmentation.

Dempster-Shafer anatomical contract of trust for fetal brain segmentation

In this section, we describe our proposed anatomical prior basic probability assignment (BPA) m^{anatomy} that is used in our trustworthy AI method (7.11).

Our anatomical prior is computed using the segmentations computed using the multi-atlas segmentation algorithm [Iglesias 15]. Atlas-based segmentation algorithms are anatomically-constrained due to the spatial smoothness that is imposed to the spatial transformation used to compute the segmentation. In practice, this is achieved thanks to the parameterization of the spatial transformation and the regularization loss in the registration optimization problem [Cardoso 15, Fidon 19, Modat 10]. Therefore, if implemented correctly, atlas-based automatic segmentations can inherit from the anatomical prior represented by segmentation atlases.

In terms of contract of trust, every binary segmentation mask corresponding to a specific region of interest in a fetal brain atlas is associated with an anatomical contract of trust. Indeed, each of those binary segmentation masks represents the anatomy of a given tissue type, for a given gestational age and a given population of fetuses. The anatomical contracts derived from atlas-based segmentation are therefore context-dependent since the segmentation masks are specific to a class, to a gestational age, and to the population of fetuses that was used to compute the atlas [Fidon 21e, Gholipour 17, Wu 21]. Since only neurotypical fetal brain atlases [Gholipour 17, Wu 21] and a spina bifida fetal brain atlas [Fidon 21e] are available in our work, our anatomical contract of trust will hold only for neurotypical and spina bifida fetuses.

Due to the spatial smoothness imposed to the spatial transformation, atlas-based automatic segmentations will usually be correct up to a spatial margin. Therefore, we propose to add spatial margins to the atlas-based segmentation to compute the BPAs of our anatomical contract of trust. This approach is inspired by the safety margins used in radiotherapy to account for errors including spatial registration errors [Niyazi 16] and is illustrated in Fig. 7.3 for the white matter of a fetal brain 3D MRI.

Formally, let M^c a 3D (binary) mask from an atlas for class $c \in \mathbf{C}$. We propose to define the BPA map $m^{(c)} = \left(m_{\mathbf{x}}^{(c)} \right)_{\mathbf{x} \in \Omega}$ associated with M^c as

$$\forall \mathbf{x}, \quad \begin{cases} m_{\mathbf{x}}^{(c)}(\mathbf{C} \setminus \{c\}) = 1 - \phi(d(\mathbf{x}, M^c)) \\ m_{\mathbf{x}}^{(c)}(\mathbf{C}) = \phi(d(\mathbf{x}, M^c)) \end{cases} \quad (7.12)$$

where $d(\mathbf{x}, M^c)$ the Euclidean distance from any voxel position vector \mathbf{x} to M^c ,

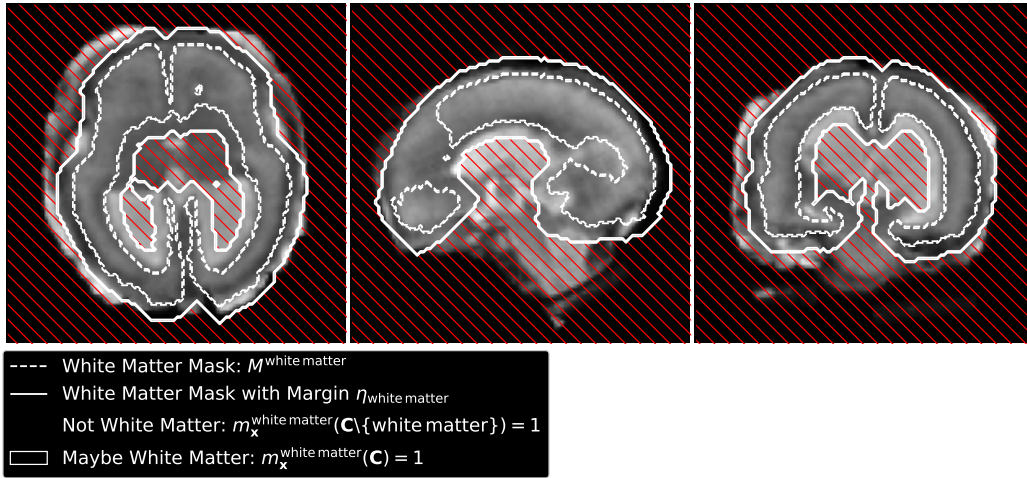


Figure 7.3: **Implementation of the anatomical BPA for the white matter of a fetus with spina bifida.** The white matter basic probability assignment (BPA) is computed by dilating the white matter mask of the fallback algorithm $M^{\text{white matter}}$ using the margin $\eta_{\text{white matter}}$. The margin aims at eliminating the false negative for the mask $M^{\text{white matter}}$ and are estimated using the training dataset. The white matter BPA imposes that no white matter can be predicted outside the dilated mask. No constraint is imposed inside the dilated mask. The same approach is applied to all the regions of interest to be segmented.

and $\phi : \mathbb{R}_+ \rightarrow [0, 1]$ with $\phi(0) = 1$ and ϕ non-increasing. In the following, we call **thresholding function** any function ϕ that satisfies the properties above. We give below two examples of thresholding functions. The first one is based on hard margins, while the second one is based on exponential soft margins.

$$\begin{aligned}
 1) \quad \forall d \geq 0, \quad \phi(d) &= \begin{cases} 1 & \text{if } d \leq \eta \\ 0 & \text{otherwise} \end{cases} \\
 2) \quad \forall d \geq 0, \quad \phi(d) &= \exp\left(-\frac{d}{\eta}\right)
 \end{aligned} \tag{7.13}$$

In both case, $\eta > 0$ is a hyper-parameter homogeneous to a distance and can be interpreted as a safety margin for the anatomical prior. The BPA for the first thresholding function (hard margins) can be implemented efficiently without computing explicitly the distance between every voxel \mathbf{x} and the mask M^c . An illustration is given in Fig. 7.3 for the white matter. We describe a method to tune the margins at training time for each class at the end of this section.

With the definition of the BPA $m_{\mathbf{x}}^{(c)}$ in (7.12), we formalize the following belief: far enough from the mask M^c we know for sure that the true class is not c , i.e. $m_{\mathbf{x}}^{(c)}(\mathbf{C} \setminus \{c\}) = 1$, otherwise we do not know anything for sure regarding class c ,

i.e. $m_{\mathbf{x}}^{(c)}(\mathbf{C}) > 0$.

No contradiction between the anatomical contracts of trust: Following the assumption of Dempster’s rule of combination in (7.3), we need to make sure that the BPAs m_c defined as in (7.12) are nowhere completely contradictory.

Proof: We show that there is always at least one class that is compatible with the set of anatomical prior. For this we need to show that for all voxel \mathbf{x} , there exists $c \in \mathbf{C}$ such that $m_{\mathbf{x}}^{(c)}(\mathbf{C} \setminus \{c\}) < 1$ and $m_{\mathbf{x}}^{(c)}(\mathbf{C}) > 0$. This holds in our case because the masks $\{M^c\}_{c \in \mathbf{C}}$ form a partition of the set of all the voxels and because, following (7.12), for the voxels \mathbf{x} inside mask M^c , $m_{\mathbf{x}}^{(c)}(\mathbf{C}) = 1$ and $m_{\mathbf{x}}^{(c)}(\mathbf{C} \setminus \{c\}) = 0$.

Formula for the anatomical prior: We can now define the anatomical prior BPA used in (7.11) for image I and voxel \mathbf{x} as

$$m_{I,\mathbf{x}}^{\text{anatomy}} = \bigoplus_{c \in \mathbf{C}} m_{\mathbf{x}}^{(c)} \quad (7.14)$$

where m_c is the BPA associated to the mask M_I^c for a given thresholding function, and M_I^c is the mask for class c of the segmentation obtained using the multi-atlas fallback segmentation algorithm.

The Dempster’s rule of combination \oplus satisfies the mathematical property of associativity. This is why, by convention, we use the symbol \oplus for this relation here. In terms of implementation, the associativity implies that one can use a for loop to compute $\bigoplus_{c \in \mathbf{C}} m_{\mathbf{x}}^{(c)}$. This also makes it possible to parallelize the computation of this quantity with respect to the contracts. Therefore, the computation of the composition of contracts scales in $O(\log(K))$ where K is the number of contracts.

We prove that for all voxel \mathbf{x} and for all subset of classes $\mathbf{C}' \subset \mathbf{C}$, the anatomical BPA mass that the true label of \mathbf{x} is not in \mathbf{C}' is equal to

$$m_{I,\mathbf{x}}^{\text{anatomy}}(\mathbf{C} \setminus \mathbf{C}') = \prod_{c \in \mathbf{C}} \left(\delta_c(\mathbf{C}') m_{\mathbf{x}}^{(c)}(\mathbf{C} \setminus \{c\}) + (1 - \delta_c(\mathbf{C}')) m_{\mathbf{x}}^{(c)}(\mathbf{C}) \right) \quad (7.15)$$

where for all $c \in \mathbf{C}$, δ_c is the Dirac measure associated with c defined as

$$\forall \mathbf{C}' \subset \mathbf{C}, \quad \delta_c(\mathbf{C}') = \begin{cases} 1 & \text{if } c \in \mathbf{C}' \\ 0 & \text{if } c \notin \mathbf{C}' \end{cases} \quad (7.16)$$

The proof of (7.15) can be found in the Appendix.

In practice, we are particularly interested in summing the anatomical prior BPA with probabilities using the particular case of Dempster’s rule in (7.6). Let \mathbf{x} a voxel and $p_{I,\mathbf{x}}$ a probability on \mathbf{C} for voxel \mathbf{x} of image I that is not completely

contradictory with $m_{I,\mathbf{x}}^{\text{anatomy}}$. For all $c \in \mathbf{C}$, we can show that

$$\left(p_{I,\mathbf{x}} \oplus m_{I,\mathbf{x}}^{\text{anatomy}}\right)(c) = \frac{p_{I,\mathbf{x}}(c)m_{\mathbf{x}}^{(c)}(\mathbf{C})}{\sum_{c' \in \mathbf{C}} p_{I,\mathbf{x}}(c')m_{\mathbf{x}}^{(c')}(\mathbf{C})} \quad (7.17)$$

A proof of this equality can be found in the Appendix. It is worth noting that, due to the specific form of $m_{I,\mathbf{x}}^{\text{anatomy}}$ and because $p_{I,\mathbf{x}}$ is a probability, the computational cost of $p_{I,\mathbf{x}} \oplus m_{I,\mathbf{x}}^{\text{anatomy}}$ is $\mathcal{O}(\mathbf{C})$ even though there are $2^{|\mathbf{C}|}$ elements in $2^{\mathbf{C}}$.

Another important remark is that when $p_{I,\mathbf{x}}$ is completely contradictory with $m_{I,\mathbf{x}}^{\text{anatomy}}$, we have $\sum_{c' \in \mathbf{C}} p_{I,\mathbf{x}}(c')m_{\mathbf{x}}^{(c')}(\mathbf{C}) = 0$.

No contradiction between the anatomical prior and the fallback: For our trustworthy AI model (7.11) to be valid, we need to show that the probability $\left((1 - \epsilon)p_{I,\mathbf{x}}^{\text{AI}} + \epsilon p_{I,\mathbf{x}}^{\text{fallback}}\right)$, is not completely contradictory with the anatomical prior BPA.

Proof: Since $\epsilon > 0$, it is sufficient to show that $p_{I,\mathbf{x}}^{\text{fallback}}$ is not completely contradictory with $m_{I,\mathbf{x}}^{\text{anatomy}}$ for every voxel \mathbf{x} . In (7.12) and (7.14) we have defined the BPA maps $m_{I,c}$ based on the multi-atlas segmentation which is equal to p_I^{fallback} . Therefore, for any voxel \mathbf{x} , let $c \in \mathbf{C}$ the class such that $\mathbf{x} \in M^c$. We have $d(\mathbf{x}, M^c) = 0$ and therefore $m_{I,\mathbf{x}}(\mathbf{C}) = \phi(d(\mathbf{x}, M^c)) = 1$. And we have $p_{I,\mathbf{x}}^{\text{fallback}}(c) > 0$. This shows that $p_{I,\mathbf{x}}^{\text{fallback}}$ and $m_{I,\mathbf{x}}^{\text{anatomy}}$ are not completely contradictory.

Tuning the margins: The margins η were tuned for each class and each condition independently using the 3D MRIs of the fold 0 of the training dataset.

In our definition of the anatomical prior BPAs (7.12), the margins account for false negatives in the multi-atlas segmentation. The anatomical prior BPAs for a class c will impose to the probabilities of class c to be zeros for every voxel outside of the mask after adding the margins using dilation. Therefore, we chose the margin for a given class c to be the minimal dilation radius for the dilated mask to cover entirely the true region of class c even if it creates overlaps with other regions.

For this purpose, we propose to use a modified Hausdorff distance, called *margin distance*, that considers only the false negatives. An illustration is given in Fig. 7.4. Let $\text{HD}_{95}(M_{\text{pred}}, M_{\text{gt}})$ denotes the Hausdorff distance at 95% of percentile between a predicted binary mask M_{pred} and the ground-truth mask M_{gt} . The margin distance of interest between M_{pred} and M_{gt} is defined as

$$\text{HD}_{95}^{FN}(M_{\text{pred}}, M_{\text{gt}}) = \text{HD}_{95}(M_{\text{pred}}, M_{\text{pred}} \cup M_{\text{gt}}) \quad (7.18)$$

The margin $\eta_{c,\text{cond}}$ for class $c \in \mathbf{C}$ and condition *cond* (neurotypical or spina bifida) is chosen as the 95% percentile value of HD_{95}^{FN} on the fold 0 of the training

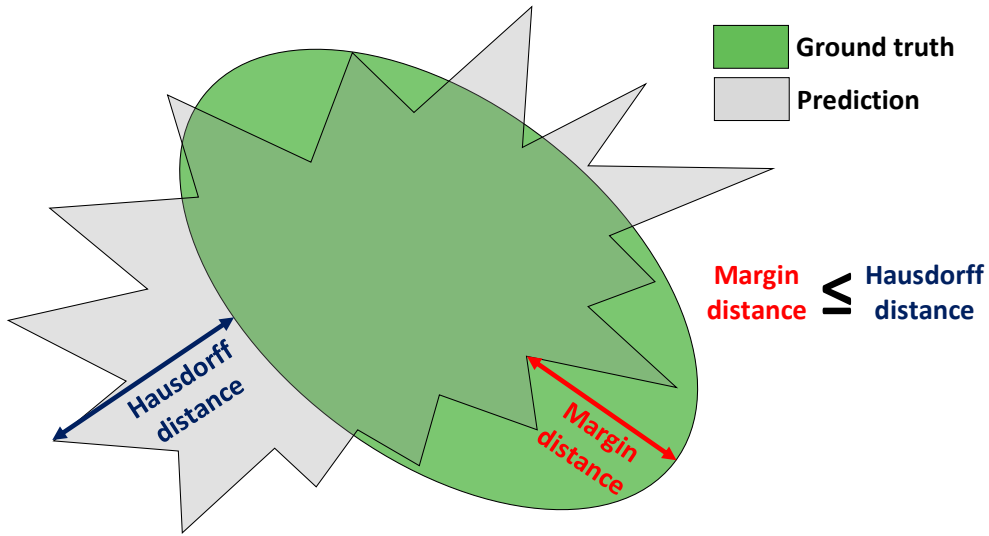


Figure 7.4: **Illustration of the margin distance.** The margin distance is the minimal dilation radius to apply to the predicted binary mask so that it covers entirely the ground-truth binary mask. We have proposed to use the margin distance to define our margins used in our definition of the anatomical BPAs.

dataset for the given class and condition.

For fetuses with a condition other than neurotypical or spina bifida, we chose $\eta_{c,other\ pathologies} = \max\{\eta_{c,neurotypical}, \eta_{c,spina\ bifida}\}$.

Dempster-Shafer intensity-based contract of trust for fetal brain segmentation

In this section, we describe our proposed intensity prior basic probability assignment (BPA) $m^{\text{intensity}}$ that is used in our trustworthy AI method for fetal brain 3D MRI segmentation (7.11).

In T2-weighted MRI, which is the MRI modality used in this work, it is known that the hyper-intense voxels inside the brain are highly likely to be part of the cerebrospinal fluid (CSF). We therefore propose to model this intensity prior about high intensities as a contract of trust.

Regarding hypo-intense voxels, it is unclear how to derive similar prior because even the CSF classes contain hypo-intense voxels, such as the choroid plexus for the intra-axial CSF class and the vein of Galena and straight sinus for the extra-axial CSF class [Payette 21]. It is also worth noting that voxels outside the brain (*background* class) can also be hyper-intense.

Formula for the intensity BPA: Let $C_{high} \subset C$ be the subset of classes that contain all the classes that partition the entire CSF (intra-axial CSF and

extra-axial CSF) and the background. Let $I = \{I_{\mathbf{x}}\}_{\mathbf{x} \in \Omega}$ be the volume and Ω the volume domain of a fetal brain 3D MRI. We propose to fit a Gaussian mixture model (GMM) with two components to the image intensity distribution of I . The two components of parameters $(\mu_{high}, \sigma_{high})$ and $(\mu_{low}, \sigma_{low})$ are associated to high and low intensities. We propose to define the intensity prior BPA for all voxels $\forall \mathbf{x}$, up to a normalization factor, as

$$\begin{cases} m_{I,\mathbf{x}}^{\text{intensity}}(\mathbf{C}_{high}) \propto \frac{1}{\sigma_{high}} \exp\left(\frac{1}{2} \left(\frac{I_{\mathbf{x}} - \mu_{high}}{\sigma_{high}}\right)^2\right) \\ m_{I,\mathbf{x}}^{\text{intensity}}(\mathbf{C}) \propto \frac{1}{\sigma_{low}} \exp\left(\frac{1}{2} \left(\frac{I_{\mathbf{x}} - \mu_{low}}{\sigma_{low}}\right)^2\right) \end{cases} \quad (7.19)$$

It is worth noting that $m_{I,\mathbf{x}}^{\text{intensity}}(\mathbf{C}) > 0$. Therefore, no probability will be set to 0 using the Dempster's rule of combination with $m^{\text{intensity}}$. In other words, $m^{\text{intensity}}$ does not forbid any assignment. This is in contrast with the anatomical BPAs defined in Dempster-Shafer anatomical contract of trust for fetal brain segmentation.

Let \mathbf{x} a voxel and $p_{I,\mathbf{x}}$ a probability on \mathbf{C} for voxel \mathbf{x} of image I . Since $m_{I,\mathbf{x}}^{\text{intensity}}(\mathbf{C}) > 0$, $p_{I,\mathbf{x}}$ is not completely contradictory with $m_{I,\mathbf{x}}^{\text{intensity}}$. Using Dempster's rule, we have, for all class $c \in \mathbf{C}$

$$\left(p_{I,\mathbf{x}} \oplus m_{I,\mathbf{x}}^{\text{intensity}}\right)(c) \propto \begin{cases} \left(m_{I,\mathbf{x}}^{\text{intensity}}(\mathbf{C}_{high}) + m_{I,\mathbf{x}}^{\text{intensity}}(\mathbf{C})\right) p_{I,\mathbf{x}}(c) & \text{if } c \in \mathbf{C}_{high} \\ m_{I,\mathbf{x}}^{\text{intensity}}(\mathbf{C}) p_{I,\mathbf{x}}(c) & \text{otherwise} \end{cases} \quad (7.20)$$

This can be interpreted as a soft-thresholding operation

$$\left(p_{I,\mathbf{x}} \oplus m_{I,\mathbf{x}}^{\text{intensity}}\right)(c) \propto \begin{cases} \left(1 + \frac{m_{I,\mathbf{x}}^{\text{intensity}}(\mathbf{C}_{high})}{m_{I,\mathbf{x}}^{\text{intensity}}(\mathbf{C})}\right) p_{I,\mathbf{x}}(c) & \text{if } c \in \mathbf{C}_{high} \\ p_{I,\mathbf{x}}(c) & \text{otherwise} \end{cases} \quad (7.21)$$

Thus, only the probabilities for the background and CSF classes in \mathbf{C}_{high} are increased in the case of a voxel \mathbf{x} with relatively high intensity. In particular, the probabilities remain approximately unchanged for a voxel \mathbf{x} with relatively low or medium intensity. This reflects the fact that the background and CSF classes also contain hypo-intense voxels. The hyper-intense voxels must be in \mathbf{C}_{high} while we can not say anything about hypo-intense voxels in general. There are hypo-intense voxels in every class.

nnU-Net as backbone AI segmentation algorithm

The AI segmentation algorithm used is based on nnU-Net [Isensee 21] which is a state-of-the-art deep learning-based method for medical image segmentation. We have chosen the nnU-Net deep learning pipeline because it has lead to state-of-the-art results on several segmentation challenge, including the FeTA challenge 2021 for automatic fetal brain 3D MRI segmentation [Fidon 21c, Payette 21]. We have used the code available at <https://github.com/MIC-DKFZ/nnUNet> without modification for our backbone AI.

Deep learning pipeline: The nnU-Net pipeline is based on a set of heuristics to automatically select the deep neural network architecture and other training hyper-parameters such as the patch size. In this work, a 3D U-Net [Çiçek 16] was selected with one input block, 4 down-sampling blocks, one bottleneck block, 5 up-sampling blocks, 32 features in the first level, instance normalization [Ulyanov 16], and the leaky-ReLU activation function with slope 0.01. This 3D U-Net has a total of 31.2M trainable parameters. The patch size selected is $96 \times 112 \times 96$ voxels.

Preprocessing: We have used the same pre-processing as in our previous work [Fidon 21c]. The 3D MRIs are skull-stripped using the brain mask after applying a dilation operation (3 iterations using a structuring element with a square connectivity equal to one) and setting the values outside the dilated brain mask to 0. The brain masks are all computed automatically either during the 3D reconstruction for the Leuven data using NiftyMIC [Ebner 20, Ranzini 21], or for the other data using a multi-atlas segmentation method based on affine registration [Modat 14] and three fetal brain atlases [Fidon 21e, Gholipour 17, Wu 21]. The intensity values inside the dilated brain mask are clipped to the percentile values at 0.5% and 99.5%, and after clipping the intensity values inside the dilated brain mask are normalized to zero mean and unit variance.

Training: the training dataset is split at random into 5 folds. In total, five 3D U-Nets are trained with one for each possible combination of 4 folds for training and 1 fold for validation. The AI segmentation algorithm consists of the ensemble of those five 3D U-Nets. Each 3D U-Net is initialized at random using He initialization [He 15]. The loss function consists of the sum of the Dice loss and the cross entropy loss. Stochastic gradient descent with Nesterov momentum is used to minimize the empirical mean loss on the training dataset, with batch size 4, weight decay 3×10^{-5} , initial learning rate 0.01, deep supervision on 4 levels, and polynomial learning rate decay with power 0.9 for a total of 250,000 training iterations. The data augmentation methods used are: random cropping of a patch, random zoom, gamma intensity augmentation, multiplicative brightness, random rotations,

random mirroring along all axes, contrast augmentation, additive Gaussian noise, Gaussian blurring, and simulation of low resolution. For more implementation details, we refer the interested reader to [Isensee 21] and the nnU-Net GitHub page.

Inference: The probabilistic segmentation prediction of the AI segmentation algorithm is the average of the five probabilistic segmentation prediction of the five 3D U-Nets after training. In addition, for each 3D U-Net, test-time data augmentation with flip around the 3 spatial axis is performed.

Multi-atlas segmentation as fallback segmentation algorithm

The fallback segmentation algorithm that we propose to use is based on a multi-atlas segmentation approach. Multi-atlas segmentation [Iglesias 15] is one of the most trustworthy approaches for medical image segmentation in terms of anatomical plausibility. The multi-atlas segmentation that we use is inspired by the Geodesic Information Flows method (GIF) [Cardoso 15], which is a state-of-the-art multi-atlas segmentation algorithm.

In this section, we give details about the three main steps of the multi-atlas segmentation algorithm used. First, the selection of the atlas volumes to use to compute the automatic segmentation. Second, the non-linear registration algorithm to propagate each atlas segmentation to the 3D MRI to be segmented. And third, the fusion method used to combine the propagated segmentations from the atlas volumes.

Atlas volumes selection: We used the volumes from two neurotypical fetal brain 3D MRI atlases [Gholipour 17, Wu 21] and one spina bifida fetal brain 3D MRI atlas [Fidon 21e]. Let GA be the gestational age rounded to the closest number of weeks of the 3D MRI to be segmented. We select all the atlas volumes with a gestation age in the interval $[GA - \Delta GA, GA + \Delta GA]$ with $\Delta GA = 1$ week for the neurotypical fetuses and $\Delta GA = 3$ for spina bifida fetuses. This way approximately the same number of atlas volumes are used for neurotypical and spina bifida fetuses.

Non-linear registration: Our image registration step aims at spatially aligning the selected atlas volumes with the 3D MRI to be segmented. We used `NiftyReg` [Modat 10] to compute the non-linear image registrations. The non-linear image registration optimization problem is the following

$$\begin{cases} \min_{\Theta} \mathcal{L}(I_{subject}, I_{atlas}, \phi(\Theta)) + R(\Theta) \\ R(\Theta) = \alpha_{BE} BE(\phi(\Theta)) + \alpha_{LE} LE(\phi(\Theta)) \end{cases} \quad (7.22)$$

where I_{atlas} is the segmented atlas volume to be registered to the 3D reconstructed MRI $I_{subject}$ that we aim to segment, $\phi(\Theta)$ is a spatial transformation parameterized

by cubic B-splines of parameters Θ with a grid size of 4 mm. The data term \mathcal{L} is the local normalized cross correlation (LNCC) with the standard deviation of the Gaussian kernel of the LNCC was set to 6 mm. The regularization term R is a linear combination of the bending energy (BE) and the linear energy (LE) regularization functions applied to $\phi(\Theta)$ with $\alpha_{BE} = 0.1$ and $\alpha_{LE} = 0.3$.

Prior to the non-linear registration, the brain mask of $I_{subject}$ was used to mask the voxels outside the brain and I_{atlas} was registered to $I_{subject}$ using an affine transformation. The affine transformation was computed using a symmetric block-matching approach [Modat 14] based on image intensities and the brain masks. The optimization is performed using conjugate gradient descent and a pyramidal approach with 3 levels [Modat 10]. The hyper-parameters for the non-linear registration were chosen to be the same as in a recent registration pipeline to compute a fetal brain atlas [Fidon 21e].

Segmentations fusion: Once all the atlas volumes $\{I_k\}_{k=1}^K$ and their probabilistic segmentations $\{S_k\}_{k=1}^K$ have been registered to the 3D MRI to be segmented $I_{subject}$ using the transformations $\{\phi_k\}_{k=1}^K$, we need to fuse the aligned segmentations $\{S_k \circ \phi_k\}_{k=1}^K$ into one segmentation. This fusion is computed via a voxel-wise weighted average using heat kernels [Cardoso 15].

The heat map for atlas k at voxel \mathbf{x} is defined as [Cardoso 15]

$$w_k(\mathbf{x}) = \exp\left(-D(k, \mathbf{x})^2\right) \quad (7.23)$$

where $D(k, \mathbf{x})$ is a surrogate of the morphological similarity between $I_{subject}$ and $I_k \circ \phi_k$ at voxel \mathbf{x} . The distance $D(k, \mathbf{x})$ is the sum of two components

$$D(k, \mathbf{x}) = \alpha L(I_{subject}, I_k \circ \phi_k)(\mathbf{x}) + (1 - \alpha) F(\phi_k)(\mathbf{x}) \quad (7.24)$$

with $\alpha = 0.5$, $L(I_{subject}, I_k \circ \phi_k) = B * (I_{subject} - (I_k \circ \phi_k))^2$ the local sum of squared differences convoluted (convolution operator $*$) by a B-spline kernel B of order 3, and $F(\phi_k)(\mathbf{x})$ the Euclidean norm of the displacement field at voxel \mathbf{x} (in mm) after removing the low spatial frequencies of ϕ_k using a Gaussian kernel with a standard deviation of 20 mm. The hyper-parameters chosen are the same as in GIF [Cardoso 15]. Before computing D , the intensity values of the images are normalized to zero mean and unit variance inside the brain mask.

The multi-atlas segmentation at voxel \mathbf{x} is computed using the heat kernels as

$$S_{multi-atlas}(\mathbf{x}) = \frac{\sum_{k=1}^K w_k(\mathbf{x})(S_k \circ \phi_k)(\mathbf{x})}{\sum_{k=1}^K w_k(\mathbf{x})} \quad (7.25)$$

Our implementation is available at [trustworthy-ai-fetal-brain-segmentation](https://github.com/trustworthy-ai/fetal-brain-segmentation).

Hyper-parameters tuning: The hyper-parameters that we tuned are ΔGA , the selection strategy for the atlas volumes, and the fusion strategy for combining the probabilistic segmentation of the atlas volumes after non-linear registration. For ΔGA we tried the values $\{0, 1, 2, 3, 4\}$. For the selection strategy we compared the condition-specific strategy described above to using all the atlases irrespective of the condition of the fetus. And for the fusion strategy we compared the GIF-like fusion strategy described in above to a simple average.

The data used for the selection of the hyper-parameters are the training data of the first fold that was used for the training of the AI segmentation algorithm. The mean Dice score across all the segmentation classes and the number of volumes to register were used as our selection criteria to find a trade-off between segmentation accuracy and computational time. The results can be found in the appendix. The approach selected consists of GIF-like atlas segmentations fusions, condition specific atlas selection and $\Delta GA = 1$ for the neurotypical condition and $\Delta GA = 3$ for the spina bifida condition.

7.2.4 Human expert scoring method for evaluating the trustworthiness of fetal brain 3D MRI segmentation

The trustworthiness scoring is done for each of the tissue types: white matter, intra-axial CSF, cerebellum, extra-axial CSF, cortical gray matter, deep gray matter, and brainstem.

The evaluation is performed using a Likert scale ranging from 0 star to 5 stars to answer the question *"Is the automatic segmentation of the tissue type X trustworthy?"*:

☆☆☆☆☆ Strongly disagree / there are several severe violations of the anatomy that are totally unacceptable

★☆☆☆☆ Disagree / there is one severe violation of the anatomy that is totally unacceptable

★★☆☆☆ Moderately disagree / there are violations of the anatomy that make the acceptability of the segmentation questionable

★★★☆☆ Moderately agree / there are many minor violations of the anatomy that are acceptable

★★★★☆ Agree / there are a few minor violations of the anatomy that are acceptable

★★★★★ Strongly agree / perfect fit of the anatomy

This evaluation is performed on 50 3D MRIs from the FeTA dataset. We selected at random 20 neurotypical cases, 20 spina bifida cases, and 10 cases with other brain pathologies.

The scoring was performed independently by 4 individuals or groups of expert raters: MA, paediatric radiologist at University Hospital Leuven with several years of experience in manual segmentation of fetal brain MRI; AJ, MD and group leader at University Children’s Hospital Zurich; AB, professor of neuroradiology at University Hospital Zurich; and by MS and PK jointly, two MDs at Medical University of Vienna (MUV) with more than 400 hours of experience in manual segmentation of fetal brain MRI, under the supervision of 3 experts: DP, professor of radiology at MUV, GK, professor of paediatric radiology at MUV, and IP, neuroradiologist at MUV.

The human expert raters were given access to the 3D MRIs, the backbone AI segmentation, the fallback segmentation, the trustworthy AI segmentation, and the ground-truth manual segmentation for each case. The segmentation algorithms are anonymized for the raters by assigning to each of them a number from 1 to 3. The assignment of numbers to the segmentation methods was performed randomly for each case independently, i.e. we used a different random assignment for each case.

The segmentation protocol that was used for the manual segmentations can be found at <http://neuroimaging.ch/feta>. An empty csv file `ranking.csv` is made available to each rater to complete.

7.3 Code Availability

The code for our trustworthy AI segmentation algorithm of fetal brain 3D MRI is publicly available at [trustworthy-ai-fetal-brain-segmentation](https://github.com/trustworthy-ai-fetal-brain-segmentation). It included our implementation of the fallback algorithm. For medical image registration we have used the `NiftyReg` software that is publicly available at <https://github.com/KCL-BMEIS/niftyreg>. For the backbone AI algorithm we have used the `nnU-Net` software that is publicly available at <https://github.com/MIC-DKFZ/nnUNet>. `nnU-Net` is based on the PyTorch deep learning library and we have used PyTorch version 1.10.

We have used python 3.8.10 for all experiments. The plots in Fig.7.6, 7.6c, 7.6d and Fig. A.4, A.5, including the confidence intervals, were computed using `seaborn` version 0.11.2. The statistical test were computed using `scipy` version 1.6.3.

7.4 Results

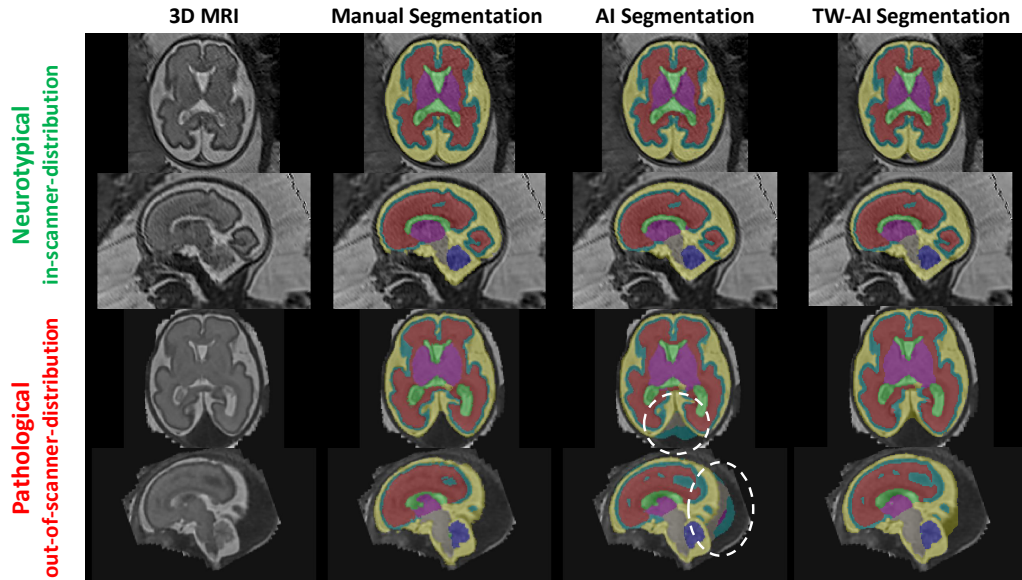


Figure 7.5: Illustration of the improved robustness of the proposed trustworthy AI method (TW-AI) as compared to a state-of-the-art AI method. (Top) 3D MRI of a neurotypical fetus at 28 weeks of gestation acquired at the same center as the training data for the AI. (Bottom) 3D MRI of a fetus with a high-flow dural sinus malformation at 28 weeks of gestation acquired at a different center as the training data for the AI. Severe violations of the anatomy by the AI, but not the TW-AI, are highlighted in white.

Evaluation on a large multi-center fetal brain T2w MRI dataset. To effectively evaluate the performance of the proposed trustworthy AI framework as a suitable method to improve the trustworthiness of a backbone AI model using a fallback model, we have selected the task of fetal brain segmentation in 3D MRI. This task is clinically relevant and is characterized by large image protocol variations and large anatomical variations.

Deep learning-based AI methods for fetal brain MRI segmentation have recently defined state-of-the-art segmentation performance [Fetit 20, Fidon 21a, Fidon 21c, Hong 20, Khalili 19, Li 21, Payette 21, Zhao 22], gradually replacing image registration-based segmentation methods [Makropoulos 18] in the literature. Most previous work on deep learning for fetal brain MRI segmentation trained and evaluated their models using only MRIs of healthy fetuses or only MRIs acquired at one center. However, the segmentation performance of deep learning methods typically degrades when images from a different center or a different scanner vendor as the

one used for training are used or when evaluating the segmentation performance on abnormal anatomy [Alis 21, Kamraoui 22, Mårtensson 20, Oakden-Rayner 20, Perone 19, Redko 19]. One study has reported such issues for fetal brain MRI segmentation [Fidon 21b].

Thus, we have compared the proposed trustworthy AI algorithm to the backbone AI algorithm only [Isensee 21] and the fallback algorithm only, consisting of a registration-based segmentation method [Cardoso 15]. We have used a large multi-centric fetal brain 3D MRI dataset that consists of a total of 540 fetal brain 3D MRIs with neurotypical or abnormal brain development, with gestational ages ranging from 19 weeks to 40 weeks, and with MRIs acquired at 13 hospitals across 6 countries. The task consists of segmenting automatically a fetal brain 3D MRI into eight clinically relevant tissue types: the corpus callosum, the white matter, the cortical gray matter, the deep gray matter, the cerebellum, the brainstem, the intra-axial cerebrospinal fluid (CSF), and the extra-axial CSF.

Stratified evaluation across brain conditions and acquisition centers. The evaluation of AI-based segmentation algorithms has shown that the performance of deep learning models can vary widely across clinically relevant populations and across data acquisition protocols [Fidon 21b] (Fig. 7.1b, Fig. 7.5).

Therefore, we performed a stratified comparison of the backbone AI algorithm, the fallback algorithm, and the trustworthy AI algorithm across two groups of acquisition centers and three groups of brain conditions. The composition of the dataset for each group is summarized in Fig. 7.2 and detailed in MRI Datasets. The acquisition centers were split into two groups, that we called *in-scanner distribution* and *out-of-scanner distribution*, depending if 3D MRIs acquired at a given center were present in the training dataset or not. Four out of thirteen data sources were used for the training of the backbone AI algorithm. In addition, the 3D MRIs were also separated based on the underlying brain condition of the fetus. The first group, *neurotypical*, contains the fetuses diagnosed by radiologists with a normal brain development using ultrasound and MRI. The second group, *spina bifida*, contains the fetuses with a condition called spina bifida aperta. We use the term *spina bifida* for short in this work. Cases of spina bifida aperta are typically accompanied by severe anatomical brain abnormalities [Fidon 21e, Pollenus 20] with a type II Chiari malformation and an enlargement of the ventricles being most prevalent. The Chiari malformation type II is characterized by a small posterior fossa and hindbrain herniation in which the medulla, cerebellum, and fourth ventricle are displaced caudally into the direction of the spinal canal [Naidich 80]. The third group, *other pathologies*, contains fetuses with various pathologies other than spina

bifida and causing an abnormal brain development, such as corpus callosum agenesis and dysgenesis, intracranial hemorrhage and cyst, aqueductal stenosis, and Dandy-Walker malformation. Those other pathologies were not present in the training dataset of the backbone AI algorithm and spatio-temporal atlases are not available for the fallback and the fail-safe algorithm. Hence, the testing 3D MRIs classified as other pathologies allow us to measure the segmentation performance of the trustworthy AI algorithm outside of the domain covered by the anatomical contracts of trust.

Figures 7.6a,7.6b show the results of the overall stratified evaluation in terms of Dice score and Hausdorff distances at 95% percentile. The detailed results per region of interest can be found in the appendix (Fig. A.2,A.3).

Scoring of trustworthiness by a panel of radiologists. The Dice score and the Hausdorff distance are the two most standard metrics used for measuring the quality of automatic segmentations [Bakas 18]. However, those two metrics do not directly measure the trustworthiness of segmentation algorithms [Kofler 21b]. Therefore, we have also conducted an evaluation of the trustworthiness of the automatic segmentations as perceived by radiologists. We have asked a panel of 8 experts from 4 different hospitals to score the trustworthiness of automatic segmentations from 0 (totally unacceptable) to 5 (perfect fit) for each region of interest and for the three segmentation algorithms. Independent scoring were performed by raters at different hospitals. The scoring protocol and details about the panel of experts can be found in section Human expert scoring method for evaluating the trustworthiness of fetal brain 3D MRI segmentation. The scoring was performed for the same 3D MRIs by all radiologists. We have used a subset of 50 3D MRIs from the out-of-distribution group of the testing dataset consisting of 20 neurotypical fetuses, 20 spina bifida fetuses, and 10 fetuses with other abnormalities. Those cases were selected per condition at random among the 3D MRIs of the publicly available FeTA dataset [Payette 21]. We have chosen to restrict this analysis to fetal brain 3D MRIs from the FeTA dataset, a subset of the *out-of-scanner distribution* group, because those data are publicly available which facilitated collaborations across centers and because rating of the quality of the 3D MRIs had been performed in previous work [Payette 21]. The *out-of-scanner distribution* group is the most relevant group for the evaluation of trustworthiness because this corresponds to the situation in which AI algorithms generalization is the most challenging and clinically relevant. In addition, this allows us to share our segmentations and scores publicly, thereby improving the reproducibility of our results. The overall scoring results can be found in Fig. 7.6e and the detailed results per region of interest can

be found in the appendix (Fig. A.6).

Expert raters reported that most of the 3D MRIs were of good quality. However, they noticed that the algorithms were very dependent on the quality of the 3D MRIs they were based on for the *spina bifida* group. We found a positive correlation between the mean-class trustworthiness scores and the quality of the 3D MRI for the *spina bifida* group (Pearson $r = 0.43$). There was no correlation between scores and 3D MRI quality for the *neurotypical* group (Pearson $r = -0.1$) and the 3D MRIs of the *other pathologies* were all of high quality. The 3D MRI quality scores used to compute the correlations above were performed by the authors of the FeTA dataset [Payette 21]. In addition, the more structurally abnormal the brains were due to the pathologies, the more difficult it was to compare the algorithms. In the case of the Chiari malformations, this applies in particular to the cerebellum and brainstem.

Stratified evaluation across gestational ages. The anatomy and the size of the fetal brain change significantly from 19 weeks of gestation until term for both neurotypical fetuses [Gholipour 17] and fetuses with spina bifida [Fidon 21e]. This age-related variability is a challenge for segmentation algorithms for fetal brain MRI [Fidon 21b].

We analysed the performance of the proposed trustworthy AI algorithm for fetal brain segmentation as a function of the gestational age and compared it to the backbone AI algorithm based on deep learning [Isensee 21] and the fallback algorithm based on image registration [Cardoso 15]. We grouped the fetuses with neurotypical or spina bifida condition with the same gestational age rounded to the closest week. The mean and the confidence intervals at 95% for the overall performance in terms of Dice score (resp. Hausdorff distance) across regions of interest can be found in Fig. 7.6c (resp. Fig. 7.6d). The detailed results per region of interest can be found in the appendix (Fig. A.4,A.5).

Our results show how the backbone-AI algorithm, based on deep learning, and the fallback algorithm, based on image registration, are complementary. Overall, the backbone-AI algorithm achieves higher Dice scores than the fallback algorithm, while the fallback achieved lower Hausdorff distances than the backbone-AI method (Fig. 7.6). Our proposed trustworthy AI algorithm successfully combines the backbone AI and the fallback algorithms. It achieves higher or similar segmentation performance than those two algorithms in terms of established segmentation quality metrics such as the Dice score and the Hausdorff distance across all gestational ages for *neurotypical* and *spina bifida*. Using a Wilcoxon signed-rank test, we found that the trustworthy AI method significantly outperforms the backbone AI in terms

of both Dice score and Hausdorff distance for every group ($p < 0.05$), except for the Dice score of the in-scanner distribution *other pathologies* group for which there is no statistical difference between the trustworthy AI and AI methods. The trustworthy AI method also significantly outperforms the fallback for the two metrics for all groups, except for the Hausdorff distances of the out-of-scanner-distribution *spina bifida* group for which there is no statistical difference between the trustworthy AI and fallback methods. This result is further supported by the trustworthiness scores of expert paediatric radiologists specialized in fetal brain anatomy. The trustworthy AI method outperformed the AI and performed on a par with the fallback for the *neurotypical* and *spina bifida* groups and the trustworthy AI method outperformed the fallback and performed on a par with the AI method for the *other pathologies* group.

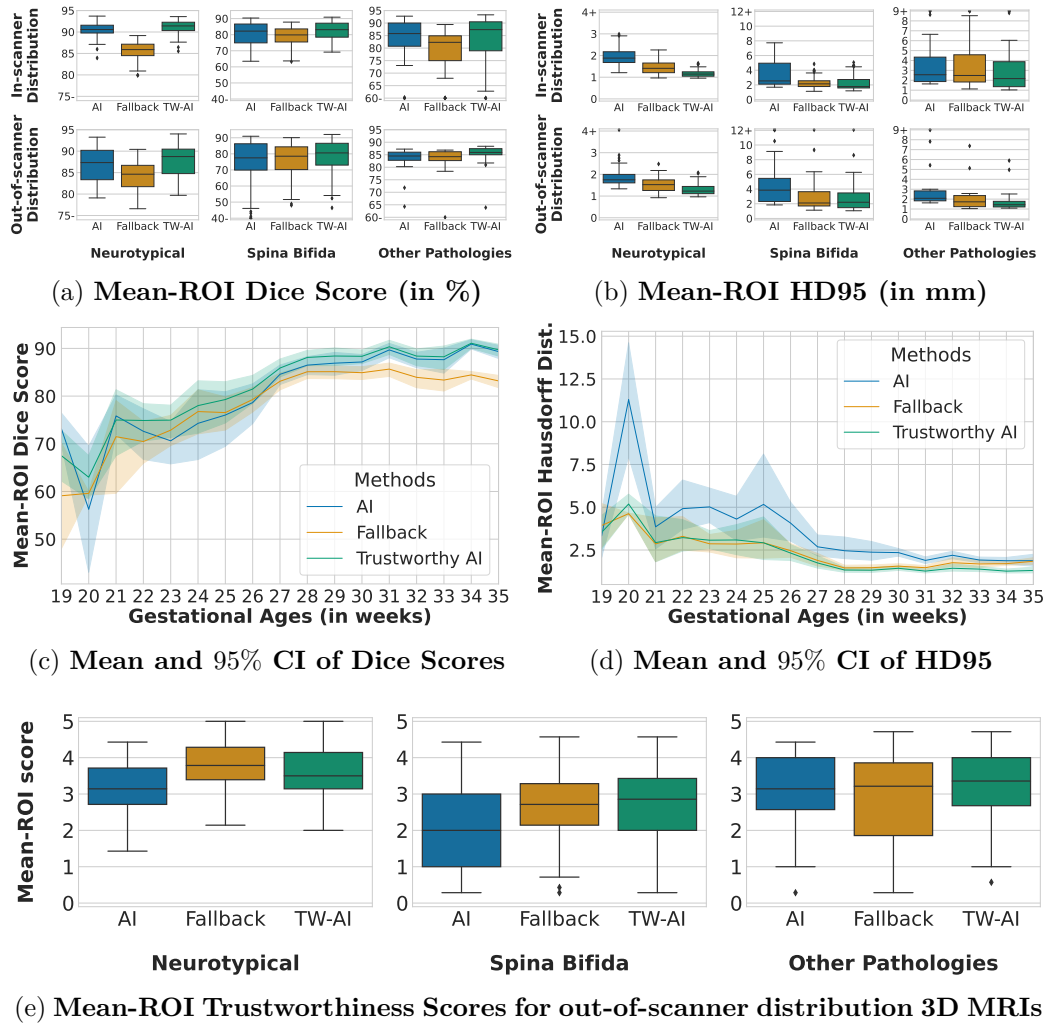


Figure 7.6: **Comparison of the backbone AI, fallback, and trustworthy AI segmentation algorithms.** In (a) (resp. (b)), we report for each algorithm the distributions of Dice scores (resp. Hausdorff distances at 95% percentile (HD95)) for in-scanner distribution ($n = 182$) and out-of-scanner distribution ($n = 167$) images and for neurotypical ($n = 141$), spina bifida ($n = 157$), and other pathologies ($n = 51$). In (c) (resp. (d)), we report mean and 95% confidence intervals for the Dice scores (resp. HD95) across gestational ages, for neurotypical and spina bifida cases. In (e), we report 4 scoring by a panel of 8 experts of the trustworthiness of the automatic segmentations for a subset of the out-of-scanner distribution testing 3D MRIs ($n = 50$). Each expert was asked to score from 0 (totally unacceptable) to 5 (perfect fit) the trustworthiness of each ROI. The scores displayed here are averaged across ROIs. Results per ROI can be found in the appendix (Fig. A.2, A.3, A.4, A.5, A.6). Box limits are the first quartiles and third quartiles. The central ticks are the median values. The whiskers extend the boxes to show the rest of the distribution, except for points that are determined to be outliers. Outliers are data points outside the range median $\pm 1.5 \times$ interquartile range.

7.5 Discussion

A principled and practical trustworthy AI method. We have mathematically formalized a method for trustworthy AI with a fallback based on Dempster-Shafer theory. For application to fetal brain MRI segmentation, we have shown that our trustworthy AI method can be implemented using anatomy-based and intensity-based priors. We have proposed to interpret those priors as contracts of trust in Human-AI trust theory. Altogether, we showed that our principled trustworthy AI method improves the robustness and the trustworthiness of a state-of-the-art AI algorithm for fetal brain 3D MRI segmentation.

AI-based and registration-based algorithms are complementary. AI-based algorithms and registration-based algorithms have different error patterns. In several situations we have found that the registration-based method tends to achieve better segmentation performance in terms of Hausdorff distance as compared to the AI-based method while the AI-based method achieved better segmentation performance in terms of Dice score. We have found that the segmentation performance of the fallback algorithm decreases less than for the backbone AI algorithm, when comparing out-of-scanner distribution to in-scanner distribution for neurotypical and spina bifida fetal brain 3D MRIs. In our scoring of trustworthiness on out-of-scanner distribution data, we have also found that the fallback algorithm outperformed the backbone AI algorithm for neurotypical and spina bifida cases (Fig. 7.6e). We think this is because the anatomical prior used by registration-based segmentation methods prevents mislabelling voxels far from the real anatomy. In contrast, AI-based methods are unconstrained and such errors can occur. This is what we observe for the out-of-distribution cases displayed in Fig. 7.1c, 7.5. Our proposed fail-safe method uses the registration-based segmentation with added margins with the aim to automatically detect and discard such errors that were found to occur more often for AI-based approach than for registration-based approach.

The contracts of trust hold for sub-populations covered by brain atlases. Our implementation of trustworthy AI for fetal brain segmentation depends on the availability of spatio-temporal segmentation atlases of the fetal brain in 3D MRI. While such atlases currently exist for neurotypical fetal brain [Gholipour 17, Wu 21] and fetuses with spina bifida [Fidon 21e], it is not the case for other fetal brain pathologies. Therefore, our contracts of trust are not expected to hold for the group *other pathologies*. This illustrates how AI trustworthiness is context-dependent. We found that the *other pathologies* group is the only one for which radiologists asso-

ciated the fallback method, based solely on the atlases, with a lower trustworthy scores than the backbone AI algorithm (Fig. 7.6e). Surprisingly, we found that the trustworthy AI algorithm still performs better or on a par with the backbone AI algorithm for the *other pathologies* group. We associate this with the use of our margins and to the proposed voxel intensity prior for the cerebrospinal fluid that are specific to the trustworthy AI algorithm. For the *other pathologies* group, we used the margin values estimated for spina bifida. Our group *other pathologies* gathers diverse rare developmental diseases associated with different variations of the fetal brain anatomy. However, due to the low number of examinations available per pathology, grouping them was necessary for evaluation purposes. This introduces biases when comparing the segmentation performance for the *other pathologies* groups associated with in-scanner and out-of-scanner distribution. In particular, some of the fetuses with *other pathologies* in the in-scanner distribution had very severe brain anatomical abnormalities, such as aqueductal stenosis with large supratentorial ventricles and caudal displacement of the cerebellum or intracranial hemorrhage with parenchymal destruction and ventriculomegaly. In contrast, the one in the out-of-scanner distribution have milder brain abnormalities, such as moderate ventriculomegaly, and there were no cases with parenchymal destruction. This explains why, for this condition, we observe more outliers with low Dice scores and high Hausdorff distances for the backbone AI algorithm for in-scanner-distribution as compared to out-of-distribution 3D MRIs (Fig. 7.6a,7.6b). This is also the only group for which the trustworthy AI method does not significantly outperform the AI method in terms of Dice score (Fig. A.2a).

The two histograms of gestational ages for the training spina bifida 3D MRIs and the in-scanner-distribution testing spina bifida 3D MRIs are not uniform and have the same shape (see Fig. 7.2). In contrast the histogram of gestational ages for the out-of-scanner-distribution testing spina bifida is more uniform. This might partly explain the degradation of Dice scores and Hausdorff distances, with the appearance of outliers, between in-scanner-distribution and out-of-scanner-distribution for the backbone AI algorithm (Fig. 7.6a,7.6b). Training and in-scanner-distribution testing spina bifida MRIs were mostly clinical data acquired at UHL. In this center, MRI of spina bifida are typically performed a few days before and after the surgery that is performed prior to 26 weeks of gestation. In addition, a follow-up MRI is sometimes performed one month after the surgery. This explains the two modes observed in the histograms for those two groups. In the training data, the use of the spina bifida atlas [Fidon 21e], that has a uniform gestational age distribution, makes the second mode less visible. Our results suggest the trustworthy AI algorithm is more robust than the AI algorithm to the gestational ages distributional

shift between training and testing.

For gestational ages lower than 27 weeks, the Dice scores and Hausdorff distances degrade for all the algorithms (Fig. 7.6c,7.6d). For the backbone AI algorithm this is surprising given that more MRIs acquired at gestational ages lower than 27 weeks than higher were present in the training dataset (Fig. 7.2). Poorer MRI quality, which is typical for younger fetuses, might explain this degradation. In addition, the ratio of spina bifida over neurotypical examinations is higher for gestational ages lower than 27 weeks in our dataset. The abnormal brain anatomy of spina bifida cases leads to more difficult segmentation compared to neurotypical cases. This is particularly the case for several classes: the cerebellum, the extra-axial cerebrospinal fluid (CSF), the cortical gray matter, and the brainstem (Fig. A.2,A.3,A.4,A.5,A.6). The cerebellum is more difficult to detect using MRI before surgery as compared to early or late after surgery [Aertsen 19, Danzer 07]. This has already been found to affect the segmentation performance of AI-based algorithms in previous work [Fidon 21b]. For neurotypical fetuses, the extra-axial CSF is present all around the cortex. However, for fetal brain MRI of spina bifida fetuses with gestational ages of 27 weeks or less this is often not the case and the extra-axial CSF might be reduced to several small connected components that do not embrace the entire cortex anymore [Fidon 21e]. We hypothesize that the spina bifida atlas does not cover well this variability of the extra-axial CSF [Fidon 21e]. Due to the explicit spatial regularization, medical image registration cannot tackle such differences of topology. Therefore, using the atlas currently available, the contract of trust for extra-axial CSF does not apply for this group of spina bifida cases. It can also influence nearby regions, such as the cortical gray matter in this case. For the fallback algorithm and the trustworthy AI algorithm, a further degradation of the segmentation performance for gestational ages lower than 21 weeks was expected because the fetal brain atlases used start at 21 weeks. For gestational ages of 21 weeks or higher, the trustworthy AI outperforms either the backbone AI-algorithm or the fallback algorithm and performs better or on a par with the best other algorithms for all regions of interest in terms of Dice score and Hausdorff distance (Fig. A.4,A.5). The confidence intervals are also similar or narrower for the trustworthy AI algorithm than for the other algorithms for gestational ages higher or equal to 21 weeks. This illustrates that our contracts of trust improve the robustness of the proposed trustworthy AI algorithm for spina bifida for the range of gestational ages covered by the atlas used [Fidon 21e].

Future work. For this work we have created the largest manually segmented fetal brain MRI dataset to date that consists of 540 fetal brain 3D MRIs from

13 acquisition centers. A recent trend in medical image processing using AI is to gather even larger multi-institutional datasets using methods such as federated learning [Rieke 20]. One can hypothesize that, with enough data, the AI algorithm would get more accurate even in the worst case until eventually reaching the same accuracy as the trustworthy AI algorithm in all cases. However, results of our stratified evaluation suggest that this will require manually annotated 3D MRIs for every scanner acquisition protocol, for every condition, and for every gestational age. To give an order of magnitude of the required dataset size, if we consider that 10 3D MRIs are required for each gestational age from 19 weeks to 38 weeks, for each of 10 conditions and each of 5 hospitals, we would already need 10,000 3D MRIs for both training and testing. Given the low prevalence of some conditions [Fidon 21b] and the cost of obtaining fully-segmented data, classical supervised learning approaches might not be sufficient. This rough estimation does not even include important confounding factors such as ethnicity and gender. Altogether, this suggests that gathering more training data to improve the AI algorithm prior to deployment might not be sufficient to make the AI algorithm alone trustworthy.

The proposed fail-safe mechanism, that is part of our trustworthy AI method, could be used to help improving the backbone AI continuously after its deployment. An AI incident could be declared when a large part of the AI algorithm prediction was discarded by the *fail-safe mechanism*. This would allow automatic detection of images to correct and include in priority in the training set to update the backbone AI algorithm. In addition, reporting such incidents could help to further improve the trust of the user. In the context of trust, it is important to report such issues even when the incidents were handled correctly using the fallback segmentation algorithm. In addition, as part of the European Union Medical Device Regulations (EU MDR) Article 87 on “Reporting of serious incidents and field safety corrective actions” [European Union 17], it is a requirement for medical device manufacturers to report device-related incidents. Previous methods for global segmentation failures detection, i.e. at the image-level, were proposed [Kofler 21a, Robinson 19]. In contrast, our fail-safe mechanism approaches the problem locally, i.e. at the voxel-level, by using an atlas-based anatomical prior and an intensity-based prior.

The margins used in our trustworthy AI segmentation algorithm for fetal brain MRI could also support interactive segmentation. Instead of providing voxel-level corrections or scribbles, the annotator could interact with the automatic segmentation by manually adapting the margins for its annotation. After manual adjustment, the voxels outside the margins are automatically marked as correctly labelled while for the voxel inside the margins will be assigned a set of possible labels. This yields partial annotations that can be exploited to improve the backbone AI method using

partially-supervised learning methods [Fidon 21a]. This use of margins is similar, in terms of user interaction, to the safety margins that are used in clinics for radiation therapy planning [Niyazi 16].

The expert raters also emphasized that some of the most frequent major violations in the cortex layer could be quickly removed manually and that they would have given higher scores to the segmentations if they could interact with them. This echoes previous work on computational-aided decision making that found that users are more satisfied with imperfect algorithms if they can interact with them [Dietvorst 18]. Our findings suggest that allowing interactions would also increase the trust of human users in AI algorithms for medical image segmentation.

Conclusion

Table of Contents

8.1 Conclusion	175
8.2 Discussion and Future Work	177
8.2.1 Semi-automatic segmentation for trustworthy AI	177
8.2.2 Future work on fetal brain segmentation	178
8.2.3 Impact of the fetal brain MRI segmentation algorithm developed in this thesis	179

8.1 Conclusion

Throughout this thesis, it has been shown that current state-of-the-art deep learning methods are not trustworthy. In **Chapter 5** and **Chapter 7** we show that a state-of-the-art deep learning pipeline for fetal brain MRI segmentation can fail spectacularly on MRIs of fetuses with an abnormal brain and/or on MRIs acquired in a different hospital as the MRIs used for training. In **Chapter 5**, we found that state-of-the-art deep learning pipelines for fetal brain MRI segmentation and brain tumor segmentation using multi-parametric MRI under-perform on subpopulations that are underrepresented in the training dataset. In the case of fetal brain MRI segmentation, the quantification of this problem was only possible thanks to the multi-center fetal brain MRI dataset created in **Chapter 3** and that contains the highest number of brain MRIs of fetuses with normal and abnormal brain developments reported to date.

Novel deep learning methods have been proposed in this thesis to tackle this problem. In **Chapter 4**, a method has been proposed to train deep neural networks using partially segmented images. We have shown empirically that it allows to train deep neural networks for fetal brain MRI segmentation with order of magnitude more MRIs. It has been observed that training with more data, even partially segmented, leads to improved segmentation accuracy and robustness. In **Chapter 5**, a new optimization problem and optimizer for training deep learning is proposed. In practice, the new method makes the deep neural network learn more on the training

images seen as *hard samples* during the training process. We show that for fetal brain MRI segmentation, the proposed optimization leads to deep neural network with an improved worst-case testing performance corresponding to brain MRI of subpopulations of fetuses with abnormal development that were underrepresented in the training dataset. However, as expected, no improvement was observed for subpopulations of fetuses that were not represented at all in the training dataset. In **Chapter 7**, we propose a practical implementation of trustworthy AI for fetal brain MRI segmentation. Our approach combines deep learning-based and atlas-based segmentation methods. Our experiments show that the proposed method can successfully detect and correct violations of the anatomy in the segmentation prediction of a state-of-the-art deep learning pipeline for fetal brain MRI. We measured an improved robustness on MRIs acquired in a different hospital as the MRIs used for training and/or MRIs of fetuses with an abnormal brain when the normal or abnormal subpopulations is one of those covered by an existing fetal brain atlas. Therefore, the fetal brain atlas for spina bifida aperta proposed in **Chapter 6** can be used to improve the trustworthiness of deep learning-based methods for the segmentation of brain MRIs of fetuses with spina bifida aperta.

This thesis also presents several theoretical contributions. In **Chapter 4** an axiomatic construction of the set of loss functions that should be used when using partially segmented images for training a deep neural network has been proposed. We propose the name *label-set loss functions* for this family of loss functions because they rely on the interpretation of partial segmentation as images segmented using set of labels instead of labels as voxel-level annotation. We proved a necessary and sufficient condition for a loss function to satisfy the axiom of label-set loss functions. We propose the leaf-Dice loss and proved that it is a label-set loss function. Last but not least, we propose a method to convert any existing loss function for fully-supervised learning into a label-set loss function and prove a unicity result regarding the proposed conversion method. Therefore, there is an infinity of possible label-set loss functions. In **Chapter 5**, we propose an adaptive sampling strategy that can be used during the training of a deep neural network with any optimizer based on stochastic gradient descent (SGD). We call this sampling strategy *harness weighted sampling* because it samples more often those samples, seen as *hard samples*, that were found to lead to a higher value of the loss function previously during training. For overparameterized deep neural network trained using SGD, we formally proved that using our hardness weighted sampling corresponds to solve a distributionally robust optimization (DRO) problem instead of the classic empirical risk minimization problem. In addition, we formally link the proposed hardness weighted sampling with hard example mining and we studied the link

between DRO and the minimization of percentiles of the loss function on the training dataset. In **Chapter 6**, it has been proved that sparse linear constraints on the parameters of divergence-conforming B-Splines stationary velocity fields (SVFs) lead to being exactly divergence-free at any point of the continuous spatial domain. When using divergence-conforming B-splines SVFs for incompressible registration this results in velocity fields that are exactly divergence-free and we proved a bound on the numerical incompressibility error for the transformation in the case of an Euler integration. In **Chapter 7**, we propose a principled implementation of trustworthy AI with a fallback and a fail-safe mechanism using Dempster-Shafer (DS) theory. We theoretically show how Dempster’s rule of combination allows to automatically switch from the AI to the fallback when the AI segmentation prediction violate anatomical priors. A compact and computationally-efficient formula for our proposed implementation of trustworthy AI for fetal brain MRI is also proved.

8.2 Discussion and Future Work

The methods proposed in this thesis were found to improve the trustworthiness of deep learning methods applied to fetal brain MRI segmentation. However, the proposed methods remain insufficient to guarantee robustness and safety of deep learning-based methods in every case. It is therefore hypothesized that further theoretical contributions in the field of trustworthy AI is needed.

8.2.1 Semi-automatic segmentation for trustworthy AI

Semi-automatic segmentation methods are promising for improving the trustworthiness of segmentation methods. In **Chapter 7**, some of the experts conducting the trustworthiness scoring of the segmentations stressed that they would have given a higher scores to some segmentation if they were able to correct them manually even slightly. In interactive segmentation, experts are allowed to partially correct automatic segmentations to improve them. Experts interactions are typically partial to limit the interaction time required. As result, only a small fraction of the voxels are annotated by the expert in this context. This suggests the label-set loss functions proposed in **Chapter 4** could be extended for this purpose. Indeed, label-set loss functions allow to model unannotated voxels by assigning them a set of classes. If no information has been given about a voxel, it corresponds to assigning the set of all classes to this voxel.

Label-set loss functions also allow to model voxels marked as *error* by the annotator. In this case, the set of all classes except the class predicted and marked as

incorrect is assigned to this voxel.

One major difference between training with a fixed training set and training in an interactive segmentation framework is the fact that for the latter the manual annotations are related to an automatic segmentation. There are therefore two sources of information to learn from: the annotations of the expert and the automatic segmentation that has been corrected. Since, in essence, Dempster-Shafer theory aims at combining information potentially partial but certain and coming from different sources in a safe manner, it appears as a promising mathematical theory for interactive segmentation. The margins used in our Dempster-Shafer approach trustworthy AI segmentation algorithm could also support interactive segmentation. Instead of providing voxel-level corrections or scribbles, the annotator could interact with the automatic segmentation by manually adapting the margins for its annotation. After manual adjustment, the voxels outside the margins are automatically marked as correctly labelled while for the voxel inside the margins will be assigned a set of possible labels. This yields partial annotations that can be exploited to improve the backbone AI method using partially-supervised learning methods such as the label-set loss functions. This use of margins is similar, in terms of user interaction, to the safety margins that are used in clinics for radiation therapy planning [Niyazi 16]. In addition, domain knowledge, such as the one used in **Chapter 7**, could be used in conjunction with expert interactions to make the best of every interactions using Dempster-Shafer theory.

8.2.2 Future work on fetal brain segmentation

Regarding fetal brain MRI segmentation specifically, the reconstructed 3D MRIs used in this thesis are the result of a super-resolution and reconstruction (SRR) post-processing of the 2D MRI slices coming directly from the scanner. Therefore, one can hypothesize that information lost during this post-processing may be useful to achieving more trustworthy segmentations and segmenting the fetal brain directly in the 2D MRI slices could be beneficial. It is however worth noting that SRR algorithms also do provide an important piece of information not present in the 2D MRI slices taken independently: the spatial mapping between the 2D MRI slices and the reconstructed 3D MRI that reflects the non-trivial spatial correspondence between the slices and between the stacks. In this sense, the output of a SRR algorithm is better represented by the pair of the input 2D MRI slices and the output spatial transformations than by the output reconstructed 3D MRI. The 2D MRI slices and spatial transformations are complementary information whose corresponding reconstructed 3D MRI is only a summary that is useful for visualization

and for volumetric and shape analysis.

Combining segmentations in the 2D MRI slices and in the reconstructed 3D MRI is also a promising avenue of research. In this context, the spatial transformation computed by the SRR algorithm can be used as an interface between segmentations in the 2D MRI slices and a segmentation in the corresponding reconstructed 3D MRI. The same way the intensity of voxels in the 3D reconstructed MRI are interpolation of voxels intensity in different 2D MRI slices, the same interpolation can be used to combine the segmentations in the different 2D MRI slices into a combined segmentation of the reconstructed 3D MRI. This process is already used to compute 3D brain masks in NiftyMIC [Ebner 20]. Conversely, the spatial transformations computed by the SRR can be used to propagate segmentation in the reconstructed 3D MRI back to the 2D MRI slices. We hypothesize that the manual segmentation of fetal brain MRI is easier and more accurate when performed using the reconstructed 3D MRI. Therefore, it may be beneficial to perform the manual segmentation of the 2D MRI slices by segmenting manually in the reconstructed 3D MRI. In contrast to the 2D MRI slices, reconstructed 3D MRI can always be registered to a standard clinical view where the axial, sagittal, and coronal planes are aligned with the axis of the image. In addition, the reconstructed 3D MRIs have less image artefacts and it offers the annotator the possibility to using the three planes for the annotation task.

8.2.3 Impact of the fetal brain MRI segmentation algorithm developed in this thesis

The impact of the methods for trustworthy fetal brain T2w MRI segmentation developed in this thesis remains to be fully demonstrated. Recent advances in fetal neuroimaging have permitted more in-depth analysis of the normal fetal brain development but the challenging application of advanced fetal neuroimaging under pathological conditions is still in its infancy. Some cases of congenital brain defects can be prevented, while the severity of others can be reduced by prenatal interventions including fetal surgery. Anticipation of the potential long-term outcomes is also critical for parental counselling in these pathologies. We expect trustworthy fetal brain MRI segmentation to play a critical role in these applications where quantitative volumetric and shape analysis are currently not fully exploited. Encouraging preliminary results have already been obtained using the segmentation methods developed in this thesis. In [Mufti 21, Mufti 23], a segmentation algorithm based on **Chapter 5** and **Chapter 7** has been used to study cerebral volume, shape and cortical folding quantitatively for fetuses with spina bi-

fidia aperta as compared to fetuses with a normal brain development. In [Emam 23], a segmentation algorithm based on **Chapter 4** and **Chapter 5** has allowed the quantitative analysis of the intra-axial and extra-axial cerebrospinal fluid spaces and to compute the local gyrification index for a population of fetuses with isolated congenital diaphragmatic hernia (CDH) and a population of fetuses with a normal brain development. It has been found that longitudinal brain development on MRI in CDH fetuses is significantly altered compared to normal controls in the third trimester. This is one of the first evidence that fetuses with CDH have an abnormal prenatal brain development. In [Depest 23], a segmentation algorithm based on **Chapter 5** has been tested on brain 3D MRIs of fetuses with severe brain anatomical abnormalities. Segmentation errors were analyzed in detail from a clinical point of view. Those results guided us for creating the dataset described in **Chapter 3** and to develop the trustworthy AI method described in **Chapter 7**. To further accelerate discoveries, we have made publicly available a software for automatic fetal brain T2w MRI segmentation at <https://github.com/LucasFidon/trustworthy-ai-fetal-brain-segmentation>. With a unique command line, the software makes it possible to compute automatic segmentation with a backbone state-of-the-art deep learning pipeline trained using the entire dataset described in **Chapter 3** and the distributionally robust optimization method described in **Chapter 5**. The full software pipeline also includes the method for trustworthy AI described in **Chapter 7** on top of the backbone deep learning pipeline. This software will need to be tested to establish its segmentation accuracy and its limitations.

Bibliography

- [Adzick 11] N Scott Adzick, Elizabeth A Thom, Catherine Y Spong, John W Brock III, Pamela K Burrows, Mark P Johnson, Lori J Howell, Jody A Farrell, Mary E Dabrowiak, Leslie N Sutton *et al.* *A randomized trial of prenatal versus postnatal repair of myelomeningocele.* New England Journal of Medicine, volume 364, number 11, pages 993–1004, 2011. 50, 51, 220
- [Aertsen 19] M Aertsen, J Verduyckt, F De Keyzer, T Vercauteren, F Van Calenbergh, L De Catte, S Dymarkowski, P Demaerel and J Deprest. *Reliability of MR imaging-based posterior fossa and brain stem measurements in open spinal dysraphism in the era of fetal surgery.* American Journal of Neuroradiology, volume 40, number 1, pages 191–198, 2019. 40, 49, 50, 51, 65, 82, 103, 104, 117, 118, 135, 171, 220
- [Alansary 17] Amir Alansary, Martin Rajchl, Steven G McDonagh, Maria Murgasova, Mellisa Damodaram, David FA Lloyd, Alice Davidson, Mary Rutherford, Joseph V Hajnal, Daniel Rueckert *et al.* *Pvr: Patch-to-volume reconstruction for large area motion correction of fetal mri.* IEEE transactions on medical imaging, volume 36, number 10, page 2031, 2017. 52
- [Alis 21] Deniz Alis, Mert Yergin, Ceren Alis, Cagdas Topel, Ozan Asmakutlu, Omer Bagcilar, Yeseren Deniz Senli, Ahmet Ustundag, Vefa Salt, Sebahat Nacar Dogan *et al.* *Inter-vendor performance of deep learning in segmenting acute ischemic lesions on diffusion-weighted imaging: a multicenter study.* Scientific reports, volume 11, number 1, pages 1–10, 2021. 164
- [Allen-Zhu 19a] Zeyuan Allen-Zhu, Yuanzhi Li and Zhao Song. *A convergence theory for deep learning via over-*

- parameterization*. In ICML, pages 242–252, 2019. 84, 93, 108, 227, 237, 238, 239, 242, 243, 244, 245, 248, 249, 254
- [Allen-Zhu 19b] Zeyuan Allen-Zhu, Yuanzhi Li and Zhao Song. *On the convergence rate of training recurrent neural networks*. In Advances in Neural Information Processing Systems 32, pages 6676–6688. Curran Associates, Inc., 2019. 84, 237
- [Allen 21] Bibb Allen, Sheela Agarwal, Laura Coombs, Christoph Wald and Keith Dreyer. *2020 ACR data science institute artificial intelligence survey*. Journal of the American College of Radiology, volume 18, number 8, pages 1153–1159, 2021. 33
- [Andres 20] Emilie Alvarez Andres, Lucas Fidon, Maria Vakalopoulou, Marvin Lrousseau, Alexandre Carré, Roger Sun, Guillaume Klausner, Samy Ammari, Nathan Benzazon, Sylvain Reuzéet al. *Dosimetry-driven quality measure of brain pseudo computed tomography generated from deep learning for mri-only radiation therapy treatment planning*. International Journal of Radiation Oncology* Biology* Physics, volume 108, number 3, pages 813–823, 2020. 142
- [Asad 22] Muhammad Asad, Lucas Fidon and Tom Vercauteren. *ECONet: Efficient convolutional online likelihood network for scribble-based interactive segmentation*. In Medical Imaging with Deep Learning. PMLR, 2022.
- [Ashburner 07] J Ashburner and KJ Friston. *Non-linear registration. Statistical parametric mapping: The analysis of functional brain images*, pages 63–80, 2007. 121, 122
- [Bahmani 22] Sherwin Bahmani, Oliver Hahn, Eduard Zamfir, Nikita Araslanov, Daniel Cremers and Stefan Roth. *Semantic self-adaptation: Enhancing generalization with a single sample*. arXiv preprint arXiv:2208.05788, 2022. 38, 39
- [Baid 21] Ujjwal Baid, Satyam Ghodasara, Michel Bilello, Suyash Mohan, Evan Calabrese, Errol Colak, Keyvan Fara-

- hani, Jayashree Kalpathy-Cramer, Felipe C Kitamura, Sarthak Patiet *al.* *The rsna-asnr-miccai brats 2021 benchmark on brain tumor segmentation and radiogenomic classification.* arXiv preprint arXiv:2107.02314, 2021. 71
- [Bakas 17a] Spyridon Bakas, Hamed Akbari, Aristeidis Sotiras, Michel Bilello, Martin Rozycki, Justin S Kirby, John B Freymann, Keyvan Farahani and Christos Davatzikos. *Advancing the cancer genome atlas glioma MRI collections with expert segmentation labels and radiomic features.* Scientific data, volume 4, page 170117, 2017. 71, 99
- [Bakas 17b] Spyridon Bakas, Hamed Akbari, Aristeidis Sotiras, Michel Bilello, Martin Rozycki, Justin S Kirby, John B Freymann, Keyvan Farahani and Christos Davatzikos. *Segmentation labels and radiomic features for the pre-operative scans of the TCGA-GBM collection.* The Cancer Imaging Archive, 2017. 71, 98
- [Bakas 17c] Spyridon Bakas, Hamed Akbari, Aristeidis Sotiras, Michel Bilello, Martin Rozycki, Justin S Kirby, John B Freymann, Keyvan Farahani and Christos Davatzikos. *Segmentation labels and radiomic features for the pre-operative scans of the TCGA-LGG collection.* The Cancer Imaging Archive, 2017. 71, 98
- [Bakas 18] Spyridon Bakas, Mauricio Reyes, Andras Jakab, Stefan Bauer, Markus Rempfler, Alessandro Crimi, Russell Takeshi Shinohara, Christoph Berger, Sung Min Ha, Martin Rozyckiet *al.* *Identifying the best machine learning algorithms for brain tumor segmentation, progression assessment, and overall survival prediction in the brats challenge.* arXiv preprint arXiv:1811.02629, 2018. 32, 33, 71, 83, 86, 99, 101, 106, 109, 165
- [Bayer 05] Shirley A Bayer and Joseph Altman. The human brain during the second trimester. CRC Press, 2005. 42

- [Benkarim 17] Oualid M Benkarim, Gerard Sanroma, Veronika A Zimmer, Emma Muñoz-Moreno, Nadine Hahner, Elisenda Eixarch, Oscar Camara, Miguel Angel Gonzalez Ballester and Gemma Piella. *Toward the automatic quantification of in utero brain development in 3D structural MRI: A review*. Human brain mapping, volume 38, number 5, pages 2772–2787, 2017. 40, 50, 51, 65
- [Berger 18] Lorenz Berger, Hyde Eoin, M Jorge Cardoso and Sébastien Ourselin. *An adaptive sampling scheme to efficiently train fully convolutional networks for semantic segmentation*. In Annual Conference on Medical Image Understanding and Analysis, pages 277–286. Springer, 2018. 83, 94
- [Bône 20] Alexandre Bône, Paul Vernhet, Olivier Colliot and Stanley Durrleman. *Learning joint shape and appearance representations with metamorphic auto-encoders*. In International Conference on Medical Image Computing and Computer-Assisted Intervention, pages 202–211. Springer, 2020. 137
- [Bottou 18] Léon Bottou, Frank E Curtis and Jorge Nocedal. *Optimization methods for large-scale machine learning*. Siam, 2018. 87
- [Bourbaki 04] Nicolas Bourbaki. *Theory of sets*. In Theory of Sets, pages 65–129. Springer, 2004. 67
- [Byrd 19] Jonathon Byrd and Zachary Lipton. *What is the effect of importance weighting in deep learning?* In ICML, pages 872–881, 2019. 87
- [Cabitza 19] Federico Cabitza. *Biases affecting human decision making in AI-supported second opinion settings*. In International Conference on Modeling Decisions for Artificial Intelligence, pages 283–294. Springer, 2019. 33
- [Cachier 03] Pascal Cachier, Eric Bardinet, Didier Dormont, Xavier Pennec and Nicholas Ayache. *Iconic feature based non-*

- rigid registration: the pasha algorithm*. Computer vision and image understanding, volume 89, number 2-3, pages 272–298, 2003. 122
- [Cao 20] Yuan Cao and Quanquan Gu. *Generalization error bounds of gradient descent for learning overparameterized deep relu networks*. In AAAI, 2020. 84
- [Cardoso 15] M Jorge Cardoso, Marc Modat, Robin Wolz, Andrew Melbourne, David Cash, Daniel Rueckert and Sebastien Ourselin. *Geodesic information flows: spatially-variant graphs and their application to segmentation and fusion*. IEEE transactions on medical imaging, volume 34, number 9, pages 1976–1988, 2015. 39, 141, 152, 159, 160, 164, 166
- [Chandra 18] Siddhartha Chandra, Maria Vakalopoulou, Lucas Fidon, Enzo Battistella, Théo Estienne, Roger Sun, Charlotte Robert, Eric Deutsch and Nikos Paragios. *Context aware 3D CNNs for brain tumor segmentation*. In International MICCAI Brainlesion Workshop, pages 299–310. Springer, 2018. 32
- [Chang 17] Haw-Shiuan Chang, Erik Learned-Miller and Andrew McCallum. *Active bias: Training more accurate neural networks by emphasizing high variance samples*. In Advances in Neural Information Processing Systems, pages 1002–1012, 2017. 83
- [Chapelle 00] Olivier Chapelle, Jason Weston, Léon Bottou and Vladimir Vapnik. *Vicinal risk minimization*. Advances in neural information processing systems, volume 13, 2000. 31, 88
- [Chen 21] Jieneng Chen, Yongyi Lu, Qihang Yu, Xiangde Luo, Ehsan Adeli, Yan Wang, Le Lu, Alan L Yuille and Yuyin Zhou. *Transunet: Transformers make strong encoders for medical image segmentation*. arXiv preprint arXiv:2102.04306, 2021. 32
- [Chernoff 52] Herman Chernoff *et al.* *A measure of asymptotic efficiency for tests of a hypothesis based on the sum of*

- observations*. The Annals of Mathematical Statistics, volume 23, number 4, pages 493–507, 1952. 94
- [Choi 21] Sungha Choi, Sanghun Jung, Huiwon Yun, Joanne T Kim, Seungryong Kim and Jaegul Choo. *Robustnet: Improving domain generalization in urban-scene segmentation via instance selective whitening*. In Proceedings of the IEEE/CVF Conference on Computer Vision and Pattern Recognition, pages 11580–11590, 2021. 39
- [Chouzenoux 19] Emilie Chouzenoux, Henri Gérard and Jean-Christophe Pesquet. *General risk measures for robust machine learning*. Foundations of Data Science, volume 1, page 249, 2019. 83, 86
- [Çiçek 16] Özgün Çiçek, Ahmed Abdulkadir, Soeren S Lienkamp, Thomas Brox and Olaf Ronneberger. *3d u-net: learning dense volumetric segmentation from sparse annotation*. In International conference on medical image computing and computer-assisted intervention, pages 424–432. Springer, 2016. 32, 34, 45, 58, 72, 100, 158
- [Crawley 14] Jennifer T Crawley, Khader Hasan, H Julia Hannay, Maureen Dennis, Catherine Jockell and Jack M Fletcher. *Structure, integrity, and function of the hypoplastic corpus callosum in spina bifida myelomeningocele*. Brain connectivity, volume 4, number 8, pages 608–618, 2014. 51
- [Csiszár 04] Imre Csiszár, Paul C Shields *et al.* *Information theory and statistics: A tutorial*. Foundations and Trends® in Communications and Information Theory, volume 1, number 4, pages 417–528, 2004. 86
- [Dalca 19] Adrian Dalca, Marianne Rakic, John Guttag and Mert Sabuncu. *Learning conditional deformable templates with convolutional networks*. Advances in neural information processing systems, volume 32, 2019. 137
- [Danzer 07] Enrico Danzer, Mark P Johnson, Michael Bebbington, Erin M Simon, R Douglas Wilson, Larrissa T Bilaniuk,

- Leslie N Sutton and N Scott Adzick. *Fetal head biometry assessed by fetal magnetic resonance imaging following in utero myelomeningocele repair*. Fetal diagnosis and therapy, volume 22, number 1, pages 1–6, 2007. 104, 171
- [Danzer 20] Enrico Danzer, Luc Joyeux, Alan W Flake and Jan Deprest. *Fetal surgical intervention for myelomeningocele: lessons learned, outcomes, and future implications*. Developmental Medicine & Child Neurology, volume 62, number 4, pages 417–425, 2020. 50, 51, 65, 103, 112, 113, 118
- [Davis 10] Brad C Davis, P Thomas Fletcher, Elizabeth Bullitt and Sarang Joshi. *Population shape regression from random design data*. International journal of computer vision, volume 90, number 2, pages 255–266, 2010. 41
- [Dennis 16] Maureen Dennis, Paul T Cirino, Nevena Simic, Jenifer Juranek, W Pat Taylor and Jack M Fletcher. *White and grey matter relations to simple, choice, and cognitive reaction time in spina bifida*. Brain imaging and behavior, volume 10, number 1, pages 238–251, 2016. 51
- [Deprest 23] T Deprest, L Fidon, F De Keyzer, M Ebner, J Deprest, P Demaerel, L De Catte, T Vercauteren, S Ourselin, S Dymarkowski et al. *Application of automatic segmentation on super-resolution reconstruction MR images of the abnormal fetal brain*. American Journal of Neuroradiology, volume 44, number 4, pages 486–491, 2023. 180
- [Dey 21] Neel Dey, Mengwei Ren, Adrian V Dalca and Guido Gerig. *Generative adversarial registration for improved conditional deformable templates*. In Proceedings of the IEEE/CVF International Conference on Computer Vision, pages 3929–3941, 2021. 137

- [Dice 45] Lee R Dice. *Measures of the amount of ecologic association between species*. Ecology, volume 26, number 3, pages 297–302, 1945. 101, 133
- [Dietvorst 18] Berkeley J Dietvorst, Joseph P Simmons and Cade Massey. *Overcoming algorithm aversion: People will use imperfect algorithms if they can (even slightly) modify them*. Management Science, volume 64, number 3, pages 1155–1170, 2018. 173
- [Dittrich 11] Eva Dittrich, Tammy Riklin-Raviv, Gregor Kasprian, Peter C Brugger, Daniela Prayer and Georg Langs. *Learning a spatio-temporal latent atlas for fetal brain segmentation*. In Proceedings of the MICCAI 2011 Workshop on Image Analysis of Human Brain Development (IAHBD 2011), 2011. 113
- [Dittrich 14] Eva Dittrich, Tammy Riklin Raviv, Gregor Kasprian, René Donner, Peter C Brugger, Daniela Prayer and Georg Langs. *A spatio-temporal latent atlas for semi-supervised learning of fetal brain segmentations and morphological age estimation*. Medical image analysis, volume 18, number 1, pages 9–21, 2014. 42, 112, 113
- [Dmitriev 19] Konstantin Dmitriev and Arie E Kaufman. *Learning multi-class segmentations from single-class datasets*. In Proceedings of the IEEE/CVF Conference on Computer Vision and Pattern Recognition, pages 9501–9511, 2019. 66, 68
- [Dorent 21] Reuben Dorent, Thomas Booth, Wenqi Li, Carole H Sudre, Sina Kafiabadi, Jorge Cardoso, Sebastien Ourselin and Tom Vercauteren. *Learning joint segmentation of tissues and brain lesions from task-specific hetero-modal domain-shifted datasets*. Medical Image Analysis, volume 67, page 101862, 2021. 66, 68
- [Doyle 10] Arthur Conan Doyle. The sign of four. Broadview Press, 2010. 150
- [Dubois 14] Jessica Dubois, Ghislaine Dehaene-Lambertz, S Kulikova, Cyril Poupon, Petra S Hüppi and Lucie Hertz-

- Pannier. *The early development of brain white matter: a review of imaging studies in fetuses, newborns and infants*. neuroscience, volume 276, pages 48–71, 2014. 40
- [Duchi 16] John Duchi, Peter Glynn and Hongseok Namkoong. *Statistics of robust optimization: A generalized empirical likelihood approach*. arXiv preprint arXiv:1610.03425, 2016. 83, 86
- [Ebner 19] Michael Ebner. *Volumetric mri reconstruction from 2d slices in the presence of motion*. PhD thesis, UCL (University College London), 2019. 52
- [Ebner 20] Michael Ebner, Guotai Wang, Wenqi Li, Michael Aertsen, Premal A Patel, Rosalind Aughwane, Andrew Melbourne, Tom Doel, Steven Dymarkowski, Paolo De Coppi *et al.* *An automated framework for localization, segmentation and super-resolution reconstruction of fetal brain MRI*. NeuroImage, volume 206, page 116324, 2020. 48, 49, 52, 56, 62, 116, 137, 158, 179
- [Eisenmann 22] Matthias Eisenmann, Annika Reinke, Vivienn Weru, Minu Dietlinde Tizabi, Fabian Isensee, Tim J Adler, Patrick Godau, Veronika Cheplygina, Michal Kozubek, Sharib Aliet *et al.* *Biomedical image analysis competitions: The state of current participation practice*. arXiv preprint arXiv:2212.08568, 2022.
- [Emam 23] D Emam, M Aertsen, L Van der Veeken, L Fidon, P Patkee, V Kyriakopoulou, L De Catte, F Russo, P Demaerel, T Vercauteren *et al.* *Longitudinal MRI evaluation of brain development in fetuses with congenital diaphragmatic hernia around the time of fetal endotracheal occlusion*. American Journal of Neuroradiology, 2023. 99, 180
- [Engle 04] William A Engle. *Age terminology during the perinatal period*. Pediatrics, volume 114, number 5, pages 1362–1364, 2004. 221

- [EU Commission 19] EU Commission. *Ethics guidelines for trustworthy AI*. Report, European Commission, 2019. 33, 34, 38, 83, 140, 141
- [EU Commission 21] EU Commission. *Proposal for a regulation of the european parliament and of the council laying down harmonised rules on artificial intelligence (artificial intelligence act) and amending certain union legislative acts com/2021/206 final*. Report, European Commission, 2021. 33, 140
- [European Union 17] European Union. *The European Union Medical Device Regulation – Regulation (EU) 2017/745 (EU MDR)*. Regulation, European Union, 2017. 172
- [Evans 12] Alan C Evans, Andrew L Janke, D Louis Collins and Sylvain Baillet. *Brain templates and atlases*. Neuroimage, volume 62, number 2, pages 911–922, 2012. 112
- [Fang 20] Xi Fang and Pingkun Yan. *Multi-organ segmentation over partially labeled datasets with multi-scale feature abstraction*. IEEE Transactions on Medical Imaging, volume 39, number 11, pages 3619–3629, 2020. 66, 68, 70, 76
- [Fenchel 49] Werner Fenchel. *On conjugate convex functions*. Canadian Journal of Mathematics, volume 1, number 1, pages 73–77, 1949. 89
- [Fetit 20] Ahmed E Fetit, Amir Alansary, Lucilio Cordero-Grande, John Cupitt, Alice B Davidson, A David Edwards, Joseph V Hajnal, Emer Hughes, Konstantinos Kamnitsas, Vanessa Kyriakopoulou *et al.* *A deep learning approach to segmentation of the developing cortex in fetal brain mri with minimal manual labeling*. In Medical Imaging with Deep Learning, pages 241–261. PMLR, 2020. 45, 65, 163
- [Fidon 17a] Lucas Fidon, Wenqi Li, Luis C Garcia-Peraza-Herrera, Jinendra Ekanayake, Neil Kitchen, Sébastien Ourselin and Tom Vercauteren. *Generalised Wasserstein Dice*

- score for imbalanced multi-class segmentation using holistic convolutional networks.* In International MICCAI Brainlesion Workshop, pages 64–76. Springer, 2017. 32, 68, 70, 73, 101, 133
- [Fidon 17b] Lucas Fidon, Wenqi Li, Luis C Garcia-Peraza-Herrera, Jinendra Ekanayake, Neil Kitchen, Sebastien Ourselin and Tom Vercauteren. *Scalable multimodal convolutional networks for brain tumour segmentation.* In International Conference on Medical Image Computing and Computer-Assisted Intervention, pages 285–293. Springer, 2017. 32
- [Fidon 19] Lucas Fidon, Michael Ebner, Luis C Garcia-Peraza-Herrera, Marc Modat, Sébastien Ourselin and Tom Vercauteren. *Incompressible image registration using divergence-conforming B-splines.* In International Conference on Medical Image Computing and Computer-Assisted Intervention, pages 438–446. Springer, 2019. 152
- [Fidon 20] Lucas Fidon, Sébastien Ourselin and Tom Vercauteren. *Generalized Wasserstein Dice score, distributionally robust deep learning, and ranger for brain tumor segmentation: Brats 2020 challenge.* In International MICCAI Brainlesion Workshop, pages 200–214. Springer, 2020. 29
- [Fidon 21a] Lucas Fidon, Michael Aertsen, Doaa Emam, Nada Mufti, Frédéric Guffens, Thomas Deprest, Philippe Demaerel, Anna L David, Andrew Melbourne, Sébastien Ourselin *et al.* *Label-set loss functions for partial supervision: application to fetal brain 3D MRI parcellation.* In International Conference on Medical Image Computing and Computer-Assisted Intervention, pages 647–657. Springer, 2021. 45, 65, 99, 163, 173
- [Fidon 21b] Lucas Fidon, Michael Aertsen, Nada Mufti, Thomas Deprest, Doaa Emam, Frédéric Guffens, Ernst Schwartz, Michael Ebner, Daniela Prayer, Gregor

- Kasprianet *al.* *Distributionally robust segmentation of abnormal fetal brain 3D MRI*. In *Uncertainty for Safe Utilization of Machine Learning in Medical Imaging, and Perinatal Imaging, Placental and Preterm Image Analysis*, pages 263–273. Springer, 2021. 29, 33, 59, 62, 82, 84, 142, 164, 166, 171, 172
- [Fidon 21c] Lucas Fidon, Michael Aertsen, Suprosanna Shit, Philippe Demaerel, Sébastien Ourselin, Jan Deprest and Tom Vercauteren. *Partial supervision for the FeTA challenge 2021*. In *Uncertainty for Safe Utilization of Machine Learning in Medical Imaging, and Perinatal Imaging, Placental and Preterm Image Analysis*. Springer, 2021. 45, 59, 62, 123, 137, 158, 163
- [Fidon 21d] Lucas Fidon, Suprosanna Shit, Ivan Ezhov, Johannes C Paetzold, Sébastien Ourselin and Tom Vercauteren. *Generalized Wasserstein Dice loss, test-time augmentation, and transformers for the BraTS 2021 challenge*. In *International MICCAI Brainlesion Workshop*. Springer, 2021. 32, 73
- [Fidon 21e] Lucas Fidon, Elizabeth Viola, Nada Mufti, Anna David, Andrew Melbourne, Philippe Demaerel, Sébastien Ourselin, Tom Vercauteren, Jan Deprest and Michael Aertsen. *A spatio-temporal atlas of the developing fetal brain with spina bifida aperta*. *Open Research Europe*, volume 1, number 123, 2021. 19, 42, 43, 54, 59, 62, 71, 99, 112, 152, 158, 159, 160, 164, 166, 169, 170, 171, 263
- [Fidon 21f] Lucas Fidon, Elizabeth Viola, Nada Mufti, Anna David, Andrew Melbourne, Philippe Demaerel, Sébastien Ourselin, Tom Vercauteren, Jan Deprest and Michael Aertsen. *Spina Bifida Aperta Spatio-temporal Brain MRI Atlas*, July 2021. 133, 135, 136
- [Fidon 22a] Lucas Fidon, Michael Aertsen, Florian Kofler, Andrea Bink, Anna L David, Thomas Deprest, Doaa Emam, Fr Guffens, András Jakab, Gregor Kasprianet *al.* *A*

- Dempster-Shafer approach to trustworthy AI with application to fetal brain MRI segmentation.* arXiv preprint arXiv:2204.02779, 2022. 29, 46, 140
- [Fidon 22b] Lucas Fidon, Michael Aertsen, Nada Mufti, Thomas Deprest, Doaa Emam, Frédéric Guffens, Ernst Schwartz, Michael Ebner, Daniela Prayer, Gregor Kasprian *et al.* *Distributionally robust deep learning using hardness weighted sampling.* Machine Learning for Biomedical Imaging, volume 1, 2022. 29, 44, 59, 82
- [Fonov 11] Vladimir Fonov, Alan C Evans, Kelly Botteron, C Robert Almli, Robert C McKinsty, D Louis Collins, Brain Development Cooperative Group *et al.* *Unbiased average age-appropriate atlases for pediatric studies.* Neuroimage, volume 54, number 1, pages 313–327, 2011. 118
- [Garcia-Peraza-Herrera 17] Luis C Garcia-Peraza-Herrera, Wenqi Li, Lucas Fidon, Caspar Gruijthuijzen, Alain Devreker, George Attiakos, Jan Deprest, Emmanuel Vander Poorten, Danail Stoyanov, Tom Vercauteren *et al.* *Toolnet: holistically-nested real-time segmentation of robotic surgical tools.* In 2017 IEEE/RSJ International Conference on Intelligent Robots and Systems (IROS), pages 5717–5722. IEEE, 2017. 32
- [Garcia-Peraza-Herrera 21] Luis C Garcia-Peraza-Herrera, Lucas Fidon, Claudia D’Ettorre, Danail Stoyanov, Tom Vercauteren and Sébastien Ourselin. *Image compositing for segmentation of surgical tools without manual annotations.* IEEE transactions on medical imaging, volume 40, number 5, pages 1450–1460, 2021. 31
- [Garel 01] Catherine Garel, Emmanuel Chantrel, Hervé Brisse, Monique Elmaleh, Dominique Luton, Jean-François Oury, Guy Sebag and Max Hassan. *Fetal cerebral cortex: normal gestational landmarks identified using prenatal MR imaging.* American Journal of Neuroradiology, volume 22, number 1, pages 184–189, 2001. 117

- [Geerdink 12] Niels Geerdink, Ton van der Vliet, Jan J Rotteveel, Ton Feuth, Nel Roeleveld and Reinier A Mullaart. *Essential features of chiari II malformation in MR imaging: an interobserver reliability study—part 1*. Child’s Nervous System, volume 28, number 7, pages 977–985, 2012. 51, 117
- [Gholipour 10] Ali Gholipour, Judy A Estroff and Simon K Warfield. *Robust super-resolution volume reconstruction from slice acquisitions: application to fetal brain mri*. IEEE transactions on medical imaging, volume 29, number 10, pages 1739–1758, 2010. 52
- [Gholipour 12] Ali Gholipour, Alireza Akhondi-Asl, Judy A Estroff and Simon K Warfield. *Multi-atlas multi-shape segmentation of fetal brain mri for volumetric and morphometric analysis of ventriculomegaly*. NeuroImage, volume 60, number 3, pages 1819–1831, 2012. 42
- [Gholipour 17] Ali Gholipour, Caitlin K Rollins, Clemente Velasco-Annis, Abdelhakim Ouaalam, Alireza Akhondi-Asl, Onur Afacan, Cynthia M Ortinau, Sean Clancy, Catherine Limperopoulos, Edward Yanget *al*. *A normative spatiotemporal MRI atlas of the fetal brain for automatic segmentation and analysis of early brain growth*. Scientific reports, volume 7, number 1, pages 1–13, 2017. 18, 19, 21, 42, 43, 54, 56, 61, 62, 67, 70, 71, 99, 113, 115, 116, 119, 132, 133, 134, 152, 158, 159, 166, 169, 263
- [Gibson 18] Eli Gibson, Wenqi Li, Carole Sudre, Lucas Fidon, Dzhoshkun I Shakir, Guotai Wang, Zach Eaton-Rosen, Robert Gray, Tom Doel, Yipeng Huet *al*. *NiftyNet: a deep-learning platform for medical imaging*. Computer methods and programs in biomedicine, volume 158, pages 113–122, 2018. 32
- [Glatter 20] S Glatter, D Prayer, GM Gruber, D Bettelheim, M Weber, G Dovjak, R Seidl, G Kasprianet *al*. *Improved prognostication in isolated callosal agenesis: fetal mag-*

- netic resonance imaging-based scoring system.* *Ultrasound in Obstetrics & Gynecology: the Official Journal of the International Society of Ultrasound in Obstetrics and Gynecology*, 2020. 118
- [Gonzalez 21] Camila Gonzalez, Karol Gotkowski, Andreas Bucher, Ricarda Fischbach, Isabel Kaltenborn and Anirban Mukhopadhyay. *Detecting when pre-trained nnu-net models fail silently for covid-19 lung lesion segmentation.* In *International Conference on Medical Image Computing and Computer-Assisted Intervention*, pages 304–314. Springer, 2021. 33
- [Gousias 12] Ioannis S Gousias, A David Edwards, Mary A Rutherford, Serena J Counsell, Jo V Hajnal, Daniel Rueckert and Alexander Hammers. *Magnetic resonance imaging of the newborn brain: manual segmentation of labelled atlases in term-born and preterm infants.* *Neuroimage*, volume 62, number 3, pages 1499–1509, 2012. 42
- [Gousias 13] Ioannis S Gousias, Alexander Hammers, Serena J Counsell, Latha Srinivasan, Mary A Rutherford, Rolf A Heckemann, Jo V Hajnal, Daniel Rueckert and A David Edwards. *Magnetic resonance imaging of the newborn brain: automatic segmentation of brain images into 50 anatomical regions.* *PloS one*, volume 8, number 4, page e59990, 2013. 42
- [Gower 75] John C Gower. *Generalized procrustes analysis.* *Psychometrika*, volume 40, number 1, pages 33–51, 1975. 120, 121
- [Gower 10] John C Gower. *Procrustes methods.* *Wiley Interdisciplinary Reviews: Computational Statistics*, volume 2, number 4, pages 503–508, 2010. 120, 121
- [Grabner 06] GŘnther Grabner, Andrew L Janke, Marc M Budge, David Smith, Jens Pruessner and D Louis Collins. *Symmetric atlasing and model based segmentation: an application to the hippocampus in older adults.* In

- International Conference on Medical Image Computing and Computer-Assisted Intervention, pages 58–66. Springer, 2006. 118
- [Grant 11] Ryan A Grant, Gregory G Heuer, Geneive M Carrión, N Scott Adzick, Erin S Schwartz, Sherman C Stein, Phillip B Storm and Leslie N Sutton. *Morphometric analysis of posterior fossa after in utero myelomeningocele repair*. *Journal of Neurosurgery: Pediatrics*, volume 7, number 4, pages 362–368, 2011. 220
- [Habas 10a] Piotr A Habas, Kio Kim, James M Corbett-Detig, Francois Rousseau, Orit A Glenn, A James Barkovich and Colin Studholme. *A spatiotemporal atlas of MR intensity, tissue probability and shape of the fetal brain with application to segmentation*. *Neuroimage*, volume 53, number 2, pages 460–470, 2010. 41, 45, 112, 113
- [Habas 10b] Piotr A Habas, Kio Kim, Francois Rousseau, Orit A Glenn, A James Barkovich and Colin Studholme. *Atlas-based segmentation of developing tissues in the human brain with quantitative validation in young fetuses*. *Human brain mapping*, volume 31, number 9, pages 1348–1358, 2010. 41
- [Haenni 02] Rolf Haenni. *Are alternatives to Dempster’s rule of combination real alternatives?: Comments on “about the belief function combination and the conflict management problem”—Lefevre et al.* *Information Fusion*, volume 3, number 3, pages 237–239, 2002. 150
- [Harwood 17] Ben Harwood, BG Kumar, Gustavo Carneiro, Ian Reid, Tom Drummond et al. *Smart mining for deep metric learning*. In *Proceedings of the IEEE International Conference on Computer Vision*, pages 2821–2829, 2017. 83, 94
- [Hasan 08] Khader M Hasan, Ambika Sankar, Christopher Halphen, Larry A Kramer, Linda Ewing-Cobbs, Maureen Dennis and Jack M Fletcher. *Quantitative diffu-*

- sion tensor imaging and intellectual outcomes in spina bifida*. Journal of Neurosurgery: Pediatrics, volume 2, number 1, pages 75–82, 2008. 51
- [Hatamizadeh 22] Ali Hatamizadeh, Yucheng Tang, Vishwesh Nath, Dong Yang, Andriy Myronenko, Bennett Landman, Holger R Roth and Daguang Xu. *Unetr: Transformers for 3d medical image segmentation*. In Proceedings of the IEEE/CVF Winter Conference on Applications of Computer Vision, pages 574–584, 2022. 32
- [Hausdorff 91] Felix Hausdorff. Set theory. American Mathematical Society (RI), 1991. 133
- [He 15] Kaiming He, Xiangyu Zhang, Shaoqing Ren and Jian Sun. *Delving deep into rectifiers: Surpassing human-level performance on imagenet classification*. In Proceedings of the IEEE international conference on computer vision, pages 1026–1034, 2015. 158
- [Hiriart-Urruty 13] Jean-Baptiste Hiriart-Urruty and Claude Lemaréchal. Convex analysis and minimization algorithms i: Fundamentals, volume 305. Springer science & business media, 2013. 231, 233
- [Hoffman 17] Robert R Hoffman. *A taxonomy of emergent trusting in the human-machine relationship*. Cognitive Systems Engineering, pages 137–164, 2017. 38, 140
- [Hong 20] Jinwoo Hong, Hyuk Jin Yun, Gilsoon Park, Seonggyu Kim, Cynthia T Laurentys, Leticia C Siqueira, Tomo Tarui, Caitlin K Rollins, Cynthia M Ortinau, P Ellen Grant *et al*. *Fetal cortical plate segmentation using fully convolutional networks with multiple plane aggregation*. Frontiers in neuroscience, page 1226, 2020. 44, 163
- [Hou 18] Benjamin Hou, Bishesh Khanal, Amir Alansary, Steven McDonagh, Alice Davidson, Mary Rutherford, Jo V Hajnal, Daniel Rueckert, Ben Glocker and Bernhard Kainz. *3-d reconstruction in canonical co-ordinate space from arbitrarily oriented 2-d images*. IEEE transactions

- on medical imaging, volume 37, number 8, pages 1737–1750, 2018. 52
- [Hu 18] Weihua Hu and et al. *Does distributionally robust supervised learning give robust classifiers?* In ICML, 2018. 87
- [Iglesias 15] Juan Eugenio Iglesias and Mert R Sabuncu. *Multi-atlas segmentation of biomedical images: a survey*. Medical image analysis, volume 24, number 1, pages 205–219, 2015. 152, 159
- [Irzan 20] Hassna Irzan, Lucas Fidon, Tom Vercauteren, Sebastien Ourselin, Neil Marlow and Andrew Melbourne. *Min-cut max-flow for network abnormality detection: Application to preterm birth*. In Uncertainty for Safe Utilization of Machine Learning in Medical Imaging, and Graphs in Biomedical Image Analysis, pages 164–173. Springer, 2020.
- [Isensee 21] Fabian Isensee, Paul F Jaeger, Simon AA Kohl, Jens Petersen and Klaus H Maier-Hein. *nnu-net: a self-configuring method for deep learning-based biomedical image segmentation*. Nature methods, volume 18, number 2, pages 203–211, 2021. 17, 18, 23, 30, 32, 33, 34, 39, 60, 77, 98, 99, 100, 101, 102, 104, 141, 158, 159, 164, 166, 227
- [Jacovi 21] Alon Jacovi, Ana Marasović, Tim Miller and Yoav Goldberg. *Formalizing trust in artificial intelligence: Prerequisites, causes and goals of human trust in ai*. In Proceedings of the 2021 ACM Conference on Fairness, Accountability, and Transparency, pages 624–635, 2021. 37, 38, 140
- [Jin 19] Chi Jin, Praneeth Netrapalli and Michael I Jordan. *Minmax optimization: Stable limit points of gradient descent ascent are locally optimal*. arXiv preprint arXiv:1902.00618, 2019. 83, 84, 89
- [Juranek 10] Jenifer Juranek and Michael S Salman. *Anomalous development of brain structure and function in spina bi-*

- fida myelomeningocele*. *Developmental Disabilities Research Reviews*, volume 16, number 1, pages 23–30, 2010. 220
- [Kahn 53] Herman Kahn and Andy W Marshall. *Methods of reducing sample size in Monte Carlo computations*. *Journal of the Operations Research Society of America*, volume 1, number 5, pages 263–278, 1953. 92
- [Kahn 14] Lora Kahn, Nnenna Mbabuike, Edison P Valle-Giler, Juanita Garces, R Clifton Moore, Hugo St Hilaire and Cuong J Bui. *Fetal surgery: the ochsner experience with in utero spina bifida repair*. *Ochsner Journal*, volume 14, number 1, pages 112–118, 2014. 51
- [Kainz 15] Bernhard Kainz, Markus Steinberger, Wolfgang Wein, Maria Kuklisova-Murgasova, Christina Malamateniou, Kevin Keraudren, Thomas Torsney-Weir, Mary Rutherford, Paul Aljabar, Joseph V Hajnal *et al.* *Fast volume reconstruction from motion corrupted stacks of 2d slices*. *IEEE transactions on medical imaging*, volume 34, number 9, pages 1901–1913, 2015. 52
- [Kamnitsas 16] Konstantinos Kamnitsas, Enzo Ferrante, Sarah Parisot, Christian Ledig, Aditya V Nori, Antonio Criminisi, Daniel Rueckert and Ben Glocker. *DeepMedic for brain tumor segmentation*. In *International workshop on Brainlesion: Glioma, multiple sclerosis, stroke and traumatic brain injuries*, pages 138–149. Springer, 2016. 32, 45
- [Kamraoui 22] Reda Abdellah Kamraoui, Vinh-Thong Ta, Thomas Tourdias, Boris Mansencal, José V Manjon and Pierriek Coupé. *Deeplesionbrain: Towards a broader deep-learning generalization for multiple sclerosis lesion segmentation*. *Medical Image Analysis*, volume 76, page 102312, 2022. 164
- [Karani 21] Neerav Karani, Ertunc Erdil, Krishna Chaitanya and Ender Konukoglu. *Test-time adaptable neural networks*

- for robust medical image segmentation*. Medical Image Analysis, volume 68, page 101907, 2021. 39
- [Kasprian 11] Gregor Kasprian, Georg Langs, Peter C Brugger, Mario Bittner, Michael Weber, Mavilde Arantes and Daniela Prayer. *The prenatal origin of hemispheric asymmetry: an in utero neuroimaging study*. Cerebral cortex, volume 21, number 5, pages 1076–1083, 2011. 118
- [Khalili 19] Nadieh Khalili, N Lessmann, Elise Turk, N Claessens, R de Heus, T Kolk, MA Viergever, MJNL Benders and I Išgum. *Automatic brain tissue segmentation in fetal MRI using convolutional neural networks*. Magnetic resonance imaging, volume 64, pages 77–89, 2019. 43, 44, 45, 65, 163
- [Khawam 21] Marie Khawam, Priscille De Dumast, Pierre Deman, Hamza Kebiri, Thomas Yu, Sébastien Tourbier, H el ene Lajous, Patric Hagmann, Philippe Maeder, Jean-Philippe Thiran *et al*. *Fetal brain biometric measurements on 3d super-resolution reconstructed t2-weighted mri: an intra-and inter-observer agreement study*. Frontiers in pediatrics, volume 9, 2021. 49, 52
- [Khoshnood 15] Babak Khoshnood, Maria Loane, Hermien De Walle, Larraitz Arriola, Marie-Claude Addor, Ingeborg Barisic, Judit Beres, Fabrizio Bianchi, Carlos Dias, Elizabeth Draper *et al*. *Long term trends in prevalence of neural tube defects in europe: population based study*. Bmj, volume 351, 2015. 50
- [Kim 09] Kio Kim, Piotr A Habas, Francois Rousseau, Orit A Glenn, Anthony J Barkovich and Colin Studholme. *Intersection based motion correction of multislice mri for 3-d in utero fetal brain image formation*. IEEE transactions on medical imaging, volume 29, number 1, pages 146–158, 2009. 52
- [Kingma 14] Diederik P Kingma and Jimmy Ba. *Adam: A method for stochastic optimization*. arXiv preprint arXiv:1412.6980, 2014. 72

- [Kofler 21a] Florian Kofler, Ivan Ezhov, Lucas Fidon, Carolin M Pirkel, Johannes C Paetzold, Egon Burian, Sarthak Pati, Malek El Hussein, Fernando Navarro, Suprosanna Shit *et al.* *Robust, primitive, and unsupervised quality estimation for segmentation ensembles.* *Frontiers in Neuroscience*, volume 15, 2021. 172
- [Kofler 21b] Florian Kofler, Ivan Ezhov, Fabian Isensee, Fabian Balmiger, Christoph Berger, Maximilian Koerner, Johannes Paetzold, Hongwei Li, Suprosanna Shit, Richard McKinley *et al.* *Are we using appropriate segmentation metrics? identifying correlates of human expert perception for cnn training beyond rolling the dice coefficient.* *arXiv preprint arXiv:2103.06205*, 2021. 165
- [Kofler 22a] Florian Kofler, Ivan Ezhov, Lucas Fidon, Izabela Horvath, Ezequiel de la Rosa, John LaMaster, Hongwei Li, Tom Finck, Suprosanna Shit, Johannes Paetzold *et al.* *Deep quality estimation: Creating surrogate models for human quality ratings.* *arXiv preprint arXiv:2205.10355*, 2022.
- [Kofler 22b] Florian Kofler, Suprosanna Shit, Ivan Ezhov, Lucas Fidon, Izabela Horvath, Rami Al-Maskari, Hongwei Li, Harsharan Bhatia, Timo Loehr, Marie Piraud *et al.* *blob loss: instance imbalance aware loss functions for semantic segmentation.* *arXiv preprint arXiv:2205.08209*, 2022.
- [Kubik-Huch 00] Rahel A Kubik-Huch, Thierry AGM Huisman, Josef Wisser, Nadine Gottstein-Aalame, Jörg F Debatin, Burkhardt Seifert, Mark E Ladd, Thomas Stallmach and Borut Marincek. *Ultrafast MR imaging of the fetus.* *American Journal of Roentgenology*, volume 174, number 6, pages 1599–1606, 2000. 49
- [Kuklisova-Murgasova 11] Maria Kuklisova-Murgasova, Paul Aljabar, Latha Srinivasan, Serena J Counsell, Valentina Doria, Ahmed Serag, Ioannis S Gousias, James P Boardman, Mary A Rutherford, A David Edwards *et al.* *A dynamic 4d prob-*

- abilistic atlas of the developing brain*. NeuroImage, volume 54, number 4, pages 2750–2763, 2011. 59
- [Kuklisova-Murgasova 12] Maria Kuklisova-Murgasova, Gerardine Quaghebeur, Mary A Rutherford, Joseph V Hajnal and Julia A Schnabel. *Reconstruction of fetal brain mri with intensity matching and complete outlier removal*. Medical image analysis, volume 16, number 8, pages 1550–1564, 2012. 52
- [Kunpalin 21] Yada Kunpalin, Jan Deprest, Ioannis Papastefanou, Emma Bredaki, Adalina Sacco, Francesca Russo, Jute Richter, Katrien Jansen, Sebastien Ourselin, Paolo De Coppiet *al*. *Incidence and patterns of abnormal corpus callosum in fetuses with isolated spina bifida aperta*. Prenatal Diagnosis, 2021. 51
- [Larrazabal 20] Agostina J Larrazabal, Nicolás Nieto, Victoria Peterson, Diego H Milone and Enzo Ferrante. *Gender imbalance in medical imaging datasets produces biased classifiers for computer-aided diagnosis*. Proceedings of the National Academy of Sciences, volume 117, number 23, pages 12592–12594, 2020. 33, 82, 83, 86
- [LeCun 98] Yann LeCun. *The MNIST database of handwritten digits*. <http://yann.lecun.com/exdb/mnist/>, 1998. 96
- [Lee 15] Chen-Yu Lee, Saining Xie, Patrick Gallagher, Zhengyou Zhang and Zhuowen Tu. *Deeply-supervised nets*. In Artificial intelligence and statistics, pages 562–570, 2015. 100
- [Lei 20] Tao Lei, Risheng Wang, Yong Wan, Bingtao Zhang, Hongying Meng and Asoke K Nandi. *Medical image segmentation using deep learning: a survey*. arXiv preprint arXiv:2009.13120, 2020. 31
- [Levine 03] Deborah Levine, Patrick D Barnes, Richard R Robertson, Geoffrey Wong and Tejas S Mehta. *Fast MR imaging of fetal central nervous system abnormalities*. Radiology, volume 229, number 1, pages 51–61, 2003. 49

- [Li 17] Wenqi Li, Guotai Wang, Lucas Fidon, Sebastien Ourselin, M Jorge Cardoso and Tom Vercauteren. *On the compactness, efficiency, and representation of 3D convolutional networks: brain parcellation as a pretext task*. In International Conference on Information Processing in Medical Imaging, pages 348–360. Springer, 2017. 32
- [Li 21] Liu Li, Matthew Sinclair, Antonios Makropoulos, Joseph V Hajnal, A David Edwards, Bernhard Kainz, Daniel Rueckert and Amir Alansary. *Cas-net: Conditional atlas generation and brain segmentation for fetal mri*. In Uncertainty for Safe Utilization of Machine Learning in Medical Imaging, and Perinatal Imaging, Placental and Preterm Image Analysis, pages 221–230. Springer, 2021. 46, 163
- [Lin 19] Tianyi Lin, Chi Jin and Michael I Jordan. *On gradient descent ascent for nonconvex-concave minimax problems*. arXiv preprint arXiv:1906.00331, 2019. 83, 84, 89
- [Liu 21a] Evan Z Liu, Behzad Haghgoo, Annie S Chen, Aditi Raghunathan, Pang Wei Koh, Shiori Sagawa, Percy Liang and Chelsea Finn. *Just train twice: Improving group robustness without training group information*. In International Conference on Machine Learning, pages 6781–6792. PMLR, 2021. 87
- [Liu 21b] Xiangbin Liu, Liping Song, Shuai Liu and Yudong Zhang. *A review of deep-learning-based medical image segmentation methods*. Sustainability, volume 13, number 3, page 1224, 2021. 31
- [Liu 22a] Quande Liu, Cheng Chen, Qi Dou and Pheng-Ann Heng. *Single-domain generalization in medical image segmentation via test-time adaptation from shape dictionary*. 2022. 39
- [Liu 22b] Zhuang Liu, Hanzi Mao, Chao-Yuan Wu, Christoph Feichtenhofer, Trevor Darrell and Saining Xie. *A convnet*

- for the 2020s*. arXiv preprint arXiv:2201.03545, 2022. 32
- [Loshchilov 16] Ilya Loshchilov and Frank Hutter. *Online batch selection for faster training of neural networks*. ICLR Workshop, 2016. 83
- [Lundervold 19] Alexander Selvikvåg Lundervold and Arvid Lundervold. *An overview of deep learning in medical imaging focusing on mri*. Zeitschrift für Medizinische Physik, volume 29, number 2, pages 102–127, 2019. 31
- [Ma 21] Jun Ma, Jianan Chen, Matthew Ng, Rui Huang, Yu Li, Chen Li, Xiaoping Yang and Anne L Martel. *Loss odyssey in medical image segmentation*. Medical Image Analysis, volume 71, page 102035, 2021. 32
- [Makropoulos 14] Antonios Makropoulos, Ioannis S Gousias, Christian Ledig, Paul Aljabar, Ahmed Serag, Joseph V Hajnal, A David Edwards, Serena J Counsell and Daniel Rueckert. *Automatic whole brain mri segmentation of the developing neonatal brain*. IEEE transactions on medical imaging, volume 33, number 9, pages 1818–1831, 2014. 45
- [Makropoulos 18] Antonios Makropoulos, Serena J Counsell and Daniel Rueckert. *A review on automatic fetal and neonatal brain MRI segmentation*. NeuroImage, volume 170, pages 231–248, 2018. 40, 112, 163
- [Mandell 15] Jason G Mandell, Abhaya V Kulkarni, Benjamin C Warf and Steven J Schiff. *Volumetric brain analysis in neurosurgery: Part 2. brain and CSF volumes discriminate neurocognitive outcomes in hydrocephalus*. Journal of Neurosurgery: Pediatrics, volume 15, number 2, pages 125–132, 2015. 51
- [Mårtensson 20] Gustav Mårtensson, Daniel Ferreira, Tobias Granberg, Lena Cavallin, Ketil Oppedal, Alessandro Padovani, Irena Rektorova, Laura Bonanni, Matteo Pardini, Milica G Kramberger *et al*. *The reliability of a deep learning*

- model in clinical out-of-distribution mri data: a multi-cohort study.* Medical Image Analysis, volume 66, page 101714, 2020. 164
- [Menze 14] Bjoern H Menze, Andras Jakab, Stefan Bauer, Jayashree Kalpathy-Cramer, Keyvan Farahani, Justin Kirby, Yuliya Burren, Nicole Porz, Johannes Slotboom, Roland Wiest *et al.* *The multimodal brain tumor image segmentation benchmark (brats).* IEEE transactions on medical imaging, volume 34, number 10, pages 1993–2024, 2014. 71, 99
- [Milletari 16] Fausto Milletari, Nassir Navab and Seyed-Ahmad Ahmadi. *V-net: Fully convolutional neural networks for volumetric medical image segmentation.* In 2016 fourth international conference on 3D vision (3DV), pages 565–571. IEEE, 2016. 44, 68, 70, 73
- [Modat 10] Marc Modat, Gerard R Ridgway, Zeike A Taylor, Manja Lehmann, Josephine Barnes, David J Hawkes, Nick C Fox and Sébastien Ourselin. *Fast free-form deformation using graphics processing units.* Computer methods and programs in biomedicine, volume 98, number 3, pages 278–284, 2010. 121, 122, 152, 159, 160
- [Modat 14] Marc Modat, David M Cash, Pankaj Daga, Gavin P Winston, John S Duncan and Sébastien Ourselin. *Global image registration using a symmetric block-matching approach.* Journal of Medical Imaging, volume 1, number 2, page 024003, 2014. 122, 158, 160
- [Moise Jr 16] Kenneth J Moise Jr, Julie S Moldenhauer, Kelly A Bennett, William Goodnight, Francois I Luks, Stephen P Emery, Kuojen Tsao, Anita J Moon-Grady, R Clifton Moore, Marjorie C Treadwellet *al.* *Current selection criteria and perioperative therapy used for fetal myelomeningocele surgery.* Obstetrics & Gynecology, volume 127, number 3, pages 593–597, 2016. 50, 51, 65

- [Moldenhauer 17] Julie S Moldenhauer and N Scott Adzick. *Fetal surgery for myelomeningocele: After the management of myelomeningocele study (MOMS)*. In *Seminars in Fetal and Neonatal Medicine*, volume 22, pages 360–366. Elsevier, 2017. 51
- [Moreau 65] Jean-Jacques Moreau. *Proximité et dualité dans un espace hilbertien*. *Bulletin de la Société mathématique de France*, volume 93, pages 273–299, 1965. 89
- [Mufti 21] Nada Mufti, Michael Aertsen, Michael Ebner, Lucas Fidon, Premal Patel, Muhamad Bin Abdul Rahman, Yannick Brackener, Gregor Ekart, Virginia Fernandez, Tom Vercauteren *et al.* *Cortical spectral matching and shape and volume analysis of the fetal brain pre-and post-fetal surgery for spina bifida: a retrospective study*. *Neuroradiology*, volume 63, number 10, pages 1721–1734, 2021. 51, 99, 118, 179
- [Mufti 23] N. Mufti, J. Chappell, M. Aertsen, M. Ebner, L. Fidon, J. Deprest, A. L. David, A. Melbourne and the GIFT-Surg Imaging Working Group. *Assessment of longitudinal brain development using super-resolution magnetic resonance imaging following fetal open spina bifida surgery*. *Ultrasound in Obstetrics & Gynecology*, 2023. 179
- [Naidich 80] Thomas P Naidich, Rochelle M Pudlowski, JB Naidich, M Gornish and FJ Rodriguez. *Computed tomographic signs of the chiari II malformation. part i: Skull and dural partitions*. *Radiology*, volume 134, number 1, pages 65–71, 1980. 50, 164
- [Namkoong 16] Hongseok Namkoong and John C Duchi. *Stochastic gradient methods for distributionally robust optimization with f -divergences*. In *Advances in Neural Information Processing Systems*, pages 2208–2216, 2016. 83
- [Niyazi 16] Maximilian Niyazi, Michael Brada, Anthony J Chalmers, Stephanie E Combs, Sara C Erridge, Alba Fiorentino, Anca L Grosu, Frank J Lagerwaard,

- Giuseppe Minniti, René-Olivier Mirimanoff *et al.* *Estro-acrop guideline “target delineation of glioblastomas”*. *Radiotherapy and oncology*, volume 118, number 1, pages 35–42, 2016. 142, 152, 173, 178
- [Oakden-Rayner 20] Luke Oakden-Rayner, Jared Dunnmon, Gustavo Carneiro and Christopher Ré. *Hidden stratification causes clinically meaningful failures in machine learning for medical imaging*. In *Proceedings of the ACM conference on health, inference, and learning*, pages 151–159, 2020. 33, 82, 83, 164
- [Orasanu 16] Eliza Orasanu, Andrew Melbourne, Manuel Jorge Cardoso, Herve Lomabert, Giles S Kendall, Nicola J Robertson, Neil Marlow and Sebastien Ourselin. *Cortical folding of the preterm brain: a longitudinal analysis of extremely preterm born neonates using spectral matching*. *Brain and behavior*, volume 6, number 8, page e00488, 2016. 58, 59
- [Owen 00] Art Owen and Yi Zhou. *Safe and effective importance sampling*. *Journal of the American Statistical Association*, volume 95, number 449, pages 135–143, 2000. 92
- [Payette 19] Kelly Payette, Ueli Moehrlen, Luca Mazzone, Nicole Ochsenein-Kölble, Ruth Tuura, Raimund Kottke, Martin Meuli and Andras Jakab. *Longitudinal analysis of fetal MRI in patients with prenatal spina bifida repair*. In *Smart Ultrasound Imaging and Perinatal, Preterm and Paediatric Image Analysis*, pages 161–170. Springer, 2019. 43, 44, 65
- [Payette 20] Kelly Payette, Raimund Kottke and Andras Jakab. *Efficient multi-class fetal brain segmentation in high resolution mri reconstructions with noisy labels*. In *Medical Ultrasound, and Preterm, Perinatal and Paediatric Image Analysis*, pages 295–304. Springer, 2020. 44, 46, 65

- [Payette 21] Kelly Payette, Priscille de Dumast, Hamza Kebiri, Ivan Ezhov, Johannes C Paetzold, Suprosanna Shit, Asim Iqbal, Romesa Khan, Raimund Kottke, Patrice Grethenet *et al.* *An automatic multi-tissue human fetal brain segmentation benchmark using the fetal tissue annotation dataset*. Scientific Data, volume 8, number 1, pages 1–14, 2021. 20, 44, 48, 54, 57, 59, 60, 61, 62, 71, 99, 104, 113, 114, 123, 132, 156, 158, 163, 165, 166
- [Payette 23] Kelly Payette, Hongwei Li, Priscille de Dumast, Roxane Licandro, Hui Ji, Md Mahfuzur Rahman Siddiquee, Daguang Xu, Andriy Myronenko, Hao Liu, Yuchen Peiet *et al.* *Fetal brain tissue annotation and segmentation challenge results*. Medical Image Analysis, page 102833, 2023.
- [Perone 19] Christian S Perone, Pedro Ballester, Rodrigo C Barros and Julien Cohen-Adad. *Unsupervised domain adaptation for medical imaging segmentation with self-ensembling*. NeuroImage, volume 194, pages 1–11, 2019. 164
- [Pollenus 20] Julie Pollenus, Lieven Lagae, Michael Aertsen and Katrien Jansen. *The impact of cerebral anomalies on cognitive outcome in patients with spina bifida: A systematic review*. European Journal of Paediatric Neurology, 2020. 50, 51, 135, 164
- [Puyol-Antón 21] Esther Puyol-Antón, Bram Ruijsink, Stefan K Piechnik, Stefan Neubauer, Steffen E Petersen, Reza Razavi and Andrew P King. *Fairness in cardiac mr image analysis: An investigation of bias due to data imbalance in deep learning based segmentation*. In International Conference on Medical Image Computing and Computer-Assisted Intervention, pages 413–423. Springer, 2021. 33, 82, 83, 86
- [Rafique 18] Hassan Rafique, Mingrui Liu, Qihang Lin and Tianbao Yang. *Non-convex min-max optimization: Provable algorithms and applications in machine learning*. arXiv preprint arXiv:1810.02060, 2018. 83, 84, 89

- [Rahimian 19] Hamed Rahimian and Sanjay Mehrotra. *Distributionally robust optimization: A review*. arXiv preprint arXiv:1908.05659, 2019. 88
- [Ranzini 21] Marta Ranzini, Lucas Fidon, Sébastien Ourselin, Marc Modat and Tom Vercauteren. *MONAI4bs: MONAI-based fetal brain MRI deep learning segmentation*. IEEE International Symposium on Biomedical Imaging, 2021. 55, 116, 136, 158
- [Redko 19] Ievgen Redko, Emilie Morvant, Amaury Habrard, Marc Sebban and Younes Bennani. *Advances in domain adaptation theory*. Elsevier, 2019. 164
- [Rieke 20] Nicola Rieke, Jonny Hancox, Wenqi Li, Fausto Milletari, Holger R Roth, Shadi Albarqouni, Spyridon Bakas, Mathieu N Galtier, Bennett A Landman, Klaus Maier-Hein et al. *The future of digital health with federated learning*. NPJ digital medicine, volume 3, number 1, pages 1–7, 2020. 172
- [Robinson 19] Robert Robinson, Vanya V Valindria, Wenjia Bai, Ozan Oktay, Bernhard Kainz, Hideaki Suzuki, Mihir M Sanghvi, Nay Aung, José Miguel Paiva, Filip Zemraket et al. *Automated quality control in image segmentation: application to the uk biobank cardiovascular magnetic resonance imaging study*. Journal of Cardiovascular Magnetic Resonance, volume 21, number 1, pages 1–14, 2019. 172
- [Ronneberger 15] Olaf Ronneberger, Philipp Fischer and Thomas Brox. *U-net: Convolutional networks for biomedical image segmentation*. In International Conference on Medical image computing and computer-assisted intervention, pages 234–241. Springer, 2015. 32, 44
- [Roulet 19] Nicolas Roulet, Diego Fernandez Slezak and Enzo Ferrante. *Joint learning of brain lesion and anatomy segmentation from heterogeneous datasets*. In International Conference on Medical Imaging with Deep Learning, pages 401–413. PMLR, 2019. 66, 68, 70, 76

- [Rousseau 06] Francois Rousseau, Orit A Glenn, Bistra Iordanova, Claudia Rodriguez-Carranza, Daniel B Vigneron, James A Barkovich and Colin Studholme. *Registration-based approach for reconstruction of high-resolution in utero fetal mr brain images*. Academic radiology, volume 13, number 9, pages 1072–1081, 2006. 52
- [Rousseau 16] François Rousseau, Colin Studholme, Renaud Jardri and Moriah E Thomason. *In vivo human fetal brain analysis using mr imaging*. In Fetal Development, pages 407–427. Springer, 2016. 40
- [Rueckert 99] Daniel Rueckert, Luke I Sonoda, Carmel Hayes, Derek LG Hill, Martin O Leach and David J Hawkes. *Nonrigid registration using free-form deformations: application to breast mr images*. IEEE transactions on medical imaging, volume 18, number 8, pages 712–721, 1999. 41
- [Sacco 19] Adalina Sacco, Fred Ushakov, Dominic Thompson, Donald Peebles, Pranav Pandya, Paolo De Coppi, Ruwan Wimalasundera, George Attilakos, Anna Louise David and Jan Deprest. *Fetal surgery for open spina bifida*. The Obstetrician & Gynaecologist, volume 21, number 4, page 271, 2019. 50, 51, 65, 103
- [Sagawa 20] Shiori Sagawa, Pang Wei Koh, Tatsunori B Hashimoto and Percy Liang. *Distributionally robust neural networks for group shifts: On the importance of regularization for worst-case generalization*. ICLR, 2020. 85, 86
- [Sanroma 18] Gerard Sanroma, Oualid M Benkarim, Gemma Piella, Karim Lekadir, Nadine Hahner, Elisenda Eixarch and Miguel A Gonzalez Ballester. *Learning to combine complementary segmentation methods for fetal and 6-month infant brain mri segmentation*. Computerized Medical Imaging and Graphics, volume 69, pages 52–59, 2018. 46

- [Serag 12a] Ahmed Serag, Paul Aljabar, Gareth Ball, Serena J Counsell, James P Boardman, Mary A Rutherford, A David Edwards, Joseph V Hajnal and Daniel Rueckert. *Construction of a consistent high-definition spatio-temporal atlas of the developing brain using adaptive kernel regression*. Neuroimage, volume 59, number 3, pages 2255–2265, 2012. 41
- [Serag 12b] Ahmed Serag, V Kyriakopoulou, MA Rutherford, AD Edwards, JV Hajnal, P Aljabar, SJ Counsell, JP Boardman and D Rueckert. *A multi-channel 4D probabilistic atlas of the developing brain: application to fetuses and neonates*. Annals of the BMVA, volume 2012, number 3, pages 1–14, 2012. 41, 43, 45, 112, 113
- [Shafer 76] Glenn Shafer. *A mathematical theory of evidence*. Princeton university press, 1976. 144, 150
- [Shi 21] Gonglei Shi, Li Xiao, Yang Chen and S Kevin Zhou. *Marginal loss and exclusion loss for partially supervised multi-organ segmentation*. Medical Image Analysis, page 101979, 2021. 66, 68, 70, 74, 76, 224
- [Shrivastava 16] Abhinav Shrivastava, Abhinav Gupta and Ross Girshick. *Training region-based object detectors with on-line hard example mining*. In Proceedings of the IEEE conference on computer vision and pattern recognition, pages 761–769, 2016. 83
- [Siddique 21] Nahian Siddique, Sidike Paheding, Colin P Elkin and Vijay Devabhaktuni. *U-net and its variants for medical image segmentation: A review of theory and applications*. IEEE Access, 2021. 31
- [Simon 00] Erin M Simon, Ruth B Goldstein, Fergus V Coakley, Roy A Filly, Kelly C Broderick, Thomas J Musci and A James Barkovich. *Fast MR imaging of fetal CNS anomalies in utero*. American journal of neuroradiology, volume 21, number 9, pages 1688–1698, 2000. 49

- [Sinha 18] Aman Sinha, Hongseok Namkoong and John Duchi. *Certifying some distributional robustness with principled adversarial training*. ICLR, 2018. 86, 87
- [Smets 93] Philippe Smets. *Belief functions: the disjunctive rule of combination and the generalized bayesian theorem*. International Journal of approximate reasoning, volume 9, number 1, pages 1–35, 1993. 150
- [Staib 17] Matthew Staib and Stefanie Jegelka. *Distributionally robust deep learning as a generalization of adversarial training*. In NIPS workshop on Machine Learning and Computer Security, 2017. 86, 87
- [Suh 19] Yumin Suh, Bohyung Han, Wonsik Kim and Kyoung Mu Lee. *Stochastic class-based hard example mining for deep metric learning*. In Proceedings of the IEEE Conference on Computer Vision and Pattern Recognition, pages 7251–7259, 2019. 83
- [Sutton 99] Leslie N Sutton, N Scott Adzick, Larissa T Bilaniuk, Mark P Johnson, Timothy M Crombleholme and Alan W Flake. *Improvement in hindbrain herniation demonstrated by serial fetal magnetic resonance imaging following fetal surgery for myelomeningocele*. Jama, volume 282, number 19, pages 1826–1831, 1999. 51
- [Tilborghs 20] Sofie Tilborghs, Ine Dirks, Lucas Fidon, Siri Willems, Tom Eelbode, Jeroen Bertels, Bart Ilse, Arne Brys, Adriana Dubbeldam, Nico Bulset *al*. *Comparative study of deep learning methods for the automatic segmentation of lung, lesion and lesion type in ct scans of covid-19 patients*. arXiv preprint arXiv:2007.15546, 2020. 98
- [Torrents-Barrena 19] Jordina Torrents-Barrena, Gemma Piella, Narcís Masoller, Eduard Gratacós, Elisenda Eixarch, Mario Ceresa and Miguel Ángel González Ballester. *Segmentation and classification in mri and us fetal imaging: recent trends and future prospects*. Medical Image Analysis, volume 51, pages 61–88, 2019. 40

- [Tourbier 17] Sébastien Tourbier, Clemente Velasco-Annis, Vahid Taimouri, Patric Hagmann, Reto Meuli, Simon K Warfield, Meritxell Bach Cuadra and Ali Gholipour. *Automated template-based brain localization and extraction for fetal brain mri reconstruction*. NeuroImage, volume 155, pages 460–472, 2017. 52
- [Treble-Barna 15] Amery Treble-Barna, Jenifer Juranek, Karla K Stuebing, Paul T Cirino, Maureen Dennis and Jack M Fletcher. *Prospective and episodic memory in relation to hippocampal volume in adults with spina bifida myelomeningocele*. Neuropsychology, volume 29, number 1, page 92, 2015. 51
- [Treble 13] Amery Treble, Jenifer Juranek, Karla K Stuebing, Maureen Dennis and Jack M Fletcher. *Functional significance of atypical cortical organization in spina bifida myelomeningocele: relations of cortical thickness and gyrification with iq and fine motor dexterity*. Cerebral Cortex, volume 23, number 10, pages 2357–2369, 2013. 51
- [Tubbs 11] R Shane Tubbs, Sanjay Krishnamurthy, Ketan Verma, Mohammadali M Shoja, Marios Loukas, Martin M Mortazavi and Aaron A Cohen-Gadol. *Cavum velum interpositum, cavum septum pellucidum, and cavum vergae: a review*. Child’s Nervous System, volume 27, number 11, pages 1927–1930, 2011. 57
- [Tulipan 15] Noel Tulipan, John C Wellons, Elizabeth A Thom, Nalin Gupta, Leslie N Sutton, Pamela K Burrows, Diana Farmer, William Walsh, Mark P Johnson, Larry Randet *al*. *Prenatal surgery for myelomeningocele and the need for cerebrospinal fluid shunt placement*. Journal of Neurosurgery: Pediatrics, volume 16, number 6, pages 613–620, 2015. 221
- [Ulyanov 16] Dmitry Ulyanov, Andrea Vedaldi and Victor Lempit-sky. *Instance normalization: The missing ingredient for fast stylization*. arXiv preprint arXiv:1607.08022, 2016. 72, 100, 158

- [Van Leemput 99] Koen Van Leemput, Frederik Maes, Dirk Vandermeulen and Paul Suetens. *Automated model-based tissue classification of mr images of the brain*. IEEE transactions on medical imaging, volume 18, number 10, pages 897–908, 1999. 41
- [van Leeuwen 21] Kicky G van Leeuwen, Steven Schalekamp, Matthieu JCM Rutten, Bram van Ginneken and Maarten de Rooij. *Artificial intelligence in radiology: 100 commercially available products and their scientific evidence*. European radiology, volume 31, number 6, pages 3797–3804, 2021. 33
- [Vaswani 17] Ashish Vaswani, Noam Shazeer, Niki Parmar, Jakob Uszkoreit, Llion Jones, Aidan N Gomez, Łukasz Kaiser and Illia Polosukhin. *Attention is all you need*. Advances in neural information processing systems, volume 30, 2017. 32
- [Wachinger 19] Christian Wachinger, Benjamin Gutierrez Becker, Anna Rieckmann and Sebastian Pölsterl. *Quantifying confounding bias in neuroimaging datasets with causal inference*. In International Conference on Medical Image Computing and Computer-Assisted Intervention, pages 484–492. Springer, 2019. 86
- [Wang 17] Guotai Wang, Wenqi Li, Sébastien Ourselin and Tom Vercauteren. *Automatic brain tumor segmentation using cascaded anisotropic convolutional neural networks*. In International MICCAI Brainlesion Workshop, pages 178–190. Springer, 2017. 32, 44
- [Wang 21] Wenxuan Wang, Chen Chen, Meng Ding, Hong Yu, Sen Zha and Jiangyun Li. *Transbts: Multimodal brain tumor segmentation using transformer*. In International Conference on Medical Image Computing and Computer-Assisted Intervention, pages 109–119. Springer, 2021. 32
- [Wang 22a] Guotai Wang, Tom Vercauteren, Sébastien Ourselin, Wenqi Li and Lucas Fidon. *System and computer-*

- implemented method for segmenting an image*, July 5 2022. US Patent 11,379,985. 32
- [Wang 22b] Jindong Wang, Cuiling Lan, Chang Liu, Yidong Ouyang, Tao Qin, Wang Lu, Yiqiang Chen, Wenjun Zeng and Philip Yu. *Generalizing to unseen domains: A survey on domain generalization*. IEEE Transactions on Knowledge and Data Engineering, 2022. 38, 39
- [Warfield 04] Simon K Warfield, Kelly H Zou and William M Wells. *Simultaneous truth and performance level estimation (staple): an algorithm for the validation of image segmentation*. IEEE transactions on medical imaging, volume 23, number 7, pages 903–921, 2004. 39, 42
- [Welinder 10] Peter Welinder, Steve Branson, Pietro Perona and Serge Belongie. *The multidimensional wisdom of crowds*. Advances in neural information processing systems, volume 23, 2010. 39
- [Wells 96] William M Wells, W Eric L Grimson, Ron Kikinis and Ferenc A Jolesz. *Adaptive segmentation of mri data*. IEEE transactions on medical imaging, volume 15, number 4, pages 429–442, 1996. 41
- [Wong 18] Ken CL Wong, Mehdi Moradi, Hui Tang and Tanveer Syeda-Mahmood. *3d segmentation with exponential logarithmic loss for highly unbalanced object sizes*. In International Conference on Medical Image Computing and Computer-Assisted Intervention, pages 612–619. Springer, 2018. 44
- [Wu 17] Chao-Yuan Wu, R Manmatha, Alexander J Smola and Philipp Krahenbuhl. *Sampling matters in deep embedding learning*. In Proceedings of the IEEE International Conference on Computer Vision, pages 2840–2848, 2017. 83, 94
- [Wu 21] Jiangjie Wu, Taotao Sun, Boliang Yu, Zhenghao Li, Qing Wu, Yutong Wang, Zhaoxia Qian, Yuyao Zhang, Ling Jiang and Hongjiang Wei. *Age-specific structural*

- fetal brain atlases construction and cortical development quantification for chinese population.* NeuroImage, page 118412, 2021. 19, 42, 43, 54, 62, 113, 152, 158, 159, 169, 263
- [Xie 21] Yutong Xie, Jianpeng Zhang, Chunhua Shen and Yong Xia. *Cotr: Efficiently bridging cnn and transformer for 3d medical image segmentation.* In International conference on medical image computing and computer-assisted intervention, pages 171–180. Springer, 2021. 32
- [Yamashita 97] Y Yamashita, T Namimoto, Y Abe, M Takahashi, J Iwamasa, K Miyazaki and H Okamura. *MR imaging of the fetus by a HASTE sequence.* AJR. American journal of roentgenology, volume 168, number 2, pages 513–519, 1997. 49
- [Yushkevich 16] Paul A Yushkevich, Yang Gao and Guido Gerig. *Itk-snap: an interactive tool for semi-automatic segmentation of multi-modality biomedical images.* In 2016 38th Annual International Conference of the IEEE Engineering in Medicine and Biology Society (EMBC), pages 3342–3345. IEEE, 2016. 58, 117, 124
- [Zadeh 79] Lotfi A. Zadeh. *On the validity of dempster’s rule of combination of evidence.* 1979. 149, 150
- [Zagoruyko 16] Sergey Zagoruyko and Nikos Komodakis. *Wide residual networks.* In Proceedings of the British Machine Vision Conference (BMVC), pages 87.1–87.12. BMVA Press, 2016. 96
- [Zarutskie 19] A Zarutskie, C Guimaraes, M Yopez, P Torres, A Shetty, H Sangi-Haghpeykar, W Lee, J Espinoza, AA Shamshirsaz, A Nassret *al.* *Prenatal brain imaging for predicting need for postnatal hydrocephalus treatment in fetuses that had neural tube defect repair in utero.* Ultrasound in Obstetrics & Gynecology, volume 53, number 3, pages 324–334, 2019. 50, 51, 52, 65

- [Zhan 13] Jinfeng Zhan, Ivo D Dinov, Junning Li, Zhonghe Zhang, Sam Hobel, Yonggang Shi, Xiangtao Lin, Alen Zamanyan, Lei Feng, Gaojun Tenget *al.* *Spatial-temporal atlas of human fetal brain development during the early second trimester*. Neuroimage, volume 82, pages 115–126, 2013. 113
- [Zhang 20] Ling Zhang, Xiaosong Wang, Dong Yang, Thomas Sanford, Stephanie Harmon, Baris Turkbey, Bradford J Wood, Holger Roth, Andriy Myronenko, Daguang Xu et *al.* *Generalizing deep learning for medical image segmentation to unseen domains via deep stacked transformation*. IEEE transactions on medical imaging, volume 39, number 7, pages 2531–2540, 2020. 39
- [Zhao 22] L Zhao, JD Asis-Cruz, X Feng, Y Wu, K Kapse, A Largent, J Quistorff, C Lopez, D Wu, K Qing et *al.* *Automated 3D fetal brain segmentation using an optimized deep learning approach*. American Journal of Neuroradiology, 2022. 45, 163
- [Zhou 19] Yuyin Zhou, Zhe Li, Song Bai, Chong Wang, Xinlei Chen, Mei Han, Elliot Fishman and Alan L Yuille. *Prior-aware neural network for partially-supervised multi-organ segmentation*. In Proceedings of the IEEE/CVF International Conference on Computer Vision, pages 10672–10681, 2019. 66, 68
- [Zhou 21] Hong-Yu Zhou, Jiansen Guo, Yinghao Zhang, Lequan Yu, Liansheng Wang and Yizhou Yu. *nnformer: Interleaved transformer for volumetric segmentation*. arXiv preprint arXiv:2109.03201, 2021. 32
- [Zou 19] Difan Zou and Quanquan Gu. *An improved analysis of training over-parameterized deep neural networks*. In Advances in Neural Information Processing Systems 32, pages 2055–2064. Curran Associates, Inc., 2019. 84

Appendix

Table of Contents

A.1 Appendix of chapter 3	220
A.1.1 Lexic of Fetal Neuroanatomy for Engineers	220
A.2 Proofs of chapter 4	222
A.2.1 Summary of mathematical notations	222
A.2.2 Proof of equation (4.3)	222
A.2.3 Proof that the leaf-Dice is a label-set loss function	223
A.2.4 Proof of equation (4.7)	223
A.2.5 Relation to the marginal Dice loss	224
A.3 Additional Experiments on BraTS 2021	225
A.4 Proofs of chapter 5	226
A.4.1 Summary of the Notations used in the Proofs	226
A.4.2 Evaluation of the Influence of β on the Segmentation Performance for BraTS	227
A.4.3 Importance Sampling Approximation in Algorithm 1	228
A.4.4 Proof of Example 5.3.1: Formula of the Sampling Probabilities for the KL Divergence	228
A.4.5 Proof of Lemma 5.3.1: Regularity Properties of R	230
A.4.6 Proof of Lemma 5.3.2: Formula of the Distributionally Robust Loss Gradient	232
A.4.7 Proof of Theorem 5.3.4: Distributionally Robust Optimization as Principled Hard Example Mining	233
A.4.8 Proof of Equivalence between (5.17) and (5.18): Link between DRO and Percentile Loss	236
A.4.9 Proof of Theorem 5.3.3: convergence of SGD with Hardness Weighted Sampling for Over-parameterized Deep Neural Networks with ReLU	237
A.5 Additional Results for chapter 7	258
A.5.1 Class-wise Quantitative Evaluation.	258
A.5.2 Tuning of the Registration Parameters	263
A.6 Proofs of chapter 7	264
A.6.1 Proof of the Formula (7.15) for the Anatomical BPA.	264

A.6.2 Proof of Equality (7.17). 269

A.1 Appendix of chapter 3

A.1.1 Lexic of Fetal Neuroanatomy for Engineers

This section contains useful definitions about fetal neuroanatomy. The terms are defined in alphabetical order.

Brain parenchyma The brain parenchyma is the functional tissue in the brain. It's comprised of two types of cells that are used specifically for cognition and controlling the rest of the body. The remaining brain tissue is known as stroma, which is the supportive or structural tissue. Damage or trauma to the brain parenchyma often results in a loss of cognitive ability or even death.

Caudal An anatomic term meaning: 1. Pertaining to the tail or the hind part. 2. Situated in or directed toward the tail or hind part. 3. Inferior to another structure, in the sense of being below it.

Cerebellar Herniation Level (CHL) This is the level of descent of the cerebellum caudally into the spinal canal past the foramen magnum. This is caused by a small posterior fossa, and the development of hydrocephalus which obstructs the normal cerebrospinal fluid flow around the body.

Cerebrospinal Fluid (CSF) The Cerebrospinal Fluid is the colorless fluid found in the brain and the spinal cord. It is made of 99% of water.

Chiari II hindbrain malformation - hindbrain herniation (HBH) The HBH seen in spina bifida is caused by a downward displacement of the cerebellum below the level of the foramen magnum. It may result in brainstem dysfunction such as apnoea, dysphagia, torticollis, and spasticity. The 5 year mortality rate in patients born with MMC is 14% which rises to 35% in patients whose Chiari II malformation leads to brainstem dysfunction [Juraneck 10, Grant 11]. This obstruction can prevent the movement of CSF and results in hydrocephalus. The Chiari II malformation is characterised by a small posterior fossa with downward displacement of the cerebellum, medulla and fourth ventricle. Previous studies suggest that Chiari II malformation can be (manually) measured reliably using an MRI [Adzick 11, Aertsen 19].

Cognitive impairment When a person has difficulty in short, and long-term memory, learning new skills, concentrating or making decisions that affect their

everyday life.

Gestional age (GA) “Gestational age” (or “menstrual age”) is the time elapsed between the first day of the last normal menstrual period and the day of delivery [Engle 04]. GA is expressed as completed weeks. The GA can be calculated from the first day of the last menstrual period otherwise, it can be estimated using an US via a measurement known as *crown-rump-length*. It is worth noting that GA is not calculated from the day of conception (more difficult to estimate in practice).

Hydrocephalus Hydrocephalus is a condition in which an accumulation of cerebrospinal fluid (CSF) occurs within the brain. This typically causes increased pressure inside the skull.

Medulla or Medulla oblongata The medulla is a long stem-like structure which makes up part of the brainstem. It is anterior and partially inferior to the cerebellum. It is a cone-shaped neuronal mass responsible for autonomic (involuntary) functions ranging from vomiting to sneezing.

Myelomeningocele (MMC) Most common type of spina bifida. It is characterised by a fluid-filled sac containing exposed spinal cord and neural tissues.

Posterior Fossa (PF) Small region in the back of the skull that houses the cerebellum and brain stem.

Ventricles Brain cavities in the middle of the brain where CSF circulates and is produced.

Ventriculomegaly Ventriculomegaly occurs when the ventricular width is larger than the reference ranges. They can be graded as mild (8-10mm), moderate (10-15mm), and severe (> 15 mm) [Tulipan 15].

A.2 Proofs of chapter 4

A.2.1 Summary of mathematical notations

- N : number of voxels.
- \mathbf{L} : set of final labels (e.g. white matter, ventricular system). We call the elements of \mathbf{L} *leaf-labels*.
- $2^{\mathbf{L}}$: set of subsets of \mathbf{L} . We call the elements of $2^{\mathbf{L}}$ *label-sets*.
- $P(\mathbf{L})$: space of probability vectors for leaf-labels.
- $\mathbb{1}$: indicator function. let A an assertion, $\mathbb{1}(A) = 1$ if A is true and $\mathbb{1}(A) = 0$ if A is false.

A.2.2 Proof of equation (4.3)

Let $\mathcal{L} : \mathbf{E} \rightarrow \mathbb{R}$, with $\mathbf{E} := P(\mathbf{L})^N \times (2^{\mathbf{L}})^N$. Let us first remind that we have defined label-set loss functions as the losses $\tilde{\mathcal{L}}$ that satisfy the axiom

$$\forall \mathbf{g} \in (2^{\mathbf{L}})^N, \forall \mathbf{p}, \mathbf{q} \in P(\mathbf{L})^N, \quad \Phi(\mathbf{p}; \mathbf{g}) = \Phi(\mathbf{q}; \mathbf{g}) \implies \tilde{\mathcal{L}}(\mathbf{p}, \mathbf{g}) = \tilde{\mathcal{L}}(\mathbf{q}, \mathbf{g}) \quad (\text{A.1})$$

First implication.

Let us assume that $\forall (\mathbf{p}, \mathbf{g}) \in \mathbf{E}$, $\mathcal{L}(\mathbf{p}, \mathbf{g}) = \mathcal{L}(\Phi(\mathbf{p}; \mathbf{g}), \mathbf{g})$. Let $\mathbf{g} \in (2^{\mathbf{L}})^N$ and $\mathbf{p}, \mathbf{q} \in P(\mathbf{L})^N$, such that $\Phi(\mathbf{p}; \mathbf{g}) = \Phi(\mathbf{q}; \mathbf{g})$. We have

$$\mathcal{L}(\mathbf{p}, \mathbf{g}) = \mathcal{L}(\Phi(\mathbf{p}; \mathbf{g}), \mathbf{g}) = \mathcal{L}(\Phi(\mathbf{q}; \mathbf{g}), \mathbf{g}) = \mathcal{L}(\mathbf{q}, \mathbf{g}) \quad \blacksquare$$

Second implication.

Let us assume that \mathcal{L} is a label-set loss function. We will use the following lemma which is proved at the end of this paragraph.

Lemma A.2.1. *For all $\mathbf{g} \in (2^{\mathbf{L}})^N$, the function $\Phi(\cdot; \mathbf{g}) : \mathbf{p} \mapsto \Phi(\mathbf{p}; \mathbf{g})$ is idempotent, i.e. $\forall \mathbf{p} \in P(\mathbf{L})^N$, $\Phi(\Phi(\mathbf{p}; \mathbf{g}); \mathbf{g}) = \Phi(\mathbf{p}; \mathbf{g})$.*

Let $(\mathbf{p}, \mathbf{g}) \in \mathbf{E}$. By Lemma A.2.1, $\Phi(\Phi(\mathbf{p}; \mathbf{g}); \mathbf{g}) = \Phi(\mathbf{p}; \mathbf{g})$. Therefore, by applying (A.1) for \mathbf{p} and $\mathbf{q} = \Phi(\mathbf{p}; \mathbf{g})$ we eventually obtain $\mathcal{L}(\mathbf{p}, \mathbf{g}) = \mathcal{L}(\Phi(\mathbf{p}; \mathbf{g}), \mathbf{g})$

■

Proof of Lemma A.2.1

Let $\mathbf{g} = (g_i) \in (2^{\mathbf{L}})^N$ and $\mathbf{p} = (p_{i,c}) \in P(\mathbf{L})^N$. Let us denote $\Phi(\mathbf{p}; \mathbf{g}) = (\tilde{p}_{i,c})$ and $\Phi(\Phi(\mathbf{p}; \mathbf{g}); \mathbf{g}) = (\tilde{\tilde{p}}_{i,c})$. For all i, c , if $c \notin g_i$, $\tilde{\tilde{p}}_{i,c} = \tilde{p}_{i,c}$, and if $c \in g_i$, $\tilde{\tilde{p}}_{i,c} = \frac{1}{|g_i|} \sum_{c' \in g_i} \tilde{p}_{i,c'} = \frac{1}{|g_i|} \sum_{c' \in g_i} \left(\frac{1}{|g_i|} \sum_{c'' \in g_i} p_{i,c''} \right) = \tilde{p}_{i,c}$ ■

A.2.3 Proof that the leaf-Dice is a label-set loss function

Let $\mathbf{g} \in (2^{\mathbf{L}})^N$ be a partial segmentation that takes its value in a partition of \mathbf{L} of the form $\{\mathbf{L}'\} \cup \{\{c\} \mid c \in \mathbf{L} \setminus \mathbf{L}'\}$ with $\mathbf{L}' \subsetneq \mathbf{L}$ that contains all the labels of the regions of interest that were not manually segmented. Let $\mathbf{p} \in P(\mathbf{L})^N$.

$$\begin{aligned} \mathcal{L}_{Leaf-Dice}(\mathbf{p}, \mathbf{g}) &= 1 - \frac{1}{|\mathbf{L}|} \sum_{c \in \mathbf{L}} \frac{2 \sum_i \mathbb{1}(g_i = \{c\}) p_{i,c}}{\sum_i \mathbb{1}(g_i = \{c\})^\alpha + \sum_i p_{i,c}^\alpha + \epsilon} \\ &= 1 - \frac{1}{|\mathbf{L}|} \sum_{c \in \mathbf{L} \setminus \mathbf{L}'} \frac{2 \sum_i \mathbb{1}(g_i = \{c\}) p_{i,c}}{\sum_i \mathbb{1}(g_i = \{c\})^\alpha + \sum_i p_{i,c}^\alpha + \epsilon} \end{aligned} \quad (\text{A.2})$$

because the terms of the sum for the leaf-labels $c \in \mathbf{L}'$ have a numerator equal to 0.

To prove that $\mathcal{L}_{Leaf-Dice}$ is a label-set loss function it is sufficient to prove that $\mathcal{L}_{Leaf-Dice}(\mathbf{p}, \mathbf{g}) = \mathcal{L}_{Leaf-Dice}(\Phi(\mathbf{p}; \mathbf{g}), \mathbf{g})$. For all voxel i and leaf-label c

$$[\Phi(\mathbf{p}; \mathbf{g})]_{i,c} = \begin{cases} \frac{1}{|g_i|} \sum_{c' \in g_i} p_{i,c'} & \text{if } c \in g_i \\ p_{i,c} & \text{if } c \notin g_i \end{cases} = \begin{cases} \frac{1}{|\mathbf{L}'|} \sum_{c' \in \mathbf{L}'} p_{i,c'} & \text{if } c \in g_i \text{ and } g_i = \mathbf{L}' \\ p_{i,c} & \text{if } c \in g_i \text{ and } g_i = \{c\} \\ p_{i,c} & \text{if } c \notin g_i \end{cases}$$

where the second equality comes from the partition.

We observe that $[\Phi(\mathbf{p}; \mathbf{g})]_{i,c} \neq p_{i,c}$ only when $c \in \mathbf{L}'$. Using (A.2) we obtain $\mathcal{L}_{Leaf-Dice}(\mathbf{p}, \mathbf{g}) = \mathcal{L}_{Leaf-Dice}(\Phi(\mathbf{p}; \mathbf{g}), \mathbf{g})$ ■

A.2.4 Proof of equation (4.7)

Using previous results and the fact that $\mathcal{L}_{partial}$ is here defined as a converted fully-supervised loss function, $\mathcal{L}_{partial}$ is a label-set loss function if and only if for all $(\mathbf{p}, \mathbf{g}) \in P(\mathbf{L})^N \times (2^{\mathbf{L}})^N$

$$\mathcal{L}_{partial}(\mathbf{p}, \mathbf{g}) = \mathcal{L}_{partial}(\Phi(\mathbf{p}; \mathbf{g}), \mathbf{g}) = \mathcal{L}_{fully}(\Phi(\mathbf{p}; \mathbf{g}), \Psi(\mathbf{g}))$$

As a result, we only need to prove that if $\mathcal{L}_{partial}$ is a label-set loss function then $\Psi = \Psi_0$. Let us suppose that $\mathcal{L}_{partial}$ is a label-set loss function. Therefore, for all

$\mathbf{g} \in (2^{\mathbf{L}})^N$, $\mathcal{L}_{fully}(\Phi(\Psi(\mathbf{g}); \mathbf{g}), \Psi(\mathbf{g})) = \mathcal{L}_{partial}(\Phi(\Psi(\mathbf{g}); \mathbf{g}), \mathbf{g}) = \mathcal{L}_{partial}(\Psi(\mathbf{g}), \mathbf{g}) = \mathcal{L}_{fully}(\Psi(\mathbf{g}), \Psi(\mathbf{g}))$. Using the unicity of the minima of \mathcal{L}_{fully} we can therefore conclude that $\forall \mathbf{g} \in (2^{\mathbf{L}})^N$, $\Psi(\mathbf{g}) = \Phi(\Psi(\mathbf{g}); \mathbf{g})$. For all \mathbf{g}, i, c ,

$$[\Phi(\Psi(\mathbf{g}); \mathbf{g})]_{i,c} = \begin{cases} \frac{1}{|g_i|} \sum_{c' \in g_i} [\Psi(\mathbf{g})]_{i,c'} & \text{if } c \in g_i \\ [\Psi(\mathbf{g})]_{i,c} & \text{if } c \notin g_i \end{cases} = \begin{cases} \frac{1}{|g_i|} & \text{if } c \in g_i \\ 0 & \text{if } c \notin g_i \end{cases} = [\Psi_0(\mathbf{g})]_{i,c}$$

where in the second inequality we have used $\forall i, c, [\Psi(\mathbf{g})]_{i,c} > 0 \implies c \in g_i$ ■

A.2.5 Relation to the marginal Dice loss

Let $P = \{\mathbf{L}_j\}$ a partition of \mathbf{L} and $\mathbf{g} \in (2^{\mathbf{L}})^N$ with its values in P . For all $c \in \mathbf{L}$, we denote $j(c)$ the unique index such that $c \in \mathbf{L}_{j(c)}$.

Using the definitions of Ψ_0 , Φ , and the partition P , we obtain

$$\begin{aligned} \mathcal{L}_{Dice}(\Phi(\mathbf{p}; \mathbf{g}), \Psi_0(\mathbf{g})) &= 1 - \frac{1}{|\mathbf{L}|} \sum_{c \in \mathbf{L}} \frac{\sum_i \Psi_0(\mathbf{g})_{i,c} \Phi(\mathbf{p}; \mathbf{g})_{i,c}}{\sum_i \Psi_0(\mathbf{g})_{i,c} + \sum_i \Phi(\mathbf{p}; \mathbf{g})_{i,c}} \\ &= 1 - \frac{1}{|\mathbf{L}|} \sum_{c \in \mathbf{L}} \frac{\sum_i \left(\frac{1}{|\mathbf{L}_{j(c)}} \mathbf{1}(g_i = \mathbf{L}_{j(c)}) \right) \left(\frac{1}{|\mathbf{L}_{j(c)}} \sum_{c' \in \mathbf{L}_{j(c)}} p_{i,c'} \right)}{\sum_i \frac{1}{|\mathbf{L}_{j(c)}} \mathbf{1}(g_i = \mathbf{L}_{j(c)}) + \sum_i \frac{1}{|\mathbf{L}_{j(c)}} \sum_{c' \in \mathbf{L}_{j(c)}} p_{i,c'}} \\ &= 1 - \frac{1}{|\mathbf{L}|} \sum_{c \in \mathbf{L}} \frac{\left(\frac{1}{|\mathbf{L}_{j(c)}} \right)^2 \sum_i \mathbf{1}(g_i = \mathbf{L}_{j(c)}) \left(\sum_{c' \in \mathbf{L}_{j(c)}} p_{i,c'} \right)}{\frac{1}{|\mathbf{L}_{j(c)}} \left(\sum_i \mathbf{1}(g_i = \mathbf{L}_{j(c)}) + \sum_i \sum_{c' \in \mathbf{L}_{j(c)}} p_{i,c'} \right)} \\ &= 1 - \frac{1}{|\mathbf{L}|} \sum_{c \in \mathbf{L}} \frac{1}{|\mathbf{L}_{j(c)}} \frac{\sum_i \mathbf{1}(g_i = \mathbf{L}_{j(c)}) \left(\sum_{c' \in \mathbf{L}_{j(c)}} p_{i,c'} \right)}{\sum_i \mathbf{1}(g_i = \mathbf{L}_{j(c)}) + \sum_i \sum_{c' \in \mathbf{L}_{j(c)}} p_{i,c'}} \end{aligned}$$

By grouping the terms of the first sum with respect to the label-sets in P

$$\begin{aligned} \mathcal{L}_{Dice}(\Phi(\mathbf{p}; \mathbf{g}), \Psi_0(\mathbf{g})) &= 1 - \frac{1}{|\mathbf{L}|} \sum_{\mathbf{L}' \in P} \sum_{c \in \mathbf{L}'} \frac{1}{|\mathbf{L}_{j(c)}} \frac{\sum_i \mathbf{1}(g_i = \mathbf{L}_{j(c)}) \left(\sum_{c' \in \mathbf{L}_{j(c)}} p_{i,c'} \right)}{\sum_i \mathbf{1}(g_i = \mathbf{L}_{j(c)}) + \sum_i \sum_{c' \in \mathbf{L}_{j(c)}} p_{i,c'}} \\ &= 1 - \frac{1}{|\mathbf{L}|} \sum_{\mathbf{L}' \in P} \sum_{c \in \mathbf{L}'} \frac{1}{|\mathbf{L}'|} \frac{\sum_i \mathbf{1}(g_i = \mathbf{L}') \left(\sum_{c' \in \mathbf{L}'} p_{i,c'} \right)}{\sum_i \mathbf{1}(g_i = \mathbf{L}') + \sum_i \sum_{c' \in \mathbf{L}'} p_{i,c'}} \\ &= 1 - \frac{1}{|\mathbf{L}|} \sum_{\mathbf{L}' \in P} \frac{\sum_i \mathbf{1}(g_i = \mathbf{L}') \left(\sum_{c' \in \mathbf{L}'} p_{i,c'} \right)}{\sum_i \mathbf{1}(g_i = \mathbf{L}') + \sum_i \sum_{c' \in \mathbf{L}'} p_{i,c'}} \end{aligned}$$

because for all $\mathbf{L}' \in P$ and all $c \in \mathbf{L}'$, $\mathbf{L}_{j(c)} = \mathbf{L}'$.

The right hand-side of the last equality is the marginal Dice loss [Shi 21] up to the multiplicative constant $\frac{1}{|\mathbf{L}|}$ ■

A.3 Additional Experiments on BraTS 2021

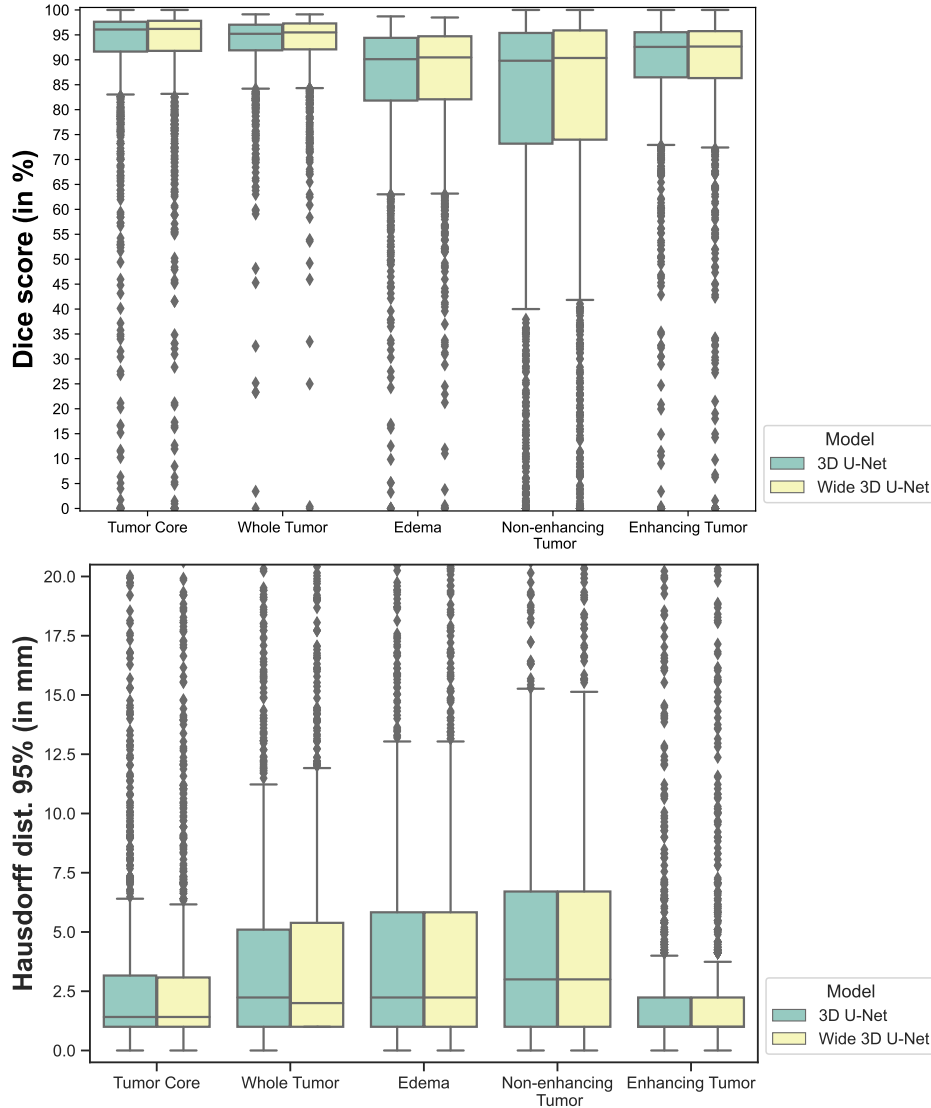


Figure A.1: **Evaluating the capacity of the 3D U-Net architecture on the BraTS 2021 training dataset (1251 cases).** Wide 3D U-Net has the same architecture as 3D U-Net with twice as many features in every internal layers, i.e. it has approximately 4 times more trainable parameters. There is no difference of segmentation performance between the two models which suggests that the 3D U-Net is already large enough for training on this dataset. Each box plot results from 5-fold cross validation on the 1251 cases. Box limits are the first quartiles and third quartiles. The central ticks are the median values. The whiskers extend the boxes to show the rest of the distribution, except for points that are determined to be outliers. Outliers are data points outside the range $\pm 1.5 \times$ interquartile range.

A.4 Proofs of chapter 5

A.4.1 Summary of the Notations used in the Proofs

For the ease of reading the proofs we first summarize our notations.

Probability Theory Notations

- $\Delta_n = \{(p_i)_{i=1}^n \in [0, 1]^n, \sum_i p_i = 1\}$
- Let $\mathbf{q} = (q_i) \in \Delta_n$, and f a function, we denote $\mathbb{E}_{\mathbf{q}}[f(\mathbf{x})] := \sum_{i=1}^n q_i f(\mathbf{x}_i)$.
- Let $\mathbf{q} \in \Delta_n$, and f a function, we denote $\mathbb{V}_{\mathbf{q}}[f(\mathbf{x})] := \sum_{i=1}^n q_i \|f(\mathbf{x}_i) - \mathbb{E}_{\mathbf{q}}[f(\mathbf{x})]\|^2$.
- $\mathbf{p}_{\text{train}}$ is the uniform training data distribution, i.e. $\mathbf{p}_{\text{train}} = \left(\frac{1}{n}\right)_{i=1}^n \in \Delta_n$

Machine Learning Notations

- n is the number of training examples
- d is the dimension of the output
- \mathfrak{d} is the dimension of the input
- m is the number of nodes in each layer
- Training data: $\{(x_i, y_i)\}_{i=1}^n$, where for all $i \in \{1, \dots, n\}$, $x_i \in \mathbb{R}^{\mathfrak{d}}$ and $y_i \in \mathbb{R}^d$
- $h : \mathbf{x} \mapsto y$ is the predictor (deep neural network)
- $\boldsymbol{\theta}$ is the set of parameters of the predictor
- For all i , $h_i : \boldsymbol{\theta} \mapsto h(\mathbf{x}_i; \boldsymbol{\theta})$ is the output of the network for example i as a function of $\boldsymbol{\theta}$
- \mathcal{L} is the objective function
- $\mathcal{L}_i : \mathbf{v} \mapsto \mathcal{L}(\mathbf{v}, y_i)$ is the objective function for example i .
- We denote by \mathbf{L} the vector-valued function $\mathbf{L} : (\mathbf{v}_i)_{i=1}^n \mapsto (\mathcal{L}_i(\mathbf{v}_i))_{i=1}^n$
- $b \in \{1, \dots, n\}$ is the batch size
- $\eta > 0$ is the learning rate
- ERM is short for Empirical Risk Minimization

Distributionally Robust Optimisation Notations

- For all θ , $R(\mathbf{L}(h(\theta))) = \max_{q \in \Delta_n} \mathbb{E}_q [\mathcal{L}(h(x; \theta), y)] - \frac{1}{\beta} D_\phi(q \| \mathbf{p}_{\text{train}})$ is the **Distributionally Robust Loss** evaluated at θ , where $\beta > 0$ is the parameter that adjusts the distributionally robustness. For short, we also used the terms **distributionally robust loss** or just **robust loss** for $R(\mathbf{L}(h(\theta)))$
- DRO is short for Distributionally Robust Optimisation

Miscellaneous

By abuse of notation, and similarly to [Allen-Zhu 19a], we use the Bachmann-Landau notations to hide constants that do not depend on our main hyper-parameters. Let f and g be two scalar functions, we note:

$$\begin{cases} f \leq O(g) & \iff & \exists c > 0 & \text{s.t.} & f \leq cg \\ f \geq \Omega(g) & \iff & \exists c > 0 & \text{s.t.} & f \geq cg \\ f = \Theta(g) & \iff & \exists c_1 > 0 \text{ and } \exists c_2 > c_1 & \text{s.t.} & c_1 g \leq f \leq c_2 g \end{cases}$$

A.4.2 Evaluation of the Influence of β on the Segmentation Performance for BraTS

Table A.1: **Detailed evaluation on the BraTS 2019 online validation set (125 cases)**. All the models in this table were trained using the default **SGD with Nesterov momentum** of nnU-Net [Isensee 21]. Dice scores were computed using the BraTS online platform for evaluation <https://ipp.cbica.upenn.edu/>. ERM: Empirical Risk Minimization, DRO: Distributionally Robust Optimization, IS: Importance Sampling is used, IQR: Interquartile range. The best values are in bold.

Optimization problem	Enhancing Tumor			Whole Tumor			Tumor Core		
	Mean	Median	IQR	Mean	Median	IQR	Mean	Median	IQR
ERM	73.0	87.1	15.6	90.7	92.6	5.4	83.9	90.5	14.3
DRO $\beta = 10$	74.6	86.8	14.1	90.8	93.0	5.9	83.4	90.7	14.5
DRO $\beta = 10$ IS	75.3	86.0	13.3	90.0	91.9	7.0	82.8	89.1	14.3
DRO $\beta = 100$	73.4	86.7	14.3	90.6	92.6	6.2	84.5	90.9	13.7
DRO $\beta = 100$ IS	74.5	87.3	13.8	90.6	92.6	5.9	84.1	90.0	12.5
DRO $\beta = 1000$	74.5	84.2	33.0	89.5	91.8	5.9	71.1	87.2	41.1
DRO $\beta = 1000$ IS	72.2	85.7	15.0	90.3	92.2	6.3	81.1	89.4	15.1

A.4.3 Importance Sampling Approximation in Algorithm 1

In this section, we give additional details about the approximation made in the computation of the importance weights (step 9 of Algorithm 1).

Let $\boldsymbol{\theta}$ be the parameters of the neural network h , $\mathbf{L} = (L_i)_{i=1}^n$ be the stale per-example loss vector, and let i be an index in the current batch I .

We start from the definition of the importance weight w_i for example i and use the formula for the hardness weighted sampling probabilities of Example 5.3.1.

$$\begin{aligned} w_i &= \frac{p_i^{new}}{p_i^{old}} \\ &= \frac{\exp(\beta L_i^{new})}{\exp(\beta L_i^{new}) + \sum_{j \neq i} \exp(\beta L_j^{old})} \times \frac{\sum_{j=1}^n \exp(\beta L_j^{old})}{\exp(\beta L_i^{old})} \quad (\text{A.3}) \\ &\approx \exp(\beta(L_i^{new} - L_i^{old})) \end{aligned}$$

where we have assumed that the two sums of exponentials are approximately equal.

A.4.4 Proof of Example 5.3.1: Formula of the Sampling Probabilities for the KL Divergence

We give here a simple proof of the formula of the sampling probabilities for the KL divergence as ϕ -divergence (i.e. $\phi : z \mapsto z \log(z) - z + 1$)

$$\forall \boldsymbol{\theta}, \quad \bar{p}(\mathbf{L}(h(\boldsymbol{\theta}))) = \text{softmax}(\beta \mathbf{L}(h(\boldsymbol{\theta})))$$

Proof: For any $\boldsymbol{\theta}$, the distributionally robust loss for the KL divergence at $\boldsymbol{\theta}$ is given by

$$\begin{aligned} R \circ \mathbf{L} \circ h(\boldsymbol{\theta}) &= \max_{\mathbf{q} \in \Delta_n} \left(\sum_{i=1}^n q_i \mathcal{L}_i \circ h_i(\boldsymbol{\theta}) - \frac{1}{\beta} \sum_{i=1}^n q_i \log(nq_i) \right) \\ &= \max_{\mathbf{q} \in \Delta_n} \sum_{i=1}^n \left(q_i \mathcal{L}_i \circ h_i(\boldsymbol{\theta}) - \frac{1}{\beta} q_i \log(nq_i) \right) \end{aligned}$$

where we have used that $\frac{1}{p_{\text{train},i}} = n$ inside the log function. To simplify the notations, let us denote $\mathbf{v} = (v_i)_{i=1}^n := (\mathcal{L}_i \circ h_i(\boldsymbol{\theta}))_{i=1}^n$, and $\bar{\mathbf{p}} = (\bar{p}_i)_{i=1}^n := \bar{\mathbf{p}}(\mathbf{L}(h(\boldsymbol{\theta})))$. Thus $\bar{\mathbf{p}}(\mathbf{L}(h(\boldsymbol{\theta})))$ is, by definition, solution of the optimization problem

$$\arg \max_{\mathbf{q} \in \Delta_n} \sum_{i=1}^n \left(q_i v_i - \frac{1}{\beta} q_i \log(nq_i) \right) \quad (\text{A.4})$$

First, let us remark that the function $q \mapsto \sum_{i=1}^n q_i \log(nq_i)$ is strictly convex on the non empty closed convex set Δ_n as a sum of strictly convex functions. This implies that the optimization (A.4) has a unique solution and as a result $\bar{p}(\mathbf{L}(h(\boldsymbol{\theta})))$ is well defined.

We now reformulate the optimization problem (A.4) as a convex smooth constrained optimization problem by writing the condition $\mathbf{q} \in \Delta_n$ as constraints.

$$\begin{aligned} \arg \max_{\mathbf{q} \in \mathbb{R}_+^n} \sum_{i=1}^n \left(q_i v_i - \frac{1}{\beta} q_i \log(nq_i) \right) \\ \text{s.t. } \sum_{i=1}^n q_i = 1 \end{aligned} \quad (\text{A.5})$$

There exists a Lagrange multiplier $\lambda \in \mathbb{R}$, such that the solution \bar{p} of (A.5) is characterized by

$$\begin{cases} \forall i \in \{1, \dots, n\}, & v_i - \frac{1}{\beta} (\log(n\bar{p}_i) + 1) + \lambda = 0 \\ & \sum_{i=1}^n \bar{p}_i = 1 \end{cases} \quad (\text{A.6})$$

Which we can rewrite as

$$\begin{cases} \forall i \in \{1, \dots, n\}, & \bar{p}_i = \frac{1}{n} \exp(\beta(v_i + \lambda) - 1) \\ & \frac{1}{n} \sum_{i=1}^n \exp(\beta(v_i + \lambda) - 1) = 1 \end{cases} \quad (\text{A.7})$$

The last equality gives

$$\exp(\beta\lambda - 1) = \frac{n}{\sum_{i=1}^n \exp(\beta v_i)}$$

And by replacing in the formula of the \bar{p}_i

$$\begin{aligned} \forall i \in \{1, \dots, n\}, \quad \bar{p}_i &= \frac{1}{n} \exp(\beta v_i) \exp(\beta\lambda - 1) \\ &= \frac{\exp(\beta v_i)}{\sum_{j=1}^n \exp(\beta v_j)} \end{aligned}$$

Which corresponds to $\bar{\mathbf{p}} = \text{softmax}(\beta \mathbf{v})$ ■

A.4.5 Proof of Lemma 5.3.1: Regularity Properties of R

For the ease of reading, let us first recall that given a ϕ -divergence D_ϕ that satisfies Definition 5.3.1, we have defined in (5.3)

$$\begin{aligned} R : \mathbb{R}^n &\rightarrow \mathbb{R} \\ \mathbf{v} &\mapsto \max_{\mathbf{q} \in \Delta_n} \sum_i q_i v_i - \frac{1}{\beta} D_\phi(\mathbf{q} \| \mathbf{p}_{\text{train}}) \end{aligned} \quad (\text{A.8})$$

And in (5.4)

$$\begin{aligned} G : \mathbb{R}^n &\rightarrow \mathbb{R} \\ \mathbf{p} &\mapsto \frac{1}{\beta} D_\phi(\mathbf{p} \| \mathbf{p}_{\text{train}}) + \delta_{\Delta_n}(\mathbf{p}) \end{aligned} \quad (\text{A.9})$$

where δ_{Δ_n} is the characteristic function of the closed convex set Δ_n , i.e.

$$\forall \mathbf{p} \in \mathbb{R}^n, \delta_{\Delta_n}(\mathbf{p}) = \begin{cases} 0 & \text{if } \mathbf{p} \in \Delta_n \\ +\infty & \text{otherwise} \end{cases} \quad (\text{A.10})$$

We now prove Lemma 5.3.1 on the regularity of R .

Lemma A.4.1 (Regularity of R – Restated from Lemma 5.3.1). *Let ϕ that satisfies Definition 5.3.1, G and R satisfy*

$$G \text{ is } \left(\frac{n\rho}{\beta}\right)\text{-strongly convex} \quad (\text{A.11})$$

$$R(\mathbf{L}(h(\boldsymbol{\theta}))) = \max_{\mathbf{q} \in \mathbb{R}^n} (\langle \mathbf{L}(h(\boldsymbol{\theta})), \mathbf{q} \rangle - G(\mathbf{q})) = G^*(\mathbf{L}(h(\boldsymbol{\theta}))) \quad (\text{A.12})$$

$$R \text{ is } \left(\frac{\beta}{n\rho}\right)\text{-gradient Lipschitz continuous.} \quad (\text{A.13})$$

Proof: ϕ is ρ -strongly convex on $[0, n]$ so

$$\forall x, y \in [0, n]^2, \forall \lambda \in [0, 1], \phi(\lambda x + (1 - \lambda)y) \leq \lambda\phi(x) + (1 - \lambda)\phi(y) - \frac{\rho\lambda(1 - \lambda)}{2} |y - x|^2 \quad (\text{A.14})$$

Let $\mathbf{p} = (p_i)_{i=1}^n$, $\mathbf{q} = (q_i)_{i=1}^n \in \Delta_n$, and $\lambda \in [0, 1]$, using (A.14) and the convexity of δ_{Δ_n} , we obtain:

$$\begin{aligned} G(\lambda\mathbf{p} + (1-\lambda)\mathbf{q}) &= \frac{1}{\beta n} \sum_{i=1}^n \phi(n\lambda p_i + n(1-\lambda)q_i) + \delta_{\Delta_n}(\lambda\mathbf{p} + (1-\lambda)\mathbf{q}) \\ &\leq \lambda G(\mathbf{p}) + (1-\lambda)G(\mathbf{q}) - \frac{1}{\beta n} \sum_{i=1}^n \frac{\rho\lambda(1-\lambda)}{2} |np_i - nq_i|^2 \quad (\text{A.15}) \\ &\leq \lambda G(\mathbf{p}) + (1-\lambda)G(\mathbf{q}) - \frac{n\rho}{\beta} \frac{\lambda(1-\lambda)}{2} \|\mathbf{p} - \mathbf{q}\|^2 \end{aligned}$$

This proves that G is $\frac{n\rho}{\beta}$ -strongly convex.

Since G is convex, $R = G^*$ is also convex, and $R^* = (G^*)^* = G$ [Hiriart-Urruty 13]. We obtain (A.12) using Definition 5.3.2.

We now show that R is Frechet differentiable on \mathbb{R}^n . Let $\mathbf{v} \in \mathbb{R}^n$.

G is strongly-convex, so in particular G is strictly convex. This implies that the following optimization problem has a unique solution that we denote $\hat{\mathbf{p}}(\mathbf{v})$.

$$\arg \max_{\mathbf{q} \in \mathbb{R}^n} (\langle \mathbf{v}, \mathbf{q} \rangle - G(\mathbf{q})) \quad (\text{A.16})$$

In addition

$$\begin{aligned} \hat{\mathbf{p}} \in \Delta_n \text{ solution of (A.16)} &\iff 0 \in \mathbf{v} - \partial G(\hat{\mathbf{p}}) \\ &\iff \mathbf{v} \in \partial G(\hat{\mathbf{p}}) \\ &\iff \hat{\mathbf{p}} \in \partial G^*(\mathbf{v}) \\ &\iff \hat{\mathbf{p}} \in \partial R(\mathbf{v}) \end{aligned}$$

where we have used [Hiriart-Urruty 13, Proposition 6.1.2 p.39] for the third equivalence, and (A.12) for the last equivalence.

As a result, $\partial R(\mathbf{v}) = \{\hat{\mathbf{p}}(\mathbf{v})\}$. this implies that R admit a gradient at \mathbf{v} , and

$$\nabla_{\mathbf{v}} R(\mathbf{v}) = \hat{\mathbf{p}}(\mathbf{v}) \quad (\text{A.17})$$

Since this holds for any $\mathbf{v} \in \mathbb{R}^n$, we deduce that R is Frechet differentiable on \mathbb{R}^n . ■

We are now ready to show that R is $\frac{\beta}{n\rho}$ -gradient Lipchitz continuous by using the following lemma [Hiriart-Urruty 13, Theorem 6.1.2 p.280].

Lemma A.4.2. *A necessary and sufficient condition for a convex function f :*

$\mathbb{R}^n \rightarrow \mathbb{R}$ to be c -strongly convex on a convex set C is that for all $x_1, x_2 \in C$

$$\langle s_2 - s_1, x_2 - x_1 \rangle \geq c \|x_2 - x_1\|^2 \quad \text{for all } s_i \in \partial f(x_i), i = 1, 2.$$

Using this lemma for $f = G$, $c = \frac{n\rho}{\beta}$, and $C = \Delta_n$, we obtain:

For all $\mathbf{p}_1, \mathbf{p}_2 \in \Delta_n$, for all $\mathbf{v}_1 \in \partial G(\mathbf{p}_1)$, $\mathbf{v}_2 \in \partial G(\mathbf{p}_2)$,

$$\langle \mathbf{v}_2 - \mathbf{v}_1, \mathbf{p}_2 - \mathbf{p}_1 \rangle \geq \frac{n\rho}{\beta} \|\mathbf{p}_2 - \mathbf{p}_1\|^2$$

In addition, for $i \in \{1, 2\}$, $\mathbf{v}_i \in \partial G(\mathbf{p}_i) \iff \mathbf{p}_i \in \partial R(\mathbf{v}_i) = \{\nabla_{\mathbf{v}} R(\mathbf{v}_i)\}$.

And using Cauchy Schwarz inequality

$$\|\mathbf{v}_2 - \mathbf{v}_1\| \|\mathbf{p}_2 - \mathbf{p}_1\| \geq \langle \mathbf{v}_2 - \mathbf{v}_1, \mathbf{p}_2 - \mathbf{p}_1 \rangle$$

We conclude that

$$\frac{n\rho}{\beta} \|\nabla_{\mathbf{v}} R(\mathbf{v}_2) - \nabla_{\mathbf{v}} R(\mathbf{v}_1)\| \leq \|\mathbf{v}_2 - \mathbf{v}_1\|$$

Which implies that R is $\frac{\beta}{n\rho}$ -gradient Lipschitz continuous. ■

A.4.6 Proof of Lemma 5.3.2: Formula of the Distributionally Robust Loss Gradient

We prove Lemma 5.3.2 that we restate here for the ease of reading.

Lemma A.4.3 (Stochastic Gradient of the DRO Loss – Restated from Lemma 5.3.2). *For all $\boldsymbol{\theta}$, we have*

$$\bar{\mathbf{p}}(\mathbf{L}(h(\boldsymbol{\theta}))) = \nabla_{\mathbf{v}} R(\mathbf{L}(h(\boldsymbol{\theta}))) \quad (\text{A.18})$$

$$\nabla_{\boldsymbol{\theta}}(R \circ \mathbf{L} \circ h)(\boldsymbol{\theta}) = \mathbb{E}_{\bar{\mathbf{p}}(\mathcal{L}(h(\boldsymbol{\theta})))} [\nabla_{\boldsymbol{\theta}} \mathcal{L}(h(\mathbf{x}; \boldsymbol{\theta}), y)] \quad (\text{A.19})$$

where $\nabla_{\mathbf{v}} R$ is the gradient of R with respect to its input.

Proof: For a given $\boldsymbol{\theta}$, equality (A.18) is a special case of (A.17) for $\mathbf{v} = \mathcal{L}(h(\boldsymbol{\theta}))$.

Then using the chain rule and (A.18),

$$\begin{aligned} \nabla_{\boldsymbol{\theta}}(R \circ \mathbf{L} \circ h)(\boldsymbol{\theta}) &= \sum_{i=1}^n \frac{\partial R}{\partial v_i}(\mathbf{L} \circ h(\boldsymbol{\theta})) \nabla_{\boldsymbol{\theta}}(\mathcal{L}_i \circ h_i)(\boldsymbol{\theta}) \\ &= \sum_{i=1}^n \bar{p}_i(\mathbf{L}(h(\boldsymbol{\theta}))) \nabla_{\boldsymbol{\theta}}(\mathcal{L}_i \circ h_i)(\boldsymbol{\theta}) \\ &= \mathbb{E}_{\bar{\mathbf{p}}(\mathcal{L}(h(\boldsymbol{\theta})))} [\nabla_{\boldsymbol{\theta}} \mathcal{L}(h(\mathbf{x}; \boldsymbol{\theta}), y)] \end{aligned}$$

Which concludes the proof. ■

A.4.7 Proof of Theorem 5.3.4: Distributionally Robust Optimization as Principled Hard Example Mining

In this section, we demonstrate that the proposed hardness weighted sampling can be interpreted as a principled hard example mining method.

Let D_ϕ an ϕ -divergence satisfying Definition 5.3.1, and $\mathbf{v} = (v_i)_{i=1}^n \in \mathbb{R}^n$. \mathbf{v} will play the role of a generic loss vector.

ϕ is strongly convex, and Δ_n is closed and convex, so the following optimization problem has one and only one solution

$$\max_{\mathbf{p}=(p_i)_{i=1}^n \in \Delta_n} \langle \mathbf{v}, \mathbf{p} \rangle - \frac{1}{\beta n} \sum_{i=1}^n \phi(np_i) \quad (\text{A.20})$$

Making the constraints associated with $p \in \Delta_n$ explicit, this can be rewritten as

$$\begin{aligned} \max_{\mathbf{p}=(p_i)_{i=1}^n \in \mathbb{R}^n} \quad & \langle \mathbf{v}, \mathbf{p} \rangle - \frac{1}{\beta n} \sum_{i=1}^n \phi(np_i) \\ \text{s.t.} \quad & \forall i \in \{1, \dots, n\}, p_i \geq 0 \\ \text{s.t.} \quad & \sum_{i=1}^n p_i = 1 \end{aligned} \quad (\text{A.21})$$

There exists KKT multipliers $\lambda \in \mathbb{R}$ and $\forall i, \mu_i \geq 0$ such that the solution $\bar{\mathbf{p}} = (\bar{p}_i)_{i=1}^n$ satisfies

$$\left\{ \begin{array}{l} \forall i \in \{1, \dots, n\}, \quad v_i - \frac{1}{\beta} \phi'(n\bar{p}_i) + \lambda - \mu_i = 0 \\ \forall i \in \{1, \dots, n\}, \quad \mu_i p_i = 0 \\ \forall i \in \{1, \dots, n\}, \quad p_i \geq 0 \\ \sum_{i=1}^n \bar{p}_i = 1 \end{array} \right. \quad (\text{A.22})$$

Since ϕ is continuously differentiable and strongly convex, we have $(\phi')^{-1} = (\phi^*)'$, where ϕ^* is the Fenchel conjugate of ϕ [Hiriart-Urruty 13, Proposition 6.1.2]. As a

result, (A.22) can be rewritten as

$$\begin{cases} \forall i \in \{1, \dots, n\}, & \bar{p}_i = \frac{1}{n} (\phi^*)'(\beta(v_i + \lambda - \mu_i)) \\ \forall i \in \{1, \dots, n\}, & \mu_i p_i = 0 \\ \forall i \in \{1, \dots, n\}, & p_i \geq 0 \\ & \frac{1}{n} \sum_{i=1}^n (\phi^*)'(\beta(v_i + \lambda - \mu_i)) = 1 \end{cases} \quad (\text{A.23})$$

We now show that the KKT multipliers are uniquely defined.

The μ_i 's are uniquely defined by \mathbf{v} and λ :

Since $\forall i \in \{1, \dots, n\}$, $\mu_i p_i = 0$, $p_i \geq 0$ and $\mu_i \geq 0$, for all $\forall i \in \{1, \dots, n\}$, either $p_i = 0$ or $\mu_i = 0$. In the case $p_i = 0$ and using (A.23) it comes $(\phi^*)'(\beta(v_i + \lambda - \mu_i)) = 0$.

According to Definition 5.3.1, ϕ is strongly convex and continuously differentiable, so ϕ' and $(\phi^*)' = (\phi')^{-1}$ are continuous and strictly increasing functions. As a result, it exists a unique μ_i (dependent to \mathbf{v} and λ) such that:

$$(\phi^*)'(\beta(v_i + \lambda - \mu_i)) = 0$$

And (A.23) can be rewritten as

$$\begin{cases} \forall i \in \{1, \dots, n\}, & \bar{p}_i = \text{ReLU} \left(\frac{1}{n} (\phi^*)'(\beta(v_i + \lambda)) \right) = \frac{1}{n} \text{ReLU} \left((\phi^*)'(\beta(v_i + \lambda)) \right) \\ & \frac{1}{n} \sum_{i=1}^n \text{ReLU} \left((\phi^*)'(\beta(v_i + \lambda)) \right) = 1 \end{cases} \quad (\text{A.24})$$

The KKT multiplier λ is uniquely defined by \mathbf{v} and a continuous function of \mathbf{v} :

Let $\lambda \in \mathbb{R}$ that satisfies (A.24). We have $\frac{1}{n} \sum_{i=1}^n \text{ReLU} \left((\phi^*)'(\beta(v_i + \lambda)) \right) = 1$. So there exists at least one index i_0 such that

$$\text{ReLU} \left((\phi^*)'(\beta(v_{i_0} + \lambda)) \right) = (\phi^*)'(\beta(v_{i_0} + \lambda)) \geq 1$$

Since $(\phi^*)^{-1}$ is continuous and strictly increasing, $\lambda' \mapsto \text{ReLU} \left((\phi^*)'(\beta(v_{i_0} + \lambda')) \right)$ is continuous and strictly increasing on a neighborhood of λ . In addition ReLU is continuous and increasing, so for all $i \in \{1, \dots, n\}$, $\lambda' \mapsto \text{ReLU} \left((\phi^*)'(\beta(v_i + \lambda')) \right)$ is a continuous and increasing function.

As a result, $\lambda' \mapsto \frac{1}{n} \sum_{i=1}^n \text{ReLU} \left((\phi^*)' (\beta(v_i + \lambda')) \right)$ is a continuous function that is increasing on \mathbb{R} , and strictly increasing on a neighborhood of λ . This implies that λ is uniquely defined by \mathbf{v} , and that $\mathbf{v} \mapsto \lambda(\mathbf{v})$ is continuous.

Link between Hard Weighted Sampling and Hard Example Mining

For any pseudo loss vector $\mathbf{v} = (v_i)_{i=1}^n \in \mathbb{R}^n$, there exists a unique KKT multiplier λ and a unique $\bar{\mathbf{p}}$ that satisfies (A.24), so we can define the mapping:

$$\begin{aligned} \bar{\mathbf{p}} : \mathbb{R}^n &\rightarrow \Delta_n \\ \mathbf{v} &\mapsto \bar{\mathbf{p}}(\mathbf{v}; \lambda(\mathbf{v})) \end{aligned} \tag{A.25}$$

where for all \mathbf{v} , $\lambda(\mathbf{v})$ is the unique $\lambda \in \mathbb{R}$ satisfying (A.24).

We will now demonstrate that each $\bar{p}_{i_0}(\mathbf{v})$ for $i_0 \in \{1, \dots, n\}$ is an increasing function of v_{i_0} and a decreasing function of the v_i for $i \neq i_0$. Without loss of generality we assume $i_0 = 1$.

Let $\mathbf{v} = (v_i)_{i=1}^n \in \mathbb{R}^n$, and $\epsilon > 0$. Let us define $\mathbf{v}' = (v'_i)_{i=1}^n \in \mathbb{R}^n$, such that $v'_1 = v_1 + \epsilon$ and $\forall i \in \{2, \dots, n\}$, $v'_i = v_i$. Similarly as in the proof of the uniqueness of λ above, we can show that there exists $\eta > 0$ such that the function

$$F : \lambda' \mapsto \frac{1}{n} \sum_{i=1}^n \text{ReLU} \left((\phi^*)' (\beta(v_i + \lambda')) \right)$$

is continuous and strictly increasing on $[\lambda(\mathbf{v}) - \eta, \lambda(\mathbf{v}) + \eta]$, and $F(\lambda(\mathbf{v})) = 1$.

$\mathbf{v} \mapsto \lambda(\mathbf{v})$ is continuous, so for ϵ small enough $\lambda(\mathbf{v}') \in [\lambda(\mathbf{v}) - \eta, \lambda(\mathbf{v}) + \eta]$.

Let us now prove by contradiction that $\lambda(\mathbf{v}') \leq \lambda(\mathbf{v})$. Therefore, let us assume that $\lambda(\mathbf{v}') > \lambda(\mathbf{v})$. Then, as $\text{ReLU} \circ (\phi^*)'$ is an increasing function and F is strictly increasing on $[\lambda(\mathbf{v}) - \eta, \lambda(\mathbf{v}) + \eta]$, and $\epsilon > 0$ we obtain

$$\begin{aligned} 1 &= \frac{1}{n} \sum_{i=1}^n \text{ReLU} \left((\phi^*)' (\beta(v'_i + \lambda(\mathbf{v}')) \right) \\ &\geq \frac{1}{n} \sum_{i=1}^n \text{ReLU} \left((\phi^*)' (\beta(v_i + \lambda(\mathbf{v}')) \right) \\ &\geq F(\lambda(\mathbf{v}')) \\ &> F(\lambda(\mathbf{v})) \\ &> 1 \end{aligned}$$

which is a contradiction. As a result

$$\lambda(\mathbf{v}') \leq \lambda(\mathbf{v}) \tag{A.26}$$

Using equations (A.24) and (A.26), and the fact that $\text{ReLU} \circ (\phi^*)'$ is an increasing function, we obtain for all $i \in \{2, \dots, n\}$

$$\begin{aligned} \bar{p}_i(\mathbf{v}') &= \frac{1}{n} \text{ReLU} \left((\phi^*)' (\beta(v'_i + \lambda(\mathbf{v}')))) \right) \\ &= \frac{1}{n} \text{ReLU} \left((\phi^*)' (\beta(v_i + \lambda(\mathbf{v}')))) \right) \\ &\leq \frac{1}{n} \text{ReLU} \left((\phi^*)' (\beta(v_i + \lambda(\mathbf{v}))) \right) \\ &\leq \bar{p}_i(\mathbf{v}) \end{aligned} \tag{A.27}$$

In addition

$$\sum_{i=1}^n \bar{p}_i(\mathbf{v}') = 1 = \sum_{i=1}^n \bar{p}_i(\mathbf{v})$$

So necessarily

$$\bar{p}_1(\mathbf{v}') \geq \bar{p}_1(\mathbf{v}) \tag{A.28}$$

This holds for any i_0 and any \mathbf{v} , which concludes the proof. ■

A.4.8 Proof of Equivalence between (5.17) and (5.18): Link between DRO and Percentile Loss

In the DRO optimization problem of equation (5.18), the optimal \mathbf{q} for any $\boldsymbol{\theta}$ has the closed-form formula as shown in Appendix A.4.4

$$\forall \boldsymbol{\theta}, \quad \mathbf{q}^*(\boldsymbol{\theta}) = \text{softmax} \left((\beta \mathcal{L}(h(\mathbf{x}_i; \boldsymbol{\theta}), \mathbf{y}_i))_{i=1}^n \right)$$

By injecting this in equation (5.18), we obtain

$$\begin{aligned} &\min_{\boldsymbol{\theta}} \max_{\mathbf{q} \in \Delta_n} \left(\sum_{i=1}^n q_i \mathcal{L}(h(\mathbf{x}_i; \boldsymbol{\theta}), \mathbf{y}_i) - \frac{1}{\beta} D_{KL} \left(\mathbf{q} \parallel \frac{1}{n} \mathbf{1} \right) \right) \\ &= \min_{\boldsymbol{\theta}} \left(\sum_{i=1}^n q_i^*(\boldsymbol{\theta}) \mathcal{L}(h(\mathbf{x}_i; \boldsymbol{\theta}), \mathbf{y}_i) - \frac{1}{\beta} \sum_{i=1}^n q_i^*(\boldsymbol{\theta}) \log \left(\frac{\exp(\beta \mathcal{L}(h(\mathbf{x}_i; \boldsymbol{\theta}), \mathbf{y}_i))}{\frac{1}{n} \sum_{j=1}^n \exp(\beta \mathcal{L}(h(\mathbf{x}_j; \boldsymbol{\theta}), \mathbf{y}_j))} \right) \right) \\ &= \min_{\boldsymbol{\theta}} \left(\sum_{i=1}^n q_i^*(\boldsymbol{\theta}) \mathcal{L}(h(\mathbf{x}_i; \boldsymbol{\theta}), \mathbf{y}_i) - \sum_{i=1}^n q_i^*(\boldsymbol{\theta}) \frac{1}{\beta} \log(\exp(\beta \mathcal{L}(h(\mathbf{x}_i; \boldsymbol{\theta}), \mathbf{y}_i))) \right. \\ &\quad \left. + \frac{1}{\beta} \left(\sum_{i=1}^n q_i^*(\boldsymbol{\theta}) \right) \times \log \left(\frac{1}{n} \sum_{j=1}^n \exp(\beta \mathcal{L}(h(\mathbf{x}_j; \boldsymbol{\theta}), \mathbf{y}_j)) \right) \right) \end{aligned}$$

Since the first two terms cancel each other and $\sum_{i=1}^n q_i^*(\boldsymbol{\theta}) = 1$, we obtain

$$\begin{aligned} & \min_{\boldsymbol{\theta}} \max_{\mathbf{q} \in \Delta_n} \left(\sum_{i=1}^n q_i \mathcal{L}(h(\mathbf{x}_i; \boldsymbol{\theta}), \mathbf{y}_i) - \frac{1}{\beta} D_{KL} \left(\mathbf{q} \parallel \frac{1}{n} \mathbf{1} \right) \right) \\ &= \min_{\boldsymbol{\theta}} \frac{1}{\beta} \log \left(\sum_{j=1}^n \exp(\beta \mathcal{L}(h(\mathbf{x}_j; \boldsymbol{\theta}), \mathbf{y}_j)) \right) - \frac{1}{\beta} \log(n) \\ &= \min_{\boldsymbol{\theta}} \frac{1}{\beta} \log \left(\sum_{j=1}^n \exp(\beta \mathcal{L}(h(\mathbf{x}_j; \boldsymbol{\theta}), \mathbf{y}_j)) \right) \end{aligned}$$

which is equivalent to the optimization problem (5.17) because the term $\frac{1}{\beta} \log(n)$ above and the term $\frac{1}{\beta} \log(\alpha n)$ in (5.17) are independent of $\boldsymbol{\theta}$ ■

A.4.9 Proof of Theorem 5.3.3: convergence of SGD with Hardness Weighted Sampling for Over-parameterized Deep Neural Networks with ReLU

In this section, we provide the proof of Theorem 5.3.3. This generalizes the convergence of SGD for empirical risk minimization in [Allen-Zhu 19a, Theorem 2] to the convergence of SGD and our proposed hardness weighted sampler for distributionally robust optimization.

We start by describing in details the assumptions made for our convergence result in Section A.4.9.

In Section A.4.9, we restate Theorem 5.3.3 using the assumptions and notations previously introduced in Section A.4.1.

In Section A.4.9, we give the proof of the convergence theorem. We focus on providing theoretical tools that could be used to generalize any convergence result for ERM using SGD to DRO using SGD with hardness weighted sampling as described in Algorithm 1.

Assumptions

Our analysis is based on the results developed in [Allen-Zhu 19a] which is a simplified version of [Allen-Zhu 19b]. Improving on those theoretical results would automatically improve our results as well.

In the following we state our assumptions on the neural network h , and the per-example loss function \mathcal{L} .

Assumption A.4.1 (Deep Neural Network). *In this section, we use the following notations and assumptions similar to [Allen-Zhu 19a]:*

- h is a fully connected neural network with $L + 2$ layers, ReLU as activation functions, and m nodes in each hidden layer
- For all $i \in \{1, \dots, n\}$, we denote $h_i : \boldsymbol{\theta} \mapsto h_i(\mathbf{x}_i; \boldsymbol{\theta})$ the d -dimensional output scores of h applied to example \mathbf{x}_i of dimension \mathfrak{d} .
- For all $i \in \{1, \dots, n\}$, we denote $\mathcal{L}_i : h \mapsto \mathcal{L}(h, y_i)$ where y_i is the ground truth associated to example i .
- $\boldsymbol{\theta} = (\boldsymbol{\theta}_l)_{l=0}^{L+1}$ is the set of parameters of the neural network h , where $\boldsymbol{\theta}_l$ is the set of weights for layer l with $\boldsymbol{\theta}_0 \in \mathbb{R}^{\mathfrak{d} \times m}$, $\boldsymbol{\theta}_{L+1} \in \mathbb{R}^{m \times d}$, and $\boldsymbol{\theta}_l \in \mathbb{R}^{m \times m}$ for any other l .
- (Data separation) It exists $\delta > 0$ such that for all $i, j \in \{1, \dots, n\}$, if $i \neq j$, $\|\mathbf{x}_i - \mathbf{x}_j\| \geq \delta$.
- We assume $m \geq \Omega(d \times \text{poly}(n, L, \delta^{-1}))$ for some sufficiently large polynomial poly , and $\delta \geq O\left(\frac{1}{L}\right)$. We refer the reader to [Allen-Zhu 19a] for details about the polynomial poly .
- The parameters $\boldsymbol{\theta} = (\boldsymbol{\theta}_l)_{l=0}^{L+1}$ are initialized at random such that:
 - $[\boldsymbol{\theta}_0]_{i,j} \sim \mathcal{N}\left(0, \frac{2}{m}\right)$ for every $(i, j) \in \{1, \dots, m\} \times \{1, \dots, \mathfrak{d}\}$
 - $[\boldsymbol{\theta}_l]_{i,j} \sim \mathcal{N}\left(0, \frac{2}{m}\right)$ for every $(i, j) \in \{1, \dots, m\}^2$ and $l \in \{1, \dots, L\}$
 - $[\boldsymbol{\theta}_{L+1}]_{i,j} \sim \mathcal{N}\left(0, \frac{1}{d}\right)$ for every $(i, j) \in \{1, \dots, d\} \times \{1, \dots, m\}$

Assumption A.4.2 (Regularity of \mathcal{L}). For all i , \mathcal{L}_i is a $C(\nabla \mathcal{L})$ -gradient Lipschitz continuous, $C(\mathcal{L})$ -Lipschitz continuous, and bounded (potentially non-convex) function.

Convergence theorem (restated)

In this section, we restate the convergence Theorem 5.3.3 for SGD with hardness weighted sampling and stale per-example loss vector.

As an intermediate step, we will first generalize the convergence of SGD in [Allen-Zhu 19a, Theorem 2] to the minimization of the distributionally robust loss using SGD and an *exact* hardness weighted sampling (5.10), i.e. with an exact per-example loss vector.

Theorem A.4.4 (Convergence with exact per-example loss vector). Let batch size $1 \leq b \leq n$, and $\epsilon > 0$. Suppose there exists constants $C_1, C_2, C_3 > 0$ such that the number of hidden units satisfies $m \geq C_1(d\epsilon^{-1} \times \text{poly}(n, L, \delta^{-1}))$, $\delta \geq \left(\frac{C_2}{L}\right)$, and the

learning rate be $\eta_{exact} = C_3 \left(\min \left(1, \frac{\alpha n^2 \rho}{\beta C(\mathcal{L})^2 + 2n\rho C(\nabla \mathcal{L})} \right) \times \frac{b\delta d}{\text{poly}(n, L)m \log^2(m)} \right)$. There exists constants $C_4, C_5 > 0$ such that with probability at least $1 - \exp(-C_4(\log^2(m)))$ over the randomness of the initialization and the mini-batches, SGD with hardness weighted sampling and exact per-example loss vector guarantees $\|\nabla_{\boldsymbol{\theta}}(R \circ \mathbf{L} \circ h)(\boldsymbol{\theta})\| \leq \epsilon$ after $T = C_5 \left(\frac{Ln^3}{\eta_{exact}\delta\epsilon^2} \right)$ iterations.

The proof can be found in Appendix A.4.9.

$\alpha = \min_{\boldsymbol{\theta}} \min_i \bar{p}_i(\mathbf{L}(\boldsymbol{\theta}))$ is a lower bound on the sampling probabilities. For the Kullback-Leibler ϕ -divergence, and for any ϕ -divergence satisfying Definition 5.3.1 with a robustness parameter β small enough, we have $\alpha > 0$. We refer the reader to [Allen-Zhu 19a, Theorem 2] for the values of the constants C_1, C_2, C_3, C_4, C_5 and the definitions of the polynomials.

Compared to [Allen-Zhu 19a, Theorem 2] only the learning rate differs. The $\min(1, \cdot)$ operation in the formula for η_{exact} allows us to guarantee that $\eta_{exact} \leq \eta'$ where η' is the learning rate of [Allen-Zhu 19a, Theorem 2].

It is worth noting that for the KL ϕ -divergence, $\rho = \frac{1}{n}$. In addition, in the limit $\beta \rightarrow 0$, which corresponds to ERM, we have $\alpha \rightarrow \frac{1}{n}$. As a result, we recover exactly Theorem 2 of [Allen-Zhu 19a] as extended in their Appendix A for any smooth loss function \mathcal{L} that satisfies assumption A.4.2 with $C(\nabla \mathcal{L}) = 1$.

We now restate the convergence of SGD with hardness weighted sampling and a stale per-example loss vector as in Algorithm 1.

Theorem A.4.5 (Convergence with a stale per-example loss vector). *Let batch size $1 \leq b \leq n$, and $\epsilon > 0$. Under the conditions of Theorem A.4.4, the same notations, and with the learning rate $\eta_{stale} = C_6 \min \left(1, \frac{\alpha \rho d^{3/2} \delta b \log(\frac{1}{1-\alpha})}{\beta C(\mathcal{L})A(\nabla \mathcal{L})Lm^{3/2}n^{3/2} \log^2(m)} \right) \times \eta_{exact}$ for a constant $C_6 > 0$. With probability at least $1 - \exp(-C_4(\log^2(m)))$ over the randomness of the initialization and the mini-batches, SGD with hardness weighted sampling and stale per-example loss vector guarantees $\|\nabla_{\boldsymbol{\theta}}(R \circ \mathbf{L} \circ h)(\boldsymbol{\theta})\| \leq \epsilon$ after $T = C_5 \left(\frac{Ln^3}{\eta_{stale}\delta\epsilon^2} \right)$ iterations.*

The proof can be found in Appendix A.4.9.

$C(\mathcal{L}) > 0$ is a constant such that \mathcal{L} is $C(\mathcal{L})$ -Lipschitz continuous, and $A(\nabla \mathcal{L}) > 0$ is a constant that bounds the gradient of \mathcal{L} with respect to its input. $C(\mathcal{L})$ and $A(\nabla \mathcal{L})$ are guaranteed to exist under assumptions A.4.1.

Compared to Theorem A.4.4 only the learning rate differs. Similarly to Theorem A.4.4, when β tends to zero we recover Theorem 2 of [Allen-Zhu 19a].

It is worth noting that when β increases, $\frac{\alpha \rho d^{3/2} \delta b \log(\frac{1}{1-\alpha})}{\beta C(\mathcal{L})A(\nabla \mathcal{L})Lm^{3/2}n^{3/2} \log^2(m)}$ decreases. This implies that η_{stale} decreases faster than η_{exact} when β increases. This was to

be expected since the error that is made by using the stale per-example loss vector instead of the exact loss increases when β increases.

Proofs of convergence

In this section, we prove the results of Theorem A.4.4 and A.4.5.

For the ease of reading the proof, we remind here the chain rules for the distributionally robust loss that we are going to use intensively in the following proofs.

Chain rule for the derivative of $R \circ L$ with respect to the network outputs h :

$$\begin{aligned} \nabla_h(R \circ L)(h(\boldsymbol{\theta})) &= (\nabla_{h_i}(R \circ L)(h(\boldsymbol{\theta})))_{i=1}^n \\ \forall i \in \{1, \dots, n\}, \quad \nabla_{h_i}(R \circ L)(h(\boldsymbol{\theta})) &= \sum_{j=1}^n \frac{\partial R}{\partial v_j}(\mathbf{L}(h(\boldsymbol{\theta}))) \nabla_{h_i} \mathcal{L}_j(h_j(\boldsymbol{\theta})) \\ &= \bar{p}_i(\mathbf{L}(h(\boldsymbol{\theta}))) \nabla_{h_i} \mathcal{L}_i(h_i(\boldsymbol{\theta})) \end{aligned} \quad (\text{A.29})$$

Chain rule for the derivative of $R \circ L \circ h$ with respect to the network parameters $\boldsymbol{\theta}$:

$$\begin{aligned} \nabla_{\boldsymbol{\theta}}(R \circ L \circ h)(\boldsymbol{\theta}) &= \sum_{i=1}^n \nabla_{\boldsymbol{\theta}} h_i(\boldsymbol{\theta}) \nabla_{h_i}(R \circ L)(h(\boldsymbol{\theta})) \\ &= \sum_{i=1}^n \bar{p}_i(\mathbf{L}(h(\boldsymbol{\theta}))) \nabla_{\boldsymbol{\theta}} h_i(\boldsymbol{\theta}) \nabla_{h_i} \mathcal{L}_i(h_i(\boldsymbol{\theta})) \\ &= \sum_{i=1}^n \bar{p}_i(\mathbf{L}(h(\boldsymbol{\theta}))) \nabla_{\boldsymbol{\theta}} (\mathcal{L}_i \circ h_i)(\boldsymbol{\theta}) \end{aligned} \quad (\text{A.30})$$

where for all $i \in \{1, \dots, n\}$, $\nabla_{\boldsymbol{\theta}} h_i(\boldsymbol{\theta})$ is the transpose of the Jacobian matrix of h_i as a function of $\boldsymbol{\theta}$.

Proof that $R \circ L$ is one-sided gradient Lipschitz

This property that $R \circ L$ is one-sided gradient Lipschitz is a key element for the proof of the semi-smoothness theorem for the distributionally robust loss Theorem A.4.6.

Under Definition 5.3.1 for the ϕ -divergence, we have shown that R is $\frac{\beta}{n\rho}$ -gradient Lipschitz continuous (Lemma 5.3.1). And under assumption A.4.2, for all i , \mathcal{L}_i is $C(\mathcal{L})$ -Lipschitz continuous and $C(\nabla \mathcal{L})$ -gradient Lipschitz continuous.

Let $\mathbf{z} = (z_i)_{i=1}^n$, $\mathbf{z}' = (z'_i)_{i=1}^n \in \mathbb{R}^{dn}$.

We want to show that $R \circ \mathbf{L}$ is one-sided gradient Lipschitz, i.e. we want to prove the existence of a constant $C > 0$, independent to z and z' , such that:

$$\langle \nabla_{\mathbf{z}}(R \circ \mathbf{L})(z) - \nabla_{\mathbf{z}}(R \circ \mathbf{L})(z'), z - z' \rangle \leq C \|z - z'\|^2$$

We have

$$\begin{aligned} & \langle \nabla_{\mathbf{z}}(R \circ \mathbf{L})(z) - \nabla_{\mathbf{z}}(R \circ \mathbf{L})(z'), z - z' \rangle \\ &= \sum_{i=1}^n \langle \nabla_{z_i}(R \circ \mathbf{L})(z) - \nabla_{z_i}(R \circ \mathbf{L})(z'), z_i - z'_i \rangle \\ &= \sum_{i=1}^n \langle \bar{p}_i(\mathbf{L}(z)) \nabla_{z_i} \mathcal{L}_i(z_i) - \bar{p}_i(\mathbf{L}(z')) \nabla_{z_i} \mathcal{L}_i(z'_i), z_i - z'_i \rangle \\ &= \sum_{i=1}^n \bar{p}_i(\mathbf{L}(z)) \langle \nabla_{z_i} \mathcal{L}_i(z_i) - \nabla_{z_i} \mathcal{L}_i(z'_i), z_i - z'_i \rangle \\ &\quad + \sum_{i=1}^n (\bar{p}_i(\mathbf{L}(z)) - \bar{p}_i(\mathbf{L}(z'))) \langle \nabla_{z_i} \mathcal{L}_i(z'_i), z_i - z'_i \rangle \end{aligned} \tag{A.31}$$

Where for all $i \in \{1, \dots, n\}$ we have used the chain rule

$$\nabla_{z_i}(R \circ \mathbf{L})(z) = \sum_{j=1}^n \frac{\partial R}{\partial v_j}(\mathcal{L}(z)) \nabla_{z_i} \mathcal{L}_j(z_j) = \bar{p}_i(\mathbf{L}(z)) \nabla_{z_i} \mathcal{L}_i(z_i)$$

Let

$$A = \left| \sum_{i=1}^n \bar{p}_i(\mathbf{L}(z)) \langle \nabla_{z_i} \mathcal{L}_i(z_i) - \nabla_{z_i} \mathcal{L}_i(z'_i), z_i - z'_i \rangle \right|$$

For all i , \mathcal{L}_i is $C(\nabla \mathcal{L})$ -gradient Lipschitz continuous, so using Cauchy-Schwarz inequality

$$A \leq \sum_{i=1}^n C(\nabla \mathcal{L}) \|z_i - z'_i\|^2 = C(\nabla \mathcal{L}) \|z - z'\|^2 \tag{A.32}$$

Let

$$B = \left| \sum_{i=1}^n (\bar{p}_i(\mathbf{L}(z)) - \bar{p}_i(\mathbf{L}(z'))) \langle \nabla_{z_i} \mathcal{L}_i(z'_i), z_i - z'_i \rangle \right|$$

Using the triangular inequality:

$$\begin{aligned}
B &\leq \left| \sum_{i=1}^n (\bar{p}_i(\mathbf{L}(\mathbf{z})) - \bar{p}_i(\mathbf{L}(\mathbf{z}')))(\mathcal{L}_i(z_i) - \mathcal{L}_i(z'_i)) \right| \\
&\quad + \left| \sum_{i=1}^n (\bar{p}_i(\mathbf{L}(\mathbf{z})) - \bar{p}_i(\mathbf{L}(\mathbf{z}')))(\mathcal{L}_i(z'_i) + \langle \nabla_{z_i} \mathcal{L}_i(z'_i), z_i - z'_i \rangle - \mathcal{L}_i(z_i)) \right| \\
&\leq \langle \nabla_{\mathbf{L}} R(\mathbf{L}(\mathbf{z})) - \nabla_{\mathbf{L}} R(\mathbf{L}(\mathbf{z}')), \mathbf{L}(\mathbf{z}) - \mathbf{L}(\mathbf{z}') \rangle \\
&\quad + 2 \sum_{i=1}^n \left| \mathcal{L}_i(z'_i) + \langle \nabla_{z_i} \mathcal{L}_i(z'_i), z_i - z'_i \rangle - \mathcal{L}_i(z_i) \right| \\
&\leq \frac{\beta}{n\rho} \|\mathbf{L}(\mathbf{z}) - \mathbf{L}(\mathbf{z}')\|^2 + 2 \frac{C(\nabla \mathcal{L})}{2} \|\mathbf{z} - \mathbf{z}'\|^2 \\
&\leq \left(\frac{\beta C(\mathcal{L})^2}{n\rho} + C(\nabla \mathcal{L}) \right) \|\mathbf{z} - \mathbf{z}'\|^2
\end{aligned} \tag{A.33}$$

Combining equations (A.31), (A.32) and (A.33) we finally obtain

$$\langle \nabla_{\mathbf{z}}(R \circ \mathbf{L})(\mathbf{z}) - \nabla_{\mathbf{z}}(R \circ \mathbf{L})(\mathbf{z}'), \mathbf{z} - \mathbf{z}' \rangle \leq \left(\frac{\beta C(\mathcal{L})^2}{n\rho} + 2C(\nabla \mathcal{L}) \right) \|\mathbf{z} - \mathbf{z}'\|^2 \tag{A.34}$$

From there, we can obtain the following inequality that will be used for the proof of the semi-smoothness property in Theorem A.4.6

$$\begin{aligned}
&R(\mathbf{L}(\mathbf{z}')) - R(\mathbf{L}(\mathbf{z})) - \langle \nabla_{\mathbf{z}}(R \circ \mathbf{L})(\mathbf{z}), \mathbf{z}' - \mathbf{z} \rangle \\
&= \int_{t=0}^1 \langle \nabla_{\mathbf{z}}(R \circ \mathbf{L})(\mathbf{z} + t(\mathbf{z}' - \mathbf{z})) - \nabla_{\mathbf{z}}(R \circ \mathbf{L})(\mathbf{z}), \mathbf{z}' - \mathbf{z} \rangle dt \\
&\leq \frac{1}{2} \left(\frac{\beta C(\mathcal{L})^2}{n\rho} + 2C(\nabla \mathcal{L}) \right) \|\mathbf{z} - \mathbf{z}'\|^2
\end{aligned} \tag{A.35}$$

Semi-smoothness property of the distributionally robust loss

We prove the following lemma which is a generalization of Theorem 4 in [Allen-Zhu 19a] for the distributionally robust loss.

Theorem A.4.6 (Semi-smoothness of the distributionally robust loss).

Let $\omega \in \left[\Omega \left(\frac{d^{3/2}}{m^{3/2} L^{3/2} \log^{3/2}(m)} \right), O \left(\frac{1}{L^{4.5} \log^3(m)} \right) \right]$, and the $\boldsymbol{\theta}^{(0)}$ being initialized randomly as described in assumption A.4.1. With probability at least $1 - \exp\{-\Omega(m\omega^{3/2}L)\}$ over the initialization, we have for all $\boldsymbol{\theta}, \boldsymbol{\theta}' \in (\mathbb{R}^{m \times m})^L$ with $\|\boldsymbol{\theta} - \boldsymbol{\theta}^{(0)}\|_2 \leq \omega$, and

$$\|\boldsymbol{\theta} - \boldsymbol{\theta}'\|_2 \leq \omega$$

$$\begin{aligned} R(\mathbf{L}(h(\boldsymbol{\theta}')) &\leq R(\mathbf{L}(h(\boldsymbol{\theta}))) + \langle \nabla_{\boldsymbol{\theta}}(R \circ \mathbf{L} \circ h)(\boldsymbol{\theta}), \boldsymbol{\theta}' - \boldsymbol{\theta} \rangle \\ &+ \|\nabla_h(R \circ \mathbf{L})(h(\boldsymbol{\theta}))\|_{2,1} O\left(\frac{L^2 \omega^{1/3} \sqrt{m \log(m)}}{\sqrt{d}}\right) \|\boldsymbol{\theta}' - \boldsymbol{\theta}\|_{2,\infty} \quad (\text{A.36}) \\ &+ O\left(\left(\frac{\beta C(\mathcal{L})^2}{n\rho} + 2C(\nabla \mathcal{L})\right) \frac{nL^2 m}{d}\right) \|\boldsymbol{\theta}' - \boldsymbol{\theta}\|_{2,\infty}^2 \end{aligned}$$

where for all layer $l \in \{1, \dots, L\}$, $\boldsymbol{\theta}_l$ is the vector of parameters for layer l , and

$$\begin{aligned} \|\boldsymbol{\theta}' - \boldsymbol{\theta}\|_{2,\infty} &= \max_l \|\boldsymbol{\theta}'_l - \boldsymbol{\theta}_l\|_2 \\ \|\boldsymbol{\theta}' - \boldsymbol{\theta}\|_{2,\infty}^2 &= \left(\max_l \|\boldsymbol{\theta}'_l - \boldsymbol{\theta}_l\|_2^2\right) = \max_l \|\boldsymbol{\theta}'_l - \boldsymbol{\theta}_l\|_2^2 \\ \|\nabla_h(R \circ \mathbf{L})(h(\boldsymbol{\theta}))\|_{2,1} &= \sum_{i=1}^n \|\nabla_{h_i}(R \circ \mathbf{L})(h(\boldsymbol{\theta}))\|_2 \\ &= \sum_{i=1}^n \left\| \bar{p}_i(\mathbf{L}(h(\boldsymbol{\theta}))) \nabla_{h_i} \mathcal{L}_i(h_i(\boldsymbol{\theta})) \right\|_2 \quad (\text{chain rule (A.29)}) \end{aligned}$$

To compare this semi-smoothness result to the one in [Allen-Zhu 19a, Theorem 4], let us first remark that

$$\|\nabla_h(R \circ \mathbf{L})(h(\boldsymbol{\theta}))\|_{2,1} \leq \sqrt{n} \|\nabla_h(R \circ \mathbf{L})(h(\boldsymbol{\theta}))\|_{2,2}$$

As a result, our result is analogous to [Allen-Zhu 19a, Theorem 4], up to an additional multiplicative factor $\left(\frac{\beta C(\mathcal{L})^2}{n\rho} + 2C(\nabla \mathcal{L})\right)$ in the last term of the right-hand side. It is worth noting that there is also implicitly an additional multiplicative factor $C(\nabla \mathcal{L})$ in Theorem 3 of [Allen-Zhu 19a] since [Allen-Zhu 19a] make the assumption that $C(\nabla \mathcal{L}) = 1$ [Allen-Zhu 19a, Appendix A].

Let $\boldsymbol{\theta}, \boldsymbol{\theta}' \in (\mathbb{R}^{m \times m})^L$ verifying the conditions of Theorem A.4.6.

Let $A = R(\mathbf{L}(h(\boldsymbol{\theta}')) - R(\mathbf{L}(h(\boldsymbol{\theta}))) - \langle \nabla_{\boldsymbol{\theta}}(R \circ \mathbf{L} \circ h)(\boldsymbol{\theta}), \boldsymbol{\theta}' - \boldsymbol{\theta} \rangle$, the quantity we want to bound.

Using (A.35) for $\mathbf{z} = h(\boldsymbol{\theta})$ and $\mathbf{z}' = h(\boldsymbol{\theta}')$, we obtain

$$\begin{aligned} A &\leq \frac{1}{2} \left(\frac{\beta C(\mathcal{L})^2}{n\rho} + 2C(\nabla \mathcal{L}) \right) \|h(\boldsymbol{\theta}') - h(\boldsymbol{\theta})\|_2^2 \\ &+ \langle \nabla_h(R \circ \mathbf{L})(h(\boldsymbol{\theta})), h(\boldsymbol{\theta}') - h(\boldsymbol{\theta}) \rangle \\ &- \langle \nabla_{\boldsymbol{\theta}}(R \circ \mathbf{L} \circ h)(\boldsymbol{\theta}), \boldsymbol{\theta}' - \boldsymbol{\theta} \rangle \end{aligned} \quad (\text{A.37})$$

Then using the chain rule (A.30)

$$\begin{aligned}
A &\leq \frac{1}{2} \left(\frac{\beta C(\mathcal{L})^2}{n\rho} + 2C(\nabla \mathcal{L}) \right) \|h(\boldsymbol{\theta}') - h(\boldsymbol{\theta})\|_2^2 \\
&\quad + \sum_{i=1}^n \langle \nabla_{h_i}(R \circ \mathbf{L})(h(\boldsymbol{\theta})), h_i(\boldsymbol{\theta}') - h_i(\boldsymbol{\theta}) - (\nabla_{\boldsymbol{\theta}} h_i(\boldsymbol{\theta}))^T (\boldsymbol{\theta}' - \boldsymbol{\theta}) \rangle
\end{aligned} \tag{A.38}$$

For all $i \in \{1, \dots, n\}$, let us denote $\check{\text{loss}}_i := \nabla_{h_i}(R \circ \mathbf{L})(h(\boldsymbol{\theta}))$ to match the notations used in [Allen-Zhu 19a] for the derivative of the loss with respect to the output of the network for example i of the training set.

With this notation, we obtain exactly equation (11.3) in [Allen-Zhu 19a] up to the multiplicative factor $\left(\frac{\beta C(\mathcal{L})^2}{n\rho} + 2C(\nabla \mathcal{L})\right)$ for the distributionally robust loss.

From there the proof of Theorem 4 in [Allen-Zhu 19a] being independent to the formula for $\check{\text{loss}}_i$, we can conclude the proof of our Theorem A.4.6 as in [Allen-Zhu 19a, Appendix A].

Gradient bounds for the distributionally robust loss

We prove the following lemma which is a generalization of Theorem 3 in [Allen-Zhu 19a] for the distributionally robust loss.

Theorem A.4.7 (Gradient Bounds for the Distributionally Robust Loss).

Let $\omega \in O\left(\frac{\delta^{3/2}}{n^{9/2}L^6 \log^3(m)}\right)$, and $\boldsymbol{\theta}^{(0)}$ being initialized randomly as described in assumption A.4.1. With probability as least $1 - \exp\{-\Omega(m\omega^{3/2}L)\}$ over the initialization, we have for all $\boldsymbol{\theta} \in (\mathbb{R}^{m \times m})^L$ with $\|\boldsymbol{\theta} - \boldsymbol{\theta}^{(0)}\|_2 \leq \omega$

$$\begin{aligned}
&\forall i \in \{1, \dots, n\}, \forall l \in \{1, \dots, L\}, \forall \hat{\mathbf{L}} \in \mathbb{R}^n \\
&\left\| \bar{p}_i(\hat{\mathbf{L}}) \nabla_{\boldsymbol{\theta}_l} (\mathcal{L}_i \circ h_i)(\boldsymbol{\theta}) \right\|_2^2 \leq O\left(\frac{m}{d} \left\| \bar{p}_i(\hat{\mathbf{L}}) \nabla_{h_i} \mathcal{L}_i(h_i(\boldsymbol{\theta})) \right\|_2^2\right) \\
&\forall l \in \{1, \dots, L\}, \forall \hat{\mathbf{L}} \in \mathbb{R}^n \\
&\left\| \sum_{i=1}^n \bar{p}_i(\hat{\mathbf{L}}) \nabla_{\boldsymbol{\theta}_l} (\mathcal{L}_i \circ h_i)(\boldsymbol{\theta}) \right\|_2^2 \leq O\left(\frac{mn}{d} \sum_{i=1}^n \left\| \bar{p}_i(\hat{\mathbf{L}}) \nabla_{h_i} \mathcal{L}_i(h_i(\boldsymbol{\theta})) \right\|_2^2\right) \\
&\left\| \sum_{i=1}^n \bar{p}_i(\hat{\mathbf{L}}) \nabla_{\boldsymbol{\theta}_L} (\mathcal{L}_i \circ h_i)(\boldsymbol{\theta}) \right\|_2^2 \geq \Omega\left(\frac{m\delta}{dn^2} \sum_{i=1}^n \left\| \bar{p}_i(\hat{\mathbf{L}}) \nabla_{h_i} \mathcal{L}_i(h_i(\boldsymbol{\theta})) \right\|_2^2\right)
\end{aligned} \tag{A.39}$$

It is worth noting that the loss vector $\hat{\mathbf{L}}$ used for computing the robust probabilities $\bar{\mathbf{p}}(\hat{\mathbf{L}}) = \left(\bar{p}_i(\hat{\mathbf{L}})\right)_{i=1}^n$ does not have to be equal to $\mathbf{L}(h(\boldsymbol{\theta}))$.

We will use this for the proof of the Robust SGD with stale per-example loss vector.

The adaptation of the proof of Theorem 3 in [Allen-Zhu 19a] is straightforward.

Let $\boldsymbol{\theta} \in (\mathbb{R}^{m \times m})^L$ satisfying the conditions of Theorem A.4.7, and $\hat{\mathbf{L}} \in \mathbb{R}^n$.

Let us denote $\mathbf{v} := \left(\bar{p}_i(\hat{\mathbf{L}}) \nabla_{h_i} \mathcal{L}_i(h_i(\boldsymbol{\theta})) \right)_{i=1}^n$, applying the proof of Theorem 3 in [Allen-Zhu 19a] to our \mathbf{v} gives:

$$\begin{aligned} & \forall i \in \{1, \dots, n\}, \forall l \in \{1, \dots, L\}, \\ & \left\| \bar{p}_i(\hat{\mathbf{L}}) \nabla_{\boldsymbol{\theta}_l} (\mathcal{L}_i \circ h_i)(\boldsymbol{\theta}) \right\|_2^2 \leq O \left(\frac{m}{d} \left\| \bar{p}_i(\hat{\mathbf{L}}) \nabla_{h_i} \mathcal{L}_i(h_i(\boldsymbol{\theta})) \right\|_2^2 \right) \\ & \forall l \in \{1, \dots, L\}, \forall \hat{\mathbf{L}} \in \mathbb{R}^n \\ & \left\| \sum_{i=1}^n \bar{p}_i(\hat{\mathbf{L}}) \nabla_{\boldsymbol{\theta}_l} (\mathcal{L}_i \circ h_i)(\boldsymbol{\theta}) \right\|_2^2 \leq O \left(\frac{mn}{d} \sum_{i=1}^n \left\| \bar{p}_i(\hat{\mathbf{L}}) \nabla_{h_i} \mathcal{L}_i(h_i(\boldsymbol{\theta})) \right\|_2^2 \right) \\ & \left\| \sum_{i=1}^n \bar{p}_i(\hat{\mathbf{L}}) \nabla_{\boldsymbol{\theta}_L} (\mathcal{L}_i \circ h_i)(\boldsymbol{\theta}) \right\|_2^2 \geq \Omega \left(\frac{m\delta}{dn} \max_i \left(\left\| \bar{p}_i(\hat{\mathbf{L}}) \nabla_{h_i} \mathcal{L}_i(h_i(\boldsymbol{\theta})) \right\|_2^2 \right) \right) \end{aligned}$$

In addition

$$\max_i \left(\left\| \bar{p}_i(\hat{\mathbf{L}}) \nabla_{h_i} \mathcal{L}_i(h_i(\boldsymbol{\theta})) \right\|_2^2 \right) \geq \frac{1}{n} \sum_{i=1}^n \left\| \bar{p}_i(\hat{\mathbf{L}}) \nabla_{h_i} \mathcal{L}_i(h_i(\boldsymbol{\theta})) \right\|_2^2$$

This allows us to conclude the proof of our Theorem A.4.7. ■

Convergence of SGD with Hardness Weighted Sampling and exact per-example loss vector

We can now prove Theorem A.4.4.

Similarly to the proof of the convergence of SGD for the mean loss (Theorem 2 in [Allen-Zhu 19a]), the convergence of SGD for the distributionally robust loss will mainly rely on the semi-smoothness property (Theorem A.4.6) and the gradient bound (Theorem A.4.7) that we have proved previously for the distributionally robust loss.

Let $\boldsymbol{\theta} \in (\mathbb{R}^{m \times m})^L$ satisfying the conditions of Theorem A.4.4, and $\hat{\mathbf{L}}$ be the exact per-example loss vector at $\boldsymbol{\theta}$, i.e.

$$\hat{\mathbf{L}} = \left(\mathcal{L}_i(h_i(\boldsymbol{\theta})) \right)_{i=1}^n \quad (\text{A.40})$$

For the batch size $b \in \{1, \dots, n\}$, let $S = \{i_j\}_{j=1}^b$ a batch of indices drawn from $\bar{\mathbf{p}}(\hat{\mathbf{L}})$ without replacement, i.e.

$$\forall j \in \{1, \dots, b\}, i_j \stackrel{\text{i.i.d.}}{\sim} \bar{\mathbf{p}}(\hat{\mathbf{L}}) \quad (\text{A.41})$$

Let $\boldsymbol{\theta}' \in (\mathbb{R}^{m \times m})^L$ be the values of the parameters after a stochastic gradient descent step at $\boldsymbol{\theta}$ for the batch S , i.e.

$$\boldsymbol{\theta}' = \boldsymbol{\theta} - \eta \frac{1}{b} \sum_{i \in S} \nabla_{\boldsymbol{\theta}}(\mathcal{L}_i \circ h_i)(\boldsymbol{\theta}) \quad (\text{A.42})$$

where $\eta > 0$ is the learning rate.

Assuming that $\boldsymbol{\theta}$ and $\boldsymbol{\theta}'$ satisfies the conditions of Theorem A.4.6, we obtain

$$\begin{aligned} R(\mathbf{L}(h(\boldsymbol{\theta}')) &\leq R(\mathbf{L}(h(\boldsymbol{\theta})) - \eta \langle \nabla_{\boldsymbol{\theta}}(R \circ \mathbf{L} \circ h)(\boldsymbol{\theta}), \frac{1}{b} \sum_{i \in S} \nabla_{\boldsymbol{\theta}}(\mathcal{L}_i \circ h_i)(\boldsymbol{\theta}) \rangle \\ &+ \eta \sqrt{n} \|\nabla_h(R \circ \mathbf{L})(h(\boldsymbol{\theta}))\|_{2,2} O\left(\frac{L^2 \omega^{1/3} \sqrt{m \log(m)}}{\sqrt{d}}\right) \left\| \frac{1}{b} \sum_{i \in S} \nabla_{\boldsymbol{\theta}}(\mathcal{L}_i \circ h_i)(\boldsymbol{\theta}) \right\|_{2,\infty} \\ &+ \eta^2 O\left(\left(\frac{\beta C(\mathcal{L})^2}{n\rho} + 2C(\nabla \mathcal{L})\right) \frac{nL^2 m}{d}\right) \left\| \frac{1}{b} \sum_{i \in S} \nabla_{\boldsymbol{\theta}}(\mathcal{L}_i \circ h_i)(\boldsymbol{\theta}) \right\|_{2,\infty}^2 \end{aligned} \quad (\text{A.43})$$

where we refer to (A.30) for the form of $\nabla_{\boldsymbol{\theta}}(R \circ \mathbf{L} \circ h)(\boldsymbol{\theta})$ and to (A.29) for the form of $\nabla_h(R \circ \mathbf{L})(h(\boldsymbol{\theta}))$.

In addition, we make the assumption that for the set of values of $\boldsymbol{\theta}$ considered the hardness weighted sampling probabilities admit an upper-bound

$$\alpha = \min_{\boldsymbol{\theta}} \min_i \bar{p}_i(\mathbf{L}(\boldsymbol{\theta})) > 0 \quad (\text{A.44})$$

Which is always satisfied under assumption A.4.2 for Kullback-Leibler ϕ -divergence, and for any ϕ -divergence satisfying Definition 5.3.1 with a robustness parameter β small enough.

Let \mathbb{E}_S be the expectation with respect to S . Applying \mathbb{E}_S to (A.43), we obtain

$$\begin{aligned} \mathbb{E}_S [R(\mathbf{L}(h(\boldsymbol{\theta}')))] &\leq R(\mathbf{L}(h(\boldsymbol{\theta})) - \eta \|\nabla_{\boldsymbol{\theta}}(R \circ \mathbf{L} \circ h)(\boldsymbol{\theta})\|_{2,2}^2 \\ &+ \eta \|\nabla_h(R \circ \mathbf{L})(h(\boldsymbol{\theta}))\|_{2,2} O\left(\frac{nL^2 \omega^{1/3} \sqrt{m \log(m)}}{\sqrt{d}}\right) \sqrt{\sum_{i=1}^n \max_l \left\| \bar{p}_i(\hat{\mathbf{L}}) \nabla_{\boldsymbol{\theta}_l}(\mathcal{L}_i \circ h_i)(\boldsymbol{\theta}) \right\|^2} \\ &+ \eta^2 O\left(\left(\frac{\beta C(\mathcal{L})^2}{n\rho} + 2C(\nabla \mathcal{L})\right) \frac{nL^2 m}{d}\right) \frac{1}{\alpha} \sum_{i=1}^n \max_l \left\| \bar{p}_i(\hat{\mathbf{L}}) \nabla_{\boldsymbol{\theta}_l}(\mathcal{L}_i \circ h_i)(\boldsymbol{\theta}) \right\|^2 \end{aligned} \quad (\text{A.45})$$

where we have used the following results:

- For any integer $k \geq 1$, and all $(\mathbf{a}_i)_{i=1}^n \in (\mathbb{R}^k)^n$, we have (see the proof in

A.4.9)

$$\mathbb{E}_S \left[\frac{1}{b} \sum_{i \in S} \mathbf{a}_i \right] = \mathbb{E}_{\bar{p}(\hat{\mathbf{L}})} [\mathbf{a}_i] \quad (\text{A.46})$$

- Using (A.46) for $(\mathbf{a}_i)_{i=1}^n = (\nabla_{\boldsymbol{\theta}}(\mathcal{L}_i \circ h_i)(\boldsymbol{\theta}))_{i=1}^n$, and the chain rule (A.30)

$$\mathbb{E}_S \left[\frac{1}{b} \sum_{i \in S} \nabla_{\boldsymbol{\theta}}(\mathcal{L}_i \circ h_i)(\boldsymbol{\theta}) \right] = \sum_{i=1}^n \bar{p}_i(\hat{\mathbf{L}}) \nabla_{\boldsymbol{\theta}}(\mathcal{L}_i \circ h_i)(\boldsymbol{\theta}) = \nabla_{\boldsymbol{\theta}}(R \circ \mathbf{L} \circ h)(\boldsymbol{\theta}) \quad (\text{A.47})$$

- Using the triangular inequality

$$\left\| \frac{1}{b} \sum_{i \in S} \nabla_{\boldsymbol{\theta}}(\mathcal{L}_i \circ h_i)(\boldsymbol{\theta}) \right\|_{2,\infty} \leq \frac{1}{b} \sum_{i \in S} \left\| \nabla_{\boldsymbol{\theta}}(\mathcal{L}_i \circ h_i)(\boldsymbol{\theta}) \right\|_{2,\infty} \quad (\text{A.48})$$

And using (A.46) for $(a_i)_{i=1}^n = (\|\nabla_{\boldsymbol{\theta}}(\mathcal{L}_i \circ h_i)(\boldsymbol{\theta})\|_{2,\infty})_{i=1}^n$,

$$\begin{aligned} \mathbb{E}_S \left[\left\| \frac{1}{b} \sum_{i \in S} \nabla_{\boldsymbol{\theta}}(\mathcal{L}_i \circ h_i)(\boldsymbol{\theta}) \right\|_{2,\infty} \right] &\leq \sum_{i=1}^n \bar{p}_i(\hat{\mathbf{L}}) \left\| \nabla_{\boldsymbol{\theta}}(\mathcal{L}_i \circ h_i)(\boldsymbol{\theta}) \right\|_{2,\infty} \\ &\leq \sum_{i=1}^n \max_l \left\| \nabla_{\boldsymbol{\theta}_l}(\bar{p}_i(\hat{\mathbf{L}}) \mathcal{L}_i \circ h_i)(\boldsymbol{\theta}) \right\|_2 \\ &\leq \sqrt{n} \sqrt{\sum_{i=1}^n \max_l \left\| \nabla_{\boldsymbol{\theta}_l}(\bar{p}_i(\hat{\mathbf{L}}) \mathcal{L}_i \circ h_i)(\boldsymbol{\theta}) \right\|_2^2} \end{aligned} \quad (\text{A.49})$$

where we have used Cauchy-Schwarz inequality for the last inequality.

- Using (A.48) and the convexity of the function $x \mapsto x^2$

$$\left\| \frac{1}{b} \sum_{i \in S} \nabla_{\boldsymbol{\theta}}(\mathcal{L}_i \circ h_i)(\boldsymbol{\theta}) \right\|_{2,\infty}^2 \leq \frac{1}{b} \sum_{i \in S} \left\| \nabla_{\boldsymbol{\theta}}(\mathcal{L}_i \circ h_i)(\boldsymbol{\theta}) \right\|_{2,\infty}^2 \quad (\text{A.50})$$

And using (A.46) for $(a_i)_{i=1}^n = (\|\nabla_{\boldsymbol{\theta}}(\mathcal{L}_i \circ h_i)(\boldsymbol{\theta})\|_{2,\infty}^2)_{i=1}^n$,

$$\begin{aligned} \mathbb{E}_S \left[\left\| \frac{1}{b} \sum_{i \in S} \nabla_{\boldsymbol{\theta}}(\mathcal{L}_i \circ h_i)(\boldsymbol{\theta}) \right\|_{2,\infty}^2 \right] &\leq \sum_{i=1}^n \bar{p}_i(\hat{\mathbf{L}}) \left\| \nabla_{\boldsymbol{\theta}}(\mathcal{L}_i \circ h_i)(\boldsymbol{\theta}) \right\|_{2,\infty}^2 \\ &\leq \sum_{i=1}^n \frac{1}{\bar{p}_i(\hat{\mathbf{L}})} \max_l \left\| \nabla_{\boldsymbol{\theta}_l}(\bar{p}_i(\hat{\mathbf{L}}) \mathcal{L}_i \circ h_i)(\boldsymbol{\theta}) \right\|_2^2 \\ &\leq \frac{1}{\alpha} \sum_{i=1}^n \max_l \left\| \nabla_{\boldsymbol{\theta}_l}(\bar{p}_i(\hat{\mathbf{L}}) \mathcal{L}_i \circ h_i)(\boldsymbol{\theta}) \right\|_2^2 \end{aligned} \quad (\text{A.51})$$

Important Remark: It is worth noting in (A.51) the apparition of α defined in (A.44). If we were using a uniform sampling as for ERM (i.e. for DRO in the limit $\beta \rightarrow 0$), we would have $\alpha = \frac{1}{n}$. So although our inequality (A.51) may seem crude, it is consistent with equation (13.2) in [Allen-Zhu 19a] and the corresponding inequality in the case of ERM.

The rest of the proof of convergence will consist in proving that $\eta \|\nabla_{\boldsymbol{\theta}}(R \circ \mathbf{L} \circ h)(\boldsymbol{\theta})\|_{2,2}^2$ dominates the two last terms in (A.43). As a result, we can already state that either the robustness parameter β , or the learning rate η will have to be small enough to control α .

Indeed, combining (A.43) with the chain rule (A.30), and the gradient bound Theorem A.4.7 where we use our $\hat{\mathbf{L}}$ defined in (A.40)

$$\begin{aligned}
\mathbb{E}_S [R(\mathbf{L}(h(\boldsymbol{\theta}')))] &\leq R(\mathbf{L}(h(\boldsymbol{\theta}))) - \Omega\left(\frac{\eta m \delta}{dn^2}\right) \sum_{i=1}^n \left\| \bar{p}_i(\hat{\mathbf{L}}) \nabla_{h_i} \mathcal{L}_i(h_i(\boldsymbol{\theta})) \right\|_2^2 \\
&\quad + \eta O\left(\frac{nL^2\omega^{1/3}\sqrt{m\log(m)}}{\sqrt{d}}\right) O\left(\sqrt{\frac{m}{d}}\right) \sum_{i=1}^n \left\| \bar{p}_i(\hat{\mathbf{L}}) \nabla_{h_i} \mathcal{L}_i(h_i(\boldsymbol{\theta})) \right\|_2^2 \\
&\quad + \eta^2 O\left(\left(\frac{\beta C(\mathcal{L})^2}{n\rho} + 2C(\nabla \mathcal{L})\right) \frac{nL^2m}{d}\right) O\left(\frac{m}{d\alpha}\right) \sum_{i=1}^n \left\| \bar{p}_i(\hat{\mathbf{L}}) \nabla_{h_i} \mathcal{L}_i(h_i(\boldsymbol{\theta})) \right\|_2^2 \\
&\leq R(\mathbf{L}(h(\boldsymbol{\theta}))) - \Omega\left(\frac{\eta m \delta}{dn^2}\right) \sum_{i=1}^n \left\| \bar{p}_i(\hat{\mathbf{L}}) \nabla_{h_i} \mathcal{L}_i(h_i(\boldsymbol{\theta})) \right\|_2^2 \\
&\quad + O\left(\frac{\eta n L^2 m \omega^{1/3} \sqrt{\log(m)}}{d} + K \frac{\eta^2 (n/\alpha) L^2 m^2}{d^2}\right) \sum_{i=1}^n \left\| \bar{p}_i(\hat{\mathbf{L}}) \nabla_{h_i} \mathcal{L}_i(h_i(\boldsymbol{\theta})) \right\|_2^2
\end{aligned} \tag{A.52}$$

where we have used

$$K := \frac{\beta C(\mathcal{L})^2}{n\rho} + 2C(\nabla \mathcal{L}) \tag{A.53}$$

There are only two differences with equation (13.2) in [Allen-Zhu 19a]:

- in the last fraction we have n/α instead of n^2 (see remark A.4.9 for more details), and an additional multiplicative term K . So in total, this term differs by a multiplicative factor $\frac{\alpha n}{K}$ from the analogous term in the proof of [Allen-Zhu 19a].
- we have $\sum_{i=1}^n \left\| \bar{p}_i(\hat{\mathbf{L}}) \nabla_{h_i} \mathcal{L}_i(h_i(\boldsymbol{\theta})) \right\|_2^2$ instead of $F(\mathbf{W}^{(t)})$. In fact they are analogous since in equation (13.2) in [Allen-Zhu 19a], $F(\mathbf{W}^{(t)})$ is the squared norm of the mean loss for the L^2 loss. We don't make such a strong assumption on the choice of \mathcal{L} (see assumption A.4.2). It is worth noting that the same analogy is used in [Allen-Zhu 19a, Appendix A] where they extend their result to the mean loss with other objective function than the L^2 loss.

Our choice of learning rate in Theorem A.4.5 can be rewritten as

$$\begin{aligned}\eta_{exact} &= \Theta \left(\frac{\alpha n^2 \rho}{\beta C(\mathcal{L})^2 + 2n\rho C(\nabla \mathcal{L})} \times \frac{b\delta d}{\text{poly}(n, L)m \log^2(m)} \right) \\ &= \Theta \left(\frac{\alpha n}{K} \times \frac{b\delta d}{\text{poly}(n, L)m \log^2(m)} \right) \\ &\leq \frac{\alpha n}{K} \times \eta'\end{aligned}\tag{A.54}$$

And we also have

$$\eta_{exact} \leq \eta' \tag{A.55}$$

where η' is the learning rate chosen in the proof of Theorem 2 in [Allen-Zhu 19a]. We refer the reader to [Allen-Zhu 19a] for the details of the constant in " Θ " and the exact form of the polynomial $\text{poly}(n, L)$.

As a result, for $\eta = \eta_{exact}$, the term $\Omega\left(\frac{\eta m \delta}{dn^2}\right)$ dominates the other term of the right-hand side of inequality (A.52) as in the proof of Theorem 2 in [Allen-Zhu 19a].

This implies that the conditions of Theorem A.4.7 are satisfied for all $\boldsymbol{\theta}^{(t)}$, and that we have for all iteration $t > 0$

$$\mathbb{E}_{S_t} \left[R(\mathbf{L}(h(\boldsymbol{\theta}^{(t+1)}))) \right] \leq R(\mathbf{L}(h(\boldsymbol{\theta}^{(t)}))) - \Omega\left(\frac{\eta m \delta}{dn^2}\right) \sum_{i=1}^n \left\| \bar{p}_i(\hat{\mathbf{L}}) \nabla_{h_i} \mathcal{L}_i(h_i(\boldsymbol{\theta}^{(t)})) \right\|_2^2 \tag{A.56}$$

And using a result in Appendix A of [Allen-Zhu 19a], since under assumption A.4.2 the distributionally robust loss is non-convex and bounded, we obtain for all $\epsilon' > 0$

$$\left\| \nabla_h (R \circ \mathbf{L})(h(\boldsymbol{\theta}^{(T)})) \right\|_{2,2} \leq \epsilon' \quad \text{if} \quad T = O\left(\frac{dn^2}{\eta \delta m \epsilon'^2}\right) \tag{A.57}$$

where according to (A.29)

$$\left\| \nabla_h (R \circ \mathbf{L})(h(\boldsymbol{\theta}^{(T)})) \right\|_{2,2} = \sum_{i=1}^n \left\| \bar{p}_i(\hat{\mathbf{L}}) \nabla_{h_i} \mathcal{L}_i(h_i(\boldsymbol{\theta}^{(t)})) \right\|_2^2 \tag{A.58}$$

However, we are interested in a bound on $\left\| \nabla_{\boldsymbol{\theta}} (R \circ \mathbf{L} \circ h)(\boldsymbol{\theta}^{(T)}) \right\|_{2,2}$, rather than a bound on $\left\| \nabla_h (R \circ \mathbf{L})(h(\boldsymbol{\theta}^{(T)})) \right\|_{2,2}$. Using the gradient bound of Theorem A.4.7 and the chain rules (A.30) and (A.29)

$$\left\| \nabla_{\boldsymbol{\theta}} (R \circ \mathbf{L} \circ h)(\boldsymbol{\theta}^{(T)}) \right\|_{2,2} \leq c_1 \sqrt{\frac{Lmn}{d}} \left\| \nabla_h (R \circ \mathbf{L})(h(\boldsymbol{\theta}^{(T)})) \right\|_{2,2} \tag{A.59}$$

where $c_1 > 0$ is the constant hidden in $O\left(\sqrt{\frac{Lmn}{d}}\right)$.

So with $\epsilon' = \frac{1}{c_1} \sqrt{\frac{d}{Lmn}} \epsilon$, we finally obtain

$$\begin{aligned} \left\| \nabla_{\boldsymbol{\theta}} (R \circ \mathbf{L} \circ h)(\boldsymbol{\theta}^{(T)}) \right\|_{2,2} &\leq c_1 \sqrt{\frac{Lmn}{d}} \left\| \nabla_h (R \circ \mathbf{L})(h(\boldsymbol{\theta}^{(T)})) \right\|_{2,2} \\ &\leq c_1 \sqrt{\frac{Lmn}{d}} \epsilon' \\ &\leq \epsilon \end{aligned} \tag{A.60}$$

If

$$T = O\left(\frac{dn^2}{\eta\delta m \epsilon'^2}\right) = O\left(\frac{dn^2}{\eta\delta m} \frac{Lmn}{d\epsilon^2}\right) = O\left(\frac{Ln^3}{\eta\delta\epsilon^2}\right) \tag{A.61}$$

which concludes the proof. ■

Proof of technical lemma 1

For any integer $k \geq 1$, and all $(\mathbf{a}_i)_{i=1}^n \in (\mathbb{R}^k)^n$, we have

$$\begin{aligned} \mathbb{E}_S \left[\frac{1}{b} \sum_{i \in S} \mathbf{a}_i \right] &= \sum_{1 \leq i_1, \dots, i_b \leq n} \left[\left(\prod_{k=1}^n \bar{p}_{i_k}(\hat{\mathbf{L}}) \right) \frac{1}{b} \sum_{j=1}^b \mathbf{a}_{i_j} \right] \\ &= \frac{1}{b} \sum_{1 \leq i_1, \dots, i_b \leq n} \left[\sum_{j=1}^b \bar{p}_{i_j}(\hat{\mathbf{L}}) \mathbf{a}_{i_j} \left(\prod_{\substack{k=1 \\ k \neq j}}^n \bar{p}_{i_k}(\hat{\mathbf{L}}) \right) \right] \\ &= \frac{1}{b} \sum_{j=1}^b \left[\sum_{1 \leq i_1, \dots, i_b \leq n} \bar{p}_{i_j}(\hat{\mathbf{L}}) \mathbf{a}_{i_j} \left(\prod_{\substack{k=1 \\ k \neq j}}^n \bar{p}_{i_k}(\hat{\mathbf{L}}) \right) \right] \\ &= \frac{1}{b} \sum_{j=1}^b \left[\left(\sum_{i_j=1}^n \bar{p}_{i_j}(\hat{\mathbf{L}}) \mathbf{a}_{i_j} \right) \prod_{\substack{k=1 \\ k \neq j}}^n \left(\sum_{i_k=1}^n \bar{p}_{i_k}(\hat{\mathbf{L}}) \right) \right] \\ &= \frac{1}{b} \sum_{j=1}^b \left(\sum_{i=1}^n \bar{p}_i(\hat{\mathbf{L}}) \mathbf{a}_i \right) \\ &= \sum_{i=1}^n \bar{p}_i(\hat{\mathbf{L}}) \mathbf{a}_i \\ &= \mathbb{E}_{\bar{\mathbf{p}}(\hat{\mathbf{L}})} [\mathbf{a}_i] \end{aligned} \tag{A.62}$$

Convergence of SGD with Hardness Weighted Sampling and stale per-example loss vector

The proof of the convergence of Algorithm 1 under the conditions of Theorem A.4.5 follows the same structure as the proof of the convergence of Robust SGD with exact per-example loss vector A.4.9. We will reuse the intermediate results of A.4.9 when possible and focus on the differences between the two proofs due to the inexactness of the per-example loss vector.

Let t be the iteration number, and let $\boldsymbol{\theta}^{(t)} \in (\mathbb{R}^{m \times m})^L$ be the parameters of the deep neural network at iteration t . We define the stale per-example loss vector at iteration t as

$$\hat{\mathbf{L}} = \left(\mathcal{L}_i(h_i(\boldsymbol{\theta}^{(t_i(t))})) \right)_{i=1}^n \quad (\text{A.63})$$

where for all i , $t_i(t) < t$ corresponds to the latest iteration before t at which the per-example loss value for example i has been updated. Or equivalently, it corresponds to the last iteration before t when example i was drawn to be part of a mini-batch.

We also define the exact per-example loss vector that is unknown in Algorithm 1, as

$$\check{\mathbf{L}} = \left(\mathcal{L}_i(h_i(\boldsymbol{\theta}^{(t)})) \right)_{i=1}^n \quad (\text{A.64})$$

Similarly to (A.42) we define

$$\boldsymbol{\theta}^{(t+1)} = \boldsymbol{\theta}^{(t)} - \eta \frac{1}{b} \sum_{i \in S} \nabla_{\boldsymbol{\theta}} (\mathcal{L}_i \circ h_i)(\boldsymbol{\theta}^{(t)}) \quad (\text{A.65})$$

and using Theorem A.4.6, similarly to (A.43), we obtain

$$\begin{aligned} R(\mathbf{L}(h(\boldsymbol{\theta}^{(t+1)}))) &\leq R(\mathbf{L}(h(\boldsymbol{\theta}^{(t)}))) - \eta \langle \nabla_{\boldsymbol{\theta}} (R \circ \mathbf{L} \circ h)(\boldsymbol{\theta}^{(t)}), \frac{1}{b} \sum_{i \in S} \nabla_{\boldsymbol{\theta}} (\mathcal{L}_i \circ h_i)(\boldsymbol{\theta}^{(t)}) \rangle \\ &\quad + \eta \left\| \nabla_h (R \circ \mathbf{L})(h(\boldsymbol{\theta}^{(t)})) \right\|_{1,2} O \left(\frac{L^2 \omega^{1/3} \sqrt{m \log(m)}}{\sqrt{d}} \right) \left\| \frac{1}{b} \sum_{i \in S} \nabla_{\boldsymbol{\theta}} (\mathcal{L}_i \circ h_i)(\boldsymbol{\theta}^{(t)}) \right\|_{2,\infty} \\ &\quad + \eta^2 O \left(\left(\frac{\beta C(\mathcal{L})^2}{n\rho} + 2C(\nabla \mathcal{L}) \right) \frac{nL^2 m}{d} \right) \left\| \frac{1}{b} \sum_{i \in S} \nabla_{\boldsymbol{\theta}} (\mathcal{L}_i \circ h_i)(\boldsymbol{\theta}^{(t)}) \right\|_{2,\infty}^2 \end{aligned} \quad (\text{A.66})$$

We can still define α as in (A.44)

$$\alpha = \min_{\boldsymbol{\theta}} \min_i \bar{p}_i(\mathbf{L}(\boldsymbol{\theta})) > 0 \quad (\text{A.67})$$

where we are guaranteed that $\alpha > 0$ under assumptions A.4.1.

Since Theorem A.4.7 is independent to the choice of $\hat{\mathbf{L}}$, taking the expectation

with respect to S , similarly to (A.52), we obtain

$$\begin{aligned} \mathbb{E}_S \left[R(\mathbf{L}(h(\boldsymbol{\theta}^{t+1}))) \right] &\leq R(\mathbf{L}(h(\boldsymbol{\theta}^{(t)}))) - \eta \langle \nabla_{\boldsymbol{\theta}} (R \circ \mathbf{L} \circ h)(\boldsymbol{\theta}^{(t)}), \sum_{i=1}^n \bar{p}_i(\hat{\mathbf{L}}) \nabla_{\boldsymbol{\theta}} (\mathcal{L}_i \circ h_i)(\boldsymbol{\theta}^{(t)}) \rangle \\ &\quad + \eta \left\| \nabla_h (R \circ \mathbf{L})(h(\boldsymbol{\theta}^{(t)})) \right\|_{1,2} O \left(\frac{L^2 \omega^{1/3} \sqrt{nm \log(m)}}{\sqrt{d}} \right) \sqrt{\sum_{i=1}^n \left\| \bar{p}_i(\hat{\mathbf{L}}) \nabla_{h_i} \mathcal{L}_i(h_i(\boldsymbol{\theta}^{(t)})) \right\|_2^2} \\ &\quad + \eta^2 O \left(\left(\frac{\beta C(\mathcal{L})^2}{n\rho} + 2C(\nabla \mathcal{L}) \right) \frac{nL^2 m}{d} \right) O \left(\frac{m}{d\alpha} \right) \sum_{i=1}^n \left\| \bar{p}_i(\hat{\mathbf{L}}) \nabla_{h_i} \mathcal{L}_i(h_i(\boldsymbol{\theta}^{(t)})) \right\|_2^2 \end{aligned} \quad (\text{A.68})$$

where the differences with respect to (A.52) comes from the fact that $\hat{\mathbf{L}}$ is not the exact per-example loss vector here, i.e. $\hat{\mathbf{L}} \neq \check{\mathbf{L}}$, which leads to

$$\begin{aligned} \nabla_{\boldsymbol{\theta}} (R \circ \mathbf{L} \circ h)(\boldsymbol{\theta}^{(t)}) &= \sum_{i=1}^n \hat{p}_i(\check{\mathbf{L}}) \nabla_{\boldsymbol{\theta}} (\mathcal{L}_i \circ h_i)(\boldsymbol{\theta}^{(t)}) \\ &\neq \sum_{i=1}^n \bar{p}_i(\hat{\mathbf{L}}) \nabla_{\boldsymbol{\theta}} (\mathcal{L}_i \circ h_i)(\boldsymbol{\theta}^{(t)}) \end{aligned} \quad (\text{A.69})$$

and

$$\begin{aligned} \left\| \nabla_h (R \circ \mathbf{L})(h(\boldsymbol{\theta}^{(t)})) \right\|_{1,2} &= \sum_{i=1}^n \left\| \hat{p}_i(\check{\mathbf{L}}) \nabla_{h_i} \mathcal{L}_i(h_i(\boldsymbol{\theta}^{(t)})) \right\|_2 \\ &\neq \sum_{i=1}^n \left\| \hat{p}_i(\hat{\mathbf{L}}) \nabla_{h_i} \mathcal{L}_i(h_i(\boldsymbol{\theta}^{(t)})) \right\|_2 \end{aligned} \quad (\text{A.70})$$

Let

$$K' = C(\mathcal{L}) A(\nabla \mathcal{L}) O \left(\frac{\beta L m^{3/2} \log^2(m)}{\alpha n^{1/2} \rho d^{3/2} b \log\left(\frac{1}{1-\alpha}\right)} \right) \quad (\text{A.71})$$

Where $C(\mathcal{L}) > 0$ is a constant such that \mathcal{L} is $C(\mathcal{L})$ -Lipschitz continuous, and $A(\nabla \mathcal{L}) > 0$ is a constant that bound the gradient of \mathcal{L} with respect to its input. $C(\mathcal{L})$ and $A(\nabla \mathcal{L})$ are guaranteed to exist under assumptions A.4.1.

We can prove that, with probability at least $1 - \exp\left(-\Omega\left(\log^2(m)\right)\right)$,

- according to lemma A.4.9

$$\left\| \hat{p}(\hat{\mathbf{L}}) - \hat{p}(\check{\mathbf{L}}) \right\|_2 = \sqrt{\sum_{i=1}^n \left(\hat{p}_i(\hat{\mathbf{L}}) - \hat{p}_i(\check{\mathbf{L}}) \right)^2} \leq \eta \alpha K' \quad (\text{A.72})$$

- according to lemma A.4.9

$$\begin{aligned} & \left| \langle \nabla_{\boldsymbol{\theta}}(R \circ \mathbf{L} \circ h)(\boldsymbol{\theta}^{(t)}) - \sum_{i=1}^n \bar{p}_i(\hat{\mathbf{L}}) \nabla_{\boldsymbol{\theta}}(\mathcal{L}_i \circ h_i)(\boldsymbol{\theta}^{(t)}), \sum_{i=1}^n \bar{p}_i(\hat{\mathbf{L}}) \nabla_{\boldsymbol{\theta}}(\mathcal{L}_i \circ h_i)(\boldsymbol{\theta}^{(t)}) \rangle \right| \\ & \leq \eta \frac{m}{d} K' \sum_{i=1}^n \left\| \bar{p}_i(\hat{\mathbf{L}}) \nabla_{\boldsymbol{\theta}}(\mathcal{L}_i \circ h_i)(\boldsymbol{\theta}^{(t)}) \right\|_2^2 \end{aligned} \quad (\text{A.73})$$

- according to lemma A.4.9

$$\left\| \nabla_h(R \circ \mathbf{L})(h(\boldsymbol{\theta}^{(t)})) \right\|_{1,2} \leq (\sqrt{n} + \eta K') \sqrt{\sum_{i=1}^n \left\| \bar{p}_i(\hat{\mathbf{L}}) \nabla_{\boldsymbol{\theta}}(\mathcal{L}_i \circ h_i)(\boldsymbol{\theta}^{(t)}) \right\|_2^2} \quad (\text{A.74})$$

Combining those three inequalities with (A.68) we obtain

$$\begin{aligned} \mathbb{E}_S \left[R(\mathbf{L}(h(\boldsymbol{\theta}^{(t+1)}))) \right] - R(\mathbf{L}(h(\boldsymbol{\theta}^{(t)}))) & \leq \\ & \eta \left[-\Omega \left(\frac{m\delta}{dn^2} \right) + O \left(\frac{nL^2m\omega^{1/3}\sqrt{\log(m)}}{d} \right) \right] \sum_{i=1}^n \left\| \bar{p}_i(\hat{\mathbf{L}}) \nabla_{h_i} \mathcal{L}_i(h_i(\boldsymbol{\theta}^{(t)})) \right\|_2^2 \\ & \eta^2 O \left(K \frac{(n/\alpha)L^2m^2}{d^2} + \left(1 + \frac{m}{d} \right) K' \right) \sum_{i=1}^n \left\| \bar{p}_i(\hat{\mathbf{L}}) \nabla_{h_i} \mathcal{L}_i(h_i(\boldsymbol{\theta}^{(t)})) \right\|_2^2 \end{aligned} \quad (\text{A.75})$$

One can see that compared to (A.52), there is only the additional term $(1 + \frac{m}{d}) K'$.

Using our choice of η ,

$$\eta = \eta_{stale} \leq O \left(\frac{\delta}{n^2 K'} \eta_{exact} \right) \quad (\text{A.76})$$

where η_{exact} is the learning rate of Theorem A.4.4, we have

$$\Omega \left(\frac{\eta m \delta}{dn^2} \right) \geq O \left(\eta^2 \left(1 + \frac{m}{d} \right) K' \right) \quad (\text{A.77})$$

As a result, $\eta^2 (1 + \frac{m}{d}) K'$ is dominated by the term $\Omega \left(\frac{\eta m \delta}{dn^2} \right)$

In addition, since $\eta_{stale} \leq \eta_{exact}$, $\Omega \left(\frac{\eta m \delta}{dn^2} \right)$ still dominates also the other terms as in the proof of Theorem A.4.4.

As a consequence, we obtain as in (A.56) that for any iteration $t > 0$

$$\mathbb{E}_{S_t} \left[R(\mathbf{L}(h(\boldsymbol{\theta}^{(t+1)}))) \right] \leq R(\mathbf{L}(h(\boldsymbol{\theta}^{(t)}))) - \Omega \left(\frac{\eta m \delta}{dn^2} \right) \sum_{i=1}^n \left\| \bar{p}_i(\hat{\mathbf{L}}) \nabla_{h_i} \mathcal{L}_i(h_i(\boldsymbol{\theta}^{(t)})) \right\|_2^2 \quad (\text{A.78})$$

This concludes the proof using the same arguments as in the end of the proof of

Theorem A.4.4 starting from (A.56). ■

Proof of technical lemma 2

Using Lemma 5.3.2 and Lemma 5.3.1 we obtain

$$\begin{aligned} \left\| \hat{\mathbf{p}}(\hat{\mathbf{L}}) - \hat{\mathbf{p}}(\check{\mathbf{L}}) \right\|_2 &= \left\| \nabla_v R(\hat{\mathbf{L}}) - \nabla_v R(\check{\mathbf{L}}) \right\|_2 \\ &\leq \frac{\beta}{n\rho} \left\| \hat{\mathbf{L}} - \check{\mathbf{L}} \right\|_2 \end{aligned} \quad (\text{A.79})$$

Using assumptions A.4.2 and [Allen-Zhu 19a, Claim 11.2]

$$\begin{aligned} \left\| \hat{\mathbf{p}}(\hat{\mathbf{L}}) - \hat{\mathbf{p}}(\check{\mathbf{L}}) \right\|_2 &\leq \frac{\beta}{n\rho} \sqrt{\sum_{i=1}^n \left(\mathcal{L}_i \circ h_i(\boldsymbol{\theta}^{(t)}) - \mathcal{L}_i \circ h_i(\boldsymbol{\theta}^{(t_i(t))}) \right)^2} \\ &\leq \frac{\beta}{n\rho} C(\mathcal{L})C(h) \sqrt{\sum_{i=1}^n \left\| \boldsymbol{\theta}^{(t)} - \boldsymbol{\theta}^{(t_i(t))} \right\|_{2,2}^2} \\ &\leq C(\mathcal{L})O\left(\frac{\beta L m^{1/2}}{n\rho d^{1/2}}\right) \sqrt{\sum_{i=1}^n \left\| \boldsymbol{\theta}^{(t)} - \boldsymbol{\theta}^{(t_i(t))} \right\|_{2,2}^2} \end{aligned} \quad (\text{A.80})$$

Where $C(\mathcal{L})$ is the constant of Lipschitz continuity of the per-example loss \mathcal{L} (see assumptions A.4.2) and $C(h)$ is the constant of Lipschitz continuity of the deep neural network h with respect to its parameters $\boldsymbol{\theta}$.

By developing the recurrence formula of $\boldsymbol{\theta}^{(t)}$ (A.65), we obtain

$$\begin{aligned} \left\| \hat{\mathbf{p}}(\hat{\mathbf{L}}) - \hat{\mathbf{p}}(\check{\mathbf{L}}) \right\|_2 &\leq C(\mathcal{L})O\left(\frac{\beta L m^{1/2}}{n\rho d^{1/2}}\right) \sqrt{\sum_{i=1}^n \left\| \boldsymbol{\theta}^{(t_i(t))} - \left(\sum_{\tau=t_i(t)}^{t-1} \frac{\eta}{b} \sum_{j \in S_\tau} \nabla_{\boldsymbol{\theta}} (\mathcal{L}_j \circ h_j)(\boldsymbol{\theta}^{(\tau)}) \right) - \boldsymbol{\theta}^{(t_i(t))} \right\|_{2,2}^2} \\ &\leq \eta C(\mathcal{L})O\left(\frac{\beta L m^{1/2}}{n\rho d^{1/2}}\right) \sqrt{\sum_{i=1}^n \left\| \sum_{\tau=t_i(t)}^{t-1} \frac{1}{b} \sum_{j \in S_\tau} \nabla_{\boldsymbol{\theta}} (\mathcal{L}_j \circ h_j)(\boldsymbol{\theta}^{(\tau)}) \right\|_{2,2}^2} \end{aligned}$$

Let $A(\nabla \mathcal{L})$ a bound on the gradient of the per-example loss function. Using Theorem A.4.7 and the chain rule

$$\forall j, \forall \tau \quad \left\| \nabla_{\boldsymbol{\theta}} (\mathcal{L}_j \circ h_j)(\boldsymbol{\theta}^{(\tau)}) \right\|_{2,2} \leq A(\nabla \mathcal{L})O\left(\frac{m}{d}\right) \quad (\text{A.81})$$

And using the triangular inequality

$$\begin{aligned}
\left\| \sum_{\tau=t_i(t)}^{t-1} \frac{1}{b} \sum_{j \in S_\tau} \nabla_{\boldsymbol{\theta}} (\mathcal{L}_j \circ h_j)(\boldsymbol{\theta}^{(\tau)}) \right\|_{2,2} &\leq \sum_{\tau=t_i(t)}^{t-1} \frac{1}{b} \sum_{j \in S_\tau} \left\| \nabla_{\boldsymbol{\theta}} (\mathcal{L}_j \circ h_j)(\boldsymbol{\theta}^{(\tau)}) \right\|_{2,2} \\
&\leq \sum_{\tau=t_i(t)}^{t-1} A(\nabla \mathcal{L}) O\left(\frac{m}{d}\right) \\
&\leq A(\nabla \mathcal{L}) O\left(\frac{m}{d}\right) (t - t_i(t))
\end{aligned} \tag{A.82}$$

As a result, we obtain

$$\left\| \hat{\boldsymbol{p}}(\hat{\mathbf{L}}) - \hat{\boldsymbol{p}}(\check{\mathbf{L}}) \right\|_2 \leq \eta C(\mathcal{L}) A(\nabla \mathcal{L}) O\left(\frac{\beta L m^{3/2}}{n \rho d^{3/2}}\right) \sqrt{\sum_{i=1}^n (t - t_i(t))^2} \tag{A.83}$$

For all i and for any τ the probability that the sample i is not in batch S_τ is lesser than $(1 - \alpha)^b$.

Therefore, for any $k \geq 1$ and for any t ,

$$P(t - t_i(t) \geq k) \leq (1 - \alpha)^{kb} \tag{A.84}$$

For $k \geq \frac{1}{b} \Omega\left(\frac{\log^2(m)}{\log\left(\frac{1}{1-\alpha}\right)}\right)$, we have $(1 - \alpha)^{kb} \leq \exp\left(-\Omega\left(\log^2(m)\right)\right)$, and thus with probability at least $1 - \exp\left(-\Omega\left(\log^2(m)\right)\right)$,

$$\forall t, \quad t - t_i(t) \leq O\left(\frac{\log^2(m)}{b \log\left(\frac{1}{1-\alpha}\right)}\right) \tag{A.85}$$

As a result, we finally obtain that with probability at least $1 - \exp\left(-\Omega\left(\log^2(m)\right)\right)$,

$$\begin{aligned}
\left\| \hat{\boldsymbol{p}}(\hat{\mathbf{L}}) - \hat{\boldsymbol{p}}(\check{\mathbf{L}}) \right\|_2 &\leq \eta C(\mathcal{L}) A(\nabla \mathcal{L}) O\left(\frac{\beta L m^{3/2}}{n \rho d^{3/2}}\right) \sqrt{n} O\left(\frac{\log^2(m)}{b \log\left(\frac{1}{1-\alpha}\right)}\right) \\
&\leq \eta \alpha O\left(\frac{\beta L m^{3/2} \log^2(m)}{\alpha n^{1/2} \rho d^{3/2} b \log\left(\frac{1}{1-\alpha}\right)}\right) \\
&\leq \eta \alpha K'
\end{aligned} \tag{A.86}$$

Proof of technical lemma 3

Let us first denote

$$\begin{aligned}
A &= \left| \langle \nabla_{\boldsymbol{\theta}}(R \circ \mathbf{L} \circ h)(\boldsymbol{\theta}^{(t)}) - \sum_{i=1}^n \bar{p}_i(\hat{\mathbf{L}}) \nabla_{\boldsymbol{\theta}}(\mathcal{L}_i \circ h_i)(\boldsymbol{\theta}^{(t)}), \sum_{i=1}^n \bar{p}_i(\hat{\mathbf{L}}) \nabla_{\boldsymbol{\theta}}(\mathcal{L}_i \circ h_i)(\boldsymbol{\theta}^{(t)}) \rangle \right| \\
&= \left| \langle \sum_{i=1}^n (\bar{p}_i(\check{\mathbf{L}}) - \bar{p}_i(\hat{\mathbf{L}})) \nabla_{\boldsymbol{\theta}}(\mathcal{L}_i \circ h_i)(\boldsymbol{\theta}^{(t)}), \sum_{i=1}^n \bar{p}_i(\hat{\mathbf{L}}) \nabla_{\boldsymbol{\theta}}(\mathcal{L}_i \circ h_i)(\boldsymbol{\theta}^{(t)}) \rangle \right|
\end{aligned} \tag{A.87}$$

Using Cauchy-Schwarz inequality

$$\begin{aligned}
A &= \left| \sum_{i=1}^n (\bar{p}_i(\check{\mathbf{L}}) - \bar{p}_i(\hat{\mathbf{L}})) \langle \nabla_{\boldsymbol{\theta}}(\mathcal{L}_i \circ h_i)(\boldsymbol{\theta}^{(t)}), \sum_{j=1}^n \bar{p}_j(\hat{\mathbf{L}}) \nabla_{\boldsymbol{\theta}}(\mathcal{L}_j \circ h_j)(\boldsymbol{\theta}^{(t)}) \rangle \right| \\
&\leq \left\| \hat{\mathbf{p}}(\hat{\mathbf{L}}) - \hat{\mathbf{p}}(\check{\mathbf{L}}) \right\|_2 \sqrt{\sum_{i=1}^n \left(\langle \nabla_{\boldsymbol{\theta}}(\mathcal{L}_i \circ h_i)(\boldsymbol{\theta}^{(t)}), \sum_{j=1}^n \bar{p}_j(\hat{\mathbf{L}}) \nabla_{\boldsymbol{\theta}}(\mathcal{L}_j \circ h_j)(\boldsymbol{\theta}^{(t)}) \rangle \right)^2}
\end{aligned} \tag{A.88}$$

Let

$$B = \langle \nabla_{\boldsymbol{\theta}}(\mathcal{L}_i \circ h_i)(\boldsymbol{\theta}^{(t)}), \sum_{j=1}^n \bar{p}_j(\hat{\mathbf{L}}) \nabla_{\boldsymbol{\theta}}(\mathcal{L}_j \circ h_j)(\boldsymbol{\theta}^{(t)}) \rangle \tag{A.89}$$

Using again Cauchy-Schwarz inequality

$$B \leq \left\| \nabla_{\boldsymbol{\theta}}(\mathcal{L}_i \circ h_i)(\boldsymbol{\theta}^{(t)}) \right\|_{2,2} \left\| \sum_{j=1}^n \bar{p}_j(\hat{\mathbf{L}}) \nabla_{\boldsymbol{\theta}}(\mathcal{L}_j \circ h_j)(\boldsymbol{\theta}^{(t)}) \right\|_{2,2} \tag{A.90}$$

As a result, A becomes

$$\begin{aligned}
A &\leq \left\| \hat{\mathbf{p}}(\hat{\mathbf{L}}) - \hat{\mathbf{p}}(\check{\mathbf{L}}) \right\|_2 \left\| \sum_{j=1}^n \bar{p}_j(\hat{\mathbf{L}}) \nabla_{\boldsymbol{\theta}}(\mathcal{L}_j \circ h_j)(\boldsymbol{\theta}^{(t)}) \right\|_{2,2} \sqrt{\sum_{i=1}^n \left\| \nabla_{\boldsymbol{\theta}}(\mathcal{L}_i \circ h_i)(\boldsymbol{\theta}^{(t)}) \right\|_{2,2}^2} \\
&\leq \left\| \hat{\mathbf{p}}(\hat{\mathbf{L}}) - \hat{\mathbf{p}}(\check{\mathbf{L}}) \right\|_2 \left\| \sum_{j=1}^n \bar{p}_j(\hat{\mathbf{L}}) \nabla_{\boldsymbol{\theta}}(\mathcal{L}_j \circ h_j)(\boldsymbol{\theta}^{(t)}) \right\|_{2,2} \sqrt{\sum_{i=1}^n \frac{1}{\alpha^2} \left\| \bar{p}_j(\hat{\mathbf{L}}) \nabla_{\boldsymbol{\theta}}(\mathcal{L}_i \circ h_i)(\boldsymbol{\theta}^{(t)}) \right\|_{2,2}^2} \\
&\leq \frac{1}{\alpha} \left\| \hat{\mathbf{p}}(\hat{\mathbf{L}}) - \hat{\mathbf{p}}(\check{\mathbf{L}}) \right\|_2 \left\| \sum_{j=1}^n \bar{p}_j(\hat{\mathbf{L}}) \nabla_{\boldsymbol{\theta}}(\mathcal{L}_j \circ h_j)(\boldsymbol{\theta}^{(t)}) \right\|_{2,2}^2
\end{aligned} \tag{A.91}$$

Using the triangular inequality, Theorem A.4.7, and Lemma A.4.9, we finally obtain

$$\begin{aligned} A &\leq \frac{m}{\alpha d} \left\| \hat{\mathbf{p}}(\hat{\mathbf{L}}) - \hat{\mathbf{p}}(\check{\mathbf{L}}) \right\|_2 \sum_{j=1}^n \left\| \bar{p}_j(\hat{\mathbf{L}}) \nabla_{h_j} \mathcal{L}_j(h_j(\boldsymbol{\theta}^{(t)})) \right\|_{2,2}^2 \\ &\leq \eta \frac{m}{d} K' \sum_{j=1}^n \left\| \bar{p}_j(\hat{\mathbf{L}}) \nabla_{h_j} \mathcal{L}_j(h_j(\boldsymbol{\theta}^{(t)})) \right\|_{2,2}^2 \end{aligned} \quad (\text{A.92})$$

Proof of technical lemma 4

We have

$$\begin{aligned} \left\| \nabla_h (R \circ \mathbf{L})(h(\boldsymbol{\theta}^{(t)})) \right\|_{1,2} &= \sum_{j=1}^n \bar{p}_j(\check{\mathbf{L}}) \left\| \nabla_{h_j} \mathcal{L}_j(h_j(\boldsymbol{\theta}^{(t)})) \right\|_{2,2} \\ &= \sum_{j=1}^n \bar{p}_j(\hat{\mathbf{L}}) \left\| \nabla_{h_j} \mathcal{L}_j(h_j(\boldsymbol{\theta}^{(t)})) \right\|_{2,2} \\ &\quad + \sum_{j=1}^n \left(\frac{\bar{p}_j(\check{\mathbf{L}}) - \bar{p}_j(\hat{\mathbf{L}})}{\bar{p}_j(\hat{\mathbf{L}})} \right) \bar{p}_j(\hat{\mathbf{L}}) \left\| \nabla_{h_j} \mathcal{L}_j(h_j(\boldsymbol{\theta}^{(t)})) \right\|_{2,2} \end{aligned} \quad (\text{A.93})$$

Using Cauchy-Schwarz inequality

$$\left\| \nabla_h (R \circ \mathbf{L})(h(\boldsymbol{\theta}^{(t)})) \right\|_{1,2} \leq \left(\sqrt{n} + \sqrt{\sum_{j=1}^n \left(\frac{\bar{p}_j(\check{\mathbf{L}}) - \bar{p}_j(\hat{\mathbf{L}})}{\bar{p}_j(\hat{\mathbf{L}})} \right)^2} \right) \sqrt{\sum_{j=1}^n \left\| \bar{p}_j(\hat{\mathbf{L}}) \nabla_{h_j} \mathcal{L}_j(h_j(\boldsymbol{\theta}^{(t)})) \right\|_{2,2}^2} \quad (\text{A.94})$$

Using Lemma A.4.9

$$\begin{aligned} \sum_{j=1}^n \left(\frac{\bar{p}_j(\check{\mathbf{L}}) - \bar{p}_j(\hat{\mathbf{L}})}{\bar{p}_j(\hat{\mathbf{L}})} \right)^2 &\leq \frac{1}{\alpha} \left\| \hat{\mathbf{p}}(\hat{\mathbf{L}}) - \hat{\mathbf{p}}(\check{\mathbf{L}}) \right\|_2 \\ &\leq \eta K' \end{aligned} \quad (\text{A.95})$$

Therefore, we finally obtain

$$\left\| \nabla_h (R \circ \mathbf{L})(h(\boldsymbol{\theta}^{(t)})) \right\|_{1,2} \leq (\sqrt{n} + \eta K') \sqrt{\sum_{j=1}^n \left\| \bar{p}_j(\hat{\mathbf{L}}) \nabla_{h_j} \mathcal{L}_j(h_j(\boldsymbol{\theta}^{(t)})) \right\|_{2,2}^2} \quad (\text{A.96})$$

A.5 Additional Results for chapter 7

A.5.1 Class-wise Quantitative Evaluation.

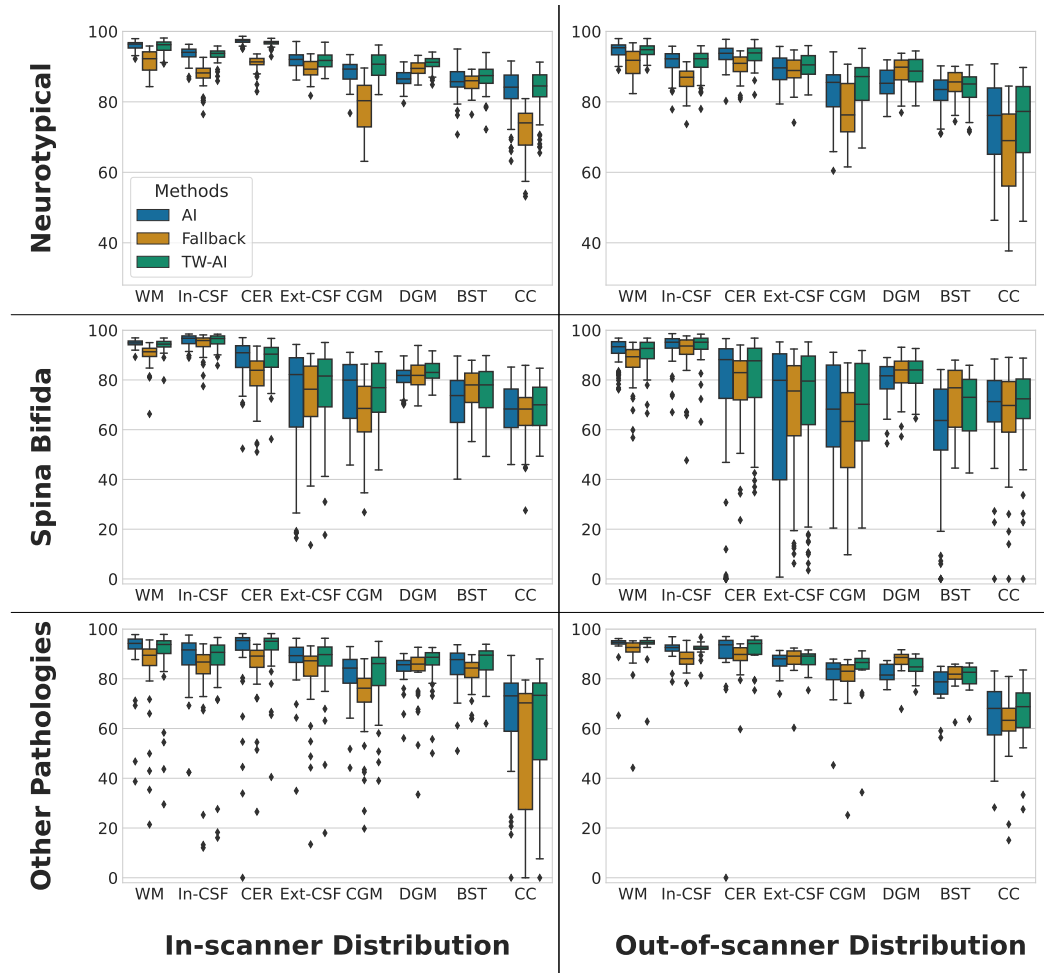


Figure A.2: **Dice score (in %) comparison of our AI, fallback, and trustworthy AI segmentation algorithms for fetal brain 3D MRI segmentation.** Dice scores are reported for all 3D MRI for 7 tissue types: white matter (**WM**), intra-axial cerebrospinal fluid (**in-CSF**), cerebellum (**Cer**), extra-axial cerebrospinal fluid (**Ext-CSF**), cortical gray matter (**CGM**), deep gray matter (**DGM**), brainstem (**BST**), and corpus callosum (**CC**). Box limits are the first quartiles and third quartiles. The central ticks are the median values. The whiskers extend the boxes to show the rest of the distribution, except for points that are determined to be outliers. Outliers are data points outside the range $\text{median} \pm 1.5 \times$ interquartile range. Fig. 7.6c was obtained from the same data after averaging the scores across regions of interest for each 3D MRI.

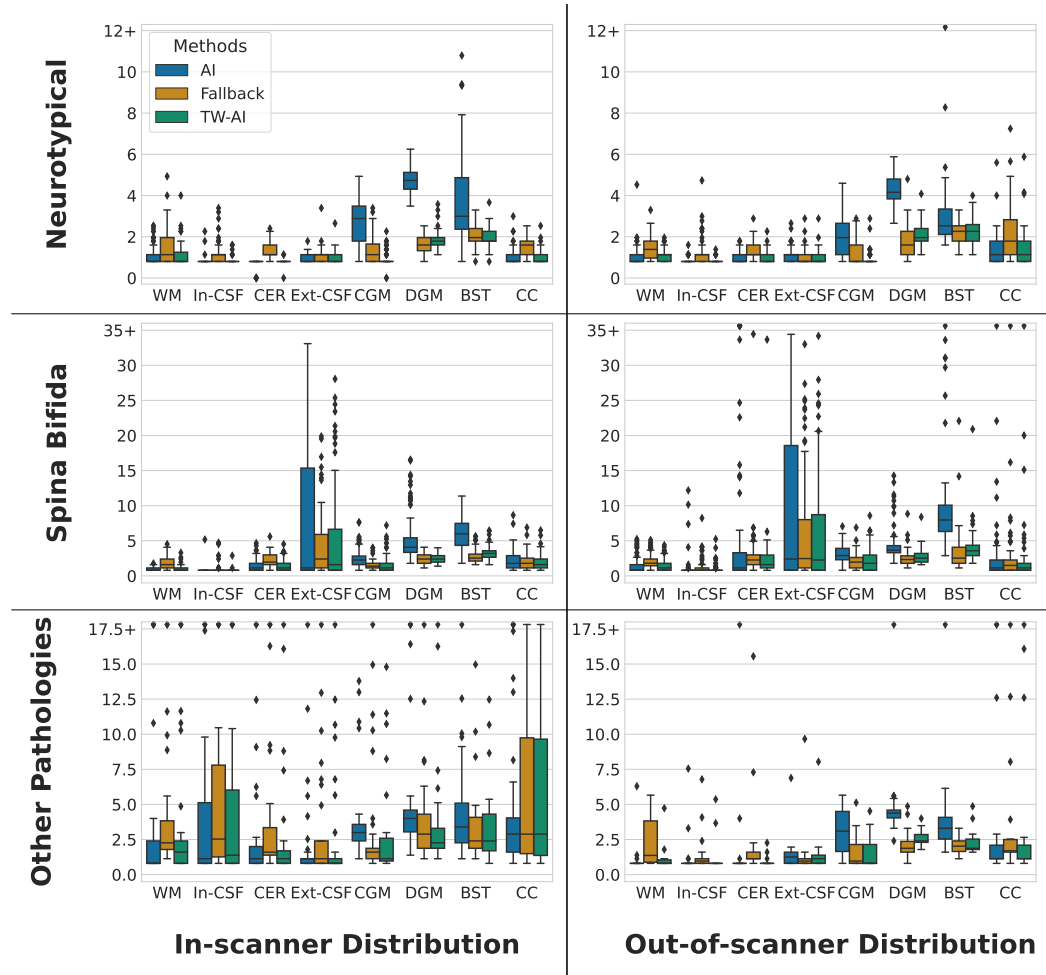


Figure A.3: **Hausdorff distance (in mm) comparison of our AI, fallback, and trustworthy AI segmentation algorithms for fetal brain 3D MRI segmentation.** The organization and legend of this figure is the same as in Fig. 7.6a, except that here the Hausdorff distance at 95% percentile is reported in place of the Dice score. To improve the visualization we have clipped the distances to a maximum value. The clipped outliers are still visible on the top of each boxplot. Fig. 7.6b was obtained from the same data after averaging the scores across regions of interest for each 3D MRI. Box limits are the first quartiles and third quartiles. The central ticks are the median values. The whiskers extend the boxes to show the rest of the distribution, except for points that are determined to be outliers. Outliers are data points outside the range $\pm 1.5 \times$ interquartile range.

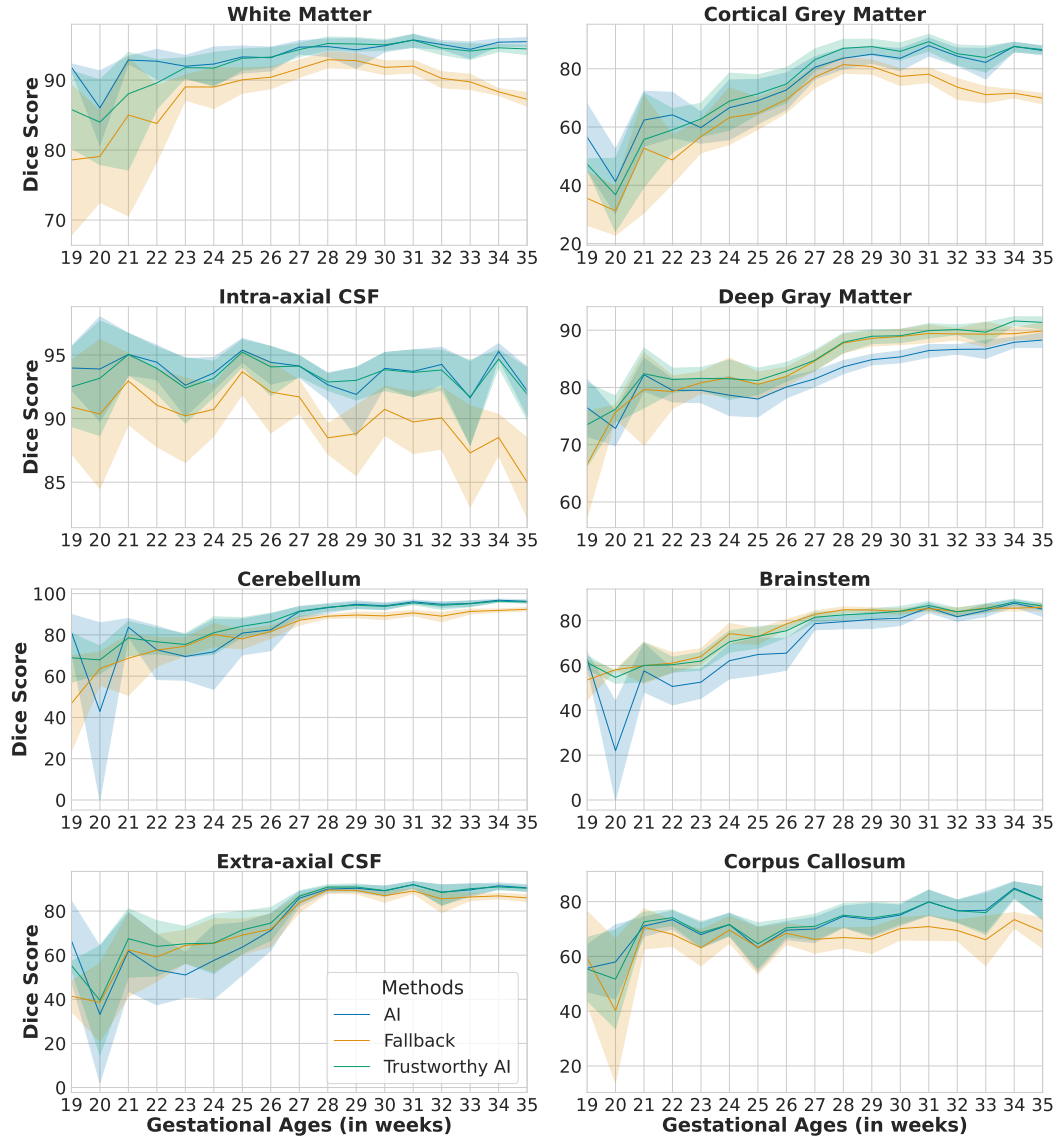


Figure A.4: **Mean Dice score (in %) and 95% confidence interval as a function of the gestational age.** Here, we have used all the neurotypical and the spina bifida cases of the testing dataset. The trustworthy AI (in green) algorithm achieves similar or higher Dice scores than the best of the backbone AI (in blue) and the fallback (in orange) for all tissue type and all gestational age. Fig. 7.6c was obtained from the same data after averaging the scores across regions of interest for each 3D MRI. Box limits are the first quartiles and third quartiles. The central ticks are the median values. The whiskers extend the boxes to show the rest of the distribution, except for points that are determined to be outliers. Outliers are data points outside the range $\text{median} \pm 1.5 \times \text{interquartile range}$.

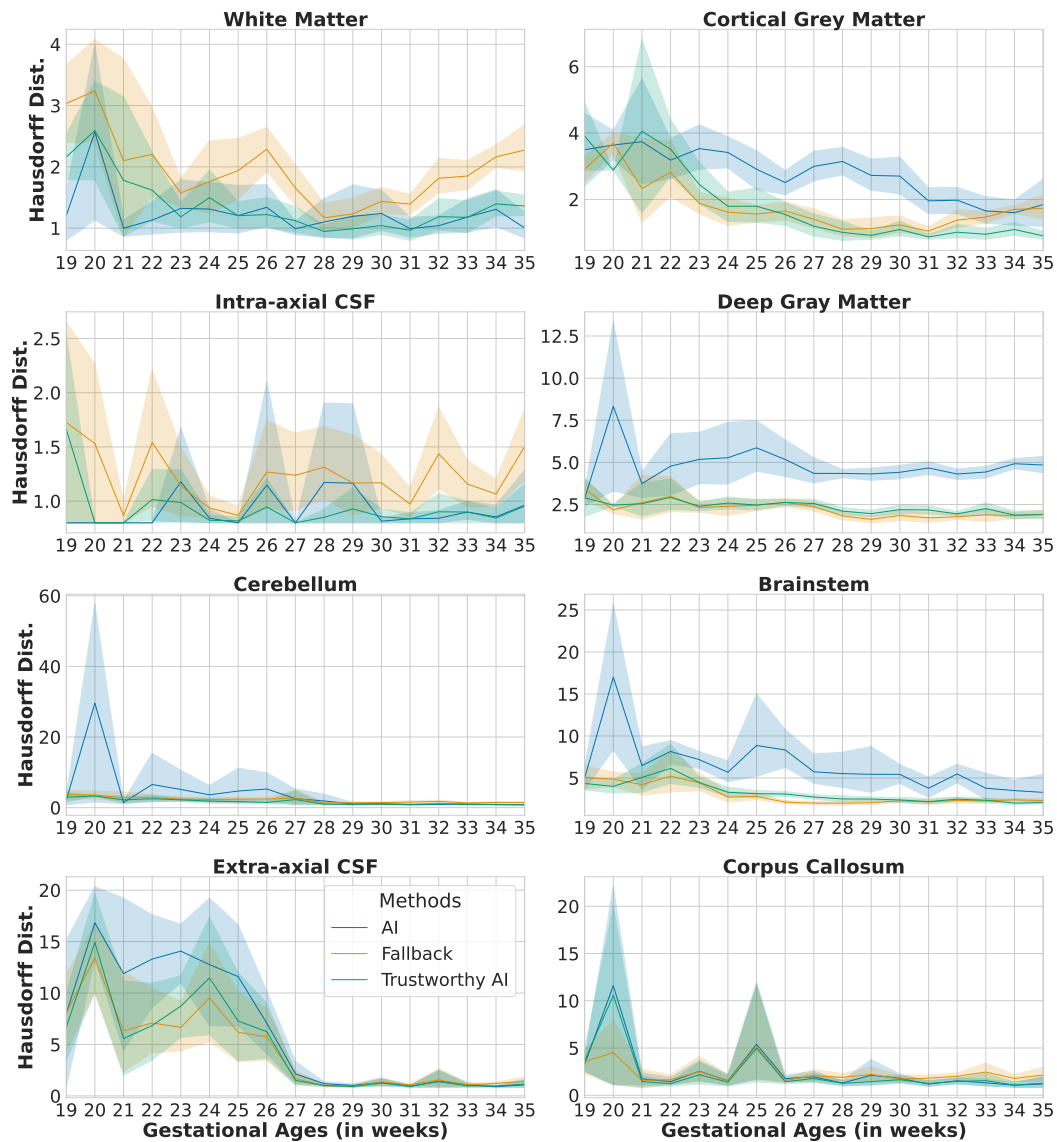


Figure A.5: Mean Hausdorff distance (in mm) and 95% confidence interval as a function of the gestational age. Here, we have used all the neurotypical and the spina bifida cases of the testing dataset. The trustworthy IA (in green) algorithm achieves similar or lower Hausdorff distance than the best of the backbone AI (in blue) and the fallback (in orange) for all tissue type and all gestational age. Fig. 7.6d was obtained from the same data after averaging the scores across regions of interest for each 3D MRI.

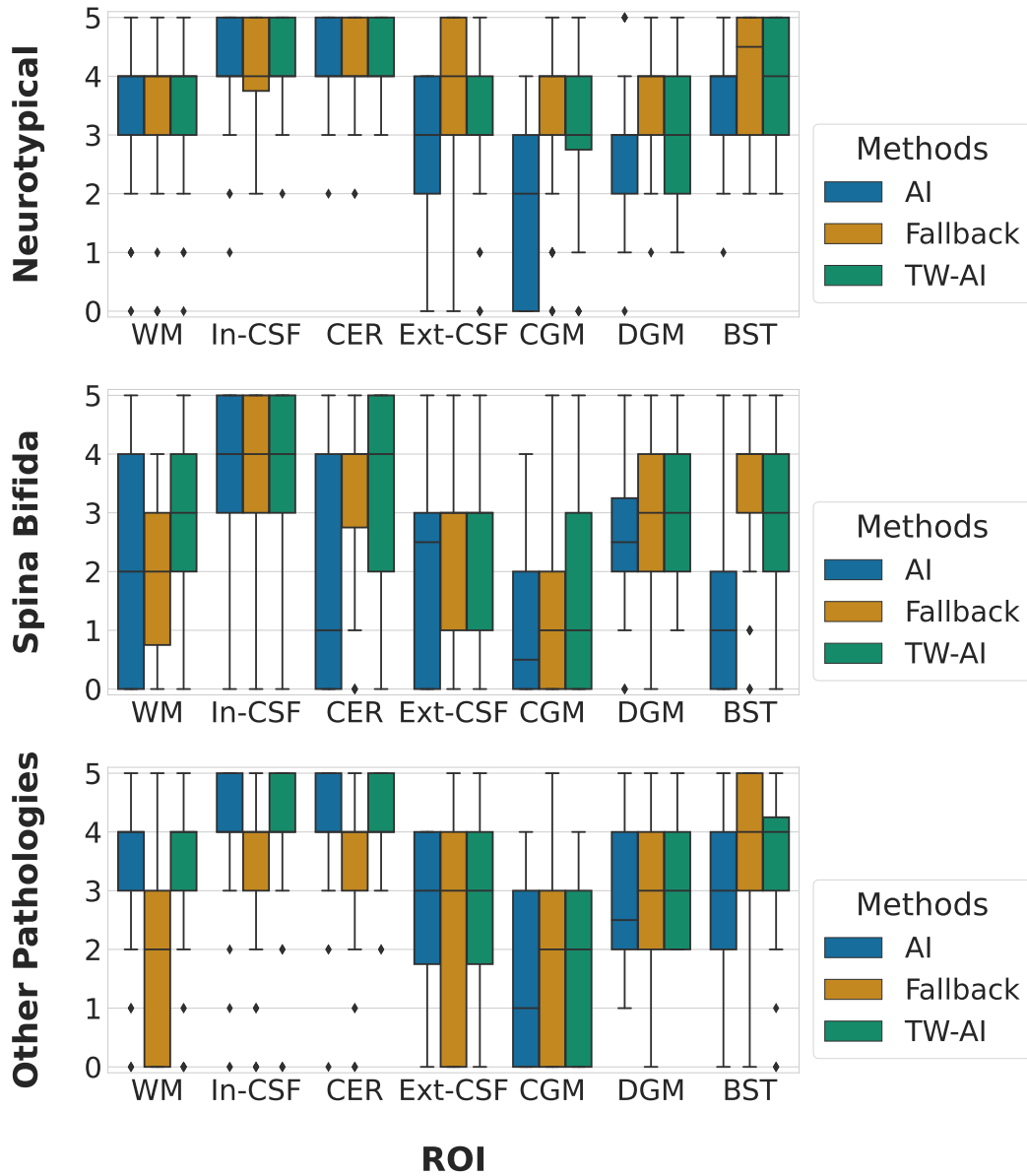


Figure A.6: **Experts scores for out-of-distribution 3D MRIs.** A panel of 8 experts performed 4 independent scoring for each ROI. The scores of different experts for a given region of interest and for a given 3D MRI were aggregated using averaging. Here, we have used 50 out-of-scanner distribution 3D MRIs from the FeTA dataset (20 neurotypical, 20 spina bifida, and 10 other pathologies). Box limits are the first quartiles and third quartiles. The central ticks are the median values. The whiskers extend the boxes to show the rest of the distribution, except for points that are determined to be outliers. Outliers are data points outside the range median $\pm 1.5 \times$ interquartile range. Fig. 7.6e was obtained from the same data after averaging the scores across regions of interest for each 3D MRI.

A.5.2 Tuning of the Registration Parameters

Table A.2: **Tuning of the registration parameters.** We report the population average of the mean-class Dice score (DSC) in percentages. We also report the average number of volumes that need to be registered for each configuration. This number is approximately proportional to the computational time for the segmentation computation. The 3D MRIs used were the fold 0 of the training dataset. The row highlighted in **blue** (resp. **orange**) correspond to the value of ΔGA selected for the neurotypical cases (resp. the spina bifida cases). A higher value of ΔGA leads to using more volumes in the fallback, registration-based segmentation method. Hence, this difference of ΔGA reflects the use of two neurotypical atlases [Gholipour 17, Wu 21] while only one spina bifida atlas [Fidon 21e] is available.

Atlas fusion	Atlas selection	ΔGA	DSC Control	DSC Spina bifida	Average #volumes
Mean	Condition	0	83.9	70.0	1.6
Mean	Condition	1	84.7	72.4	4.8
Mean	Condition	2	84.8	73.1	7.7
Mean	Condition	3	84.9	73.3	10.4
Mean	Condition	4	85.1	73.3	13.0
Mean	All	0	82.0	66.4	3.1
Mean	All	1	84.6	67.8	9.4
Mean	All	2	85.0	66.9	15.3
Mean	All	3	85.1	66.8	20.8
Mean	All	4	85.2	66.8	26.0
GIF	Condition	0	84.0	72.0	1.6
GIF	Condition	1	84.8	76.1	4.8
GIF	Condition	2	85.0	76.9	7.7
GIF	Condition	3	85.2	77.6	10.4
GIF	Condition	4	85.4	77.7	13.0
GIF	All	0	84.1	72.0	3.1
GIF	All	1	84.9	74.6	9.4
GIF	All	2	85.2	75.1	15.3
GIF	All	3	85.3	75.4	20.8
GIF	All	4	85.5	75.3	26.0

A.6 Proofs of chapter 7

A.6.1 Proof of the Formula (7.15) for the Anatomical BPA.

In this section we give the proof for the formula (7.15): For all voxel \mathbf{x} and all $\mathbf{C}' \subset \mathbf{C}$,

$$\begin{aligned} m_{I,\mathbf{x}}^{\text{anatomy}}(\mathbf{C} \setminus \mathbf{C}') &= \left(\bigoplus_{c \in \mathbf{C}} m_{\mathbf{x}}^{(c)} \right) (\mathbf{C} \setminus \mathbf{C}') \\ &= \prod_{c \in \mathbf{C}} \left(\delta_c(\mathbf{C}') m_{\mathbf{x}}^{(c)}(\mathbf{C} \setminus \{c\}) + (1 - \delta_c(\mathbf{C}')) m_{\mathbf{x}}^{(c)}(\mathbf{C}) \right) \end{aligned} \quad (\text{A.97})$$

To simplify the notations and without loss of generality, in this proof we assume that $\mathbf{C} = \{1, \dots, K\}$ with K the number of classes. This simply amounts to renaming the classes by the numbers from 1 to K .

Equation (A.97), that we want to prove, can then be rewritten as

$$m_{I,\mathbf{x}}^{\text{anatomy}}(\mathbf{C} \setminus \mathbf{C}') = \prod_{c=1}^K \left(\delta_c(\mathbf{C}') m_{\mathbf{x}}^{(c)}(\mathbf{C} \setminus \{c\}) + (1 - \delta_c(\mathbf{C}')) m_{\mathbf{x}}^{(c)}(\mathbf{C}) \right) \quad (\text{A.98})$$

Let us first give the reader an intuition of the formula that we will prove by computing the Dempster's rule of combination for the first two BPAs $m_{\mathbf{x}}^{(1)}$ and $m_{\mathbf{x}}^{(2)}$. To simplify the calculations, we will write the Dempster's rule of combination for complements of sets like in (A.97).

Let $\mathbf{C}' \subsetneq \mathbf{C}$, using the definition of Dempster's rule of combination (7.3) and using the relation $\forall \mathbf{G}, \mathbf{H} \subset \mathbf{C}, (\mathbf{C} \setminus \mathbf{G}) \cap (\mathbf{C} \setminus \mathbf{H}) = \mathbf{C} \setminus (\mathbf{G} \cup \mathbf{H})$

$$m_{\mathbf{x}}^{(1)} \oplus m_{\mathbf{x}}^{(2)}(\mathbf{C} \setminus \mathbf{C}') = \frac{\sum_{\mathbf{G}, \mathbf{H} \subset \mathbf{C} | \mathbf{G} \cup \mathbf{H} = \mathbf{C}'} m_{\mathbf{x}}^{(1)}(\mathbf{C} \setminus \mathbf{G}) m_{\mathbf{x}}^{(2)}(\mathbf{C} \setminus \mathbf{H})}{1 - \sum_{\mathbf{G}, \mathbf{H} \subset \mathbf{C} | \mathbf{G} \cup \mathbf{H} = \mathbf{C}} m_{\mathbf{x}}^{(1)}(\mathbf{C} \setminus \mathbf{G}) m_{\mathbf{x}}^{(2)}(\mathbf{C} \setminus \mathbf{H})} \quad (\text{A.99})$$

Using the definition of $m_{\mathbf{x}}^{(1)}$ and $m_{\mathbf{x}}^{(2)}$ in (7.12), $m_{\mathbf{x}}^{(1)}(\mathbf{C} \setminus \mathbf{G}) = 0$ if $\mathbf{G} \notin \{\emptyset, \{1\}\}$ and $m_{\mathbf{x}}^{(2)}(\mathbf{C} \setminus \mathbf{H}) = 0$ if $\mathbf{H} \notin \{\emptyset, \{2\}\}$.

This implies that the sum in the denominator is equal to zeros and that there are only four possible values of \mathbf{C}' such that the numerator is non zeros, i.e. $\mathbf{C}' \in \{\emptyset, \{1\}, \{2\}, \{1, 2\}\}$. This gives

$$\begin{aligned} \left(m_{\mathbf{x}}^{(1)} \oplus m_{\mathbf{x}}^{(2)} \right) (\mathbf{C}) &= m_{\mathbf{x}}^{(1)}(\mathbf{C}) m_{\mathbf{x}}^{(2)}(\mathbf{C}) \\ \left(m_{\mathbf{x}}^{(1)} \oplus m_{\mathbf{x}}^{(2)} \right) (\mathbf{C} \setminus \{1\}) &= m_{\mathbf{x}}^{(1)}(\mathbf{C} \setminus \{1\}) m_{\mathbf{x}}^{(2)}(\mathbf{C}) \\ \left(m_{\mathbf{x}}^{(1)} \oplus m_{\mathbf{x}}^{(2)} \right) (\mathbf{C} \setminus \{2\}) &= m_{\mathbf{x}}^{(1)}(\mathbf{C}) m_{\mathbf{x}}^{(2)}(\mathbf{C} \setminus \{2\}) \\ \left(m_{\mathbf{x}}^{(1)} \oplus m_{\mathbf{x}}^{(2)} \right) (\mathbf{C} \setminus \{1, 2\}) &= m_{\mathbf{x}}^{(1)}(\mathbf{C} \setminus \{1\}) m_{\mathbf{x}}^{(2)}(\mathbf{C} \setminus \{2\}) \end{aligned} \quad (\text{A.100})$$

and $(m_{\mathbf{x}}^{(1)} \oplus m_{\mathbf{x}}^{(2)})(\mathbf{C} \setminus \mathbf{C}') = 0$ for all other values of \mathbf{C}' .

A general formula is given by, $\mathbf{C}' \subset \mathbf{C}$,

$$\begin{aligned} & (m_{\mathbf{x}}^{(1)} \oplus m_{\mathbf{x}}^{(2)})(\mathbf{C} \setminus \mathbf{C}') = \\ & \prod_{c=3}^K (1 - \delta_c(\mathbf{C}')) \prod_{c=1}^2 \left(\delta_c(\mathbf{C}') m_{\mathbf{x}}^{(c)}(\mathbf{C} \setminus \{c\}) + (1 - \delta_c(\mathbf{C}')) m_{\mathbf{x}}^{(c)}(\mathbf{C}) \right) \end{aligned} \quad (\text{H}_2)$$

For clarity we remind that for all $c \in \mathbf{C}$, δ_c is the Dirac measure associated with c defined as

$$\forall \mathbf{C}' \subset \mathbf{C}, \quad \delta_c(\mathbf{C}') = \begin{cases} 1 & \text{if } c \in \mathbf{C}' \\ 0 & \text{if } c \notin \mathbf{C}' \end{cases} \quad (\text{A.101})$$

The idea of the proof is to generalize formula (H₂) to all the combinations of the first k anatomical BPAs until reaching $k = K$.

For all $k \in \{2, \dots, K\}$, we defined (H_k) as

$$\begin{aligned} & \left(\bigoplus_{c=1}^k m_{\mathbf{x}}^{(c)} \right) (\mathbf{C} \setminus \mathbf{C}') = \\ & \prod_{c=k+1}^K (1 - \delta_c(\mathbf{C}')) \prod_{c=1}^k \left(\delta_c(\mathbf{C}') m_{\mathbf{x}}^{(c)}(\mathbf{C} \setminus \{c\}) + (1 - \delta_c(\mathbf{C}')) m_{\mathbf{x}}^{(c)}(\mathbf{C}) \right) \end{aligned} \quad (\text{H}_k)$$

When $k = K$, the set of indices for the first product is empty and the product is equal to 1 by convention. Therefore, H_K is exactly the same as relation (A.97) that we want to prove. We will prove this equality by induction on the variable k for k from 2 to K .

We have already proven (H₂). It remains to demonstrate that, for all k from 2 to $K - 1$, H_k holds true implies that H_{k+1} also holds true.

Let $k \in \{2, \dots, K - 1\}$, let us assume that H_k is true.

Let $\mathbf{C}' \subsetneq \mathbf{C}$, using the same formula as in (A.99)

$$\begin{aligned} & \left(\bigoplus_{c=1}^k m_{\mathbf{x}}^{(c)} \right) \oplus m_{\mathbf{x}}^{(k+1)}(\mathbf{C} \setminus \mathbf{C}') = \\ & \frac{\sum_{\mathbf{G}, \mathbf{H} \subset \mathbf{C} \mid \mathbf{G} \cup \mathbf{H} = \mathbf{C}'} \left(\bigoplus_{c=1}^k m_{\mathbf{x}}^{(c)} \right) (\mathbf{C} \setminus \mathbf{G}) m_{\mathbf{x}}^{(k+1)}(\mathbf{C} \setminus \mathbf{H})}{1 - \sum_{\mathbf{G}, \mathbf{H} \subset \mathbf{C} \mid \mathbf{G} \cup \mathbf{H} = \mathbf{C}} \left(\bigoplus_{c=1}^k m_{\mathbf{x}}^{(c)} \right) (\mathbf{C} \setminus \mathbf{G}) m_{\mathbf{x}}^{(k+1)}(\mathbf{C} \setminus \mathbf{H})} \end{aligned} \quad (\text{A.102})$$

Let us denote

$$N = \sum_{\mathbf{G}, \mathbf{H} \subset \mathbf{C} \mid \mathbf{G} \cup \mathbf{H} = \mathbf{C}} \left(\bigoplus_{c=1}^k m_{\mathbf{x}}^{(c)} \right) (\mathbf{C} \setminus \mathbf{G}) m_{\mathbf{x}}^{(k+1)}(\mathbf{C} \setminus \mathbf{H}) \quad (\text{A.103})$$

Let us first demonstrate that $N = 0$. Using the definition of $m_{\mathbf{x}}^{(k+1)}$ in (7.12), $m_{\mathbf{x}}^{(k+1)}(\mathbf{C} \setminus \mathbf{G}) = 0$ if $\mathbf{G} \notin \{\emptyset, \{k+1\}\}$. Therefore, we need only to study the cases $G \in \{\mathbf{C}, \mathbf{C} \setminus \{k+1\}\}$.

For $G = \mathbf{C}$, $(\bigoplus_{c=1}^k m_{\mathbf{x}}^{(c)})(\mathbf{C} \setminus \mathbf{G}) = (\bigoplus_{c=1}^k m_{\mathbf{x}}^{(c)})(\emptyset) = 0$ like for every basic probability assignment (BPA).

For $G = \mathbf{C} \setminus \{k+1\}$, according to (H_k) , that we have assumed true,

$$\begin{aligned} \left(\bigoplus_{c=1}^k m_{\mathbf{x}}^{(c)}\right)(\mathbf{C} \setminus \mathbf{G}) &= \left(\bigoplus_{c=1}^k m_{\mathbf{x}}^{(c)}\right)(\{k+1\}) \\ &= \prod_{c=k+1}^K (1 - \delta_c(\mathbf{C} \setminus \{k+1\})) \prod_{c=1}^k m_{\mathbf{x}}^{(c)}(\mathbf{C} \setminus \{c\}) \end{aligned} \quad (\text{A.104})$$

We have to consider two cases, $k+1 < K$ and $k+1 = K$.

If $k+1 < K$, the second term in the first product of (A.104) is equal to 0 and therefore $(\bigoplus_{c=1}^k m_{\mathbf{x}}^{(c)})(\{k+1\})m_{\mathbf{x}}^{(k+1)}(\mathbf{C} \setminus \{k+1\}) = 0$

If $k+1 = K$, we have

$$\left(\bigoplus_{c=1}^k m_{\mathbf{x}}^{(c)}\right)(\{k+1\})m_{\mathbf{x}}^{(k+1)}(\mathbf{C} \setminus \{k+1\}) = \prod_{c=1}^K m_{\mathbf{x}}^{(c)}(\mathbf{C} \setminus \{c\}) \quad (\text{A.105})$$

Voxel \mathbf{x} belongs to at least one of the class binary masks. Let us denote c_0 the binary mask to which is voxel \mathbf{x} belongs to. Using the definition of $m_{\mathbf{x}}^{(c_0)}$ in (7.12), we have $m_{\mathbf{x}}^{(c_0)}(\mathbf{C} \setminus \{c_0\}) = 0$. Therefore, the product above is equal to 0. This allows us to conclude, in every case, that $N = 0$.

Therefore, (A.102) becomes

$$\begin{aligned} \left(\bigoplus_{c=1}^k m_{\mathbf{x}}^{(c)}\right) \oplus m_{\mathbf{x}}^{(k+1)}(\mathbf{C} \setminus \mathbf{C}') &= \\ \sum_{\mathbf{G}, \mathbf{H} \subset \mathbf{C} | \mathbf{G} \cup \mathbf{H} = \mathbf{C}'} \left(\bigoplus_{c=1}^k m_{\mathbf{x}}^{(c)}\right)(\mathbf{C} \setminus \mathbf{G})m_{\mathbf{x}}^{(k+1)}(\mathbf{C} \setminus \mathbf{H}) \end{aligned} \quad (\text{A.106})$$

Similarly as before, due to the definition of $m_{\mathbf{x}}^{(k+1)}$, we only need to study the cases of the sets \mathbf{G} that are solutions of $\mathbf{G} \cap \emptyset = \mathbf{C}'$ or $\mathbf{G} \cap \{k+1\} = \mathbf{C}'$. The first equality has the unique solution $\mathbf{G} = \mathbf{C}'$ and the second equality has either no solution, if $k+1 \notin \mathbf{C}'$, or two solutions $G \in \{\mathbf{C}' \setminus \{k+1\}, \mathbf{C}'\}$ if $k+1 \in \mathbf{C}'$. Using the Dirac

measure, we can treat all the cases at once and (A.106) becomes

$$\begin{aligned} \left(\bigoplus_{c=1}^k m_{\mathbf{x}}^{(c)} \right) \oplus m_{\mathbf{x}}^{(k+1)}(\mathbf{C} \setminus \mathbf{C}') &= \left(\bigoplus_{c=1}^k m_{\mathbf{x}}^{(c)} \right) (\mathbf{C} \setminus \mathbf{C}') m_{\mathbf{x}}^{(k+1)}(\mathbf{C}) \\ &+ \delta_{k+1}(\mathbf{C}') \left(\bigoplus_{c=1}^k m_{\mathbf{x}}^{(c)} \right) (\mathbf{C} \setminus \mathbf{C}') m_{\mathbf{x}}^{(k+1)}(\mathbf{C} \setminus \{k+1\}) \\ &+ \delta_{k+1}(\mathbf{C}') \left(\bigoplus_{c=1}^k m_{\mathbf{x}}^{(c)} \right) (\mathbf{C} \setminus (\mathbf{C}' \setminus \{k+1\})) m_{\mathbf{x}}^{(k+1)}(\mathbf{C} \setminus \{k+1\}) \end{aligned} \quad (\text{A.107})$$

Using (H_k), we can rewrite the second term of (A.107) as

$$\begin{aligned} \delta_{k+1}(\mathbf{C}') \left(\bigoplus_{c=1}^k m_{\mathbf{x}}^{(c)} \right) (\mathbf{C} \setminus \mathbf{C}') &= \\ \delta_{k+1}(\mathbf{C}') \prod_{c=k+1}^K (1 - \delta_c(\mathbf{C}')) \prod_{c=1}^k \left(\delta_c(\mathbf{C}') m_{\mathbf{x}}^{(c)}(\mathbf{C} \setminus \{c\}) + (1 - \delta_c(\mathbf{C}')) m_{\mathbf{x}}^{(c)}(\mathbf{C}) \right) \end{aligned} \quad (\text{A.108})$$

The product of the first two terms of the product on the right-hand side is $\delta_{k+1}(\mathbf{C}')(1 - \delta_{k+1}(\mathbf{C}')) = 0$, independently to the value of \mathbf{C}' . Therefore, the second term of (A.107) is equal to zeros. Using (H_k), and by remarking that

$$\begin{aligned} \delta_{k+1}(\mathbf{C}' \setminus \{k+1\}) &= 0 \\ \forall c \in \mathbf{C} \setminus \{K+1\}, \quad \delta_{k+1}(\mathbf{C}' \setminus \{k+1\}) &= \delta_{k+1}(\mathbf{C}') \end{aligned} \quad (\text{A.109})$$

we obtain

$$\begin{aligned} \left(\bigoplus_{c=1}^k m_{\mathbf{x}}^{(c)} \right) (\mathbf{C} \setminus (\mathbf{C}' \setminus \{k+1\})) &= \\ \prod_{c=k+2}^K (1 - \delta_c(\mathbf{C}')) \prod_{c=1}^k \left(\delta_c(\mathbf{C}') m_{\mathbf{x}}^{(c)}(\mathbf{C} \setminus \{c\}) + (1 - \delta_c(\mathbf{C}')) m_{\mathbf{x}}^{(c)}(\mathbf{C}) \right) \end{aligned} \quad (\text{A.110})$$

Using this equality and (H_k), we can rewrite (A.107) as

$$\begin{aligned} \left(\bigoplus_{c=1}^k m_{\mathbf{x}}^{(c)} \right) \oplus m_{\mathbf{x}}^{(k+1)}(\mathbf{C} \setminus \mathbf{C}') &= \\ m_{\mathbf{x}}^{(k+1)}(\mathbf{C})(1 - \delta_{k+1}(\mathbf{C}')) \prod_{c=k+2}^K (1 - \delta_c(\mathbf{C}')) \prod_{c=1}^k \left(\delta_c(\mathbf{C}') m_{\mathbf{x}}^{(c)}(\mathbf{C} \setminus \{c\}) + (1 - \delta_c(\mathbf{C}')) m_{\mathbf{x}}^{(c)}(\mathbf{C}) \right) \\ &+ \delta_{k+1}(\mathbf{C}') m_{\mathbf{x}}^{(k+1)}(\mathbf{C} \setminus \{k+1\}) \prod_{c=k+2}^K (1 - \delta_c(\mathbf{C}')) \prod_{c=1}^k \left(\delta_c(\mathbf{C}') m_{\mathbf{x}}^{(c)}(\mathbf{C} \setminus \{c\}) + (1 - \delta_c(\mathbf{C}')) m_{\mathbf{x}}^{(c)}(\mathbf{C}) \right) \end{aligned} \quad (\text{A.111})$$

By grouping the two terms we eventually obtain that H_{k+1} holds true, i.e.

$$\begin{aligned} \left(\bigoplus_{c=1}^{k+1} m_{\mathbf{x}}^{(c)} \right) (\mathbf{C} \setminus \mathbf{C}') = \\ \prod_{c=k+2}^K (1 - \delta_c(\mathbf{C}')) \prod_{c=1}^{k+1} \left(\delta_c(\mathbf{C}') m_{\mathbf{x}}^{(c)} (\mathbf{C} \setminus \{c\}) + (1 - \delta_c(\mathbf{C}')) m_{\mathbf{x}}^{(c)} (\mathbf{C}) \right) \end{aligned} \quad (\text{A.112})$$

We have proved that H_2 is true and we have proved that for all k from 2 to $K - 1$, H_k holds true implies that H_{k+1} also holds true. Therefore, using the induction principle, we conclude that H_K is true. ■

A.6.2 Proof of Equality (7.17).

In this section, we give a proof of (7.17). It states that for all $c \in \mathbf{C}$,

$$\left(p_{I,\mathbf{x}} \oplus m_{I,\mathbf{x}}^{\text{anatomy}}\right)(c) = \frac{p_{I,\mathbf{x}}(c)m_{\mathbf{x}}^{(c)}(\mathbf{C})}{\sum_{c' \in \mathbf{C}} p_{I,\mathbf{x}}(c')m_{\mathbf{x}}^{(c')}(\mathbf{C})} \quad (\text{A.113})$$

We start the proof from the Dempster's rule of combination for a probability and a BPA (7.6).

$$\left(p_{I,\mathbf{x}} \oplus m_{I,\mathbf{x}}^{\text{anatomy}}\right)(c) = \frac{p_{I,\mathbf{x}}(c) \sum_{\mathbf{F} \subset \mathbf{C} | c \in \mathbf{F}} m_{I,\mathbf{x}}^{\text{anatomy}}(\mathbf{F})}{1 - \sum_{c' \in \mathbf{C}} \sum_{\mathbf{F} \subset (\mathbf{C} \setminus \{c'\})} p_{I,\mathbf{x}}(c')m_{I,\mathbf{x}}^{\text{anatomy}}(\mathbf{F})} \quad (\text{A.114})$$

We now rewrite this equation using complement sets in the numerator to be able to use the formula (7.15) for the anatomical BPAs.

$$\left(p_{I,\mathbf{x}} \oplus m_{I,\mathbf{x}}^{\text{anatomy}}\right)(c) = \frac{p_{I,\mathbf{x}}(c) \sum_{\mathbf{G} \subset (\mathbf{C} \setminus \{c\})} m_{I,\mathbf{x}}^{\text{anatomy}}(\mathbf{C} \setminus \mathbf{G})}{1 - \sum_{c' \in \mathbf{C}} \sum_{\mathbf{F} \subset (\mathbf{C} \setminus \{c'\})} p_{I,\mathbf{x}}(c')m_{I,\mathbf{x}}^{\text{anatomy}}(\mathbf{F})} \quad (\text{A.115})$$

Let us first simplify the numerator. Using (7.15) we obtain, for all $\mathbf{G} \subset (\mathbf{C} \setminus \{c\})$,

$$\begin{aligned} m_{I,\mathbf{x}}^{\text{anatomy}}(\mathbf{C} \setminus \mathbf{G}) &= \prod_{c' \in \mathbf{C}} \left(\delta_{c'}(\mathbf{C}')m_{\mathbf{x}}^{(c')}(\mathbf{C} \setminus \{c'\}) + (1 - \delta_{c'}(\mathbf{C}'))m_{\mathbf{x}}^{(c')}(\mathbf{C}) \right) \\ &= m_{\mathbf{x}}^{(c)}(\mathbf{C}) \left(\prod_{c' \in (\mathbf{C} \setminus \{c\})} \left(\delta_{c'}(\mathbf{C}')m_{\mathbf{x}}^{(c')}(\mathbf{C} \setminus \{c'\}) + (1 - \delta_{c'}(\mathbf{C}'))m_{\mathbf{x}}^{(c')}(\mathbf{C}) \right) \right) \end{aligned} \quad (\text{A.116})$$

Therefore the term $m_{\mathbf{x}}^{(c)}(\mathbf{C})$ can be factorized outside of the sum in the numerator of the right-hand side of (A.115). Let us denote the sum of the numerator, after factorization, as

$$A_c = \sum_{\mathbf{G} \subset (\mathbf{C} \setminus \{c\})} \prod_{c' \in (\mathbf{C} \setminus \{c\})} \left(\delta_{c'}(\mathbf{C}')m_{\mathbf{x}}^{(c')}(\mathbf{C} \setminus \{c'\}) + (1 - \delta_{c'}(\mathbf{C}'))m_{\mathbf{x}}^{(c')}(\mathbf{C}) \right) \quad (\text{A.117})$$

One can remark that the terms of the product are all independent of c . In addition, the c' th terms of the product is either $m_{\mathbf{x}}^{(c')}(\mathbf{C} \setminus \{c'\})$ or $m_{\mathbf{x}}^{(c')}(\mathbf{C})$ depending on \mathbf{G} and when summing over all $\mathbf{G} \subset (\mathbf{C} \setminus \{c\})$ we obtain all the possible products. Therefore, the sum can be factorized as

$$A_c = \prod_{c' \in (\mathbf{C} \setminus \{c\})} \left(m_{\mathbf{x}}^{(c')}(\mathbf{C} \setminus \{c'\}) + m_{\mathbf{x}}^{(c')}(\mathbf{C}) \right) \quad (\text{A.118})$$

Using the definition of the anatomical BPAs, we have, for all $c \in \mathbf{C}$, $m_{\mathbf{x}}^{(c)}(\mathbf{C} \setminus \{c'\}) +$

$m_{\mathbf{x}}^{(c')}(\mathbf{C}) = 1$. As a result, we obtain $A_c = 1$.

This proves, that

$$\left(p_{I,\mathbf{x}} \oplus m_{I,\mathbf{x}}^{\text{anatomy}}\right)(c) \propto p_{I,\mathbf{x}}(c)m_{\mathbf{x}}^{(c)}(\mathbf{C}) \quad (\text{A.119})$$

And since $\sum_{c \in \mathbf{C}} \left(p_{I,\mathbf{x}} \oplus m_{I,\mathbf{x}}^{\text{anatomy}}\right)(c) = 1$, we can conclude without additional calculations that

$$\left(p_{I,\mathbf{x}} \oplus m_{I,\mathbf{x}}^{\text{anatomy}}\right)(c) = \frac{p_{I,\mathbf{x}}(c)m_{\mathbf{x}}^{(c)}(\mathbf{C})}{\sum_{c' \in \mathbf{C}} p_{I,\mathbf{x}}(c')m_{\mathbf{x}}^{(c')}(\mathbf{C})} \quad (\text{A.120})$$

■